TOPOLOGICAL SUPERCONDUCTIVITY AND SUPERFLUIDITY IN QUASI-ONE-DIMENSIONAL QUANTUM SYSTEMS

A THESIS
SUBMITTED TO THE FACULTY OF THE GRADUATE SCHOOL
OF THE UNIVERSITY OF MINNESOTA
BY

CHUN CHEN

IN PARTIAL FULFILLMENT OF THE REQUIREMENTS
FOR THE DEGREE OF
DOCTOR OF PHILOSOPHY

PROF. FIONA BURNELL

AUGUST, 2017

© CHUN CHEN 2017
ALL RIGHTS RESERVED

Acknowledgements

First, I would like to thank my advisor, Prof. Fiona Burnell, for her careful guidance and generous support during the past four years. I find that her critical questions and insightful comments always stimulate a great promotion on my understanding of the problem.

Second, I would like to thank Profs. Boris Shklovskii, Tony Low, and Vlad Pribiag for their kindly serving as the committee members for my thesis defense and for reviewing my dissertation. Also, I would like to thank Profs. Martin Greven, Renata Wentzcovitch, and Oriol Valls for being the committee members of my oral examination.

Third, the collaboration with Prof. Chin-Sen Ting at Texas Center for Superconductivity and Prof. Yan Chen and Dr. Wei Yan from Fudan University is appreciated. I would also like to thank the postdocs and graduate students in the condensed matter group at the University of Minnesota for interesting conversations over the years.

Last but not least, I am deeply grateful to my parents and my sister for their loving support and encouragement. This thesis is dedicated to them.

Dedication

To my parents and my sister

Abstract

Topological superconductors and superfluids are an exciting class of recently discovered materials. In one dimension, topological superconductors accommodate a novel kind of bound state, known as a Majorana zero mode, at their endpoints, and introducing strong correlations can lead to systems with related types of bound states known as parafermions. In this thesis, we systematically studied three correlated aspects of topological superconductivity and superfluidity in low-dimensional quantum systems. By using Bogoliubov–de Gennes (BdG) theory combined with proper topological-invariant calculation, we first predicted a new topological Fulde–Ferrell–Larkin–Ovchinnikov (*topo*-FFLO) superfluid state in one-dimensional (1D) spin-orbit-coupled Fermi gases (with superfluid order stabilized by 3D interactions). Specifically we demonstrate that Majorana zero modes can exist even if the superconducting/superfluid pairing is at nonzero momentum (i.e. of FFLO type), provided that the magnitude of the superconducting/superfluid gap is finite. 1D topological superfluids are typically classified and understood through BdG mean-field Hamiltonians. This raises the question of whether they can exist in truly 1D systems where particle number is conserved. We discuss a new mechanism by which Majorana zero modes can arise in a number-conserving Fermi ladder. This interaction-enabled topological phase is protected by a unitary $\mathbb{Z}_2$ symmetry that is not related to any microscopic fermion-parity symmetry. Generalizations of Majorana bound states can also occur by inducing superconductivity at the boundary states of certain types of fractional quantum Hall bilayers. Then how could we detect them experimentally? In this thesis, we discuss two answers—dynamical signatures and characterizing the finite-sized splitting of the otherwise degenerate ground-state Hilbert space associated with these bound states. Particularly, in the process we demonstrate how instanton methods can be applied to the general problem of ground-state energy splittings in these systems.

Contents

List of Tables

List of Figures

Chapter 1

Introduction

1.1 Why are topological superconductors interesting?

A growing number of contemporary condensed matter physicists are engaged in uncovering the profound roles of symmetry, topology, and interactions in stabilizing exotic quantum states of matter. This collective endeavor inspires expositions of exceptional ideas and innovative concepts that advance the intellectual and aesthetic framework within which fundamental physics operates. Indeed, topological matter manifests the sublime beauty of abstract mathematical theories in realistic materials, and narrows the distance between condensed matter physics and high energy physics to accomplish a cross fertilization.

One of the most exciting developments in this area is the realization that two dimensional solid-state systems can support excitations known as anyons, which have long-range statistical interactions making them fundamentally different from the fermions and bosons that make up matter at the microscopic scale. As is well known, in quantum mechanics, exchanging indistinguishable particles can result in a unitary transformation on the many-body wavefunction, which leaves the physics invariant. In one and three dimensions, the concept of identical particles is encoded in the Bose–Einstein statistics for bosons and the Fermi–Dirac statistics for fermions. However, in between, in two dimensions, there exist a rich variety of types of statistics for particles. Indistinguishable particles in two dimensions which are neither bosons nor fermions are called *anyons*. Generally, the exchange of the positions of identical particles could modify the wavefunction by a multiplicative factor. If it is a phase (i.e. the wavefunction gets multiplied by a complex number), then these are Abelian anyons. If it is a unitary matrix, they

are called non-Abelian anyons.

Among the phases that may harbor non-Abelian anyons, low-dimensional topological superconductors occupy a special status because we now know of a variety of ways to engineer them in one and two dimensional systems. Topological superconductors host a special type of bound state, known as a Majorana zero mode, which is among the simplest types of non-Abelian anyons. Progress in manufacturing and detecting Majorana zero modes (or Majoranas, for short), has recently been pursued in carefully engineered 1D systems. Theoretically, there now exist many intriguing proposals for realizing Majorana zero modes in different nanomaterial and/or solid state systems, such as Kitaev's 1D p-wave superconducting (SC) wires [1] and a series of heterostructures comprising s-wave superconductors, topological insulators, semiconducting wires, as well as ferromagnetic substances [2–6]. Though non-Abelian statistics do not exist in purely 1D systems, a 2D network of 1D wires can be used to carry out exchange operations that are mathematically identical to those of a 2D system [7]. Moreover, theorists further demonstrated that the physically well-separated Majoranas would allow the possible nonlocal storage of quantum information thus protecting the computational processes against the decoherence from the local perturbations.

Following the string of similar reasoning, it thus becomes an attractive idea to study the novel quantum states of matter using conventional materials that can be engineered to host other types of non-Abelian particles. Interestingly, several theoretical groups showed a more complicated type of non-Abelian bound state, known as a parafermion, can be realized if superconductivity is induced at the boundary of an appropriate fractional quantum Hall bilayer system. Thus in addition to Majorana zero modes, it may be possible to engineer other types of non-Abelian bound states in strongly correlated quasi-one-dimensional systems [8–12].

1.2 Basics of Majorana boundary states

Majorana zero modes can occur in a variety of 1D and 2D systems [13, 14]. This thesis will focus on 1D realizations of these states (as well as of their parafermion cousins). In these 1D systems, Majorana zero modes arise as bound states at the ends of a topological superconducting (SC) wire. The prototypical theoretical model of such a system is Kitaev's 1D spinless p-wave

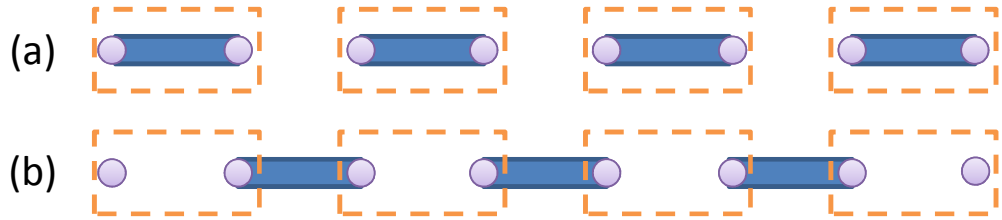

Figure 1.1: The illustration of the two limits in Kitaev's model. Panel (a) is a unique gapped dimerized SC state, which is topologically trivial. However, in panel (b), the emergence of the unpaired Majorana end modes dictates the topologically protected ground-state degeneracy. Here the orange boxes denote the normal-fermion sites, the purple dots are Majorana fermions, and the blue bonds represent couplings between adjacent Majorana fermions. The same paradigm can be extended to the parafermionic chains.

superconductor with the open boundary conditions [1],

$$H_{\text{Kitaev}} = -\mu \sum_{j=1}^{L} c_j^\dagger c_j - \sum_{j=1}^{L-1} \left(t c_j^\dagger c_{j+1} + \Delta c_j^\dagger c_{j+1}^\dagger + \text{H.c.} \right), \tag{1.1}$$

where μ and t represent the chemical potential and hopping integral, and Δ is the p-wave SC gap. This Hamiltonian does not conserve the total fermion number, but does conserve fermion parity (i.e. the number of fermions modulo 2). Manifestly, H_{Kitaev} commutes with the fermion parity operator $P = (-1)^{\sum_j c_j^\dagger c_j}$.

To see Majorana zero modes in the Kitaev's model, we can simply consider the special case of $\mu = 0$ and $t = \Delta$. The analysis will be facilitated by working in the Majorana representation. Let's first define two self-conjugate Majorana operators on each lattice site as follows, $\gamma_{2j} \equiv \frac{1}{\sqrt{2}} \left(c_j + c_j^\dagger \right) = \gamma_{2j}^\dagger$; $\gamma_{2j-1} \equiv -\frac{i}{\sqrt{2}} \left(c_j - c_j^\dagger \right) = \gamma_{2j-1}^\dagger$. After substitution into Eq. (1.1), we obtain

$$H_{\text{Kitaev}} = -2it \sum_{j=1}^{L-1} \gamma_{2j} \gamma_{2j+1} = t \sum_{j=1}^{L-1} \left(d_j^\dagger d_j - \frac{1}{2} \right), \tag{1.2}$$

where $d_j = \frac{1}{\sqrt{2}} \left(\gamma_{2j+1} + i \gamma_{2j} \right)$ is a normal-fermion annihilation operator defined in the bond connecting the adjacent sites. One salient feature of Eq. (1.2) is the appearance of two end zero-energy Majorana modes γ_1 and γ_{2L} which do not appear in the Hamiltonian, thus commute with H_{Kitaev}. This observation allows to define a unique nonlocal fermion operator $\tilde{d} = \frac{1}{\sqrt{2}} \left(\gamma_1 + i \gamma_{2L} \right)$ which exchanges the parities of the resultant degenerate ground states. It is important to emphasize that $\tilde{d}$ anticommutes with P and commutes with H_{Kitaev} in the limit

that $\mu = 0$. Namely, $|\text{GS}\rangle$ and $\tilde{d}|\text{GS}\rangle$ have different fermion parities, but share the same lowest eigenenergy. So this operator, which changes the fermion number by ± 1, takes the system between two different ground states. Kitaev and Fendley [1, 8] proved that this degeneracy remains a feature of the Hamiltonian (1.1) provided $|\mu| < 2t$. This bound can be understood by the adiabatic theorem: Namely, Eq. (1.2) tells that there exists a finite energy gap set by $t = \Delta$ that separates the degenerate ground states and the excitation spectrum. Then as the Majorana states are localized in opposite ends of the chain, their overlap is exponentially small across the bulk such that the zero-energy solutions remain stable until approaching the critical point where the superconducting gap vanishes. A schematic illustration of the two limits in Kitaev's 1D SC chain is shown in Fig. 1.1. Note that because a pair of Majoranas is needed to create a complex fermion, only hybridization between the bound states at the chain's two ends can lift the degeneracy.

Finally, we would like to clarify the difference between the Majorana zero modes and the Majorana fermions that we use to represent the normal-fermionic operators. An ordinary Majorana fermion is of course just a fermion, and does not have non-Abelian statistics! So what is different about these Majorana zero modes? (Zero means that they have zero energy, and are localized at the ends of the chain.) The basic idea is that each wire (with 2 endpoints) is a 2-state system (because it can have fermion parity ± 1). However, if we have 2 wires which initially both have fermion parity $+1$, we could change their state to be both -1 if we could exchange the Majorana zero mode at the left end of one wire with the one at the right end of the other wire twice. This double-exchange is called "braiding," and really can only happen in 2 dimensions; however there are ways to do it in 2D networks of these 1D wires [7]. This is the matrix rotation: By exchanging twice a pair of Majoranas, you have performed a rotation in the (2-dimensional) space of ground states.

From the viewpoint of symmetry classification, Kitaev's model has particle-hole symmetry, which squares to $+1$, and no other antiunitary symmetries. (This is called symmetry class D). It is known that there are two possible phases with this symmetry type—the topological phase with Majorana boundary modes, and the ordinary superconductor, which does not have protected boundary modes [15].

1.3 Experimental progress on Majoranas

Besides the conceptual novelty, a large portion of the interest on Majorana bound states comes from the real developments in experimental realizations of these unusual collective quasiparticles [16]. Exciting evidence of topological superconductivity has been discovered in 1D semiconducting nanowires and later in 1D ferromagnetic iron chains, where in both cases superconductivity is induced by proximity effect.

Although the original idea of Majorana fermion as a hypothetical fundamental particle (probably for neutrinos) which is its own antiparticle dated back to 1937 [17], the recent surge of Majorana-fermion hunting in condensed matter systems really started when the Delft group in Netherlands reported their first electrical transport measurements on the 1D superconductor-semiconductor nanowire heterostructure devices in the 2012 APS March Meeting. The observed zero-bias conductance peak at the ends of the indium antimonide wire in Delft experiment was attributed to the tunneling through the zero-energy Majorana bound states [18]. Further refined experimental data on the indium arsenide nanowires from Copenhagen experiment later verified this claim, and provided further evidence for Majorana zero modes by measuring the predicted exponential splitting of the near-zero-energy Majorana modes as a function of the wire length [19]. These experiments are highly suggestive of the existence of Majorana bound states, which we expect will be confirmed in the future by more decisive empirical measurements such as braiding.

A second promising approach for realizing Majorana bound states in solid-state architectures is the Fu–Kane proposal of inducing superconductivity in the helical edge modes in 2D topological insulators via the proximity effects from the nearby bulk superconductors [20]. As a concrete step toward topological superconductivity in an alternatively viable platform, two experimental groups have independently reported the successful achievement of the proximitized superconductivity in spin-momentum-locked and counterpropagating 1D edge modes of the semiconducting InAs/GaSb [21] and HgTe/HgCdTe [22] quantum wells by using superconducting quantum interference. Theoretically this system has less pitfalls for Majorana physics than the 1D wires, because once you establish that there is only one pair of helical edge modes at the Fermi level, inducing superconductivity basically has to give you a topological superconductor. Moreover, this approach is similar to the setup required to generate parafermion bound states, which require inducing superconductivity in counterpropagating edge modes at

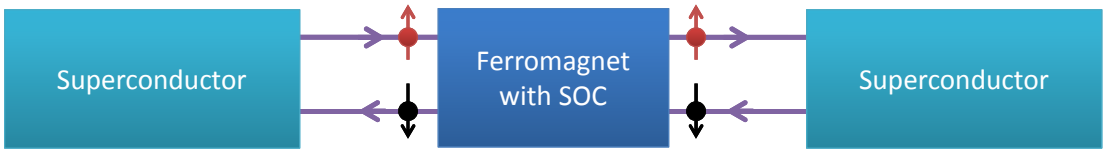

Figure 1.2: Experimental architecture hosting the $\mathbb{Z}_6$ parafermionic zero-energy states proposed in Ref. [9]. The two underlying purple lines represent the counterpropagating edge states of the fractional quantum Hall systems with opposite g-factors. Through proximity effects, this pair of edge states can be gapped by either the backscattering in the middle ferromagnetic region or the Cooper pairing elsewhere in the SC regions. Because the total spin is conserved modulo 2 (where the electronic spin is defined as one unit of spin) in the middle region gapped by the ferromagnet, but the underlying degrees of freedom carry fractional spin $1/3$, there are 6 possible spin states, which turn out to have the same energy. Although the total charge inside the ferromagnetic segment is pinned by two surrounding superconductors, the total spin degree of freedom in the middle segment bordered by the two interfaces between ferromagnet and superconductors can still take on several different values, which can be used to label the degenerate ground states in the presence of interfacial parafermions when the heterostructure is in the topological phase.

the boundary of a strongly interacting (fractional quantum Hall) 2D system. This direction might thus open the prospects for the more challenging engineering of the fractional quantum Hall edge states. Note that theoretically such more exotic non-Abelian parafermionic modes are however precluded in strictly 1D systems.

1.4 Parafermions in fractional quantum Hall heterostructures

In the latter chapters of this thesis, we will study questions related to parafermion zero modes. We will therefore review the theoretical proposals for realizing these, reported in Refs. [9–12].

In order to realize parafermions, superconductivity must be induced at the boundary of a 2D fractional quantum Hall bilayer system. The fractional quantum Hall effect (FQHE), discovered experimentally by Tsui and Stormer [23], happens when we take a 2D gas of electrons and put it in a high magnetic field (and the right electron density), then the Hall conductance of the 2D electron gas shows precisely quantized plateaus at the fractional values of e^2/h. These fractional plateaux occur because the highly mobile 2D electrons are in a highly entangled ground state which is separated from all excitation states by a finite energy gap. The resulting very strong electron correlations mean that the fundamental excitations, known as Laughlin

quasiparticles, carry a fraction of the electron's charge [24]. If the quantum Hall conductance is $\nu e^2/h$, with the electron filling factor $\nu = 1/m$ for some integer m, then this charge is equal to ν.

In the bulk, these excitations cost energy, and are usually pinned to defects in the sample. But at the edge they are necessarily gapless: Because of the magnetic field, charge at the edge can circulate only in one direction, and backscattering cannot open up a gap. So the edge of a $\nu = 1/m$ quantum Hall system on a disk looks like a chiral 1D gapless system with charge $1/m$ objects propagating (for example) counterclockwise. In the context of Laughlin states at the filling factor $\nu = 1/m$ (m is an odd integer), operators (which we write $e^{i\phi(x)}$, where ϕ is a bosonic field) that create these fractionally charged excitations at the edge obey the following commutation relation,

$$e^{i\phi(x)}e^{i\phi(x')} = e^{i\phi(x')}e^{i\phi(x)}e^{i(\pi/m)\mathrm{sgn}(x'-x)}. \tag{1.3}$$

If $m = 1$ this indicates that $e^{i\phi}$ are fermions, since they are antisymmetric under exchange. For $m > 1$ the commutation relation (1.3) is closely related to the non-Abelian statistics of parafermion zero modes, which inspired theorists proposing devices based on fractional quantum Hall [9] and/or fractional topological insulator [10] heterostructures to physically realize the localized parafermion edge zero modes in a real system. The proposed system is illustrated in Fig. 1.2, and is very similar to the Fu–Kane proposal for creating Majorana zero modes at the edges of 2D topological insulators. Specifically, in order to create a gapped 1D system, we require two copies of the quantum Hall edge with opposite chirality. Inducing backscattering in this counterpropagating pair of edges can then open a gap. It has been shown [9–12] that between the two different gapped regions there is a parafermion zero mode. (If we take $m = 1$ (i.e. the excitations at the edge carry the electron's charge), this is exactly the proposal of Fu and Kane for engineering Majorana zero modes at the boundary of a 2D topological insulator.)

1.5 Outline of the dissertation

Over the last four years, I have been working in the rapidly evolving area of topological states of quantum matter, with a focus on topological superconductors and superfluids that host the Majorana-fermion and parafermion quasiparticles. One aspect of my research has been to investigate new realizations of topological superconductors in 1D, which share the property of

accommodating Majorana zero modes at their endpoints, but whose other physical properties differ in important ways.

Julian Schwinger once said, "One of the most remarkable discoveries in elementary particle physics has been that of the existence of the complex plane." Following Schwinger's sentiment, I would like to highlight the themes of my three research achievements which respectively treat phase structure, phase coherence, and phase interference. Here the word "phase" refers specifically to the superconducting/superfluid phase in Fulde–Ferrell state, the plane-wave phase in umklapp scattering, and the Berry phase in instanton action. This dissertation is mainly constructed from these three papers, which we introduce now briefly in the following paragraphs.

Fulde–Ferrell meet Majorana: Topological FF State Predicting novel states of matter is one major driving force underpinning my research in topological matter. I am particularly interested in new situations where topological superconductivity can arise, and what other fundamental properties it may exhibit in addition to Majorana fermions. In this pursuit, I predicted a topological inhomogeneous superfluid state in 1D atomic Fermi gases where the phase of the superfluid gap is measurably different at different points in space, but the system remains topological in the sense that at its boundaries there reside gapless Majorana modes. The topologically trivial inhomogeneous state was theoretically proposed by Fulde, Ferrell [25] and Larkin, Ovchinnikov [26] (FFLO) independently in 1960s, so I named this newly-predicted phase of matter the *topo*-FFLO state, or more precisely the *topo*-FF state—a single Fourier component of the superfluid (SF) order parameter dominates.

My main motivation came from the observation that the Majorana number $\mathcal{M}$ in Kitaev's p-wave superconducting (SC) chain only depends on the absolute value of the SC order parameter [1]. This nonvanishing modulus promises a gapped bulk for the protection of probable gapless edge excitations. Nevertheless, it appeared that the phase degree of freedom was largely overlooked in the formalism. In principle, for a generic 1D topological superconductor its topological invariant can depend on both the magnitude and the phase of the superconducting gap. On the basis of analytic topological arguments and detailed numerical results from solving the Bogoliubov–de Gennes (BdG) equations, I demonstrated *for the first time* the potential of synthesizing a *topo*-FFLO superfluid state in the spin-orbit-coupled (SOC) Fermi gases where even though the SF modulus is uniform, the SF phase develops the nontrivial periodic variations in real space that coexist with the protected Majorana edge states. The physical underpinning of

this inhomogeneous topological superfluidity stems mainly from the inversion asymmetry of the Bloch bands induced by the interplay between SOC and Zeeman interactions. Chapter 3 of this thesis is largely based on the published materials of this work in Physical Review Letters [27].

As a byproduct, I also independently proved that for Majorana wires in symmetry class D, the topological index defined by Kitaev's Pfaffian based Majorana number is equivalent to the Berry phase based $\mathbb{Z}_2$ invariant adopted in my paper, which was derived from the built-in particle-hole symmetry of the BdG mean-field Hamiltonian. Similar derivations were shortly published by another group (see Ref. [30]).

Prediction of A New Type of Many-Body Majorana Bound States Searching for richer possibilities and hitherto unknown subtleties arising from interaction effects comprises another primary impetus that spurs me to venture deeper into the 1D topological superconductivity and superfluidity of strongly interacting fermions. This rewarding experience gives me the first glimpse into the interweaving of interactions with symmetry and topology. Chapter 4 of this thesis studies a number-conserving ladder system consisting of two wires coupled by pair hopping. This seemingly artificial model actually provides a simple, but distinctive platform to go beyond Kitaev's paradigm. Namely, can we get Majorana bound states in 1D systems that conserve the fermion number? As we will show, the answer is yes. One way to do it is to introduce a two-species system, and fine-tune the model so that the parity of each species is conserved. This gives a fermion-parity symmetry, which can stabilize Majorana zero modes in a manner similar to that for the Kitaev chain. (This was proposed by Zoller's group). However, we propose a second way to do this, in which by modifying the band structure of the two types of fermions, an emergent low-energy fermion-parity symmetry is related to a microscopic lattice symmetry. Thus we get Majorana zero modes in a number-conserving system protected by a unitary lattice symmetry. This is a fundamentally different mechanism than those that were previously known. Chapter 4 of this thesis is an expanded version of this work [28].

Oscillatory Splitting of the Ground-State Degeneracy in Quasi-1D Parafermion Architectures In real experiments with Majorana fermions and parafermions, the finite-length effects will inevitably engender a small but measurable splitting effect in the energies associated with these topological quasiparticles. Interestingly, researchers showed that under the mean-field approximation of Majorana states in 1D nanowires (a solvable model), this splitting will oscillate

as certain experimental parameters are tuned, leading to detectable signatures of topological Majorana excitations. These predicted oscillations have been reported in conductance measurements on 1D SC wires, and remain one of the more promising signatures of Majorana fermions in these systems. It is natural to wonder whether a similar effect should be observed in parafermion systems. However, in this new context with strong electron-electron interactions, the method used to make predictions for Majorana fermions breaks down. Consequently, the actual evaluation of parafermion splitting is a challenging problem.

In close collaboration with my thesis advisor, I undertook this task by bringing together some new insights that help elucidate the mathematical structures of the splitting for the generic QHE-based parafermion systems. Through the $U(1)$ Chern–Simons K-matrix formalism of the fractional QH liquids and the bosonized chiral Luttinger liquid description of QH edge states, we adopted a nonperturbative instanton approach to derive analytically the parafermion splitting. To capture the temporal and spatial fluctuations, we carefully evaluated the Fredholm functional determinant at one-loop order in both open and closed boundary conditions. Our central findings can be encapsulated as follows: We show that this splitting indeed has oscillations as functions of experimentally tunable parameters due to an intrinsic interference effect between distinct instanton tunneling trajectories resulting from a topological term in the effective action. Intriguingly, the scaling of the splitting with the system's size is sensitive to the choice of spatial boundary conditions. We therefore demonstrate for the first time that the oscillatory feature of the ground-state energy splitting is relatively ubiquitous for parafermions. Our instanton calculation also substantiates the general result of anyon tunneling in topological quantum field theory (TQFT). Chapter 6 of this thesis is a detailed account of this project [29].

The remaining parts of the thesis are unpublished works, which are organized as follows. Chapter 2 provides a simple introduction to the Majorana bound states via a continuum description of the Kitaev chain model. Chapter 5 proposes a parity measurement scheme to detect the signatures of parafermionic zero modes in non-equilibrium setups. Appendix A gives the additional details for deriving the dissipative terms in master equation. Appendix B includes the wavefunction-overlap calculations for the near-zero-energy splitting of the topological boundary modes in finite-size systems.

Chapter 2

Continuum Description of 1D Kitaev Chain

2.1 Continuous 1D spinless p-wave superconductor

Here we give a more concrete calculation to demonstrate the features of the spatial profiles for the Majorana-zero-mode wavefunctions in the continuous 1D spinless p-wave superconductor. Following Kitaev, we again start from the simple 1D spinless p-wave superconductor in a lattice chain,

$$H = -\mu \sum_i c_i^\dagger c_i - \sum_i \left(t c_i^\dagger c_{i+1} + \Delta e^{i\varphi} c_i c_{i+1} + \text{H.c.} \right).$$

After Fourier transforming and introducing the two-component operator in momentum space $\hat{c}_k^\dagger = [c_k^\dagger,\ c_{-k}]$, the above Hamiltonian becomes

$$H = \sum_k \hat{c}_k^\dagger \mathcal{H}(k) \hat{c}_k, \quad \mathcal{H}(k) = \begin{pmatrix} -t\cos k\mathsf{a} - \frac{\mu}{2} & i\Delta e^{-i\varphi}\sin k\mathsf{a} \\ -i\Delta e^{i\varphi}\sin k\mathsf{a} & t\cos k\mathsf{a} + \frac{\mu}{2} \end{pmatrix}. \tag{2.1}$$

We can perform a gauge transformation to eliminate the phase of the SC order parameter, and map the lattice model onto the continuous space by substituting

$$\cos k\mathsf{a} \to 1 - \frac{(k\mathsf{a})^2}{2}; \quad \sin k\mathsf{a} \to k\mathsf{a}, \tag{2.2}$$

where a is the lattice constant, and the continuum approximation is valid for wavelengths that are long compared to a, then we would have

$$H = \int dx \hat{c}_x^\dagger \mathcal{H}(x) \hat{c}_x, \quad \mathcal{H}(x) = \begin{pmatrix} -\frac{1}{2}t\mathsf{a}^2\partial_x^2 - \frac{\mu}{2} - t & \Delta\mathsf{a}\partial_x \\ -\Delta\mathsf{a}\partial_x & \frac{1}{2}t\mathsf{a}^2\partial_x^2 + \frac{\mu}{2} + t \end{pmatrix}, \tag{2.3}$$

where $\hat{c}_x^\dagger = [c_x^\dagger,\ c_x]$. Basically, we Taylor expand for wavelengths that are large compared to the lattice constant—i.e. $k\mathsf{a} \ll 1$. This will rescale the parameters t and Δ by factors of a.

Notice that the continuum approximation (2.2) holds only in the long-wavelength limit where $k\mathsf{a} \to 0$. However, topological properties of bands are typically revealed by examining the whole band structure in the Brillouin zone; that's why people typically prefer using a lattice model instead of a continuous model to study the topology of a system. Therefore, some cautions are needed when comparing the results between the lattice and continuum versions of a model. Here we will demonstrate that as a topological property, the most salient feature of a tight-binding Kitaev chain, namely the existence of Majorana zero modes, is preserved (stable) under this continuum approximation.

In order to establish the existence of Majorana zero modes in this system, we will solve the following eigenvalue problem

$$\mathcal{H}(x)\Psi_0(x) = 0 \tag{2.4}$$

for the two-component self-conjugate Majorana zero modes $\Psi_0(x)$ under the appropriate boundary conditions.

2.2 Analytical wavefunctions of Majorana zero modes

In order to see the Majorana zero modes, which are pinned to the endpoints of our 1D superconductor, we must study a real-space version of the Hamiltonian $\mathcal{H}(x)$,

$$\mathcal{H}(x) = \begin{pmatrix} -\frac{1}{2}t(x)\partial_x^2 - \frac{1}{2}\mu(x) - t(x) & \Delta(x)\partial_x \\ -\Delta(x)\partial_x & \frac{1}{2}t(x)\partial_x^2 + \frac{1}{2}\mu(x) + t(x) \end{pmatrix}, \tag{2.5}$$

where the purely real parameters $t(x)$, $\Delta(x)$, and $\mu(x)$ take on different values in the topological region when $|x| \leq \frac{L}{2}$, than in the normal region that exists for $|x| > \frac{L}{2}$ where the system is assumed to be topologically trivial (see Fig. 2.1). (For keeping the expressions uncluttered, in Eq. (2.5) we have absorbed the lattice constant into the proper t and Δ by setting the value of $\mathsf{a} = 1$. The dimensionalities of these t and Δ will change accordingly.)

To simplify our task, we divide $\mathcal{H}(x)$ into left (L) and right (R) parts,

$$\mathcal{H}(x) = \mathcal{H}_R(x) + \mathcal{U}_L(x) = \mathcal{H}_L(x) + \mathcal{U}_R(x), \tag{2.6}$$

where

$$\mathcal{H}_{R,L}(x) = \begin{pmatrix} -\frac{1}{2}t_{R,L}(x)\partial_x^2 - \frac{1}{2}\mu_{R,L}(x) - t_{R,L}(x) & \Delta_{R,L}(x)\partial_x \\ -\Delta_{R,L}(x)\partial_x & \frac{1}{2}t_{R,L}(x)\partial_x^2 + \frac{1}{2}\mu_{R,L}(x) + t_{R,L}(x) \end{pmatrix}, \tag{2.7}$$

where we choose t_L, μ_L, and Δ_L to represent a system with only a left boundary, and similarly for R (see Fig. 2.1). This simplifies our calculation because, as we will see, a system with only one boundary has an exact eigenstate of zero energy—whereas in a system with two boundaries, interactions between the left and right bound states shift this energy slightly, making the exact eigenfunctions more difficult to identify. Now we will exploit the following relations to find the zero-mode solutions:

$$t(x) = t(-x), \;\; \Delta(x) = \Delta(-x), \;\; \mu(x) = \mu(-x); \tag{2.8}$$

$$t_R(x) = t_L(-x), \;\; \Delta_R(x) = \Delta_L(-x), \;\; \mu_R(x) = \mu_L(-x). \tag{2.9}$$

To visualize these relations, we plot in Fig. 2.1 the spatial profiles of the hopping parameters. Similar configurations apply also to other listed parameters. Since $\mathcal{U}_{R,L}(x) = \mathcal{H}(x) - \mathcal{H}_{L,R}(x)$, the above symmetries of various parameters will lead to

$$\mathcal{U}_R(x) = \mathcal{U}_L(-x). \tag{2.10}$$

Also, it can be easily checked that

$$\sigma_z \mathcal{H}(x) \sigma_z = \mathcal{H}(-x), \;\; \text{and} \;\; \sigma_z \mathcal{H}_{R,L}(x) \sigma_z = \mathcal{H}_{L,R}(-x), \tag{2.11}$$

which imply that

$$\sigma_z \mathcal{U}_{L,R}(x) \sigma_z = \mathcal{U}_{R,L}(-x) = \mathcal{U}_{L,R}(x). \tag{2.12}$$

Typically, the right and left boundaries are spatially well-separated from each other, which allows us to firstly approximately focus on the Majorana zero modes from only the part of $\mathcal{H}_{R,L}(x)$, then adding the treatment of $\mathcal{U}_{L,R}(x)$ as the perturbations. Namely we would like to solve the reduced eigenvalue problem of $\mathcal{H}_R(x)$,

$$\mathcal{H}_R(x)\psi_{R,0}(x) = 0 \tag{2.13}$$

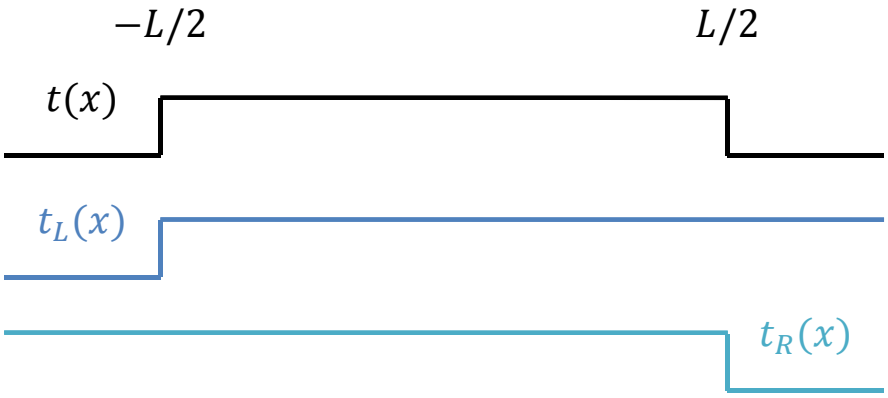

Figure 2.1: Spatial profiles for the (hopping) parameters defined in Eqs. (2.8) and (2.9).

for the two-component self-conjugate Majorana zero modes $\psi_{R,0}(x)$ under the appropriate boundary conditions. From Eq. (2.11), we know that if $\psi_{R,0}(x)$ is the Majorana zero mode of $\mathcal{H}_R(x)$, then

$$i\sigma_z\psi_{R,0}(-x) = \psi_{L,0}(x), \quad \text{which satisfies } \mathcal{H}_L(x)\psi_{L,0}(x) = 0, \tag{2.14}$$

will be the Majorana zero mode of $\mathcal{H}_L(x)$. With this observation, we only need to concentrate on solving the Majorana wavefunctions (Majoranas) for $\mathcal{H}_R(x)$. Moreover, if the zero modes are Majoranas, then by definition they must be self-conjugate. This implies the Majorana spinors must be either purely real, or purely imaginary:

$$\psi_{\text{real}}(x) = \begin{pmatrix} \phi_1(x) \\ \phi_1(x) \end{pmatrix}; \quad \psi_{\text{imag}}(x) = \begin{pmatrix} i\phi_2(x) \\ -i\phi_2(x) \end{pmatrix}, \tag{2.15}$$

where $\phi_{1,2}(x)$ are one-component real functions of x. It follows from Eq. (2.14) that for the Hamiltonian (2.5) if the left-end Majorana mode happens to be purely real (imaginary), then the right-end Majorana state will be purely imaginary (real).

2.2.1 The purely real Majorana-zero-mode wavefunction

To identify the wavefunctions for the Majorana zero modes, we first solve Eq. (2.13) in a region of space where μ, Δ, and t are uniform. We then account for their spatial variation by imposing appropriate boundary conditions at $x = L/2$ (see Fig. 2.1). The spatial differential equation for $\psi_{\text{real}}(x)$ reads

$$\left[\left(-\frac{1}{2}t_R\partial_x^2 - \nu_R\right)\sigma_z + i\sigma_y\Delta_R\partial_x\right]\psi_{\text{real}}(x) = 0, \tag{2.16}$$

or in the matrix form

$$\begin{pmatrix} -\frac{1}{2}t_R\partial_x^2 - \nu_R & \Delta_R\partial_x \\ -\Delta_R\partial_x & \frac{1}{2}t_R\partial_x^2 + \nu_R \end{pmatrix} \cdot \begin{pmatrix} \phi_1(x) \\ \phi_1(x) \end{pmatrix} = 0, \tag{2.17}$$

where we have removed the x-dependence of the parameters, and also denoted

$$\nu_R = \frac{1}{2}\mu_R + t_R. \tag{2.18}$$

Actually Eq. (2.17) is equivalent to

$$\left(-\frac{1}{2}t\partial_x^2 - \nu + \Delta\partial_x\right)\phi_1(x) = 0, \tag{2.19}$$

where $t = t_R,\ \nu = \nu_R,\ \Delta = \Delta_R$. We can assume $\phi_1(x) = e^{\pm zx}\tilde{\phi}_1$ with $\tilde{\phi}_1$ a spatially independent constant (set by the value of z), then the resulting secular equation reads

$$-\frac{1}{2}tz^2 - \nu \pm \Delta z = 0, \tag{2.20}$$

which has two solutions as follows,

$$z_+ = \frac{\Delta - \sqrt{\Delta^2 - 2t\nu}}{t}, \quad z_- = -\frac{\Delta - \sqrt{\Delta^2 - 2t\nu}}{t}. \tag{2.21}$$

Thus we would have two possible real solutions,

$$\phi_1^{\pm}(x) = \tilde{\phi}_1^{\pm} \exp\left[\left(\frac{\Delta}{t} \pm \frac{1}{t}\sqrt{\Delta^2 - 2t\nu}\right)x\right], \tag{2.22}$$

and

$$\psi_{\text{real}}^{\pm}(x) = \tilde{\phi}_1^{\pm} \exp\left[\left(\frac{\Delta}{t} \pm \frac{1}{t}\sqrt{\Delta^2 - 2t\nu}\right)x\right] \begin{pmatrix} 1 \\ 1 \end{pmatrix}. \tag{2.23}$$

2.2.2 The purely imaginary Majorana-zero-mode wavefunction

Following the similar procedure, we can also analytically solve for the imaginary type of the Majorana zero modes. The spatial differential equation for $\psi_{\text{imag}}(x)$ reads

$$\left[\left(-\frac{1}{2}t_R\partial_x^2 - \nu_R\right)\sigma_z + i\sigma_y\Delta_R\partial_x\right]\psi_{\text{imag}}(x) = 0, \tag{2.24}$$

or in the matrix form

$$\begin{pmatrix} -\frac{1}{2}t_R\partial_x^2 - \nu_R & \Delta_R\partial_x \\ -\Delta_R\partial_x & \frac{1}{2}t_R\partial_x^2 + \nu_R \end{pmatrix} \cdot \begin{pmatrix} i\phi_2(x) \\ -i\phi_2(x) \end{pmatrix} = 0, \tag{2.25}$$

Eq. (2.25) is equivalent to

$$\left(-\frac{1}{2}t\partial_x^2 - \nu - \Delta\partial_x\right)\phi_2(x) = 0. \tag{2.26}$$

Compared with Eq. (2.19), we can see that the only difference is that we have switched the sign before Δ, which, as will be shown below, will change the decaying direction of the solution. Similarly, we can assume $\phi_2(x) = e^{\pm z'x}\tilde{\phi}_2$, where $\tilde{\phi}_2$ is a spatially independent constant (set by the value of z'), then the resulting secular equation reads

$$-\frac{1}{2}tz'^2 - \nu \mp \Delta z' = 0, \tag{2.27}$$

which has two solutions as follows,

$$z'_+ = \frac{\Delta + \sqrt{\Delta^2 - 2t\nu}}{-t}, \quad z'_- = -\frac{\Delta + \sqrt{\Delta^2 - 2t\nu}}{-t}. \tag{2.28}$$

Thus we would have two possible imaginary solutions,

$$\phi_2^{\pm}(x) = \tilde{\phi}_2^{\pm}\exp\left[\left(-\frac{\Delta}{t} \pm \frac{1}{t}\sqrt{\Delta^2 - 2t\nu}\right)x\right], \tag{2.29}$$

and

$$\psi_{\text{imag}}^{\pm}(x) = \tilde{\phi}_2^{\pm}\exp\left[\left(-\frac{\Delta}{t} \pm \frac{1}{t}\sqrt{\Delta^2 - 2t\nu}\right)x\right]\begin{pmatrix} i \\ -i \end{pmatrix}. \tag{2.30}$$

2.3 The criterion for topologically nontrivial regions

Basically, from Eqs. (2.21) and (2.28), we know that depending on whether $\Delta^2 - 2t\nu$ is greater than zero or not, we would have three different types of solutions for z and z'. Specifically, let's distinguish these three situations in some detail:

(a) If $\Delta^2 > \Delta^2 - 2t\nu > 0$ (namely if $0 < 2t\nu < \Delta^2$), we would have two different real solutions of z. Moreover, the two real solutions of z will have the same sign in this case (being both positive or negative). For instance, when $\frac{\Delta}{t}$ is greater (less) than zero, these two real solutions of z will both be positive (negative). The same results also hold for z' but with the opposite sign.

(b) If $\Delta^2 - 2t\nu > \Delta^2$ (namely if $2t\nu < 0$), we still have two differing real solutions for z, but they would have the opposite signs (one positive and one negative). The same results hold for z' but need the switch of the signs.

(c) If $\Delta^2 - 2t\nu < 0$ (namely if $2t\nu > \Delta^2$), we would have two complex solutions of z, which share the same real part and have the opposite imaginary parts. Namely they are complex conjugate to each other. The same thing holds for the solutions of z', but we need to change the sign of the real part.

After counting and matching the boundary conditions in the following Section 2.4, we will see that the cases (a) and (c) correspond to the topologically nontrivial parameter regions. However, case (b) (i.e. $t\nu < 0$) will be a topologically trivial region. The reason for this is the following: We need at least two solutions to satisfy the appropriate boundary conditions, but if these two solutions decay in opposite directions, we would not be able to construct a normalizable mode that is exponentially decaying into the bulk of the chain, namely localized at the boundary. Therefore in the continuum limit, the criterion for identifying the topological regions is

$$t\nu > 0 \ \text{ or } \ t(2t+\mu) > 0 \implies \begin{cases} t < 0 \ \text{ or } \ 2t > |\mu| > 0 & \text{if } \ \mu < 0 \\ t > 0 \ \text{ or } \ 2t < -|\mu| < 0 & \text{if } \ \mu > 0 \end{cases}, \tag{2.31}$$

which is consistent with the results by Kitaev, who obtained a similar criterion—namely that the topological phase exists when $|2t| > |\mu|$—for a 1D p-wave superconductor on a discrete lattice by matrix manipulations [1].

Particularly, in Ref. [1], Kitaev considered a periodic chain of L unit cells, and each unit cell having n fermionic sites. A general lattice Hamiltonian for this 1D model can be written in real space as (see Eqs. (18), (22), and (23) in Ref. [1]):

$$H = \frac{i}{4}\sum_{l,m}\sum_{\alpha,\beta} B_{\alpha\beta}(m-l)\mathsf{c}_{l\alpha}\mathsf{c}_{m\beta}; \quad B_{\alpha\beta}(j)^* = B_{\alpha\beta}(j) = -B_{\beta\alpha}(-j), \tag{2.32}$$

where $l = 1, \ldots, L$, $\alpha = 1, \ldots, 2n$, and the Majorana operators c's satisfy the relations $\mathsf{c}_m^\dagger = \mathsf{c}_m$, $\mathsf{c}_l\mathsf{c}_m + \mathsf{c}_m\mathsf{c}_l = \delta_{lm}$. By performing the Fourier transformations, $\gamma_{p\alpha} = \frac{1}{\sqrt{L}}\sum_j e^{-ipj}\mathsf{c}_{j\alpha}$, we can obtain the same Hamiltonian in the momentum space as,

$$H = \frac{i}{4}\sum_{\alpha,\beta}\sum_{p} \tilde{B}_{\alpha\beta}(p)\gamma_{-p\alpha}\gamma_{p\beta}; \quad \tilde{B}^\dagger(p) = -\tilde{B}(p) = \tilde{B}^{\mathrm{T}}(-p), \tag{2.33}$$

where $\tilde{B}_{\alpha\beta}(p) = \sum_j e^{ipj}B_{\alpha\beta}(j)$ describing the band structure. In Ref. [1], Kitaev further constructed the Majorana number $\mathcal{M}(H)$ as the $\mathbb{Z}_2$ invariant to characterize the topological structure of the system,

$$\mathcal{M}(H) \coloneqq \mathrm{sgn}\Big\{\mathrm{Pf}\Big[\tilde{B}(p=0)\Big]\Big\} \cdot \mathrm{sgn}\Big\{\mathrm{Pf}\Big[\tilde{B}(p=\pi)\Big]\Big\}. \tag{2.34}$$

It can be shown that when $\mathcal{M}(H) = -1$ $(+1)$, the 1D superconducting wire is topologically nontrivial (trivial). Here the symbol Pfaffian (Pf) is mathematically defined by the square root of the determinant of a skew-symmetric (antisymmetric) matrix with a unique choice of the sign.

2.4 Counting and matching the boundary conditions

To prove that in cases (a) and (c) above, there exist zero-energy Majorana modes that satisfy the boundary conditions, we explicitly write down the following.

(a) When $0 < 2t\nu < \Delta^2$, we would have

$$\psi_{\text{real}}(x+\frac{L}{2}) = a\exp\left[\left(\frac{\Delta}{t}+\frac{\sqrt{\Delta^2-2t\nu}}{t}\right)x\right]\begin{pmatrix}1\\1\end{pmatrix} + b\exp\left[\left(\frac{\Delta}{t}-\frac{\sqrt{\Delta^2-2t\nu}}{t}\right)x\right]\begin{pmatrix}1\\1\end{pmatrix}, \tag{2.35}$$

$$\psi_{\text{imag}}(x+\frac{L}{2}) = a'\exp\left[\left(-\frac{\Delta}{t}+\frac{\sqrt{\Delta^2-2t\nu}}{t}\right)x\right]\begin{pmatrix}i\\-i\end{pmatrix} + b'\exp\left[\left(-\frac{\Delta}{t}-\frac{\sqrt{\Delta^2-2t\nu}}{t}\right)x\right]\begin{pmatrix}i\\-i\end{pmatrix}, \tag{2.36}$$

(c) When $2t\nu > \Delta^2$, we would have

$$\psi_{\text{real}}(x+\frac{L}{2}) = (a+bi)\exp\left[\left(\frac{\Delta}{t}+i\frac{\sqrt{|\Delta^2-2t\nu|}}{t}\right)x\right]\begin{pmatrix}1\\1\end{pmatrix} + (a-bi)\exp\left[\left(\frac{\Delta}{t}-i\frac{\sqrt{|\Delta^2-2t\nu|}}{t}\right)x\right]\begin{pmatrix}1\\1\end{pmatrix}, \tag{2.37}$$

$$\psi_{\text{imag}}(x+\frac{L}{2}) = (a'+b'i)\exp\left[\left(-\frac{\Delta}{t}+i\frac{\sqrt{|\Delta^2-2t\nu|}}{t}\right)x\right]\begin{pmatrix}i\\-i\end{pmatrix} + (a'-b'i)\exp\left[\left(-\frac{\Delta}{t}-i\frac{\sqrt{|\Delta^2-2t\nu|}}{t}\right)x\right]\begin{pmatrix}i\\-i\end{pmatrix}, \tag{2.38}$$

where $a,\ b$ and $a',\ b'$ are any real arbitrary constants to be fixed by matching the boundary conditions. Apparently, the wavefunctions in case (a) will exponentially decay into the bulk

without any appreciable oscillations. However, in case (c), typically, the wavefunctions will exponentially decay into the bulk in an oscillatory way due to the presence of the finite imaginary parts. It is worth stressing that in both cases, the wavefunctions will still be either purely real or purely imaginary to satisfy the self-conjugation conditions.

Throughout the remaining part of the chapter, we mainly consider the situation or setup that the 1D nanowire is directly connected to the vacuum at its two ends. (In this case, we require the wavefunction to vanish for $|x| \geq L/2$.) Before uniquely specifying the Majorana wavefunctions for $\mathcal{H}_R(x)$ in this case, we would like to emphasize the following point: From Eqs. (2.23) and (2.30), we know that $\psi_{\text{real}}(x)$ and $\psi_{\text{imag}}(x)$ decay in opposite directions. Their decaying behaviours are determined by the phase or the sign of the real term $\frac{\Delta}{t}$. Therefore, $\frac{\Delta}{t}$ will select which one $\left(\psi_{\text{real}}(x) \text{ or } \psi_{\text{imag}}(x)\right)$ to be the proper wavefunctions of the right Majorana end states. In other words, if $\frac{\Delta}{t}$ is positive (negative), then the right Majorana zero modes will be purely real (imaginary).

Let us assume that $\frac{\Delta}{t} > 0$.

First we choose to work in the parameter domain $0 < 2t\nu < \Delta^2$. By requiring the real wavefunction $\psi_{\text{real}}(x)$ to vanish at the right end $x = \frac{L}{2}$, we find that $a = b$ in Eq. (2.35). Namely,

$$\psi_{R,0}(x) = \psi_{\text{real}}(x) = a \left(\exp\left[\left(\frac{\Delta}{t} + \frac{\sqrt{\Delta^2 - 2t\nu}}{t} \right) \left(x - \frac{L}{2} \right) \right] \begin{pmatrix} 1 \\ 1 \end{pmatrix} - \exp\left[\left(\frac{\Delta}{t} - \frac{\sqrt{\Delta^2 - 2t\nu}}{t} \right) \left(x - \frac{L}{2} \right) \right] \begin{pmatrix} 1 \\ 1 \end{pmatrix} \right). \tag{2.39}$$

Once obtaining the right Majorana zero mode, in consultant with Eq. (2.14), we can directly write down the purely imaginary wavefunction of the left Majorana zero mode by the relation $i\sigma_z \psi_{R,0}(-x) = \psi_{L,0}(x)$,

$$\psi_{L,0}(x) = a \left(\exp\left[\left(-\frac{\Delta}{t} - \frac{\sqrt{\Delta^2 - 2t\nu}}{t} \right) \left(x + \frac{L}{2} \right) \right] \begin{pmatrix} i \\ -i \end{pmatrix} - \exp\left[\left(-\frac{\Delta}{t} + \frac{\sqrt{\Delta^2 - 2t\nu}}{t} \right) \left(x + \frac{L}{2} \right) \right] \begin{pmatrix} i \\ -i \end{pmatrix} \right). \tag{2.40}$$

The constant a is fixed by the normalization condition.

Second let us choose to work in the parameter domain $2t\nu > \Delta^2$. By setting the real wavefunction $\psi_{\text{real}}(x)$ to vanish at the right end $x = \frac{L}{2}$, we find that $a = 0$ in Eq. (2.37).

Combining the remaining two terms, we find that

$$\psi_{R,0}(x) = \psi_{\text{real}}(x) = -2b \exp\left[\frac{\Delta}{t}\left(x - \frac{L}{2}\right)\right] \sin\left[\frac{\sqrt{|\Delta^2 - 2t\nu|}}{t}\left(x - \frac{L}{2}\right)\right] \begin{pmatrix} 1 \\ 1 \end{pmatrix}. \tag{2.41}$$

Once obtaining the right Majorana zero mode, in consultant with Eq. (2.14), we can directly write down the purely imaginary wavefunction of the left Majorana zero mode by the relation $i\sigma_z \psi_{R,0}(-x) = \psi_{L,0}(x)$,

$$\psi_{L,0}(x) = 2b \exp\left[-\frac{\Delta}{t}\left(x + \frac{L}{2}\right)\right] \sin\left[\frac{\sqrt{|\Delta^2 - 2t\nu|}}{t}\left(x + \frac{L}{2}\right)\right] \begin{pmatrix} i \\ -i \end{pmatrix}. \tag{2.42}$$

The constant b can also be fixed by the normalization condition.

As can be explicitly seen, the wavefunctions in the **second** case will oscillate in the 1D chain due to the sine factors originating from the finite imaginary parts of z and z'. It would be easy to see that when we changing the sign of $\frac{\Delta}{t}$ to make it less than zero, we would just effectively switch the right (left) Majorana zero mode to the left (right) end.

For completeness, we notice that when counting the number of boundary constraints, for the case of a finite kink or jump in the parameters separating the topological and normal regions, requiring continuity of the wavefunction as well as its first spatial derivative will contribute two real constraints, since Majoranas can be only purely real or purely imaginary as stressed above. Then including the normalization condition, typically there are more free parameters, since we match to wavefunctions in the normal region, and solutions of this type can also be found.

Finally, it is worth mentioning that a potential utility of the above continuum formalism is to derive the zero-energy splitting of Majoranas induced by finite-length effects in Kitaev chain, which arises from the interaction between left and right boundary modes, which we have ignored in our analysis here. A calculation of this type is given in Appendix B. We note that understanding the nature of this splitting has practical applications, since it gives one measurable signature of Majorana bound state in nanowire setups [31].

Chapter 3

Inhomogeneous Topological Superfluidity in One-Dimensional Spin-Orbit-Coupled Fermi Gases

3.1 Introduction

As a generalization of Kitaev's work, in this chapter we theoretically predict an exotic topological superfluid state with spatially modulated (i.e. finite momentum) pairing gap in one-dimensional spin-orbit-coupled Fermi gases. To achieve this, we systematically develop a formalism that generalizes Kitaev's topological arguments and the topological-invariant calculation designed for the uniform superconductor to the realm of inhomogeneous superconductivity and superfluidity. Specifically, this inhomogeneous topological superfluidity is induced by applying simultaneously a perpendicular Zeeman magnetic field and an equally weighted Rashba and Dresselhaus spin-orbit coupling in one-dimensional optical lattices. We use the self-consistent Bogoliubov–de Gennes (BdG) mean-field theory to confirm that this novel topological phase is a unique manifestation of the inhomogeneity of a superfluid and its nontrivial topological structure. The properties of the emergent Majorana bound states are investigated in detail by examining the associated $\mathbb{Z}_2$ topological number, the eigenenergy and density of states spectra, as well as the wavefunctions of the localized Majorana end modes. Experimental feasibility of observing this new topological state of matter is also discussed.

In addition to the solid-state systems discussed in the Chapter 1, there has been considerable interest in creating Majorana bound states in ultracold fermionic superfluids [32–38]. This has been stimulated by a recent breakthrough enabling the spin-orbit coupling and effective Zeeman fields required for topological superfluidity to be generated in these systems [39–42]. One peculiar advantage of deploying ultracold atoms to probe the topological properties of a quantum fluid lies in the fact that via standard techniques of optical lattices and Feshbach resonances [43, 44], now we can not only precisely tune the inter-particle interactions over a wide range of parameters, but also have the freedom to switch the dimension, modify the geometry, and control the purity of a quantum gas to experimentally simulate various theoretical models in modern physics [45]. In comparison with the well-studied two-dimensional structures, one-dimensional (1D) nanowires and optical lattices have recently attracted growing attention in detecting and engineering Majorana zero modes due to their simple 1D confinement geometry and the resultant reduction of decoherence effects [16,35–37,46,47]. To some extent, fermionic cold atoms trapped in a tube can be free of disorders, and provide another ideal platform to further explore the new topological states of quantum matter.

In this chapter, we try such a new route to theoretically predict a topologically nontrivial Fulde–Ferrell–Larkin–Ovchinnikov (*topo*-FFLO) superfluid state [25,26,48,49] in the 1D SOC Fermi gases [41, 42, 50]. Physically, FFLO states mean spatially inhomogeneous superconductivity/superfluidity. In particular, the FF state exhibits the spatial modulation in the phase of the superconducting/superfluid (SC/SF) order parameter, while for the LO state, the amplitude of the order parameter becomes modulated in real space. Therefore, as a new quantum state of matter, our predicted *topo*-FFLO state unifies superfluidity, inhomogeneity, and Majorana fermions as a whole. Notice that such a state is new and not known to exist from previous work.

Finally, it is well known that long-range SC/SF order cannot happen in truly 1D systems. To justify the self-consistent BdG mean-field description used here, we therefore assume that there exists a 3D interaction that can drive the 1D SC/SF order via a pair-tunneling interaction between many weakly coupled 1D tubes in a 3D array that would accommodate this predicted phase.

3.2 Model and phase diagrams

Here we conceive a 1D lattice model, which is of a mean-field type in the sense that we replace the quartic fermion interaction that drives the SF order with a term quadratic in the fermion operators. Such a description is appropriate if some 3D couplings have led to a situation in which the number of fermions in each wire is not individually conserved, such as in an array of 1D tubes. We will show that this mean-field model simultaneously hosts Majorana fermions at the edges and an inhomogeneous FFLO phase in the bulk, to demonstrate the existence of a novel inhomogeneous topological superfluid in fermionic condensates. The general form of the Hamiltonian we study is:

$$\begin{aligned} H &= H_{\mathrm{K}} + H_{\mathrm{R}} + H_{\mathrm{D}} + H_{\Delta}, \\ H_{\mathrm{K}} &= -t \sum_{i,j,\sigma} \psi^{\dagger}_{i\sigma}\psi_{j\sigma} + \sum_{i,\sigma} \left[V(r_i) + h\sigma_z - \mu\right] \psi^{\dagger}_{i\sigma}\psi_{i\sigma}, \\ H_{\mathrm{R}} &= -\lambda_z \sum_{i} \left(\psi^{\dagger}_{i\downarrow}\psi_{i+\hat{x}\uparrow} - \psi^{\dagger}_{i\uparrow}\psi_{i+\hat{x}\downarrow} + \mathrm{H.c.} \right), \\ H_{\mathrm{D}} &= -\lambda_y \sum_{i} \left(i\psi^{\dagger}_{i\uparrow}\psi_{i+\hat{x}\uparrow} - i\psi^{\dagger}_{i\downarrow}\psi_{i+\hat{x}\downarrow} + \mathrm{H.c.} \right), \\ H_{\Delta} &= -\sum_{i} \left(\Delta_i \psi^{\dagger}_{i\uparrow}\psi^{\dagger}_{i\downarrow} + \Delta^{*}_{i}\psi_{i\downarrow}\psi_{i\uparrow} \right), \end{aligned} \tag{3.1}$$

where $\psi^{\dagger}_{i\sigma}$ ($\psi_{i\sigma}$) denotes the creation (annihilation) field operator with spin $\sigma \equiv (\uparrow\ ,\ \downarrow)$ at site r_i. H_{K} is the kinetic term including the nearest neighbor hopping t, the 1D harmonic trapping $V(r_i) \equiv m\omega^2 r_i^2/2$, a perpendicular Zeeman field h, and chemical potential μ. In consideration of the current experimental status that only 1D equally weighted Rashba and Dresselhaus (ERD) spin-orbit (SO) coupling has been realizable in cold gases of fermions, we explicitly adopt two different kinds of SO interactions for a general purpose [3]. H_{R} represents the spin-flip Rashba type SO coupling with strength λ_z [51], while H_{D} is a spin-conserving Dresselhaus (110) SO interaction with strength λ_y [52]. H_{Δ} denotes the spin-singlet s-wave contact attraction between atoms with the gap function $\Delta_i \equiv V_s\langle\psi_{i\downarrow}\psi_{i\uparrow}\rangle$, where V_s is the pairing strength. This form of interaction might arise from the exchange of Cooper pairs among an array of 1D tubes (which is a standard 3D cold-atom setup to mimic 1D physics). Within each of these tubes there would exist some intrinsic superfluid correlations. Moreover, these tunable intertube tunnelings can also be engineered to stabilize the mean-field solutions against the fluctuation effects which would instead play a dominant role in prohibiting any possible

long-range superconducting/superfluid order in strictly isolated 1D systems (see Chapter 4). In this regard, the model (3.1) represents an effective 1D description of a weakly-coupled 3D system, where fully self-consistent mean-field-type approximation could be justified. Finally, the s-wave contact interaction in model (3.1) is also different from tunnel-coupling to a 3D superconductor. In the latter case, due to strong proximity effects, the induced superconducting order in the wire system is rigidly fixed by the bulk superconductor. Typically, there will be no phase degree of freedom.

3.2.1 Spin-orbit interactions in cold-atom gases

Because the origins of SOC in cold Fermi gases are quite different than in solid-state systems, here we briefly review their form in that context. The general three dimensional (3D) SO interaction in the SI units is as follows:

$$H_{\mathrm{SO}}^{\mathrm{3D}} = -\frac{e\hbar}{4m^2c^2}\vec{\boldsymbol{\sigma}} \cdot \left[\vec{\mathbf{E}} \times \left(\vec{\mathbf{p}} - \frac{e}{c}\vec{\mathbf{A}}\right)\right], \tag{3.2}$$

where $\vec{\boldsymbol{\sigma}}$ are the usual Pauli matrices, and $\vec{\mathbf{E}}$ is the electric field or the gradient of a scalar potential. Let's neglect the vector potential $\vec{\mathbf{A}}$, and expand the cross product into

$$\vec{\mathbf{E}} \times \vec{\mathbf{p}} = \begin{vmatrix} \boldsymbol{i} & \boldsymbol{j} & \boldsymbol{k} \\ E_x & E_y & E_z \\ p_x & p_y & p_z \end{vmatrix} = (E_y p_z - E_z p_y)\boldsymbol{i} + (E_z p_x - E_x p_z)\boldsymbol{j} + (E_x p_y - E_y p_x)\boldsymbol{k}, \tag{3.3}$$

then

$$H_{\mathrm{SO}}^{\mathrm{3D}} = -\frac{e\hbar}{4m^2c^2}\left[\sigma_x(E_y p_z - E_z p_y) + \sigma_y(E_z p_x - E_x p_z) + \sigma_z(E_x p_y - E_y p_x)\right]. \tag{3.4}$$

If we confine the system to 1D along $\hat{x}$ direction, namely $\vec{\mathbf{p}} = (p_x, 0, 0)$, we will get the 1D SO terms used in our model building [53]:

$$H_{\mathrm{SO}}^{\mathrm{1D}} = -\frac{e\hbar}{4m^2c^2}\left(\sigma_y E_z p_x - \sigma_z E_y p_x\right). \tag{3.5}$$

This form can be understood as follows: In a 1D SOC chain constructed from a 3D optical lattice, the effect of SO interaction due to the confinement in the $\hat{z}$ direction is accounted for by a spin-flip hopping, while the effect of SO interaction due to the confinement in the $\hat{y}$ direction is taken into account by an imaginary spin-conserving hopping.

In 2D solid state systems, the structure inversion asymmetry of a confinement potential and/or the bulk inversion asymmetry of a crystal can lead to the well-known Rashba and Dresselhaus SO couplings, respectively [51, 52]. The Rashba SO interaction in a square lattice has the form

$$H_{\mathrm{R}}^{\mathrm{2D}} = -\lambda_z \left\{ \sum_i \left[\psi_{i\downarrow}^\dagger \psi_{i+\hat{x}\uparrow} - \psi_{i\uparrow}^\dagger \psi_{i+\hat{x}\downarrow} + \mathrm{H.c.} \right] + \sum_i \left[i \left(\psi_{i\downarrow}^\dagger \psi_{i+\hat{y}\uparrow} + \psi_{i\uparrow}^\dagger \psi_{i+\hat{y}\downarrow} \right) + \mathrm{H.c.} \right] \right\}. \tag{3.6}$$

Now for a 1D chain along $\hat{x}$ direction, the second term on the right-hand side can be dropped. We are thus left with the 1D Rashba term $H_{\mathrm{R}}^{\mathrm{1D}} = -\lambda_z \sum_i (\psi_{i\downarrow}^\dagger \psi_{i+\hat{x}\uparrow} - \psi_{i\uparrow}^\dagger \psi_{i+\hat{x}\downarrow} + \mathrm{H.c.})$. This is exactly the third line of Eq. (3.1), which corresponds to the term $-\frac{e\hbar}{4m^2c^2}(\sigma_y E_z p_x)$. The Dresselhaus (110) SO interaction [54] is defined as

$$\begin{aligned} H_{\mathrm{D}}^{(110)} &= -\lambda_y \sum_{i,s,s'} i\,(\sigma_z)_{ss'} \left(\psi_{i-\hat{x},s}^\dagger \psi_{i,s'} - \psi_{i+\hat{x},s}^\dagger \psi_{i,s'} \right) \\ &= -\lambda_y \sum_i \left(i\psi_{i-\hat{x}\uparrow}^\dagger \psi_{i\uparrow} - i\psi_{i-\hat{x}\downarrow}^\dagger \psi_{i\downarrow} - i\psi_{i+\hat{x}\uparrow}^\dagger \psi_{i\uparrow} + i\psi_{i+\hat{x}\downarrow}^\dagger \psi_{i\downarrow} \right) \\ &= -\lambda_y \sum_i \left(i\psi_{i\uparrow}^\dagger \psi_{i+\hat{x}\uparrow} - i\psi_{i\downarrow}^\dagger \psi_{i+\hat{x}\downarrow} + \mathrm{H.c.} \right), \end{aligned} \tag{3.7}$$

which is exactly the fourth line of Eq. (3.1), corresponding to the term $\frac{e\hbar}{4m^2c^2}(\sigma_z E_y p_x)$. Therefore, the ERD SO coupling we adopt here is an equal combination of these two kinds of SO interactions restricted to 1D ($\lambda_z = \lambda_y$).

After doing a spin rotation

$$\sigma_x \to \sigma_y, \quad \sigma_y \to \sigma_z, \quad \sigma_z \to \sigma_x$$

into an equivalent representation, the first three lines of our Hamiltonian (Eq. (3.1)) can be mapped to the model including both the National Institute of Standards and Technology (NIST) SO coupling ($-\lambda \sigma_y p_x$) and the external Zeeman field $\vec{\mathbf{B}} = (0, B_y, B_z)$ [39, 41, 42].

3.2.2 Mapping to Kitaev's spinless Majorana wire

Before proving that our system can admit a topologically nontrivial superconducting state, it is worth reviewing the intuitive reason that this is possible. Recall that a topological superfluid,

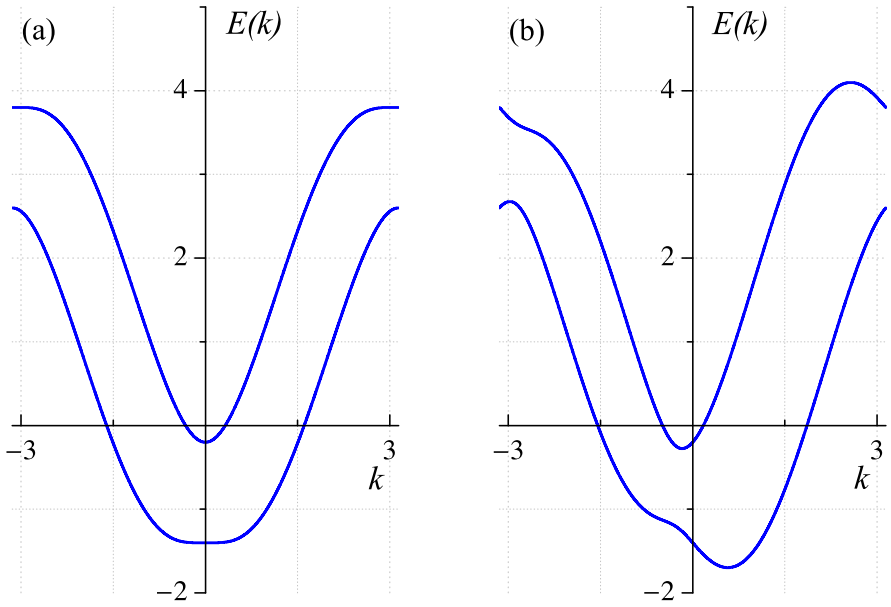

Figure 3.1: Energy spectra of the model (3.8). Panel (a) shows the band structure in the absence of Dresselhaus SO coupling ($\lambda_z = 0.56t,\ \lambda_y = 0.0t$), while panel (b) shows the band structure in the presence of both Rashba and Dresselhaus SO interactions ($\lambda_z = 0.56t,\ \lambda_y = 0.42t$). The other parameters are chosen to be $h = 0.6t$ and $\mu = -1.2t$, such that the Fermi energy is at $E(k) = 0$.

besides the nontrivial band structure, the system also needs to sustain the channel of an effective spinless p-wave pairing. In our model (Eq. (3.12)), the spin-orbit coupling effectively spin polarizes the bands, so that a nonzero Δ_q effectively describes a spinless (p-wave type) pairing.

To justify the above claim, let's divide the Hamiltonian H into the noninteracting and interacting parts: $H = H_0 + H_{\rm I}$, $H_0 = H_{\rm K} + H_{\rm R} + H_{\rm D}$, and $H_{\rm I} = H_\Delta$ (see Eq. (3.1)). To gain a simple picture of the band structure in the presence of spin-orbit interactions and the Zeeman field, we first consider the effective one-band model without superfluid pairing. The reduced single-particle Hamiltonian H_0 in the momentum space can be written under the representation $\Psi_k'^\dagger = \left(\psi_{k\uparrow}^\dagger \ \ \psi_{k\downarrow}^\dagger\right)$ as $H_0 = \sum_k \Psi_k'^\dagger \mathcal{H}'(k) \Psi_k'$, where the 2×2 BdG Hamiltonian $\mathcal{H}'(k)$ is given by

$$\mathcal{H}'(k) = \begin{pmatrix} -2t\cos k + h - \mu + 2\lambda_y \sin k & 2i\lambda_z \sin k \\ -2i\lambda_z \sin k & -2t\cos k - h - \mu - 2\lambda_y \sin k \end{pmatrix}, \qquad (3.8)$$

which can be readily diagonalized, and the obtained single-particle spectrum is

$$E_{\pm}(k) = -2t\cos k - \mu \pm \sqrt{(h + 2\lambda_y \sin k)^2 + 4\lambda_z^2 \sin^2 k}. \tag{3.9}$$

Assume that h is always nonzero. If there is no Dresselhaus SO coupling ($\lambda_y = 0$), the inversion symmetry of $\mathcal{H}'(k)$ is preserved ($E_{\pm}(k) = E_{\pm}(-k)$). However, once switching on both Rashba and Dresselhaus SO interactions, the inversion symmetry will be broken owing to the finite value of h, and the resulting asymmetry of the band structure is essential for the emergence of the FFLO state. Two typical band structures are plotted in Fig. 3.1 to illustrate the effects of including the Dresselhaus SO interaction. Panel (a) of Fig. 3.1 shows the energy spectrum $E_{\pm}(k)$ of the BdG Hamiltonian (3.8) in the presence of just Rashba SO coupling. The two resultant helical bands are symmetric under the inversion operation of the momentum k, which means that $\sigma_z \mathcal{H}'(k)\sigma_z = \mathcal{H}'(-k)$. However, after adding a Dresselhaus SO term with strength λ_y, this inversion invariance is explicitly spoiled, which gives rise to the asymmetry of the band structure as illustrated in the panel (b) of Fig. 3.1. In general, the well-separated helical bands with broken inversion symmetry would provide the possibility of realizing a topological FFLO SF pairing at finite center-of-mass momenta.

It is revealing to note that the corresponding spin-mixed helicity basis $\Phi_k'^{\dagger} = \begin{pmatrix} \phi_{k,+}^{\dagger} & \phi_{k,-}^{\dagger} \end{pmatrix}$ can be generally expressed as follows:

$$\begin{pmatrix} \psi_{k\uparrow} \\ \psi_{k\downarrow} \end{pmatrix} = \begin{pmatrix} u_k & v_k^* \\ -v_k & u_k^* \end{pmatrix} \cdot \begin{pmatrix} \phi_{k,+} \\ \phi_{k,-} \end{pmatrix}, \tag{3.10}$$

where $|u_k|^2 + |v_k|^2 = 1$. Then it would be straightforward to show that the interacting Hamiltonian H_{I} contains the designed spinless p-wave pairing after being projected onto a subset of the bands (see Fig. 3.1 for the band structure) [55],

$$\begin{aligned} H_{\mathrm{I}} =& -\Delta_q \sum_k \left(\psi_{\frac{q}{2}+k\uparrow}^{\dagger} \psi_{\frac{q}{2}-k\downarrow}^{\dagger} + \mathrm{H.c.} \right) \\ =& -\sum_k \left(\Delta_{p,+}(k) \phi_{\frac{q}{2}+k,+}^{\dagger} \phi_{\frac{q}{2}-k,+}^{\dagger} + \Delta_{p,-}(k) \phi_{\frac{q}{2}+k,-}^{\dagger} \phi_{\frac{q}{2}-k,-}^{\dagger} + \mathrm{H.c.} \right) \\ & -\sum_k \left(\Delta_s(k) \phi_{\frac{q}{2}+k,+}^{\dagger} \phi_{\frac{q}{2}-k,-}^{\dagger} + \mathrm{H.c.} \right), \end{aligned} \tag{3.11}$$

where $\Delta_{p,+}(k) = -\Delta_q u_{\frac{q}{2}+k}^* v_{\frac{q}{2}-k}^*$ and $\Delta_{p,-}(k) = \Delta_q u_{\frac{q}{2}-k} v_{\frac{q}{2}+k}$ denote the intraband p-wave fermionic pairings with a finite COM momentum q inside the upper and lower helicity branches,

respectively. $\Delta_s(k) = \Delta_q \left(u^*_{\frac{q}{2}+k} u_{\frac{q}{2}-k} + v^*_{\frac{q}{2}+k} v_{\frac{q}{2}-k} \right)$ denotes the interband s-wave pairing. If the chemical potential μ is lying within the spin-orbit gap (Fig. 3.1) and assume that Δ_q small compared to the spin-orbit gap, the only filled band is the lower helicity branch. In this case our spinful model can be mapped onto an effectively spinless system similar to Kitaev's spinless Majorana wire, suggesting that a topological superconducting phase should be possible [1,5,55]. This reasoning is further supported by the picture that even though the phase of the superfluid order varies periodically in space, its amplitude remains finite and almost spatially-independent, such that in the resulting gapped single spinless fermion band, the model (3.1) is very similar to the Kitaev chain.

3.2.3 An alternative formulation of the $\mathbb{Z}_2$ topological invariant

Before examining the phase diagram we give an alternative characterization of the topological phase, by introducing a topological invariant of the BdG band structure that is equivalent to, but conceptually distinct from, the diagnostic proposed by Kitaev.

In particular, we can verify that our intuition that strong spin-orbit coupling can drive the Hamiltonian (3.1) into a topological phase by explicitly computing the topological invariants described in Section 2.3 in a different but equivalent way.

To simplify this task, we first focus on understanding the bulk properties of the 1D SOC Fermi gas by ignoring the trapping potential and imposing the periodic boundary conditions. The resulting Hamiltonian in the momentum space can be expressed via Nambu spinor $\Psi_k^\dagger \equiv (\psi^\dagger_{\frac{q}{2}+k\uparrow}\ \psi^\dagger_{\frac{q}{2}+k\downarrow}\ \psi_{\frac{q}{2}-k\uparrow}\ \psi_{\frac{q}{2}-k\downarrow})$ as $H = \sum_k \Psi_k^\dagger \mathcal{H}(k) \Psi_k$ up to a constant, where the Bogoliubov–de Gennes (BdG) Hamiltonian reads:

$$\mathcal{H}(k) = \frac{1}{2} \begin{pmatrix} \xi^+_{\frac{q}{2}+k} & \eta_{\frac{q}{2}+k} & 0 & -\Delta_q \\ -\eta_{\frac{q}{2}+k} & \xi^-_{\frac{q}{2}+k} & \Delta_q & 0 \\ 0 & \Delta_q & -\xi^+_{\frac{q}{2}-k} & \eta_{\frac{q}{2}-k} \\ -\Delta_q & 0 & -\eta_{\frac{q}{2}-k} & -\xi^-_{\frac{q}{2}-k} \end{pmatrix}. \tag{3.12}$$

In Eq. (3.12), we assume that the superfluid order is composed of the pair condensation at a specific center-of-mass (COM) momentum q: $\Delta_i = \Delta_q e^{iqr_i}$ [48, 49], and dispersions $\xi^\pm_{\frac{q}{2}\pm k} = -2t\cos(\frac{q}{2} \pm k) - \mu \pm \left[h + 2\lambda_y \sin(\frac{q}{2} \pm k)\right]$; $\eta_{\frac{q}{2}\pm k} = 2i\lambda_z \sin(\frac{q}{2} \pm k)$.

In Chapter 2, we introduced a method due to Kitaev to determine whether a 1D superconductor is in a topological phase by computing a particular Pfaffian number of a skew matrix

(see Eq. (2.34)). For the system at hand, we will show that this quantity is equivalent to a 1D $\mathbb{Z}_2$ number $(-1)^\nu$, where the Berry phase

$$\nu = \frac{i}{\pi} \sum_{E(k)<0} \int_{-\pi}^{\pi} \langle \phi(k) | \partial_k \phi(k) \rangle dk, \tag{3.13}$$

to characterize the nontrivial topological structure of the bands of the Hamiltonian including SF order in the presence of both SO interactions and Zeeman field. When the $\mathbb{Z}_2$ number is -1 $(+1)$, the bulk system will be topologically nontrivial (trivial).

For completeness, here we provide some detailed derivations to justify the formula (3.13) such that readers can appreciate the equivalence between the seemingly different formulations based either on the Berry phase used in this chapter or on the Pfaffian of the Majorana number used in Kitaev chain (see Section 2.3). First, we may write the spinor Ψ_k in the Majorana basis $\Upsilon^\dagger_{-k} \equiv (\gamma^{\rm A}_{-k\uparrow}\ \gamma^{\rm B}_{-k\uparrow}\ \gamma^{\rm A}_{-k\downarrow}\ \gamma^{\rm B}_{-k\downarrow})$ via the following transformation, $\Psi_k = \hat{\rm T}\Upsilon_k$, namely

$$\begin{pmatrix} \psi_{\frac{q}{2}+k\uparrow} \\ \psi_{\frac{q}{2}+k\downarrow} \\ \psi^\dagger_{\frac{q}{2}-k\uparrow} \\ \psi^\dagger_{\frac{q}{2}-k\downarrow} \end{pmatrix} = \begin{pmatrix} \frac{1}{\sqrt{2}} & \frac{i}{\sqrt{2}} & 0 & 0 \\ 0 & 0 & \frac{1}{\sqrt{2}} & \frac{i}{\sqrt{2}} \\ \frac{1}{\sqrt{2}} & \frac{-i}{\sqrt{2}} & 0 & 0 \\ 0 & 0 & \frac{1}{\sqrt{2}} & \frac{-i}{\sqrt{2}} \end{pmatrix} \cdot \begin{pmatrix} \gamma^{\rm A}_{k\uparrow} \\ \gamma^{\rm B}_{k\uparrow} \\ \gamma^{\rm A}_{k\downarrow} \\ \gamma^{\rm B}_{k\downarrow} \end{pmatrix}. \tag{3.14}$$

In this basis, the Hamiltonian has the form $H = \sum_k \Upsilon^\dagger_k \hat{\rm T}^\dagger \mathcal{H}(k) \hat{\rm T} \Upsilon_k$ (see Eq. (3.12)). Here each spin species of complex fermion corresponds to a pair of Majorana fermions, which we denote $\gamma^{\rm A(B)}_{k\lambda}$, where we use A(B) to denote the Majorana index for the normal-fermionic site λ (spin-up or spin-down) in unit cell j (the Majorana operators $\gamma^{\rm A(B)}_{k\lambda}$ shall not be confused with the Bogoliubov quasiparticle operators $\gamma_{n\sigma}$ in Section 3.3). It can be easily checked that matrix $M(k) \equiv -4i\hat{\rm T}^\dagger \mathcal{H}(k) \hat{\rm T}$ satisfies the following relation

$$M^\dagger(k) = -M(k) = M^{\rm T}(-k), \tag{3.15}$$

which indicates that matrix $M(k)$ has the same symmetries as the matrix $\tilde{B}(p)$ defined in Eq. (2.33). Therefore the present model we studied in the chapter is isomorphic to the Majorana wire considered by Kitaev, but with two fermionic sites (two spin species) in one unit cell [1]. With this identification, it is not hard to see that our system is in symmetry class D [15],

and the preserved particle-hole symmetry is squared to $+1$ [33, 34]:

$$\hat{\Gamma}\mathcal{H}(k)\hat{\Gamma}^{\dagger} = -\mathcal{H}(-k)^{*},\ \hat{\Gamma} = \hat{\Gamma}^{\dagger} = \sigma_x \otimes \mathbb{1}_{2\times 2} = \begin{pmatrix} 0 & 0 & 1 & 0 \\ 0 & 0 & 0 & 1 \\ 1 & 0 & 0 & 0 \\ 0 & 1 & 0 & 0 \end{pmatrix},\ \text{and}\ \hat{\Gamma}^2 = \mathbb{1}_{4\times 4}. \quad (3.16)$$

After a lengthy but nontrivial derivation, I can further explicitly show that the topological index defined by the Pfaffian based Majorana number is completely equivalent to the Berry phase based $\mathbb{Z}_2$ index in Eq. (3.13) (see also Refs. [30, 56]). Specifically, we have the following key equation:

$$\mathcal{M}(H) = \text{sgn}\Big\{\text{Pf}\Big[-i\mathcal{H}(k=0)\hat{\Gamma}\Big]\Big\} \cdot \text{sgn}\Big\{\text{Pf}\Big[-i\mathcal{H}(k=\pi)\hat{\Gamma}\Big]\Big\} = \frac{\det U(k=0)}{\det U(k=\pi)} = (-1)^{\nu}, \quad (3.17)$$

which demonstrates the close connection between different formulations of calculating the $\mathbb{Z}_2$ topological invariant in 1D. $U(k)$ here represents the unitary matrix that diagonalizes the BdG Hamiltonian $\mathcal{H}(k)$. Hence we have the following three equivalent ways to evaluate the $\mathbb{Z}_2$ index:

(1) Perform the integral over Berry curvature of BdG bands in the first Brillouin zone to find the Berry phase ν, which equals $\frac{i}{\pi}\sum_{E(k)<0}\int_{-\pi}^{\pi}\langle\phi(k)|\partial_k\phi(k)\rangle dk$, then we can calculate $(-1)^{\nu}$.

(2) Diagonalize the BdG Hamiltonian $\mathcal{H}(k)$ at the particle-hole symmetric points $k = 0,\ \pi$ to construct the unitary matrices $U(k = 0,\ \pi)$, then the $\mathbb{Z}_2$ number is simply the ratio between their determinants.

(3) Evaluate the Pfaffians of the skew matrices $-i\mathcal{H}(k)\hat{\Gamma}$ at the points $k = 0,\ \pi$, then the Majorana number $\mathcal{M}(H)$ is the multiplication of their sign functions.

We have verified that methods (1) and (2) yield the same results as Kitaev's method (3) for Hamiltonians of the form (3.12).

3.2.4 The calculated phase diagrams

Although the Hamiltonian (3.12) is in principle quadratic in the fermion operators, its spectrum can be evaluated analytically once we have fixed the value of Δ_q. In particular, we cannot

analytically solve the mean-field consistency condition,

$$\Delta_q = \frac{V_s}{N}\sum_k \langle \psi_{\frac{q}{2}-k\downarrow}\psi_{\frac{q}{2}+k\uparrow}\rangle. \tag{3.18}$$

To evaluate its phase diagram, we therefore solve the problem numerically numerically and minimize the mean-field thermodynamic potential

$$E_g = \langle H\rangle/N + \Delta_q^2/V_s \tag{3.19}$$

(V_s is a constant) at zero temperature to self-consistently extract the values of q and Δ_q for the ground state. The basic procedure is the following. We first choose the value of q, then via diagonalizing the 4×4 $\mathcal{H}(k)$ matrix we can iteratively update the value of Δ_q by using the self-consistent equation, until the difference between two successive steps is smaller than a tiny threshold ($\sim 10^{-10}$). Finally, we determine the system's genuine ground state as well as the actual values of q and Δ_q through minimizing E_g. (Here recall that for the ease of analytical treatment we have assumed that one Fourier component at q for Δ_i dominates.) In all self-consistent calculations, we set $t = 1$ as the energy unit, the s-wave attraction magnitude $V_s = 2.5t$, and the strengths of Rashba and Dresselhaus SO couplings are determined by $\lambda_z^2+\lambda_y^2 = \lambda^2$ ($\lambda = 0.7t$). For simplicity, we only present the results at zero temperature.

Figure 3.2 shows the typical phase diagrams for the 1D Fermi gases at different intensities of SO couplings on the h-μ plane. In panel (a), we keep $\lambda_z = \lambda$ and the resulting ground states in the limit of strong Rashba interaction are thus dominated by the homogeneous states with vanishing q. Specifically, we observe that besides vacuum (empty bands without filling) and conventional Bardeen–Cooper–Schrieffer (BCS) superfluid, there exists another homogeneous but topologically nontrivial superfluid phase in the region of large h. All these results are consistent with previous studies on the Rashba SOC Fermi gases [36, 37]. The phase diagram will get much richer and more interesting if we turn on the strong ERD SO interaction (Fig. 3.2(b)). Instead of the homogeneous phases, we find that under strong Zeeman fields ($h > 0.35t$), the whole system would be driven from a BCS superfluid into an inhomogeneous pairing state with a finite COM momentum. Through tuning the band-filling, we can further get access to the topological portion of the spectrum, hence triggering the emergence of a new type of *topo*-FFLO superfluid carrying simultaneously a finite q, a nonzero Δ_q, and a nontrivial $\mathbb{Z}_2$ number "-1." The physical underpinning of this inhomogeneous topological superfluidity is mainly stemming from the inversion *asymmetry* of Bloch bands, which means that with fixed

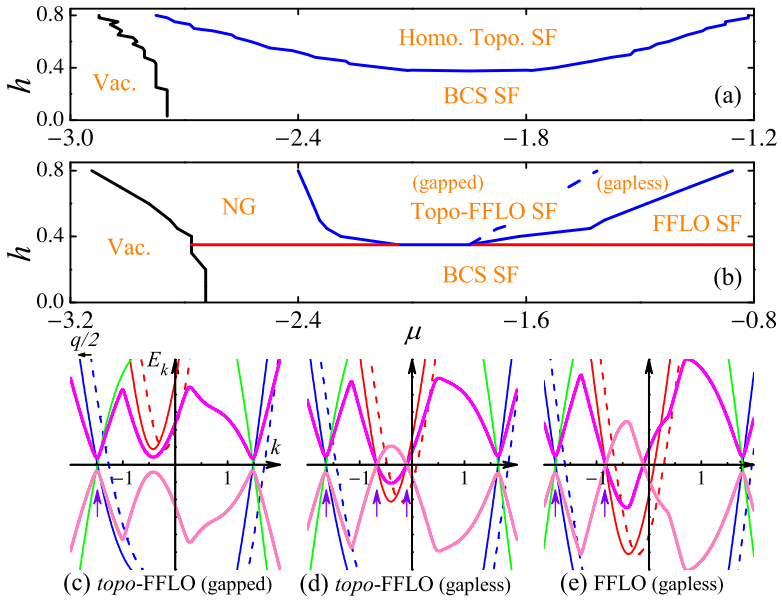

Figure 3.2: Two generic phase diagrams of a 1D SOC fermionic condensate on the h-μ coordinates. Panel (a) is for homogeneous superfluid (SF) states with Rashba SO coupling ($\lambda_z = \lambda$, $\lambda_y = 0$), while panel (b) illustrates the emergence of an inhomogeneous topological superfluid (gapped and gapless) in the ERD SOC Fermi gas ($\lambda_z = \lambda_y = \frac{\sqrt{2}}{2}\lambda$) [$\lambda = 0.7t$]. The phase boundaries are symmetric about $\mu = 0$ and NG stands for the normal gas state. Three lower panels (c)–(e) show the dispersion spectra of varied FFLO states in (b) with fixed $h = 0.6t$ and increasing $\mu = -1.6t$ (c); $-1.3t$ (d); $-1.0t$ (e), where thin solid (dashed) lines [red and blue] represent (un)shifted helical bands of the noninteracting system. The thick magenta line denotes the lowest quasihole branch of Eq. (3.12). Purple arrows mark the Fermi points of shifted noninteracting helicity bands in half of the Brillouin zone (BZ).

ERD SO coupling, the increase of h will not only modify the topology of the band structure via opening a spin-orbit gap and spoiling time reversal symmetry, but it also facilitates the effective p-wave fermionic pairing at a nonvanishing COM momentum q. As compared to Rashba and Dresselhaus, it should be able to see from the band structure why finite q is favored.

To clarify the origin of various FFLO states in Fig. 3.2(b), we highlight here their dispersions near the Fermi level. Figures 3.2 [(c)–(e)] show the following:

(1) Due to the inversion asymmetry, superfluid pairing *inside* the lower *spin-mixed* helicity branch (blue solid line) opens the energy gaps at its Fermi points. However, since we have forced the system to choose only one specific COM momentum q, the intraband

pairing inside the upper helical band will not be allowed to open extra energy gaps at its inner Fermi points, which gives rise to the gapless state if μ also crosses the upper helical band (red solid line).

(2) The $\mathbb{Z}_2$ topological invariant can now be approximated by the parity of the number of Fermi points in half of the Brillouin zone (marked by the purple arrows). The inclusion of a finite COM momentum q may also generate an additional parameter interval for μ, inside which the noninteracting helicity bands may still have an odd number of Fermi points in half of the Brillouin zone, but three points in one side and one point in the other (see Fig. 3.2(d)).

3.2.5 More details on the topological phase transition

Because of the presence of ERD SO interaction, the superfluid order parameter Δ_i is now a complex number, whose real and imaginary parts are both oscillating in the real space, but whose magnitude Δ_q can still be a real and spatially independent constant if we choose the periodic boundary conditions without a trap. Further, as shown in Eq. (3.17), the $\mathbb{Z}_2$ topological invariant depends only on the magnitude of the superfluid order parameter Δ_i and its COM momentum q, therefore, although Δ_i changes its phase periodically, the topological index is still well defined, which is sufficient to characterize the nontrivial topological structure of the 1D superfluid system.

In the following, we will try to present a detailed analysis of the topological phase transition by examining the lowest excitation spectra. To better understand the topological phase transition in the 1D ERD SOC Fermi gases, in Fig. 3.3, we plot the evolution of the two lowest eigenenergies $E_{1,2}$ of the quasihole excitations as increasing the Zeeman field h with fixed chemical potential $\mu = -1.8$. A critical point of the topological phase transition from the conventional BCS superfluid to the newly predicted *topo*-FFLO superfluid can thus be resolved around $h_c \sim 0.4$, where the calculated $\mathbb{Z}_2$ index changes its value from $+1$ to -1, indicating the emergence of unpaired zero energy states at the boundaries as E_1 illustrates. Typically, E_2 will largely amount to the value of the bulk energy gap, which, as shown in Fig. 3.3, will first close at the critical point h_c, and then reopen again to protect the resulting edge zero modes so as to ensure the appearance of physically well separated Majorana bound states. The FFLO nature of this topological superfluid phase has been partially demonstrated in the Subsection

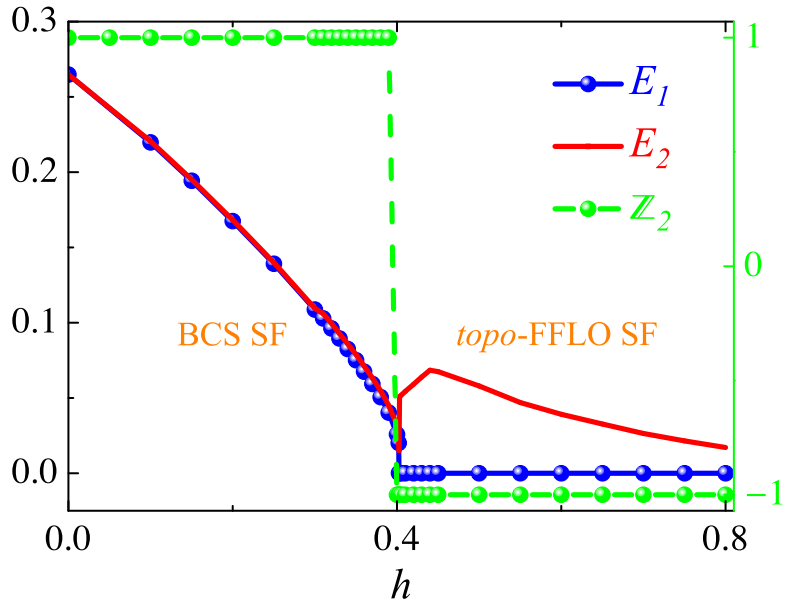

Figure 3.3: Two lowest quasihole eigenenergies $E_{1,2}$ as functions of the Zeeman field h. The critical point of the topological phase transition between BCS and *topo*-FFLO superfluids can be resolved at $h_c \sim 0.4$, where the value of the $\mathbb{Z}_2$ invariant changes from $+1$ to -1 (see the right $\hat{y}$ axis). Chemical potential μ is fixed to be -1.8. All other parameters are the same as in Fig. 3.2(b). Here for the numerical calculation, the system size is 501 sites, which is sufficiently large to avoid the finite-size effects.

3.2.2 by projecting the pairing term H_Δ onto the helicity basis and studying the corresponding dispersion spectra near the Fermi level.

3.3 Topo-FFLO superfluid in real space

Now we concentrate on real-space configurations of the emergent Majorana end states in *topo*-FFLO phase (gapped) under realistic harmonic trapping and ERD SO coupling. After performing canonical transformations:

$$\psi_{i\uparrow} = \sum_n \left[u_{n\uparrow}(r_i)\gamma_{n\uparrow} - v^*_{n\downarrow}(r_i)\gamma^\dagger_{n\downarrow} \right], \tag{3.20}$$

$$\psi^\dagger_{i\downarrow} = \sum_n \left[v_{n\uparrow}(r_i)\gamma_{n\uparrow} - u^*_{n\downarrow}(r_i)\gamma^\dagger_{n\downarrow} \right], \tag{3.21}$$

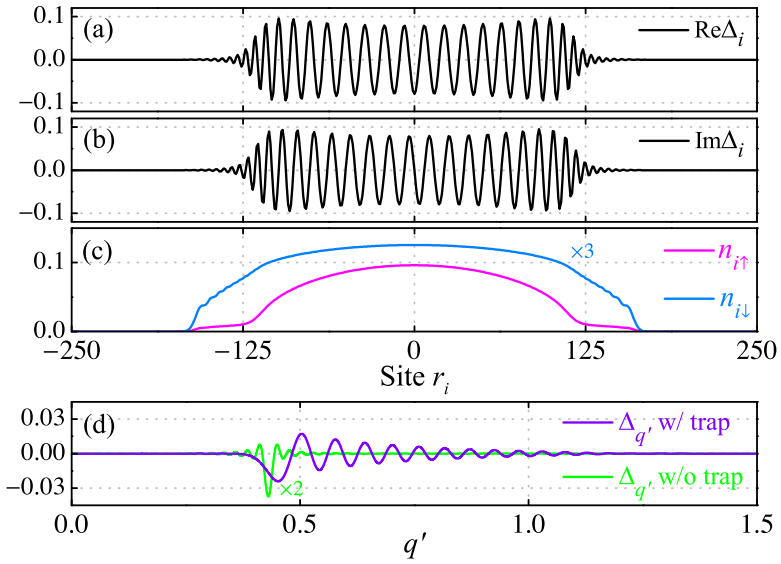

Figure 3.4: Spatial profiles of superfluid order parameter Δ_i and atomic densities $n_{i\sigma}$ for the 1D ERD SOC Fermi gas in real-space confinement. The real and imaginary parts of Δ_i are plotted in panels (a) and (b), respectively. Density distributions $n_{i\sigma}$ are shown in panel (c). Fourier transforms of Δ_i at finite momenta q' are depicted in panel (d), where the purple (green) line denotes $\Delta_{q'}$ with (without) trap. Here $V_s = 2.5t$, $\lambda = 0.7t$, $h = 0.6t$, $\mu = -1.6t$, $\lambda_z = \lambda_y = \frac{\sqrt{2}}{2}\lambda \approx 0.495t$, and $m\omega^2/2 \approx 0.0001t$.

we can obtain the self-consistency BdG equations from Eq. (3.1) as follows: $[H, \gamma_{n\sigma}] = -E_n\gamma_{n\sigma}$ and $[H, \gamma^\dagger_{n\sigma}] = E_n\gamma^\dagger_{n\sigma}$. Since the system preserves particle-hole symmetry, Bogoliubov quasiparticle operators γ's satisfy the relations $\gamma_{-E} = \gamma^\dagger_E$, which implies that the system will become topologically nontrivial if $E = 0$ and $\gamma_0 = \gamma^\dagger_0$ localized near its boundaries. The real-space computation (Fig. 3.4) is conducted on a 501×1 lattice with open boundary conditions ($V_s = 2.5t$, $h = 0.6t$, $\mu = -1.6t$, $\lambda_z = \lambda_y = \frac{\sqrt{2}}{2}\lambda$, and $m\omega^2/2 \approx 0.0001t$). The basic procedures are the following: We first plug in the initial trial configurations for the order parameters, then by implementing the Hamiltonian we iteratively evolve and update the trial solutions until all the self-consistency conditions are fulfilled. In the case of multiple self-consistent solutions, we carefully pick up the genuine ground state by comparing the total free energy.

Figure 3.4 summarizes the spatial profiles of superfluid order parameter and fermion density distributions in the confined 1D tube along $\hat{x}$-direction. Driven by the interplay between the

asymmetry of Fermi surface (points) and the superfluid pairing, real and imaginary parts of Δ_i display rapid oscillations across zero in antisymmetric ways throughout the whole region of the quantum gas with a period of about 12 sites (see Figs. 3.4(a) and (b)). To gain a concrete understanding of this spatial variation, we expand the superfluid order parameter Δ_i in terms of a spectrum of plane waves

$$\Delta_i = \sum_{q'} \Delta_{q'} e^{iq'r_i}. \tag{3.22}$$

Specifically, if only one Fourier component $\Delta_{q'}$ $(q' \neq 0)$ dominates, we would have the Fulde–Ferrell state; instead if a pair of components $\Delta_{q'} = \Delta_{-q'}$ $(q' \neq 0)$ dominate, we would have the Larkin–Ovchinnikov state. It becomes clear from Fig. 3.4(d) that the imposition of a harmonic trap induces the modulation of multiple Fourier modes $\Delta_{q'}$ in the interval ranging from $q' \sim 0.5$ to 1.0. While, for the case of free gas without trap, $\Delta_{q'}$ change to centrally distribute around a single momentum $q' \approx 0.45$ (see the green line in Fig. 3.4(d)). This is consistent with our k-space formalism in Section 3.2. With such observations, we deduce that at the given parameters, the bulk system has entered an inhomogeneous FFLO state. In Fig. 3.4(c) we add the density distributions $n_{i\sigma}$ as well, from which the bimodal structure of spin $\uparrow$ atom distribution is visible.

Remarkably, when mapping out the corresponding excitation spectrum of the system, we find that interestingly, the 1D quantum gas inside tube also possesses nontrivial topological properties. As shown in Fig. 3.5(a), after switching on the ERD SO interaction, the minimal value of eigenenergy $|E_n|$ becomes exponentially small ($\sim 10^{-10}$), which indicates the emergence of unpaired Majorana fermions at the edges because now occupying or emptying this near-zero-energy excitation state will lead to the important degeneracy. Note that there is only *one* pair of Majorana fermions in our system. The second lowest value of $|E_n|$ equals $0.012t$ with trap and $0.036t$ without trap. Since these gapless chiral edge states live only inside domain walls separating topologically distinct regimes, the fact that we see evidence for only a single pair of Majorana zero modes is signalling that besides vacuum and normal gas state, near the trap boundaries, the entire center of the trap is in a single, topologically superfluid, phase formed by fermionic atoms in the 1D optical lattice. Since Δ_i is spatially varying, this unique condensation of Cooper pairs is exactly the *topo*-FFLO state we discussed. In Figs. 3.5 [(b),(c);(d)] (with trap) and [(e),(f);(g)] (without trap), we further plot separately the amplitudes of wavefunctions and the corresponding local density of states (LDOS) spectra for the zero-energy Majorana fermions, from which we can see that these zero modes, whose wavefunctions

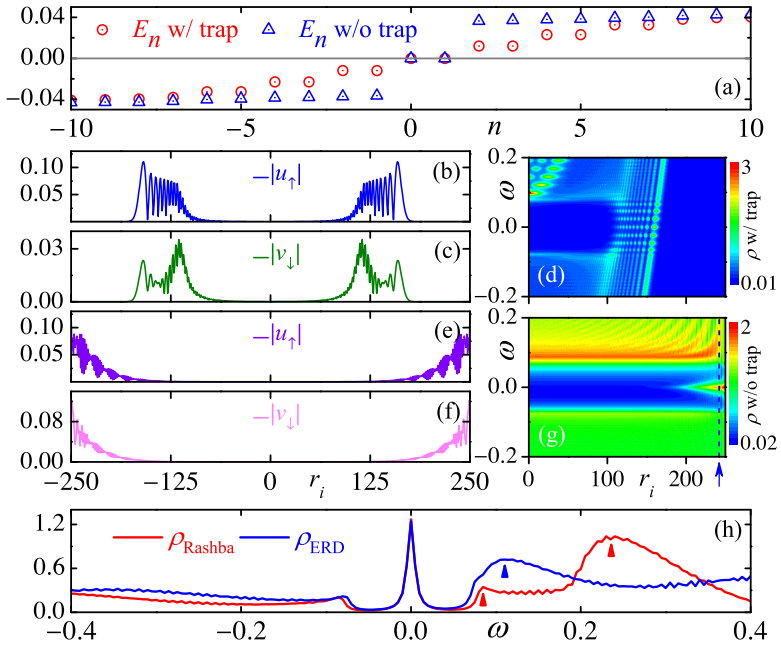

Figure 3.5: Quasiparticle spectra E_n of the 1D ERD SOC Fermi gases with (red circle) and without (blue triangle) trapping [panel (a)]. Panels [(b),(c)] and [(e),(f)] depict the amplitudes of wavefunctions for the zero energy states with and without trap, respectively. Panels (d) (with trap) and (g) (without trap) show the corresponding contours of LDOS along half of the lattice. The low-energy spectral weight appears to be reduced when imposing a trapping potential. All parameters are the same as in Fig. 3.4. Total LDOS spectra along the cut at site $r_i = 242$ (see blue dashed line in (g)) without trap are plotted in panel (h) for both topological BCS superfluid (ρ_{Rashba}; $\lambda_z = \lambda$, $\lambda_y = 0$) and *topo*-FFLO superfluid (ρ_{ERD}; $\lambda_z = \lambda_y = \frac{\sqrt{2}}{2}\lambda \approx 0.495t$). Here $\rho_i(\omega) = \sum_{n,\sigma}[|u_{n\sigma}(r_i)|^2\delta(E_n - \omega) + |v_{n\bar{\sigma}}(r_i)|^2\delta(E_n + \omega)]$.

are self-conjugate, are localized near the boundaries. One distinguishing feature of the energy-resolved LDOS contours with and without the trapping potential is the presence of a mid-gap peak at zero energy localized near the trap edge, which serves as compelling evidence for the realization of Majorana fermions in 1D SOC chain. Moreover, being specific to *topo*-FFLO phase, in Fig. 3.5(h), we compare line cuts of the spectral weight near the chain's boundary in the *topo*-FFLO and uniform topological superfluid phases. In addition to the peak at zero energy present in both cases, we find a significantly enhanced spectral weight in the FFLO regime for positive energies close to the superfluid gap (marked by triangles). This measurable feature may help differentiate these two topological states in experiments. We have also numerically

verified that the *topo*-BCS phases predicted for homogeneous systems in Section 3.2 persist in the presence of a trapping potential, in consistent with the results in Ref. [36, 37].

Similar to the mechanism proposed for semiconducting heterostructures [3, 55], this revealed coexistence of topological order and FFLO superfluidity is due to the conspiracy of a spin-singlet–pairing mediated p-wave superfluid instability in the topologically nontrivial Bloch bands with the Zeeman field facilitated breaking of time reversal and *inversion* symmetries. Non-Abelian Majorana fermions are then emerging from the phase twist of orbital motion accompanying ERD SO interaction [33, 34] in the effectively spinless topological band. In our perspective, the lattice model Eq. (3.1) demonstrates the first attainable scenario of creating the predicted inhomogeneous topological superfluidity in atomic Fermi gases [39, 41, 42, 50]. It also uncloaks a novel mechanism for the FFLO superfluidity/superconductivity in a single spin-mixed asymmetric helicity band of a SOC system.

3.4 Experimental realization

We propose to use fermionic lithium atoms as a quantum simulator to synthesize and detect this new topological state of matter in cold atom condensates. It has been shown that spin-imbalanced ^{6}Li degenerate gas loaded in an array of tubes can realize the partially polarized superfluid phase with possible FFLO correlations in 1D [50]. The ^{6}Li atoms can also be dressed up via a pair of Raman beams to produce the 1D equal-part Rashba and Dresselhaus SO coupling, and the opened spin-orbit gap has been directly observed in spin-injection spectroscopy measurements [40, 42]. Therefore, all the required techniques of simulating the model Hamiltonian Eq. (3.1) are within the scope of current experimental sophistication. Furthermore, signatures of *topo*-FFLO state may be detectable with spatially resolved radio-frequency spectroscopy and time-of-flight imaging through seeking the described features in LDOS spectrum and the bimodal structure of atom density distribution.

3.5 Conclusions

In this chapter we have predicted a new *topo*-FFLO phase in SOC Fermi gases. This generalizes the theory of homogeneous topological SF/SC to include a nonzero center-of-mass momentum

for the fermionic pairing. In the cases studied here, this requires explicitly breaking time-reversal and inversion symmetries (which are not important to protecting the Majorana bound states characteristic of 1D topological superconductors/superfluids). Also, the present work demonstrates a novel mechanism for the FFLO superfluidity/superconductivity in SOC systems, which is very different from the conventional FFLO pairing driven by a purely strong Zeeman field.

In summary, we theoretically study the phase diagram of an ERD SOC Fermi gas in 1D optical lattice, and successfully identify *for the first time* an exotic topological FFLO superfluid in the region of strong SO couplings and Zeeman field. Detailed structures of order parameters and Majorana end modes associated with this *topo*-FFLO phase are manifestly uncovered in real space through utilizing the BdG formulation. Our work might have opened up new prospects for the exploration of topological states of matter in SOC systems.

Note that this PRL work has already been cited by two recent Review articles [57,58] in the field.

Chapter 4

Flux-Stabilized Majorana Zero Modes in Coupled One-Dimensional Fermi Wires

4.1 Introduction

Topological superconductivity and superfluidity featuring Majorana bound states and beyond have been a focus of condensed matter and cold atom communities over the past few years [1–6, 9, 20, 27, 44, 55, 59–72]. One common thread of this pursuit in solid state systems entails interfacing materials with differing properties through proximity effects [2–6, 9, 20, 55, 60–62]. Experimentally, solid state architectures of Majorana fermions [18, 19, 31, 73–76] are typically in close contact with external reservoirs, such as s-wave superconductors, therefore the total particle number in these hybrid systems is not strictly conserved. The required strong proximity effects impose further restrictions on the gap structure forming upon the topological segment of interest, which renders the experimental realization challenging [21, 22].

Kitaev model, its continuum version, and the inhomogeneous topological superfluidity discussed so far in Chapters 2 and 3 belong to such 1D number-nonconserving systems, described by BdG Hamiltonians that conserve fermion number only modulo 2. Truly 1D number-conserving systems actually cannot have long-range superconducting order, and are in fact gapless [77–83]. However, can they still have Majorana zero modes? If so, what is the physical

way to manufacture them? It turns out that the answer is positive. The minimal setup requires two flavors of fermions, which can be achieved by populating spinless fermions on a two-leg ladder. One concrete model in this category was proposed by Kraus et al. [80] who showed that even starting with a topologically trivial band structure of an atomic two-leg ladder, a phase bearing the hallmarks of a 1D topological superconductor can still be accessed through coupling the wires only by terms quartic in the fermion operators. Intuitively, this means that the fermion parity in each leg is conserved modulo 2, which gives a conserved fermion parity in addition to the fixed total particle number. This proposal offers a distinctive framework to investigate fermionic topological matter in optical lattices with the advantage of controllability and flexibility.

Nonetheless, one outstanding challenge in the aforementioned pair-hopping model is to beat the ordinary interleg single-particle tunneling ($t_\perp$) that breaks the single chain's fermion parity explicitly. Almost all the existing literature [78, 80–83] focused on possible schemes for suppressing $t_\perp$. Instead, in this chapter, we will show that this obstacle can be surmounted by piercing a synthetic magnetic π-flux through each plaquette of the Fermi ladder. Based on bosonization, density matrix renormalization group (DMRG), and exact diagonalization (ED), we demonstrate that the resulting model accommodates a topological regime that is compatible with both single-particle and pair tunnelings. Specifically, even in the presence of single-particle tunneling, at low energies there is an emergent valley fermion parity, associated with the boundary Majorana zero modes. Intriguingly, the emergent valley fermion parity is intimately linked with the exact microscopic leg-interchange symmetry of the lattice Hamiltonian, thus these two identified operators provide a reliable characterization of the newly-predicted Majorana boundary states in a complementary way. Our work also exhibits the unusual impacts of the topologically trivial band structures on the interaction-enabled topological phases.

On the experimental side, currently in cold atom laboratories, a great deal of effort has been devoted to creating strong synthetic magnetic fields in optical lattices by Raman-assisted tunnelings and lattice-shaking techniques, which mimic standard Peierls substitutions through attaching an Aharanov–Bohm-like complex phase to the nearest-neighbor single-particle hopping [84–96]. The remarkable tunability of these artificial gauge fluxes has paved an experimental avenue to exploring the Bose–Einstein condensation in Harper–Hofstadter model of 2D bosonic gases [94]. Chiral edge states due to particle's cyclotron motion stirred by the uniform fluxes have also been detected in quasi-1D fermionic ladders and Hall ribbons, where a sizable

flux ϕ can reach up to 1.31π per plaquette by utilizing the technologies of synthetic dimensions and optical atomic clocks [90–93]. Therefore proposing π flux to stabilize the Majorana zero modes is not experimentally unrealistic.

This chapter is organized as follows: We will first examine the noninteracting band structure of the two-leg ladder, and then proceed to the detailed bosonization of the pair-hopping model. To clarify the underpinnings for the topological Majorana boundary states, we use the renormalization group analysis combined with the extensive DMRG and ED simulations. In particular, we highlight that the main interest of the present work is to describe a new mechanism for protecting Majorana zero modes, involving a microscopic unitary symmetry which effectively plays the role of fermion parity at long wavelengths. We emphasize that the π-flux ladder Hamiltonian exhibits topological superconductivity/superfluidity without any microscopic symmetry that can be related to fermion parity; we believe that it is the first concrete lattice model of this type. The fact that this can be done, together with the relationship between this microscopic unitary lattice symmetry and an emergent valley fermion-parity symmetry, is a useful new conceptual framework to study Majorana fermions in particle-number conserving systems which goes beyond the standard Kitaev paradigm.

4.2 Fermionic flux ladder model

Motivated by these theoretical and experimental considerations, we study an interacting two-leg ladder model of spinless fermions in a perpendicular magnetic field described by the following number-conserving Hamiltonian,

$$H = H_K + H_W, \tag{4.1}$$

$$\begin{aligned} H_K = &- \sum_{n=0}^{L-2} \left[\left(t_\parallel e^{i\frac{\phi}{2}} c^\dagger_{n,0} c_{n+1,0} + t_\parallel e^{-i\frac{\phi}{2}} c^\dagger_{n,1} c_{n+1,1} \right) + \text{H.c.} \right] \\ &- \sum_{n=0}^{L-1} \left(t_\perp c^\dagger_{n,0} c_{n,1} + \text{H.c.} \right), \end{aligned} \tag{4.2}$$

$$H_W = + \sum_{n=0}^{L-2} \left(W c^\dagger_{n,0} c^\dagger_{n+1,0} c_{n,1} c_{n+1,1} + \text{H.c.} \right), \tag{4.3}$$

where $c^{(\dagger)}_{n,\ell}$ is the fermionic annihilation (creation) operator at rung n on the leg $\ell = 0, 1$. The intraleg and interleg single-particle tunneling strengths are $t_\parallel$ and $t_\perp$, respectively. Two essential

ingredients of the above model are the synthetic Peierls phase $\phi \in [0, \pi]$ per plaquette, and the interchain pair-hopping interaction H_W. (For a schematic of the model, see Fig. 4.1.) Previous works have demonstrated the existence of Majorana fermions in this Hamiltonian at $\phi = 0$ and $t_\perp = 0$ based on a preserved fermion number parity $\mathsf{P}_\ell := (-1)^{N_\ell}$ where N_ℓ is the particle-number operator of leg ℓ [78, 80–82]. Here we will show a richer phase diagram of Eq. (4.1) in the presence of a nonzero and not necessarily small $t_\perp$ when $\phi = \pi$. Especially we predict a novel Majorana boundary state and study the associated topological quantum phase transition. Notice that without pair hopping, the bare band H_K in (4.2) is topologically trivial, so that model (4.1) is different from the interacting Kitaev chains and spin-orbit-coupled wires [59, 64, 97], where the Majorana modes originate from the nontrivial band structures. In comparison, Eq. (4.1) realizes a *generalized* interaction-driven topological phase, the status of which will be elaborated below.

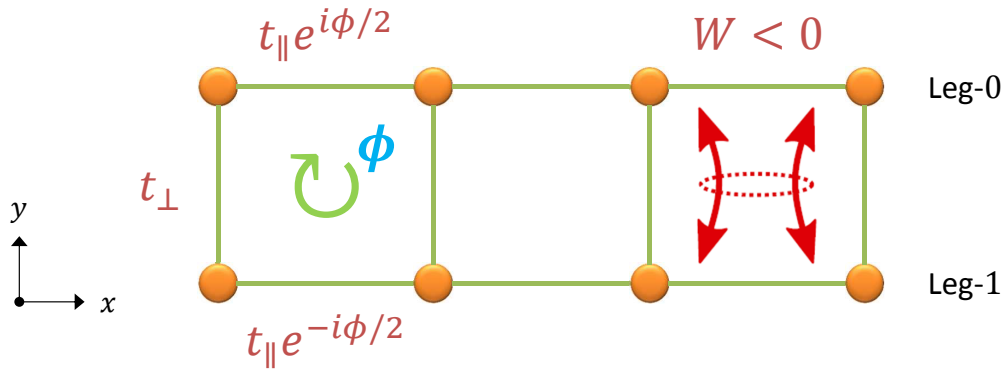

Figure 4.1: The schematic diagram of the two-leg fermionic flux ladder model where we illustrate the various terms in Eqs. (4.1) to (4.3).

4.2.1 Linearizing the band

To develop a low-energy effective field theory for the above model, the first step we take is to recast the discrete lattice Hamiltonian (4.1) into a continuum description. This can be achieved by the following standard mapping,

$$c_{k,\alpha} \longrightarrow \frac{1}{L^{d/2}}\psi_{k,\alpha}, \quad c_{j,\alpha} \longrightarrow \left(\frac{a}{2\pi}\right)^{d/2}\psi_{x,\alpha},$$
$$\sum_{k\in \mathrm{BZ}} \longrightarrow \left(\frac{L}{2\pi}\right)^d \int d^d k, \quad \sum_{r_j} \longrightarrow \frac{1}{a^d}\int d^d x,$$

where $V = N \cdot a^d = L^d$ is the system's volume, a is the lattice constant, L is the length of one edge, and d is the system's spatial dimensions. After performing the standard mapping, the Fourier-transformed Hamiltonian assumes

$$H_K = \int \frac{dk}{2\pi} \left\{ -2t_\parallel \cos\left(ka + \frac{\phi}{2}\right) \psi^\dagger_{k,0}\psi_{k,0} - 2t_\parallel \cos\left(ka - \frac{\phi}{2}\right) \psi^\dagger_{k,1}\psi_{k,1} \right. \\ \left. -t_\perp \psi^\dagger_{k,0}\psi_{k,1} - t_\perp \psi^\dagger_{k,1}\psi_{k,0} \right\}, \tag{4.4}$$

$$H_W = -\frac{aW}{(2\pi)^2} \int dx \left\{ \psi^\dagger_{x,0}\psi_{x,1}\psi^\dagger_{x+a,0}\psi_{x+a,1} + \psi^\dagger_{x+a,1}\psi_{x+a,0}\psi^\dagger_{x,1}\psi_{x,0} \right\}. \tag{4.5}$$

In this subsection we will focus on analyzing the kinetic term H_K. The all-important physics of the pair-hopping interaction H_W will be furnished in detail in the following sections.

The noninteracting kinetic Hamiltonian can be readily diagonalized by a unitary transformation,

$$\begin{aligned} H_K &= \int \frac{dk}{2\pi} \begin{pmatrix} \psi^\dagger_{k,0} & \psi^\dagger_{k,1} \end{pmatrix} \mathbb{H}(k,\phi) \begin{pmatrix} \psi_{k,0} \\ \psi_{k,1} \end{pmatrix} \\ &= \int \frac{dk}{2\pi} \begin{pmatrix} \psi^\dagger_{k,0} & \psi^\dagger_{k,1} \end{pmatrix} \begin{pmatrix} -2t_\parallel \cos\left(ka + \frac{\phi}{2}\right) & -t_\perp \\ -t_\perp & -2t_\parallel \cos\left(ka - \frac{\phi}{2}\right) \end{pmatrix} \begin{pmatrix} \psi_{k,0} \\ \psi_{k,1} \end{pmatrix} \\ &= \int dk \begin{pmatrix} \psi^\dagger_{k,+} & \psi^\dagger_{k,-} \end{pmatrix} \begin{pmatrix} E_+ & 0 \\ 0 & E_- \end{pmatrix} \begin{pmatrix} \psi_{k,+} \\ \psi_{k,-} \end{pmatrix}, \end{aligned} \tag{4.6}$$

where we have introduced the unitary matrix $\mathbb{M}(k,\phi)$ that diagonalizes $\mathbb{H}(k,\phi)$, namely

$$\mathbb{M}(k,\phi) = \begin{pmatrix} |+\rangle & |-\rangle \end{pmatrix} = \begin{pmatrix} \frac{-u_{k,\phi}}{\sqrt{1+u^2_{k,\phi}}} & \frac{1}{\sqrt{1+u^2_{k,\phi}}} \\ \frac{1}{\sqrt{1+u^2_{k,\phi}}} & \frac{u_{k,\phi}}{\sqrt{1+u^2_{k,\phi}}} \end{pmatrix},$$

$$\mathbb{M}^\dagger \mathbb{H}(k,\phi) \mathbb{M} = \begin{pmatrix} E_+(k,\phi) & 0 \\ 0 & E_-(k,\phi) \end{pmatrix},$$

where the component in the matrix elements assumes

$$u_{k,\phi} = \frac{1}{t_\perp} \left\{ 2t_\parallel \sin(ka) \sin\frac{\phi}{2} + \sqrt{t^2_\perp + \left(2t_\parallel \sin(ka)\sin\frac{\phi}{2}\right)^2} \right\},$$

and the obtained bonding and antibonding energies are given by

$$E_\pm(k,\phi) = \frac{1}{2\pi} \left\{ -2t_\parallel \cos(ka)\cos\frac{\phi}{2} \pm \sqrt{t^2_\perp + \left(2t_\parallel \sin(ka)\sin\frac{\phi}{2}\right)^2} \right\}. \tag{4.7}$$

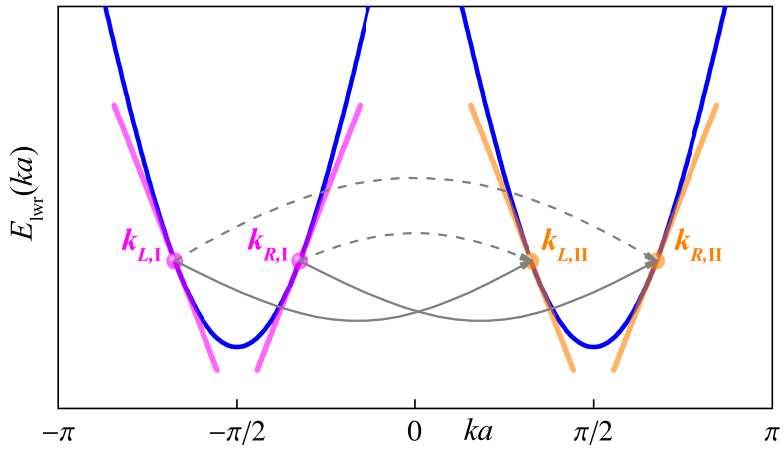

Figure 4.2: Linearization of the antibonding band (blue solid line) at $\phi = \pi$. The obtained four chiral-fermion branches can be separated into valley-I (light magenta) and valley-II (light orange) that generalize the original chain degree of freedom. Specifically, we depict the two types of umklapp processes that obey Eq. (4.13).

Accordingly fermion operators in chains and in bands are linked by

$$\psi_{k,s} = \sum_{\chi=\pm} \langle s|\chi\rangle \psi_{k,\chi},$$

where

$$\langle s=0| \equiv (1\ \ 0) \quad \text{and} \quad \langle s=1| \equiv (0\ \ 1)\,. \tag{4.8}$$

As will be shown below, the topologically nontrivial state featuring the many-body Majorana zero modes is well defined when $\phi = \pi$, so we will mainly concentrate on this special value of the magnetic flux.

Since we are focusing on the case of $\phi = \pi$ with four independent but mutually interacting chiral-fermion branches, the normal complex fermions in real space could be projected onto these four chiral branches by constructing the corresponding projective forms of their creation and annihilation operators. Here it proves important to distinguish the chain indices $s = 0, 1$ from the valley indices $v = \mathrm{I}, \mathrm{II}$ after proper band projection. As usual, we denote the bonding and antibonding band by indices $\chi = +, -$, respectively. The Fourier transform of the Dirac fermion operator gives

$$\psi_{x,s} = \frac{1}{\sqrt{2\pi}} \int dk e^{ikx} \psi_{k,s} = \frac{1}{\sqrt{2\pi}} \sum_{\chi=\pm} \int dk e^{ikx} \langle s|\chi\rangle \psi_{k,\chi}.$$

Then by a close inspection of the band structure at $\phi = \pi$, it is self-evident that once the single-particle interchain tunneling is turned on, there exist two immediate consequences. First, the bonding and antibonding bands are completely separated from each other by a gap at $ka = 0, \pm\pi$ that is set by $t_\perp$. Thus this justifies projecting out the unoccupied upper bonding band and concentrate only on the lower antibonding band if the system is less than half-filled. Second and more importantly, after projection the fermion degrees of freedom inside the remaining antibonding band are now a mixture from both chains. There are four Fermi points, which gives two right movers and two left movers, which we distinguish with a valley index that can be continuously deformed back to the chain indices when $t_\perp \to 0$. Implementing these rationales leads to the following derivations,

$$
\begin{aligned}
\psi_{x,s} &= \frac{1}{\sqrt{2\pi}} \int dk e^{ikx} \psi_{k,s} = \frac{1}{\sqrt{2\pi}} \sum_{\chi=\pm} \int dk e^{ikx} \langle s|\chi\rangle \psi_{k,\chi} \\
&\xrightarrow{\text{Project out bonding band}} \psi_{x,s} \simeq \frac{1}{\sqrt{2\pi}} \int dk e^{ikx} \langle s|-\rangle \psi_{k,-}, \\
\psi_{x,s} &\simeq \frac{1}{\sqrt{2\pi}} \int dk e^{ikx} \langle s|-\rangle \psi_{k,-} \\
&\simeq \frac{1}{\sqrt{2\pi}} \int_{k_{L,\mathrm{I}}-\Lambda}^{k_{L,\mathrm{I}}+\Lambda} dk e^{ikx} \langle s|-\rangle \psi_{k,-} + \frac{1}{\sqrt{2\pi}} \int_{k_{R,\mathrm{I}}-\Lambda}^{k_{R,\mathrm{I}}+\Lambda} dk e^{ikx} \langle s|-\rangle \psi_{k,-} \\
&+ \frac{1}{\sqrt{2\pi}} \int_{k_{L,\mathrm{II}}-\Lambda}^{k_{L,\mathrm{II}}+\Lambda} dk e^{ikx} \langle s|-\rangle \psi_{k,-} + \frac{1}{\sqrt{2\pi}} \int_{k_{R,\mathrm{II}}-\Lambda}^{k_{R,\mathrm{II}}+\Lambda} dk e^{ikx} \langle s|-\rangle \psi_{k,-} \\
&\simeq e^{ik_{L,\mathrm{I}}x} \langle s|\chi_-(k_{L,\mathrm{I}})\rangle \frac{1}{\sqrt{2\pi}} \int_{-\infty}^{\infty} dk e^{i(k-k_{L,\mathrm{I}})x} \psi_{k,-} \\
&+ e^{ik_{R,\mathrm{I}}x} \langle s|\chi_-(k_{R,\mathrm{I}})\rangle \frac{1}{\sqrt{2\pi}} \int_{-\infty}^{\infty} dk e^{i(k-k_{R,\mathrm{I}})x} \psi_{k,-} \\
&+ e^{ik_{L,\mathrm{II}}x} \langle s|\chi_-(k_{L,\mathrm{II}})\rangle \frac{1}{\sqrt{2\pi}} \int_{-\infty}^{\infty} dk e^{i(k-k_{L,\mathrm{II}})x} \psi_{k,-} \\
&+ e^{ik_{R,\mathrm{II}}x} \langle s|\chi_-(k_{R,\mathrm{II}})\rangle \frac{1}{\sqrt{2\pi}} \int_{-\infty}^{\infty} dk e^{i(k-k_{R,\mathrm{II}})x} \psi_{k,-},
\end{aligned}
$$

where we change the notation by identifying $|-\rangle = |\chi_-\rangle$ in the last two steps. Moreover, if the system's occupation is much lower than the half-filling, it is physical to project out the unoccupied higher-energy bonding band and only focus on the low-energy excitations inside the lower antibonding band. Here we have taken the continuum limit and extended the integral from the vicinity of each Fermi point to the entire real line. The resulting band structure can

thus be approximated as follows,

$$H_K \approx \int_{-\infty}^{\infty} dk E_-(k,\pi)\psi^\dagger_{k,-}\psi_{k,-}. \tag{4.9}$$

One salient feature of the above band structure is the presence of four separated Fermi points whose values are mutually interdependent (see Fig. 4.2). Here we have assumed that the fixed total particle number is determined by choosing a proper chemical potential which intersects the antibonding band at these four Fermi points. The next key step for bosonization is the linearization of the band around the vicinities of these four Fermi points, namely

$$\begin{aligned} H_K \approx & \int_{-\infty}^{\infty} dk \left[\varepsilon_F - v_F\left(k - k_{L,\mathrm{I}}\right)\right]\psi^\dagger_{k,-}\psi_{k,-} + \int_{-\infty}^{\infty} dk \left[\varepsilon_F + v_F\left(k - k_{R,\mathrm{I}}\right)\right]\psi^\dagger_{k,-}\psi_{k,-} \\ & + \int_{-\infty}^{\infty} dk \left[\varepsilon_F - v_F\left(k - k_{L,\mathrm{II}}\right)\right]\psi^\dagger_{k,-}\psi_{k,-} + \int_{-\infty}^{\infty} dk \left[\varepsilon_F + v_F\left(k - k_{R,\mathrm{II}}\right)\right]\psi^\dagger_{k,-}\psi_{k,-}, \end{aligned} \tag{4.10}$$

where the Fermi energy is set by $\varepsilon_F = E_-(k_{R,\mathrm{II}}, \phi = \pi) = -\frac{1}{2\pi}\sqrt{t_\perp^2 + 4t_\parallel^2 \sin^2(k_{R,\mathrm{II}}a)}$, and accordingly the Fermi velocity is defined by

$$v_F = \frac{dE_-}{dk}\Big|_{k=k_{R,\mathrm{II}},\phi=\pi} = -\frac{a}{\pi}\frac{t_\parallel^2 \sin(2k_{R,\mathrm{II}}a)}{\sqrt{t_\perp^2 + 4t_\parallel^2 \sin^2(k_{R,\mathrm{II}}a)}}. \tag{4.11}$$

Here we have made the approximation that the linearized band structure is valid up to the largest energy scale in the problem (which is why we take it from $-\infty$ to ∞). It is clear that $v_F > 0$ because typically $\frac{\pi}{2} < k_{R,\mathrm{II}}a < \pi$. Moreover, it is also self-evident that when $\phi = \pi$ the four Fermi points are linked with each other by the following crucial relations:

$$k_{L,\mathrm{I}} = -k_{R,\mathrm{II}}, \quad k_{R,\mathrm{I}} = -k_{L,\mathrm{II}}, \quad k_{L,\mathrm{II}} + k_{R,\mathrm{II}} = \frac{\pi}{a}, \tag{4.12}$$

which immediately imply the essential condition for the umklapp processes:

$$k_{L,\mathrm{II}} + k_{R,\mathrm{II}} - k_{L,\mathrm{I}} - k_{R,\mathrm{I}} = \frac{2\pi}{a}. \tag{4.13}$$

Namely, due to the presence of the underlying lattice, the momentum in an interaction process needs only to be conserved modulo a reciprocal vector. Obviously, the validity of these relations is independent of the band linearization, but will not hold for ϕ other than π. Therefore, after linearizing the antibonding band at finite chemical potential, we obtain two (projected) cone

structures situated at $ka = \pm\frac{\pi}{2}$ respectively. By linearizing the band structure out to infinite energy, we have created a high-energy divergence, which can be dealt with by normal ordering,

$$\begin{aligned} H_K \approx & \int_{-\infty}^{\infty} dk \left[-v_F\left(k-k_{L,\mathrm{I}}\right)\right] \psi_{k,-}^{\dagger}\psi_{k,-} + \int_{-\infty}^{\infty} dk \left[v_F\left(k-k_{R,\mathrm{I}}\right)\right] \psi_{k,-}^{\dagger}\psi_{k,-} \\ & + \int_{-\infty}^{\infty} dk \left[-v_F\left(k-k_{L,\mathrm{II}}\right)\right] \psi_{k,-}^{\dagger}\psi_{k,-} + \int_{-\infty}^{\infty} dk \left[v_F\left(k-k_{R,\mathrm{II}}\right)\right] \psi_{k,-}^{\dagger}\psi_{k,-} \\ & + \text{Infinite constant}, \\ : H_K : \approx & \int_{-\infty}^{\infty} dk \left[-v_F\left(k-k_{L,\mathrm{I}}\right)\right] : \psi_{k,-}^{\dagger}\psi_{k,-} : + \int_{-\infty}^{\infty} dk \left[v_F\left(k-k_{R,\mathrm{I}}\right)\right] : \psi_{k,-}^{\dagger}\psi_{k,-} : \\ & + \int_{-\infty}^{\infty} dk \left[-v_F\left(k-k_{L,\mathrm{II}}\right)\right] : \psi_{k,-}^{\dagger}\psi_{k,-} : + \int_{-\infty}^{\infty} dk \left[v_F\left(k-k_{R,\mathrm{II}}\right)\right] : \psi_{k,-}^{\dagger}\psi_{k,-} : . \end{aligned}$$

A direct comparison of the result with Eqs. (4.18) and (4.20) immediately suggests the central expression for the projected operator $\psi_{x,s}$ in terms of the slowly-varying chiral fermion fields $\tilde{\psi}_{L/R,\mathrm{I/II}}$ in the linearized antibonding branches close to the Fermi energy:

$$\begin{aligned} \psi_{x,s} \simeq & e^{ik_{L,\mathrm{I}}x}\langle s|\chi_-(k_{L,\mathrm{I}})\rangle\tilde{\psi}_{L,\mathrm{I}}(x) + e^{ik_{R,\mathrm{I}}x}\langle s|\chi_-(k_{R,\mathrm{I}})\rangle\tilde{\psi}_{R,\mathrm{I}}(x) \\ & + e^{ik_{L,\mathrm{II}}x}\langle s|\chi_-(k_{L,\mathrm{II}})\rangle\tilde{\psi}_{L,\mathrm{II}}(x) + e^{ik_{R,\mathrm{II}}x}\langle s|\chi_-(k_{R,\mathrm{II}})\rangle\tilde{\psi}_{R,\mathrm{II}}(x). \end{aligned} \tag{4.14}$$

Since $u_{-k,\phi} = \frac{1}{u_{k,\phi}}$ and $u_{\frac{\pi}{a}-k,\phi} = u_{k,\phi}$, it is ready to show that

$$|\chi_-(\pi/a-k,\phi)\rangle = |\chi_-(k,\phi)\rangle = \begin{pmatrix} \frac{1}{\sqrt{1+u_{k,\phi}^2}} \\ \frac{u_{k,\phi}}{\sqrt{1+u_{k,\phi}^2}} \end{pmatrix} = \begin{pmatrix} \cos\frac{\xi_{k,\phi}}{2} \\ \sin\frac{\xi_{k,\phi}}{2} \end{pmatrix},$$

$$|\chi_-(-(\pi/a-k),\phi)\rangle = |\chi_-(-k,\phi)\rangle = \begin{pmatrix} \frac{u_{k,\phi}}{\sqrt{1+u_{k,\phi}^2}} \\ \frac{1}{\sqrt{1+u_{k,\phi}^2}} \end{pmatrix} = \begin{pmatrix} \sin\frac{\xi_{k,\phi}}{2} \\ \cos\frac{\xi_{k,\phi}}{2} \end{pmatrix}.$$

Then by specifying to the case of $\phi = \pi$ and recalling the relations in Eq. (4.12), we arrive at the two frequently-used identities:

$$\begin{aligned} \psi_{x,0} \simeq & e^{-ik_{R,\mathrm{II}}x}\sin\frac{\xi(k_{R,\mathrm{II}})}{2}\tilde{\psi}_{L,\mathrm{I}}(x) + e^{-i(\frac{\pi}{a}-k_{R,\mathrm{II}})x}\sin\frac{\xi(k_{R,\mathrm{II}})}{2}\tilde{\psi}_{R,\mathrm{I}}(x) \\ & + e^{i(\frac{\pi}{a}-k_{R,\mathrm{II}})x}\cos\frac{\xi(k_{R,\mathrm{II}})}{2}\tilde{\psi}_{L,\mathrm{II}}(x) + e^{ik_{R,\mathrm{II}}x}\cos\frac{\xi(k_{R,\mathrm{II}})}{2}\tilde{\psi}_{R,\mathrm{II}}(x), \end{aligned} \tag{4.15}$$

$$\begin{aligned} \psi_{x,1} \simeq & e^{-ik_{R,\mathrm{II}}x}\cos\frac{\xi(k_{R,\mathrm{II}})}{2}\tilde{\psi}_{L,\mathrm{I}}(x) + e^{-i(\frac{\pi}{a}-k_{R,\mathrm{II}})x}\cos\frac{\xi(k_{R,\mathrm{II}})}{2}\tilde{\psi}_{R,\mathrm{I}}(x) \\ & + e^{i(\frac{\pi}{a}-k_{R,\mathrm{II}})x}\sin\frac{\xi(k_{R,\mathrm{II}})}{2}\tilde{\psi}_{L,\mathrm{II}}(x) + e^{ik_{R,\mathrm{II}}x}\sin\frac{\xi(k_{R,\mathrm{II}})}{2}\tilde{\psi}_{R,\mathrm{II}}(x). \end{aligned} \tag{4.16}$$

As a simple check, we notice that when $t_\perp = 0$, $\cos\frac{\xi}{2} = 0$ and $\sin\frac{\xi}{2} = 1$, then the valley index I (II) reduces to the chain index 0 (1) as it should. However, when $t_\perp \neq 0$, fermions in each valley (I and II) will be the superposition of degrees of freedom from both two chains. This is simply inherited from the fact that the antibonding band itself is formed by connecting (or fusing) the bands of the two chains at the points $ka = 0, \pm\pi$ in momentum space.

4.3 Bosonization and renormalization group analysis

To proceed further, we introduce the slowly-varying Dirac fields for each of the linearized branches as follows,

$$\tilde{\psi}_{L,\mathrm{I}}(x) = \frac{1}{\sqrt{2\pi}}\int_{-\infty}^{\infty} dk e^{i(k-k_{L,\mathrm{I}})x}\psi_{k,-}(L,\mathrm{I}) = e^{-ik_{L,\mathrm{I}}x}\psi_{L,\mathrm{I},-}(x), \tag{4.17}$$

$$\tilde{\psi}_{R,\mathrm{I}}(x) = \frac{1}{\sqrt{2\pi}}\int_{-\infty}^{\infty} dk e^{i(k-k_{R,\mathrm{I}})x}\psi_{k,-}(R,\mathrm{I}) = e^{-ik_{R,\mathrm{I}}x}\psi_{R,\mathrm{I},-}(x), \tag{4.18}$$

$$\tilde{\psi}_{L,\mathrm{II}}(x) = \frac{1}{\sqrt{2\pi}}\int_{-\infty}^{\infty} dk e^{i(k-k_{L,\mathrm{II}})x}\psi_{k,-}(L,\mathrm{II}) = e^{-ik_{L,\mathrm{II}}x}\psi_{L,\mathrm{II},-}(x), \tag{4.19}$$

$$\tilde{\psi}_{R,\mathrm{II}}(x) = \frac{1}{\sqrt{2\pi}}\int_{-\infty}^{\infty} dk e^{i(k-k_{R,\mathrm{II}})x}\psi_{k,-}(R,\mathrm{II}) = e^{-ik_{R,\mathrm{II}}x}\psi_{R,\mathrm{II},-}(x). \tag{4.20}$$

The resulting effective kinetic Hamiltonian that describes the four linearized branches is as follows,

$$\begin{aligned} :H_K: \approx & \int dx :\tilde{\psi}^\dagger_{L,\mathrm{I}}(x)\left(-v_F\cdot -i\partial_x\right)\tilde{\psi}_{L,\mathrm{I}}(x): + \int dx :\tilde{\psi}^\dagger_{R,\mathrm{I}}(x)\left(v_F\cdot -i\partial_x\right)\tilde{\psi}_{R,\mathrm{I}}(x): \\ & + \int dx :\tilde{\psi}^\dagger_{L,\mathrm{II}}(x)\left(-v_F\cdot -i\partial_x\right)\tilde{\psi}_{L,\mathrm{II}}(x): + \int dx :\tilde{\psi}^\dagger_{R,\mathrm{II}}(x)\left(v_F\cdot -i\partial_x\right)\tilde{\psi}_{R,\mathrm{II}}(x): . \end{aligned} \tag{4.21}$$

Having linearlized the Hamiltonian about the four Fermi points, we may now analyze the behavior of the interacting system using bosonization. (For an introduction to bosonization, see [98].) Bosonizing these in the usual way, we have $\psi_{\kappa,\nu} \sim e^{i\varphi_{\kappa,\nu}}$, with $\kappa = R\ (L)$ and $\nu = \mathrm{I}\ (\mathrm{II})$. We define the nonchiral bosonic fields: $\theta_c = \frac{1}{\sqrt{2}}(\theta_\mathrm{I} + \theta_\mathrm{II})$, $\theta_s = \frac{1}{\sqrt{2}}(\theta_\mathrm{I} - \theta_\mathrm{II})$, $\phi_c = \frac{1}{\sqrt{2}}(\phi_\mathrm{I} + \phi_\mathrm{II})$, $\phi_s = \frac{1}{\sqrt{2}}(\phi_\mathrm{I} - \phi_\mathrm{II})$, where $\theta_\nu = \frac{1}{\sqrt{2}}(\varphi_{R,\nu} - \varphi_{L,\nu})$, $\phi_\nu = \frac{1}{\sqrt{2}}(\varphi_{R,\nu} + \varphi_{L,\nu})$, such that $\varphi_{\kappa,\nu} = \frac{1}{2}[(\phi_c + \kappa\theta_c) + \nu\,(\phi_s + \kappa\theta_s)]$. To recap, the projection of H onto the resulting chiral branches can then be achieved via the mapping:

$$\psi_{x,s} \simeq \sum_{\kappa=L,R}\sum_{\nu=\mathrm{I},\mathrm{II}} e^{ik_{\kappa,\nu}x}\langle s|\chi_-(k_{\kappa,\nu})\rangle\tilde{\psi}_{\kappa,\nu}(x), \tag{4.22}$$

where by choosing $\kappa = R\ (L) = +1\ (-1)$ and $\nu = \mathrm{I}\ (\mathrm{II}) = +1\ (-1)$, the bosonization identities for the slowly-varying Dirac fields read [98]

$$\tilde{\psi}_{\kappa,\nu} \sim (1/\sqrt{2\pi a}) e^{\frac{i}{2}[(\phi_c+\kappa\theta_c)+\nu(\phi_s+\kappa\theta_s)]}. \tag{4.23}$$

In order for ψ to have fermionic anticommutation relations, the only nontrivial commutators of the bosonic fields (after including Klein factors) must be:

$$\left[\theta_c(x), \phi_c(x')\right] = -2i\pi\Theta(x'-x), \tag{4.24}$$

$$\left[\theta_s(x), \phi_s(x')\right] = +2i\pi\Theta(x-x'), \tag{4.25}$$

$$\left[\theta_s(x), \phi_c(x')\right] = -2i\pi. \tag{4.26}$$

Here $\Theta(x)$ is the Heaviside step function. Correspondingly, the related density and current operators take simple forms:

$$\rho_c = (1/\pi)\partial_x\theta_c, \ \ \rho_s = (1/\pi)\partial_x\theta_s, \ \ J_c = (1/\pi)\partial_x\phi_c, \ \ J_s = (1/\pi)\partial_x\phi_s, \tag{4.27}$$

where we define

$$\theta_c(x) = \frac{1}{2}\left\{\phi_{R,\mathrm{I}}(x) - \phi_{L,\mathrm{I}}(x) + \phi_{R,\mathrm{II}}(x) - \phi_{L,\mathrm{II}}(x)\right\}, \tag{4.28}$$

$$\theta_s(x) = \frac{1}{2}\left\{\phi_{R,\mathrm{I}}(x) - \phi_{L,\mathrm{I}}(x) - \phi_{R,\mathrm{II}}(x) + \phi_{L,\mathrm{II}}(x)\right\}, \tag{4.29}$$

$$\phi_c(x) = \frac{1}{2}\left\{\phi_{R,\mathrm{I}}(x) + \phi_{L,\mathrm{I}}(x) + \phi_{R,\mathrm{II}}(x) + \phi_{L,\mathrm{II}}(x)\right\}, \tag{4.30}$$

$$\phi_s(x) = \frac{1}{2}\left\{\phi_{R,\mathrm{I}}(x) + \phi_{L,\mathrm{I}}(x) - \phi_{R,\mathrm{II}}(x) - \phi_{L,\mathrm{II}}(x)\right\}. \tag{4.31}$$

Bosonizing the pair-hopping term H_W constitutes one major task of the derivation that produces multiple terms in the bosonized theory. Many of them contain oscillatory pieces that after spatial integration get vanished. However, it proves crucial to bear in mind the umklapp-scattering condition (4.13), which simply dictates that the seemingly oscillating prefactors $e^{\pm i(k_{R,\mathrm{II}}+k_{L,\mathrm{II}}-k_{R,\mathrm{I}}-k_{L,\mathrm{I}})x}$ equal $+1$ and their contributions must be kept in the continuum limit. Since at least four chiral-fermion operators are involved, such unfrustrated intervalley scatterings as depicted in Fig. 4.2 are intrinsically many-body processes. Long but straightforward algebras yield the following bosonized form of H which has been nicely decoupled into

the commuting charge and spin sectors (spin-charge separation):

$$H \simeq H_c + H_s, \tag{4.32}$$

$$H_c = \int \frac{dx}{2\pi} \left\{ u_c K_c \left(\partial_x \phi_c(x)\right)^2 + \frac{u_c}{K_c} \left(\partial_x \theta_c(x)\right)^2 \right\}, \tag{4.33}$$

$$\begin{aligned} H_s = & \int \frac{dx}{2\pi} \left\{ u_s K_s \left(\partial_x \phi_s(x)\right)^2 + \frac{u_s}{K_s} \left(\partial_x \theta_s(x)\right)^2 \right\} \\ & + \frac{2g_{um}}{(2\pi a)^2} \int dx \cos\left(2\phi_s(x)\right) - \frac{2g_{bs}}{(2\pi a)^2} \int dx \cos\left(2\theta_s(x)\right) \\ & - \frac{2g_{mx}}{(2\pi a)^2} \int dx \cos\left(2\theta_s(x)\right) \cdot \cos\left(2\phi_s(x)\right), \end{aligned} \tag{4.34}$$

where the varied gapping amplitudes resulting from the umklapp processes and backscatterings are given by

$$g_{um} = -\frac{aW}{\pi^2} \cos^2(k_{R,\mathrm{II}} a) \left(\sin^4 \frac{\xi}{2} + \cos^4 \frac{\xi}{2} \right), \tag{4.35}$$

$$g_{bs} = -\frac{aW}{2\pi^2} \sin^2(k_{R,\mathrm{II}} a) \sin^2 \xi, \tag{4.36}$$

$$g_{mx} = -\frac{aW}{2\pi^2} \left(\sin^4 \frac{\xi}{2} + \cos^4 \frac{\xi}{2} \right). \tag{4.37}$$

Here $\langle \chi_- | \equiv (\cos\frac{\xi}{2} \ \sin\frac{\xi}{2})$. Note that the g_{um}-term favors fermionic pairing while the competing g_{bs}-term favors the density-wave-type order. Particularly, for the spin channel

$$u_s = \sqrt{(u+g)^2 - 4g^2 \cos^2(2k_{R,\mathrm{II}} a)}, \tag{4.38}$$

$$K_s = \sqrt{\frac{u + g + 2g\cos(2k_{R,\mathrm{II}} a)}{u + g - 2g\cos(2k_{R,\mathrm{II}} a)}}, \tag{4.39}$$

where $u = \frac{1}{2} v_F \equiv \frac{1}{2} \frac{dE_{\text{A-B}}}{dk}\big|_{k=k_{R,\mathrm{II}}} > 0$ and $g = \frac{aW}{2(2\pi)^3} \sin^2 \xi$. While for the charge sector, we will have

$$u_c = \sqrt{(u-g) \cdot (u-5g)}, \tag{4.40}$$

$$K_c = \sqrt{\frac{u-g}{u-5g}}. \tag{4.41}$$

First, let's calculate the two-point correlator for the ϕ_s-fields,

$$\begin{aligned} \mathsf{C}_{um}(\mathbf{r_1} - \mathbf{r_2}) \coloneqq & \left\langle \mathsf{T}_\tau \left(\frac{2g_{um}}{(2\pi a)^2} \int d\mathbf{r_1} \cos\left(2\phi_s(\mathbf{r_1})\right) \right) \cdot \left(\frac{2g_{um}}{(2\pi a)^2} \int d\mathbf{r_2} \cos\left(2\phi_s(\mathbf{r_2})\right) \right) \right\rangle_0 \\ = & \frac{2g_{um}^2}{(2\pi a)^4} \int d\mathbf{r_1} d\mathbf{r_2} \left(\frac{|\mathbf{r_1} - \mathbf{r_2}|}{\alpha} \right)^{-4/K_s}, \end{aligned} \tag{4.42}$$

where we define

$$\mathbf{r} \coloneqq \left(x, \frac{v_F \tau}{\hbar} + \alpha \mathrm{sgn}(\tau)\right), \tag{4.43}$$

with τ the imaginary time, and $\alpha \sim a > 0$ the length-scale cutoff. Next, we perform the RG step by rescaling the cutoff $\alpha \sim a \to \alpha'$ in the way of preserving the above correlator (because the correlator should be independent of the cutoff),

$$\begin{aligned} \mathsf{C}_{um}(\mathbf{r_1} - \mathbf{r_2}) &= \frac{2\left(g_{um}(\alpha)\right)^2}{(2\pi\alpha)^4} \int d\mathbf{r_1} d\mathbf{r_2} \left(\frac{|\mathbf{r_1} - \mathbf{r_2}|}{\alpha}\right)^{-4/K_s} \\ &= \frac{2}{(2\pi)^4} \left(g_{um}(\alpha')\right)^2 \left(\frac{1}{\alpha'}\right)^{4-4K_s^{-1}} \int d\mathbf{r_1} d\mathbf{r_2} \left(|\mathbf{r_1} - \mathbf{r_2}|\right)^{-4/K_s}. \end{aligned} \tag{4.44}$$

Therefore, by comparison, we can derive that

$$\left(g_{um}(\alpha')\right)^2 = \left(g_{um}(\alpha)\right)^2 \cdot \left(\frac{\alpha'}{\alpha}\right)^{4-4K_s^{-1}}. \tag{4.45}$$

Define the corresponding dimensionless coupling constant $y_{um} \equiv g_{um}/(2u\pi) = g_{um}/(v_F\pi)$, and set $\alpha' = \alpha + d\alpha$ and linearizing in $d\alpha$, we obtain the RG flow for y_{um} after linearizing in $d\alpha$ as follows,

$$\left(y_{um}(\alpha')\right)^2 = \left(y_{um}(\alpha)\right)^2 \left(\frac{\alpha'}{\alpha}\right)^{4-4K_s^{-1}} = \left(y_{um}(\alpha)\right)^2 + \left(4 - 4K_s^{-1}\right)\left(y_{um}(\alpha)\right)^2 \frac{d\alpha}{\alpha}.$$

By setting

$$\alpha = \alpha_0 e^l, \tag{4.46}$$

we obtain the RG flow:

$$\frac{dy_{um}(l)}{dl} = \left(2 - 2K_s^{-1}(l)\right) y_{um}(l). \tag{4.47}$$

We use a similar procedure to derive similar equations for the other interaction terms. The flow equation for K_s is a bit more involved, but is standard and can be found in [98].

As the charge sector is gapless and governed by a Luttinger liquid theory, we will concentrate on the spin sector which contains more interesting gapping terms that generate the physics we are most concerned with, especially the probable topological phase accommodating Majorana fermions. Here we would like to analyze the leading instability of the gapping channels in H_s, namely to know which of the two interaction terms—the one that leads to Majorana states

or the one that leads to fermion-density wave—will dominate at low energy. To this end, we derive perturbatively the associated one-loop renormalization group (RG) flow equations:

$$\frac{dK_s(l)}{dl} = \frac{y_{um}^2(l)}{2} - \frac{y_{bs}^2(l)K_s^2(l)}{2}, \tag{4.48}$$

$$\frac{dy_{um}(l)}{dl} = (2 - 2K_s^{-1}(l))y_{um}(l), \tag{4.49}$$

$$\frac{dy_{bs}(l)}{dl} = (2 - 2K_s(l))y_{bs}(l), \tag{4.50}$$

$$\frac{dy_{mx}(l)}{dl} = (2 - 2K_s(l) - 2K_s^{-1}(l))y_{mx}(l), \tag{4.51}$$

where the dimensionless couplings

$$y_{um} = \frac{g_{um}}{2u\pi}, \quad y_{bs} = \frac{g_{bs}}{2u\pi}, \quad \text{and} \quad y_{mx} = \frac{g_{mx}}{2u\pi}.$$

The g_{mx}-channel involving dual fields is RG irrelevant as a consequence of Pauli exclusion principle when taking the continuum limit or simply by power counting. Accordingly, the gap-opening competition is between g_{um} and g_{bs}. If we assume for the initial conditions that W is negative and sufficiently strong, then in the low-occupation region when the chemical potential is near the middle of the lower band, $K_s > 1$, thus g_{um} becomes the leading instability, and the resultant pinning of ϕ_s to the minima of the cosine potential necessarily renders g_{bs} irrelevant.

In this regime, it suffices to study the following reduced sine-Gordon Hamiltonian to reveal the underpinnings of the Majorana bound states,

$$H_{\text{s-G}} = \int_{-\frac{L}{2}}^{\frac{L}{2}} \frac{dx}{2\pi} \left\{ u_s K_s \left(\partial_x \phi_s(x)\right)^2 + \frac{u_s}{K_s} \left(\partial_x \theta_s(x)\right)^2 + \frac{g_{um}}{\pi a^2} \cos\left(2\phi_s(x)\right) \right\}. \tag{4.52}$$

This "plain vanilla" version of the sine-Gordon model for the spin sector exhibits some noteworthy features. In particular, there is a sign change in the prefactor of the $\cos(2\phi_s)$ term arising from the π-flux insertion. As explained below, this sign flip proves central to the link between the emergent valley fermion parity and the exact staggered leg-interchange symmetry which stabilizes the Majorana zero modes.

4.4 Symmetry analysis and Majorana operators

We are now ready to argue for the existence of Majorana zero modes stabilized by the leg-interchange symmetry. To do this, we will formulate the algebras of valley fermion parity and

leg-interchange symmetry operations, which helps clarify explicitly their relations to Majorana end modes.

4.4.1 Emergent valley fermion-parity symmetry

The first thing we want to show from the bosonized model is that there is an emergent fermion-parity conservation, which you call valley fermion parity, which reduces to the leg parity in Ref. [80] for $t_\perp = 0$.

We proceed by first formulating the algebras of the valley fermion parity. To avoid the complication of a many-body Kramers degeneracy due to the appearance of an antiunitary symmetry, we restrict ourselves to the system with even total number of particles. Without loss of generality, we further require that

$$\sum_{v=\mathrm{I,II}} N_v = N_\mathrm{I} + N_\mathrm{II} = 2N', \tag{4.53}$$

where $N_v \coloneqq \int_{-\frac{L}{2}}^{\frac{L}{2}} dx\, [\rho_{L,v}(x) + \rho_{R,v}(x)]$ and we assume N' is a *fixed even* integer for convenience. It is easy to show that

$$N_\mathrm{I} - N_\mathrm{II} = N_\mathrm{I} - (2N' - N_\mathrm{I}) = 2N_\mathrm{I} - 2N' = \text{even integer}. \tag{4.54}$$

Therefore, a proper definition of the valley fermion parity for a particle-number conserving system can be as follows,

$$\mathsf{P}_\mathsf{v} \coloneqq (-1)^{\frac{N_\mathrm{I}-N_\mathrm{II}}{2}}, \tag{4.55}$$

If N' is odd, then there will be an inessential sign change in the definition of P_v. Note that if $N_\mathrm{I} + N_\mathrm{II} =$ odd, then the above definition of P_v will not be applicable. (In that case, $\mathsf{P}_\mathsf{v} \coloneqq (-1)^{\frac{1+N_\mathrm{I}-N_\mathrm{II}}{2}}$.) The essence here is that for a valley-parity conserving topological system, the two degenerate ground states can only be distinguished by the eigenvalues or quantum numbers of P_v which can only take the $\mathbb{Z}_2$ values ± 1. (Strictly speaking P_v is an approximate symmetry, so its eigenvalues are not yet defined.) Crucially, this emergent $\mathbb{Z}_2$ symmetry is nonlocal. It is a global property of the quantum system in the low-energy continuum description. Also it is easy to prove that which satisfies

$$\mathsf{P}_\mathsf{v}^\dagger = \mathsf{P}_\mathsf{v} = \mathsf{P}_\mathsf{v}^{-1} \quad \text{and} \quad \mathsf{P}_\mathsf{v}^2 = +1. \tag{4.56}$$

Recalling bosonization, we have

$$N_{\mathrm{I}} - N_{\mathrm{II}} = \int_{-\frac{L}{2}}^{\frac{L}{2}} dx \rho_s(x) = \int_{-\frac{L}{2}}^{\frac{L}{2}} dx \frac{1}{\pi} \partial_x \theta_s(x) = \frac{1}{\pi} \left(\theta_s \left(\frac{L}{2} \right) - \theta_s \left(-\frac{L}{2} \right) \right). \tag{4.57}$$

Accordingly, the bosonized form of the valley fermion parity operator assumes

$$\mathsf{P}_{\mathsf{v}} = \exp \left\{ i \frac{\theta_s \left(\frac{L}{2} \right) - \theta_s \left(-\frac{L}{2} \right)}{2} \right\}. \tag{4.58}$$

Some cautions are needed here when changing (-1) to $e^{i\pi}$, but in our case this is allowed because $\frac{N_I - N_{II}}{2}$ is an integer-valued operator. This is fixed by boundary conditions of θ_s. More importantly, being distinct from the chain fermion parity, the valley fermion parity operator lacks a simple expression in terms of lattice fermionic operators. This lattice representation is effectively provided by the leg-interchange symmetry as will be detailed below.

The next essential step is to understand that the action of generalized parity operator P_{v} on the conjugate bosonic field $\phi_s(x)$ in the bulk region $-\frac{L}{2} < x < \frac{L}{2}$ is represented through the following identity,

$$\mathsf{P}_{\mathsf{v}} \phi_s(x) \mathsf{P}_{\mathsf{v}}^{\dagger} = \phi_s(x) - \pi. \tag{4.59}$$

Here we use the following commutation relations and the remaining commutators are zero,

$$\left[\theta_s(x), \theta_s(x') \right] = 0 \quad \text{and} \quad \left[\theta_s(x), \phi_s(x') \right] = 2i\pi\Theta(x - x').$$

In particular, for the bulk variable $-\frac{L}{2} < x < \frac{L}{2}$, we have

$$\begin{aligned} [\theta_s(-L/2), \phi_s(x)] &= 2i\pi\Theta(-L/2 - x) = 0, \\ [\theta_s(L/2), \phi_s(x)] &= 2i\pi\Theta(L/2 - x) = 2i\pi. \end{aligned}$$

Finally, $[\mathsf{P}_{\mathsf{v}}, H_{\text{s-G}}] = 0$, which follows directly from the observation that umklapp processes conserve the fermion parity of the total particle number in one of the valleys.

4.4.2 Leg-interchange symmetry

We show that there is a microscopic symmetry that has the action (4.59) on the bosonic fields. This is only a symmetry at $\phi = \pi$, and we will later show numerically that breaking it either

by taking ϕ away from π, or by some explicit symmetry-breaking term in H at $\phi = \pi$, destroys the Majorana zero modes. We introduce the staggered leg-exchange symmetry $\mathsf{L_s}$ as follows,

$$\begin{cases} \text{For } j \text{ is odd}: & c_{j,0}^{(\dagger)} \longrightarrow +c_{j,1}^{(\dagger)} \quad \text{and} \quad c_{j,1}^{(\dagger)} \longrightarrow +c_{j,0}^{(\dagger)}, \\ \text{For } j \text{ is even}: & c_{j,0}^{(\dagger)} \longrightarrow -c_{j,1}^{(\dagger)} \quad \text{and} \quad c_{j,1}^{(\dagger)} \longrightarrow -c_{j,0}^{(\dagger)}. \end{cases} \tag{4.60}$$

Since $\mathsf{L_s}$ only commutes with the Hamiltonian at $\phi = \pi$, we tend to argue that the robust Majorana zero modes we found at $\phi = \pi$ and finite $t_\perp$ are protected by the staggered leg-exchange symmetry $\mathsf{L_s}$. This claim has been supported by the numerical results.

Next, we would like to explicitly define the operator for the leg-exchange symmetry and study its properties. In terms of c-operators,

$$\mathsf{L_s} = \prod_{n=0}^{L-1} \mathsf{L_n}, \quad \text{where} \quad \mathsf{L_n} = c_{n,0}c_{n,0}^\dagger + (-1)^n c_{n,1}c_{n,0}^\dagger - (-1)^n c_{n,1}^\dagger c_{n,0} - c_{n,1}^\dagger c_{n,1}. \tag{4.61}$$

Let us study its action in the long-wavelength theory. First, it is apparent that for any n, m in 0 to $L-1$, $[\mathsf{L_n}, \mathsf{L_m}] = 0$. Second, we can easily show that for any integer n,

$$(\mathsf{L_n})^2 = 1 \implies (\mathsf{L_s})^2 = 1 \implies \begin{cases} \mathsf{L_n} = \mathsf{L_n}^{-1} = \mathsf{L_n}^\dagger \\ \mathsf{L_s} = \mathsf{L_s}^{-1} = \mathsf{L_s}^\dagger \end{cases} \quad \text{and} \quad [\mathsf{L_s}, H(\phi = \pi)] = 0. \tag{4.62}$$

Namely, $\mathsf{L_s}$ is an exact $\mathbb{Z}_2$ unitary symmetry of the lattice model when $\phi = \pi$.

From Eq. (4.60), we know that the staggered chain interchange acts on the c-operators, and their continuum versions ψ-operators, via

$$\begin{cases} \mathsf{L_s} c_{j,0}^{(\dagger)} \mathsf{L_s}^{-1} = -e^{i\frac{\pi}{a} r_j} c_{j,1}^{(\dagger)} \\ \mathsf{L_s} c_{j,1}^{(\dagger)} \mathsf{L_s}^{-1} = -e^{i\frac{\pi}{a} r_j} c_{j,0}^{(\dagger)} \end{cases} \xrightarrow{\text{continuum limit}} \begin{cases} \mathsf{L_s} \psi_{x,0}^{(\dagger)} \mathsf{L_s}^{-1} = -e^{i\frac{\pi}{a} x} \psi_{x,1}^{(\dagger)} \\ \mathsf{L_s} \psi_{x,1}^{(\dagger)} \mathsf{L_s}^{-1} = -e^{i\frac{\pi}{a} x} \psi_{x,0}^{(\dagger)} \end{cases} \tag{4.63}$$

where $r_j = j \cdot a \approx x$. Referring to the fermion-field expressions from Eqs. (4.15) and (4.16), we can specifically examine the following identity,

$$\begin{aligned} \mathsf{L_s} \psi_{x,0} \mathsf{L_s}^{-1} = {} & e^{-ik_F x} \sin\frac{\xi(k_F)}{2} \mathsf{L_s} \tilde{\psi}_{L,\mathrm{I}}(x) \mathsf{L_s}^{-1} + e^{i(\frac{\pi}{a} + k_F)x} \sin\frac{\xi(k_F)}{2} \mathsf{L_s} \tilde{\psi}_{R,\mathrm{I}}(x) \mathsf{L_s}^{-1} \\ & + e^{i(\frac{\pi}{a} - k_F)x} \cos\frac{\xi(k_F)}{2} \mathsf{L_s} \tilde{\psi}_{L,\mathrm{II}}(x) \mathsf{L_s}^{-1} + e^{ik_F x} \cos\frac{\xi(k_F)}{2} \mathsf{L_s} \tilde{\psi}_{R,\mathrm{II}}(x) \mathsf{L_s}^{-1}, \end{aligned} \tag{4.64}$$

which can be achieved if the slowly-varying fermionic fields satisfy the following transformation relations under the staggered leg exchange:

$$\mathsf{L_s} \tilde{\psi}_{L,\mathrm{I}}^{(\dagger)}(x) \mathsf{L_s}^{-1} = -\tilde{\psi}_{L,\mathrm{II}}^{(\dagger)}(x) \quad \text{and} \quad \mathsf{L_s} \tilde{\psi}_{R,\mathrm{I}}^{(\dagger)}(x) \mathsf{L_s}^{-1} = -\tilde{\psi}_{R,\mathrm{II}}^{(\dagger)}(x), \tag{4.65}$$

$$\mathsf{L_s} \tilde{\psi}_{L,\mathrm{II}}^{(\dagger)}(x) \mathsf{L_s}^{-1} = -\tilde{\psi}_{L,\mathrm{I}}^{(\dagger)}(x) \quad \text{and} \quad \mathsf{L_s} \tilde{\psi}_{R,\mathrm{II}}^{(\dagger)}(x) \mathsf{L_s}^{-1} = -\tilde{\psi}_{R,\mathrm{I}}^{(\dagger)}(x), \tag{4.66}$$

from which we can readily derive the action of the staggered leg-interchange operation on the chiral bosonic fields:

$$\mathsf{L_s}\phi_{L,\mathrm{I}}(x)\mathsf{L_s}^{-1} = \phi_{L,\mathrm{II}}(x) + (2l+1)\pi \quad \text{and} \quad \mathsf{L_s}\phi_{R,\mathrm{I}}(x)\mathsf{L_s}^{-1} = \phi_{R,\mathrm{II}}(x) + (2l'+1)\pi,$$
$$\mathsf{L_s}\phi_{L,\mathrm{II}}(x)\mathsf{L_s}^{-1} = \phi_{L,\mathrm{I}}(x) - (2l+1)\pi \quad \text{and} \quad \mathsf{L_s}\phi_{R,\mathrm{II}}(x)\mathsf{L_s}^{-1} = \phi_{R,\mathrm{I}}(x) - (2l'+1)\pi,$$

where $l,\ l'$ are two arbitrary integers that have been assumed to be both x-independent and R/L-independent. This assumption appears reasonable in light of the fact that $\mathsf{L_s}$ is a global operation. The transformations for $\phi_{L/R,I/II}$ give the following transformations:

$$\mathsf{L_s}\theta_c(x)\mathsf{L_s}^{-1} = \theta_c(x) \quad \text{and} \quad \mathsf{L_s}\theta_s(x)\mathsf{L_s}^{-1} = -\theta_s(x) + 2\pi(l'-l), \tag{4.67}$$
$$\mathsf{L_s}\phi_c(x)\mathsf{L_s}^{-1} = \phi_c(x) \quad \text{and} \quad \mathsf{L_s}\phi_s(x)\mathsf{L_s}^{-1} = -\phi_s(x) + 2\pi(l'+l+1). \tag{4.68}$$

Accordingly, the density and current operators transform as per the following,

$$\mathsf{L_s}\rho_c(x)\mathsf{L_s}^{-1} = \rho_c(x) \quad \text{and} \quad \mathsf{L_s}\rho_s(x)\mathsf{L_s}^{-1} = -\rho_s(x), \tag{4.69}$$
$$\mathsf{L_s}J_c(x)\mathsf{L_s}^{-1} = J_c(x) \quad \text{and} \quad \mathsf{L_s}J_s(x)\mathsf{L_s}^{-1} = -J_s(x). \tag{4.70}$$

Even though we did not provide the bosonized expression of $\mathsf{L_s}$ in the continuum limit, its nontrivial action on varied bosonic quantities can still be deduced from the consistency of the bosonization definitions and the physical arguments. Note that $\mathsf{L_s}$ is a product of local operators over all sites, therefore it will not depend on the spatial degree of freedom x, and has no effects on the functions of x.

To show $[\mathsf{L_s}, H_{\text{s-G}}] = 0$, we need some simple algebras,

$$\begin{aligned}
&\mathsf{L_s}\left\{\frac{1}{2\pi}\int_{-\frac{L}{2}}^{\frac{L}{2}} dx : \left\{u_s K_s \left(\partial_x\phi_s(x)\right)^2 + \frac{u_s}{K_s}\left(\partial_x\theta_s(x)\right)^2\right\} : \right.\\
&\qquad \left. + \frac{2g_{um}}{(2\pi a)^2}\int_{-\frac{L}{2}}^{\frac{L}{2}} dx \cos\left(2\phi_s(x)\right)\right\}\mathsf{L_s}^{-1}\\
&= \frac{1}{2\pi}\int_{-\frac{L}{2}}^{\frac{L}{2}} dx : \left\{u_s K_s \left(\partial_x(-\phi_s(x))\right)^2 + \frac{u_s}{K_s}\left(\partial_x(-\theta_s(x))\right)^2\right\} :\\
&\qquad + \frac{2g_{um}}{(2\pi a)^2}\int_{-\frac{L}{2}}^{\frac{L}{2}} dx \cos\left(-2\phi_s(x) + 4\pi(l'+l+1)\right)\\
&= H_{\text{s-G}}.
\end{aligned}$$

4.4.3 Relations to Majorana end modes

Based on the understanding of both valley fermion parity and the staggered leg-exchange symmetry, we are presently well equipped to uncover the intricate linkage between these $\mathbb{Z}_2$ symmetries and the emergent Majorana end states. Along the way, we will also gain a good understanding on the structure of the degenerate ground-state manifold generated by emptying or occupying the pair of Majorana bound states.

First of all, let's start from the reduced sine-Gordon Hamiltonian that is most relevant in analyzing the many-body Majorana physics,

$$\begin{aligned} H_{\text{s-G}}(\phi=\pi) = \frac{1}{2\pi}\int dx : \left\{ u_s K_s \left(\partial_x \phi_s(x)\right)^2 + \frac{u_s}{K_s}\left(\partial_x \theta_s(x)\right)^2 \right\} : \\ - \left(e^{i\pi}\right)\cdot \frac{2g_{um}}{(2\pi a)^2}\int dx \cos\left(2\phi_s(x)\right), \end{aligned} \tag{4.71}$$

where in the second line, we intentionally factor out the factor of $(-1) = e^{i\pi}$ in the cosine term to manifestly show the nontrivial effect from the insertion of the magnetic π-fluxes. From Section 4.3 we know that when $g_{um} \gg 1$, to a good approximation, the classical ground states of $H_{\text{s-G}}$ would be determined by minimizing the potential term in the gapped region, namely

$$\cos\left(2\phi_s(x)\right) \to -1 \quad \Longrightarrow \quad \phi_s(x) = \phi_s = \pm\frac{\pi}{2} \bmod 2\pi$$

for $-\frac{L}{2} < x < \frac{L}{2}$. Here we note that the bosonic field $\phi_s(x)$ has been uniformly (namely becoming x-independent) pinned to one of the minima of the cosine potential. Moreover, ϕ_s is a compact variable such that there exist only two different classical ground-state expectation values for ϕ_s which correspond to the two physically distinct vacua of the system. The dominant role of the cosine term is to gap the system. The sign change of the prefactor in front of the cosine term means that these two classical vacua are related in two different ways: $\phi_2 = -\phi_1 = \phi_1 + \pi$.

Specifically, the classical ground states of the potential-dominated system can be denoted by

$$\left|\pm\frac{\pi}{2}\right\rangle \quad \text{such that} \quad \phi_s(x)\left|\pm\frac{\pi}{2}\right\rangle = \left(\pm\frac{\pi}{2}+2n\pi\right)\left|\pm\frac{\pi}{2}\right\rangle. \tag{4.72}$$

Here the eigenvalues of ϕ_s could only be determined up to modulo 2π and thus n can be any integer, positive, negative, or zero. Quantum mechanically, due to the presence of the kinetic term, there will be the nonperturbative instanton tunneling processes that restore the translational invariance of ϕ_s. Therefore the genuine ground states of the system should be the bonding and

antibonding combinations of these two classical states, namely

$$|+\rangle = \frac{1}{\sqrt{2}}\left(\left|\frac{\pi}{2}\right\rangle + \left|-\frac{\pi}{2}\right\rangle\right), \tag{4.73}$$

$$|-\rangle = \frac{1}{\sqrt{2}}\left(\left|\frac{\pi}{2}\right\rangle - \left|-\frac{\pi}{2}\right\rangle\right), \tag{4.74}$$

up to some unimportant phases. (Here $|\pm\rangle$ should not be confused with the previous band states.) Since we argue that states $|\pm\rangle$ are the two lowest-lying eigenstates of $H_{\text{s-G}}$ with eigenenergies $E_\pm$, namely

$$H_{\text{s-G}}\,|\pm\rangle = E_\pm\,|\pm\rangle\,.$$

The energy splitting between E_+ and E_- will be exponentially small when elongating the system's length L as can be deduced from the instanton approach. Therefore, the nearly degenerate states $|\pm\rangle$ comprise the protected ground-state manifold that is of our utmost interest.

As could be explicitly demonstrated, the valley fermion parity operator and the staggered leg-exchange operator are simultaneously commuting with the system's Hamiltonian. Furthermore, we can show that $\mathsf{P_v}$ and $\mathsf{L_s}$ also commute with each other. To this end, let's first work out the following relation,

$$\begin{aligned}
\mathsf{L_s}\left(N_{\text{I}} - N_{\text{II}}\right)\mathsf{L_s}^{-1} &= \int_{-\frac{L}{2}}^{\frac{L}{2}} dx\, \mathsf{L_s}\left[\left(\rho_{L,\text{I}}(x) + \rho_{R,\text{I}}(x)\right) - \left(\rho_{L,\text{II}}(x) + \rho_{R,\text{II}}(x)\right)\right]\mathsf{L_s}^{-1} \\
&= \int_{-\frac{L}{2}}^{\frac{L}{2}} dx\left[\left(\rho_{L,\text{II}}(x) + \rho_{R,\text{II}}(x)\right) - \left(\rho_{L,\text{I}}(x) + \rho_{R,\text{I}}(x)\right)\right] \\
&= -\left(N_{\text{I}} - N_{\text{II}}\right).
\end{aligned} \tag{4.75}$$

Accordingly, we derive that

$$\mathsf{L_s}\mathsf{P_v}\mathsf{L_s}^{-1} = \mathsf{L_s}\,(-1)^{\frac{N_{\text{I}}-N_{\text{II}}}{2}}\,\mathsf{L_s}^{-1} = (-1)^{-\frac{N_{\text{I}}-N_{\text{II}}}{2}} = \mathsf{P_v}. \tag{4.76}$$

Here it is important to note that we always assume that the total particle number of the ladder is even for the discussion of topological phases.

In summary, we have the mutual commutation relations as follows:

$$[\mathsf{P_v}, H_{\text{s-G}}] = [\mathsf{L_s}, H_{\text{s-G}}] = [\mathsf{P_v}, \mathsf{L_s}] = 0, \tag{4.77}$$

which indicates that the ground states $|\pm\rangle$ will be the simultaneous eigenstates of all these three Hermitian operators: $H_{\text{s-G}},\ \mathsf{P_v},\ \mathsf{L_s}$, whose eigenvalues define a minimal set of quantum

numbers that can distinctively label the eigenstates of the system. Especially for the interested ground-state manifold, $\mathsf{P_v}$ and $\mathsf{L_s}$ provide a unique means of distinguishing state $|+\rangle$ from state $|-\rangle$. This fundamentally important point will be elaborated in more details below.

To quantify our arguments, let's look into the transformations of ϕ_s under the operations of valley fermion parity $\mathsf{P_v}$ and the staggered leg-exchange symmetry $\mathsf{L_s}$. Therefore both $\mathsf{P_v}$ and $\mathsf{L_s}$ will shift or more precisely switch the classical states $\left|\pm\frac{\pi}{2}\right\rangle$. In particular, for $\mathsf{L_s}$,

$$\begin{aligned}\mathsf{L_s}\phi_s\left|\frac{\pi}{2}\right\rangle &= \left(\frac{\pi}{2}+2n\pi\right)\mathsf{L_s}\left|\frac{\pi}{2}\right\rangle = \mathsf{L_s}\phi_s\mathsf{L_s}^{-1}\mathsf{L_s}\left|\frac{\pi}{2}\right\rangle = \left(-\phi_s+2\pi(l'+l+1)\right)\mathsf{L_s}\left|\frac{\pi}{2}\right\rangle \\ &\Rightarrow \phi_s\mathsf{L_s}\left|\frac{\pi}{2}\right\rangle = \left(-\frac{\pi}{2}-2n'\pi+2\pi(l'+l+1)\right)\mathsf{L_s}\left|\frac{\pi}{2}\right\rangle = \left(-\frac{\pi}{2}+2n\pi\right)\mathsf{L_s}\left|\frac{\pi}{2}\right\rangle \\ &\Rightarrow \mathsf{L_s}\left|\frac{\pi}{2}\right\rangle = e^{i\varpi_i}\left|-\frac{\pi}{2}\right\rangle. \end{aligned} \tag{4.78}$$

(4.79)

In parallel, for $\mathsf{P_v}$,

$$\begin{aligned}\mathsf{P_v}\phi_s\left|\frac{\pi}{2}\right\rangle &= \left(\frac{\pi}{2}+2n\pi\right)\mathsf{P_v}\left|\frac{\pi}{2}\right\rangle = \mathsf{P_v}\phi_s\mathsf{P_v}^{-1}\mathsf{P_v}\left|\frac{\pi}{2}\right\rangle = (\phi_s-\pi)\,\mathsf{P_v}\left|\frac{\pi}{2}\right\rangle \\ &\Rightarrow \phi_s\mathsf{P_v}\left|\frac{\pi}{2}\right\rangle = \left(\frac{3\pi}{2}+2n\pi\right)\mathsf{P_v}\left|\frac{\pi}{2}\right\rangle = \left(-\frac{\pi}{2}+2n\pi\right)\mathsf{P_v}\left|\frac{\pi}{2}\right\rangle \\ &\Rightarrow \mathsf{P_v}\left|\frac{\pi}{2}\right\rangle = e^{i\varpi_v}\left|-\frac{\pi}{2}\right\rangle. \end{aligned} \tag{4.80}$$

(4.81)

Imposing $\mathsf{L_s}^2 = \mathsf{P_v}^2 = 1$, and the commutation relations $\mathsf{L_s}\mathsf{P_v} = \mathsf{P_v}\mathsf{L_s}$, requires

$$\begin{aligned}\mathsf{L_s}\mathsf{P_v}\left|\frac{\pi}{2}\right\rangle = e^{i\varpi_v}\mathsf{L_s}\left|-\frac{\pi}{2}\right\rangle = e^{i\left(\varpi_v+\varpi_i'\right)}\left|\frac{\pi}{2}\right\rangle = \mathsf{P_v}\mathsf{L_s}\left|\frac{\pi}{2}\right\rangle = e^{i\varpi_i}\mathsf{P_v}\left|-\frac{\pi}{2}\right\rangle = e^{i(\varpi_i+\varpi_v')}\left|\frac{\pi}{2}\right\rangle \\ \Longrightarrow \quad e^{i\left(\varpi_v+\varpi_i'\right)} = e^{i(\varpi_i+\varpi_v')}. \end{aligned} \tag{4.82}$$

There will be some phase ambiguity or phase degrees of freedom in defining states $\left|\frac{\pi}{2}\right\rangle$ and $\left|-\frac{\pi}{2}\right\rangle$. However, we are always able to fix the arbitrary phases in $\left|\pm\frac{\pi}{2}\right\rangle$ by requiring that the genuine ground state $|+\rangle$ is the exact eigenstate of $\mathsf{L_s}$ with eigenvalue $+1$, namely imposing the condition

$$\mathsf{L_s}\left(\left|\frac{\pi}{2}\right\rangle+\left|-\frac{\pi}{2}\right\rangle\right) = \left(\left|\frac{\pi}{2}\right\rangle+\left|-\frac{\pi}{2}\right\rangle\right) = e^{i\varpi_i}\left|-\frac{\pi}{2}\right\rangle + e^{i\varpi_i'}\left|\frac{\pi}{2}\right\rangle = e^{i\varpi_i}\left|-\frac{\pi}{2}\right\rangle + e^{-i\varpi_i}\left|\frac{\pi}{2}\right\rangle \tag{4.83}$$

will uniquely set

$$e^{i\varpi_i} = e^{i\varpi_i'} = 1. \tag{4.84}$$

Under this phase convention, we would have exactly that

$$\mathsf{L_s} \left|+\right\rangle = + \left|+\right\rangle, \tag{4.85}$$

$$\mathsf{L_s} \left|-\right\rangle = - \left|-\right\rangle. \tag{4.86}$$

The above derived constraints then require that

$$e^{i\varpi_v} = e^{i\varpi_v'} = e^{-i\varpi_v} \quad \Longrightarrow \quad \varpi_v = n\pi. \tag{4.87}$$

Therefore, for even n, $e^{i\varpi_v} = e^{i\varpi_v'} = 1$, then

$$\mathsf{P_v} \left|+\right\rangle = + \left|+\right\rangle, \tag{4.88}$$

$$\mathsf{P_v} \left|-\right\rangle = - \left|-\right\rangle. \tag{4.89}$$

While, for odd integers, $e^{i\varpi_v} = e^{i\varpi_v'} = -1$, then

$$\mathsf{P_v} \left|+\right\rangle = - \left|+\right\rangle, \tag{4.90}$$

$$\mathsf{P_v} \left|-\right\rangle = + \left|-\right\rangle. \tag{4.91}$$

Since we would like to keep the operator definition of $\mathsf{L_s}$ in Eq. (4.61) intact, once the second situation appears, we could absorb the extra minus sign into the redefinition of $\mathsf{P_v}$. In other words, with proper conventions, the eigenvalues of $\mathsf{L_s}$ and $\mathsf{P_v}$ when acting on states $|\pm\rangle$ are locked together. Detecting one will immediately imply the other. Crucially, armed with this connection, even though a direct measurement of the eigenvalues of $\mathsf{P_v}$ is typically very complicated, we can still indirectly infer its values through measuring the eigenvalues of $\mathsf{L_s}$, which is both exact and well-defined (in terms of c-operators).

In summary, we achieve an accurate characterization of the ground-state manifold of the model Hamiltonian at $\phi = \pi$, whose orthonormal basis states satisfy the following relations:

$$\left|+\right\rangle \coloneqq \frac{1}{\sqrt{2}} \left(\left|\frac{\pi}{2}\right\rangle + \left|-\frac{\pi}{2}\right\rangle \right), \quad H_{\text{s-G}} \left|+\right\rangle = E_+ \left|+\right\rangle, \quad \mathsf{P_v} \left|+\right\rangle = + \left|+\right\rangle, \quad \mathsf{L_s} \left|+\right\rangle = + \left|+\right\rangle, \tag{4.92}$$

$$\left|-\right\rangle \coloneqq \frac{1}{\sqrt{2}} \left(\left|\frac{\pi}{2}\right\rangle - \left|-\frac{\pi}{2}\right\rangle \right), \quad H_{\text{s-G}} \left|-\right\rangle = E_- \left|-\right\rangle, \quad \mathsf{P_v} \left|-\right\rangle = - \left|-\right\rangle, \quad \mathsf{L_s} \left|-\right\rangle = - \left|-\right\rangle. \tag{4.93}$$

With these preparations, the stage is set for uncovering the fact that this doubly-degenerated topological ground-state manifold is generated by the emergence of a pair of many-body Majorana end modes. The nonlocal occupation or emptying of these two Majorana bound states change simultaneously the eigenvalues of nonspatial P_{v} and L_{s} in a predicted way, thus probing the staggered leg-interchange symmetry is sufficient to identify the presence of the Majorana fermions and the associated valley fermion parity in this strongly interacting system.

4.4.4 Majorana fermion algebras

In the present subsection, for the continual flow of the derivations, we will demonstrate that these two predicted Majorana zero modes are localized at the ends of the ladder, and that they are complicated many-body mixtures of the two chains' degrees of freedom.

To obtain the Majorana fermion creation and annihilation operators, we first need to specify the description of the vacuum that surrounds the topological segment. A natural expectation is that the vacuum state should be fully gapped in both charge and spin sectors by an effectively infinite positive mass. This can be formulated by assigning the following Hamiltonian density to the vacuum in the regions of $x \in (-\infty, -L/2) \cup (L/2, \infty)$:

$$\begin{aligned}
\mathsf{H}_{\mathsf{vac}}(x) &= M\left(\tilde{\psi}^{\dagger}_{R,\mathrm{I}}(x)\tilde{\psi}_{L,\mathrm{I}}(x) + \tilde{\psi}^{\dagger}_{R,\mathrm{II}}(x)\tilde{\psi}_{L,\mathrm{II}}(x) + \mathrm{H.c.}\right) \\
&= -\frac{M}{\pi\varsigma}\left\{\sin\left[\phi_{R,\mathrm{I}}(x) - \phi_{L,\mathrm{I}}(x)\right] - \sin\left[\phi_{R,\mathrm{II}}(x) - \phi_{L,\mathrm{II}}(x)\right]\right\} \\
&= -\frac{2M}{\pi\varsigma}\sin\left[\frac{1}{2}\left(\phi_{R,\mathrm{I}}(x) - \phi_{L,\mathrm{I}}(x) - \phi_{R,\mathrm{II}}(x) + \phi_{L,\mathrm{II}}(x)\right)\right] \\
&\qquad \times \cos\left[\frac{1}{2}\left(\phi_{R,\mathrm{I}}(x) - \phi_{L,\mathrm{I}}(x) + \phi_{R,\mathrm{II}}(x) - \phi_{L,\mathrm{II}}(x)\right)\right] \\
&= -\frac{2M}{\pi\varsigma}\sin\left(\theta_s(x)\right)\cdot\cos\left(\theta_c(x)\right), \qquad (4.94)
\end{aligned}$$

where $M \to +\infty$. This assignment can be justified by noticing that for an infinite mass, both $\theta_c(x)$ and $\theta_s(x)$ will be spatially uniform in the vacuum regions, therefore their spatial gradients vanish, namely in the vacuum, $\rho_c(x) = \frac{1}{\pi}\partial_x\theta_c(x) = 0$ and $\rho_s(x) = \frac{1}{\pi}\partial_x\theta_s(x) = 0$, exactly as what we anticipated.

Majorana zero mode operators. At present stage, we are ready to work out in detail the explicit form of the Majorana operators, their defining algebraic properties, and their connection to the generalized fermion parity operator for a single valley. Since the vacuum can be described

by the potential,

$$H_{\text{vac}} = \int_{-\infty}^{-\frac{L}{2}} -\frac{2M}{\pi\varsigma}\sin\theta_s(x)\cdot\cos\theta_c(x)dx + \int_{\frac{L}{2}}^{\infty} -\frac{2M}{\pi\varsigma}\sin\theta_s(x)\cdot\cos\theta_c(x)dx,$$

then due to the infinite positive mass M, both θ_s and θ_c will be uniformly pinned to the extremes of the sine and cosine potentials in the vacuum, namely:

$$\text{At the left side:}\quad \theta_s(x) = \pm\frac{\pi}{2} + 2\hat{n}_{\theta_s}^{(1)}\pi \quad \text{for} \quad -\infty < x < -\frac{L}{2},$$
$$\text{At the right side:}\quad \theta_s(x) = \pm\frac{\pi}{2} + 2\hat{n}_{\theta_s}^{(2)}\pi \quad \text{for} \quad +\frac{L}{2} < x < +\infty,$$

where $\hat{n}_{\theta_s}^{(1)}$ and $\hat{n}_{\theta_s}^{(2)}$ are integer-valued operators. Here it is natural to assume that the operator's vacuum expectation values at left and right sides should be equal, namely $\langle\sin\theta_s\rangle_{\text{vac}}$ has to be the same either $+1$ or -1 on both sides, since the vacuum is unique. When $\langle\sin\theta_s\rangle_{\text{vac}} = \pm 1$, then $\langle\cos\theta_c\rangle_{\text{vac}} = \pm 1$ to minimize the potential. Therefore, even though $\hat{n}_{\theta_s}^{(1)}$ and $\hat{n}_{\theta_s}^{(2)}$ can take different integer values, the "$\pm\frac{\pi}{2}$" terms before them have to keep the same (i.e. take the same sign). In particular, when approaching the ends of the ladder from the vacuum, we would have

$$\theta_s(x \to -L/2) = \pm\frac{\pi}{2} + 2\hat{n}_{\theta_s}^{(1)}\pi, \tag{4.95}$$
$$\theta_s(x \to +L/2) = \pm\frac{\pi}{2} + 2\hat{n}_{\theta_s}^{(2)}\pi. \tag{4.96}$$

In a parallel analysis, we know from Eq. (4.71) that:

$$\text{In the bulk}\quad \phi_s(x) = -\frac{\pi}{2} + \hat{n}_{\phi_s}\pi \quad \text{for} \quad -\frac{L}{2} < x < +\frac{L}{2}. \tag{4.97}$$

Here $\hat{n}_{\phi_s}$ is also an integer-valued operator. Since θ_s and ϕ_s are conjugate fields satisfying the nontrivial commutation relation $[\theta_s(x), \phi_s(x')] = 2i\pi\Theta(x - x')$, it immediately follows that

$$\left[\pm\frac{\pi}{2} + 2\hat{n}_{\theta_s}^{(1)}\pi, -\frac{\pi}{2} + \hat{n}_{\phi_s}\pi\right] = 0 \quad \Longrightarrow \quad \left[\hat{n}_{\theta_s}^{(1)}, \hat{n}_{\phi_s}\right] = 0, \tag{4.98}$$
$$\left[\pm\frac{\pi}{2} + 2\hat{n}_{\theta_s}^{(2)}\pi, -\frac{\pi}{2} + \hat{n}_{\phi_s}\pi\right] = 2i\pi \quad \Longrightarrow \quad \left[\hat{n}_{\theta_s}^{(2)}, \hat{n}_{\phi_s}\right] = \frac{i}{\pi}. \tag{4.99}$$

Importantly, because $\theta_s(x)$ and $\phi_s(x')$ are conjugate fields due to their nonvanishing mutual commutator, there must exist a small but finite interval at each end of the ladder where both gapping effects or potentials are absent. In these two domain-wall regions, the Hamiltonian is free but the boundary conditions become highly nontrivial which are set by the adjacent

two very long regions that have been distinctively gapped. Solving the zero-mode solution of the free Hamiltonian inside the domain walls, we could find two Majorana bound states after imposing the boundary conditions: One is accommodated at the left end, and the other is localized at the right end. Outside the domain wall, the wavefunctions of the Majorana modes decay exponentially into the bulk region and the vacuum. People [78] have shown that the two resulting Majorana operators can be approximated as follows:

$$\gamma_1 \approx e^{i\pi\left(\hat{n}_{\theta_s}^{(1)}+\hat{n}_{\phi_s}\right)} \quad \text{localized at the left end of the ladder,} \tag{4.100}$$

$$\gamma_2 \approx e^{i\pi\left(\hat{n}_{\theta_s}^{(2)}+\hat{n}_{\phi_s}\right)} \quad \text{localized at the right end of the ladder,} \tag{4.101}$$

which are commuting with the free domain-wall Hamiltonians. Moreover, since the weights of the Majorana wavefunctions are exponentially suppressed in other regions, it is expected that to a good approximation, $\gamma_{1,2}$ will also commute with the interacting ladder Hamiltonian, namely $[\gamma_1, H] = [\gamma_2, H] \approx 0$. They indeed serve as the zero-energy operators. Numerically, this analytical expression of Majorana fermions can be directly visualized by measuring single-particle correlation functions via DMRG.

Majorana algebras. For completeness, we can explicitly verify that γ_1, γ_2 are indeed Majorana operators. First, they have to be self-conjugate:

$$\gamma_1^\dagger = e^{-i\pi\left(\hat{n}_{\theta_s}^{(1)}+\hat{n}_{\phi_s}\right)} = \gamma_1 \quad \text{and} \quad \gamma_2^\dagger = e^{-i\pi\left(\hat{n}_{\theta_s}^{(2)}+\hat{n}_{\phi_s}\right)} = \gamma_2. \tag{4.102}$$

Second, they have to square to 1:

$$\gamma_1^2 = e^{i\pi\left(\hat{n}_{\theta_s}^{(1)}+\hat{n}_{\phi_s}\right)} e^{i\pi\left(\hat{n}_{\theta_s}^{(1)}+\hat{n}_{\phi_s}\right)} = e^{2i\pi\left(\hat{n}_{\theta_s}^{(1)}+\hat{n}_{\phi_s}\right)} e^{\left[i\pi\left(\hat{n}_{\theta_s}^{(1)}+\hat{n}_{\phi_s}\right), i\pi\left(\hat{n}_{\theta_s}^{(1)}+\hat{n}_{\phi_s}\right)\right]/2} = 1,$$

$$\gamma_2^2 = e^{i\pi\left(\hat{n}_{\theta_s}^{(2)}+\hat{n}_{\phi_s}\right)} e^{i\pi\left(\hat{n}_{\theta_s}^{(2)}+\hat{n}_{\phi_s}\right)} = e^{2i\pi\left(\hat{n}_{\theta_s}^{(2)}+\hat{n}_{\phi_s}\right)} e^{\left[i\pi\left(\hat{n}_{\theta_s}^{(2)}+\hat{n}_{\phi_s}\right), i\pi\left(\hat{n}_{\theta_s}^{(2)}+\hat{n}_{\phi_s}\right)\right]/2} = 1.$$

As the fermionic operators, the Majorana operators should anticommute with each other:

$$\begin{aligned}
\{\gamma_1, \gamma_2\} &= e^{i\pi\left(\hat{n}_{\theta_s}^{(1)}+\hat{n}_{\phi_s}\right)} e^{i\pi\left(\hat{n}_{\theta_s}^{(2)}+\hat{n}_{\phi_s}\right)} + e^{i\pi\left(\hat{n}_{\theta_s}^{(2)}+\hat{n}_{\phi_s}\right)} e^{i\pi\left(\hat{n}_{\theta_s}^{(1)}+\hat{n}_{\phi_s}\right)} \\
&= e^{i\pi\left(\hat{n}_{\theta_s}^{(1)}+\hat{n}_{\phi_s}+\hat{n}_{\theta_s}^{(2)}+\hat{n}_{\phi_s}\right)} e^{\left[i\pi\left(\hat{n}_{\theta_s}^{(1)}+\hat{n}_{\phi_s}\right), i\pi\left(\hat{n}_{\theta_s}^{(2)}+\hat{n}_{\phi_s}\right)\right]/2} \\
&\quad + e^{i\pi\left(\hat{n}_{\theta_s}^{(2)}+\hat{n}_{\phi_s}+\hat{n}_{\theta_s}^{(1)}+\hat{n}_{\phi_s}\right)} e^{\left[i\pi\left(\hat{n}_{\theta_s}^{(2)}+\hat{n}_{\phi_s}\right), i\pi\left(\hat{n}_{\theta_s}^{(1)}+\hat{n}_{\phi_s}\right)\right]/2} \\
&= e^{i\pi\left(\hat{n}_{\theta_s}^{(1)}+\hat{n}_{\phi_s}+\hat{n}_{\theta_s}^{(2)}+\hat{n}_{\phi_s}\right)} e^{i\frac{\pi}{2}} + e^{i\pi\left(\hat{n}_{\theta_s}^{(2)}+\hat{n}_{\phi_s}+\hat{n}_{\theta_s}^{(1)}+\hat{n}_{\phi_s}\right)} e^{-i\frac{\pi}{2}} = 0,
\end{aligned} \tag{4.103}$$

where $\left[i\pi\left(\hat{n}_{\theta_s}^{(1)}+\hat{n}_{\phi_s}\right), i\pi\left(\hat{n}_{\theta_s}^{(2)}+\hat{n}_{\phi_s}\right)\right] = -\pi^2\left[\hat{n}_{\phi_s}, \hat{n}_{\theta_s}^{(2)}\right] = i\pi$ and $[\theta_s(x), \theta_s(x')] = 0$. More importantly, the valley fermion parity operator P_v can be recasted into a form of Majorana hopping,

$$\begin{aligned} i\gamma_1^\dagger\gamma_2 &= ie^{-i\pi\left(\hat{n}_{\theta_s}^{(1)}+\hat{n}_{\phi_s}\right)}e^{i\pi\left(\hat{n}_{\theta_s}^{(2)}+\hat{n}_{\phi_s}\right)} = ie^{-i\pi\left(\hat{n}_{\theta_s}^{(1)}+\hat{n}_{\phi_s}-\hat{n}_{\theta_s}^{(2)}-\hat{n}_{\phi_s}\right)}e^{\frac{\pi^2}{2}\left[\hat{n}_{\theta_s}^{(1)}+\hat{n}_{\phi_s},\hat{n}_{\theta_s}^{(2)}+\hat{n}_{\phi_s}\right]} \\ &= ie^{-i\pi\left(\hat{n}_{\theta_s}^{(1)}-\hat{n}_{\theta_s}^{(2)}\right)}e^{\frac{\pi^2}{2}\cdot\frac{-i}{\pi}} = e^{-i\pi\left(\hat{n}_{\theta_s}^{(1)}-\hat{n}_{\theta_s}^{(2)}\right)}. \end{aligned} \tag{4.104}$$

From the definition of the valley fermion parity in Eq. (4.58) and then by (4.95) and (4.96), we know that

$$\mathsf{P}_\mathsf{v} = (-1)^{\frac{N_\mathrm{I}-N_\mathrm{II}}{2}} = \exp\left\{i\frac{\theta_s\left(\frac{L}{2}\right)-\theta_s\left(-\frac{L}{2}\right)}{2}\right\}.$$

This is the central equation that relates the global $\mathbb{Z}_2$ symmetry (valley fermion parity) with the localized two Majorana end modes. As per the defining properties of Majorana operators, we can simply check that $\left(i\gamma_1^\dagger\gamma_2\right)^\dagger = -i\gamma_2^\dagger\gamma_1 = i\gamma_1^\dagger\gamma_2$, so P_v is Hermitian. In addition, $\left(i\gamma_1^\dagger\gamma_2\right)^2 = -\gamma_1^\dagger\gamma_2\gamma_1^\dagger\gamma_2 = +1$. In the preceding analysis, we have already underscored the observation that γ_1, γ_2 commute with the ladder Hamiltonian: $[\gamma_1, H] = [\gamma_2, H] \approx 0$ owing to the fact that Majorana wavefunctions are confined in the domain walls and have exponential-decaying weights in the bulk and vacuum. Hence $[\mathsf{P}_\mathsf{v}, H] = 0$. Furthermore, the total particle number in the ladder segment is defined by

$$\int_{-\frac{L}{2}}^{\frac{L}{2}}\rho_c(x)dx = \int_{-\frac{L}{2}}^{\frac{L}{2}}\frac{1}{\pi}\partial_x\theta_c(x)dx = \frac{1}{\pi}\left(\theta_c\left(\frac{L}{2}\right)-\theta_c\left(-\frac{L}{2}\right)\right) = 2N', \tag{4.105}$$

where Eq. (4.53) has been used and N' is a fixed even integer operator. However, since

$$\left[\theta_c(x), \theta_s(x')\right] = \left[\theta_c(x), \phi_s(x')\right] = 0 \quad \Longrightarrow \quad \left[\gamma_1, 2N'\right] = \left[\gamma_2, 2N'\right] = 0. \tag{4.106}$$

Therefore, if we define a normal fermion operator

$$d^\dagger = \frac{1}{2}\left(\gamma_1 + i\gamma_2\right), \quad \text{then} \quad \begin{cases} \left\{d^\dagger, d^\dagger\right\} = \{d, d\} = 0. \\ \left\{d^\dagger, d\right\} = 1. \end{cases}$$

$$\text{and} \quad \begin{cases} \left[d^\dagger, N'\right] = [d, N'] = 0 \leftarrow \text{total particle conservation.} \\ \left[d^\dagger, H\right] = [d, H] = 0 \leftarrow \text{zero-energy state.} \end{cases}$$

Nonlocally occupying and emptying the pair of Majorana bound states indeed has crucial consequences on the eigenvalue of the valley fermion parity operator. For the lowest-energy ground state $|+\rangle$, we have fixed the phases such that $\mathsf{P_v}\,|+\rangle = i\gamma_1^\dagger\gamma_2\,|+\rangle = +\,|+\rangle$, so

$$d^\dagger d\,|+\rangle = 0, \tag{4.107}$$

which means that the Majorana zero modes are not occupied. This can be understood by noting that

$$d^\dagger d = \frac{1}{4}\left(\gamma_1 + i\gamma_2\right)\left(\gamma_1 - i\gamma_2\right) = \frac{1}{2}\left(1 - i\gamma_1^\dagger\gamma_2\right). \tag{4.108}$$

However, we can show that the $d^{(\dagger)}$-operators anticommute with the valley fermion parity operator,

$$\{\gamma_1,\gamma_2\} = 0 \implies \begin{cases} \left\{\gamma_1, i\gamma_1^\dagger\gamma_2\right\} = 0. \\ \left\{\gamma_2, i\gamma_1^\dagger\gamma_2\right\} = 0. \end{cases} \implies \left\{d^\dagger, i\gamma_1^\dagger\gamma_2\right\} = \left\{d, i\gamma_1^\dagger\gamma_2\right\} = 0. \tag{4.109}$$

This fermionic relation ensures that the occupation of the d-fermion state will alter the eigenvalue of $\mathsf{P_v}$ (up to a phase),

$$i\gamma_1^\dagger\gamma_2 d^\dagger\,|+\rangle = -d^\dagger i\gamma_1^\dagger\gamma_2\,|+\rangle = -d^\dagger\,|+\rangle \quad \implies \quad d^\dagger\,|+\rangle \sim |-\rangle \quad \implies \quad E_- - E_+ \sim 0^+. \tag{4.110}$$

The above equation implies that $d^\dagger$ changes the eigenvalues of both $\mathsf{P_v}$ and $\mathsf{L_s}$. Namely, nonlocally occupying or emptying Majorana end states changes the eigenvalues of $\mathsf{P_v}$ and $\mathsf{L_s}$ in a predicted way. Measuring $\mathsf{L_s}$ thus amounts to probing the fermion parity. This reasoning is of both conceptual and practical significance as it shows that the emergent fermion parity is equivalent to the $\mathbb{Z}_2$ quantum numbers of the staggered leg-interchange symmetry. This demonstrates that the π-flux phase realizes many-body Majorana bound states in a number-conserving and strongly interacting system.

To recap, the characterization of the intricate relations between the Majorana-fermion determined valley fermion parity with the $\mathbb{Z}_2$ leg-exchange symmetry in the resulting ground-state manifold is the central contribution of our work. This subterranean linkage is revealed by a means of low-energy bosonization effective field theory.

4.4.5 Comparing flux equals pi with flux equals zero

There are two crucial differences between flux 0 and flux π. One has to do with the nature of the microscopic symmetry (antiunitary vs unitary). The second has to do with the effect of

single-particle interleg hopping on the umklapp processes that gap out the spin sector and lead to the Majorana zero modes.

Following this reasoning, the topological state found in Ref. [80] at $\phi = 0,\ t_\perp = 0$ is protected by the symmetry group of $U(1) \rtimes \mathbb{Z}_2^{\tilde{\mathsf{T}}} \times \mathbb{Z}_2^{\mathsf{P}_\ell}$ where for spinless fermions the time-reversal symmetry $\tilde{\mathsf{T}}$ fulfills: $\tilde{\mathsf{T}} c_{n,\ell}^{(\dagger)} \tilde{\mathsf{T}}^{-1} = c_{n,\ell}^{(\dagger)},\ \tilde{\mathsf{T}} i \tilde{\mathsf{T}}^{-1} = -i$ $(n = 0, \ldots, L-1;\ \ell = 0, 1)$. In comparison, the Majorana boundary modes we discovered at $\phi = \pi,\ t_\perp \neq 0$ might be associated with the $U(1) \rtimes \mathbb{Z}_2^{\mathsf{T}} \times \mathbb{Z}_2^{\mathsf{L_s}}$ symmetry with a modified time-reversal symmetry T: $\mathsf{T} c_{n,\ell}^{(\dagger)} \mathsf{T}^{-1} = -(-1)^n c_{n,\ell}^{(\dagger)},\ \mathsf{T} i \mathsf{T}^{-1} = -i$. Note that $\tilde{\mathsf{T}}^2 = \mathsf{T}^2 = +1$, thus according to Ref. [99], the topological indices for both quasi-1D time-reversal-invariant Majorana systems at $\phi = 0$ and $\phi = \pi$ assume $k = 1 \bmod 8$. The role of the antiunitary T symmetry will be elaborated in Subsection 4.5.1 further.

We highlight here that topologically trivial band structures can have unusual implications for interaction-driven topological states. The different topologically trivial band structures at $\phi = 0$ and $\phi = \pi$ are quite different when it comes to umklapp scattering processes. There are two reasons for this. At the level of multiparticle scattering, there exist two major detrimental effects that render the topological degeneracy sensitive to $t_\perp$. The first impact is related to the gapping-amplitude reduction from umklapp scatterings. In particular, when $\phi = t_\perp = 0$, as the two chains' bands are completely overlapped, small $t_\perp$ will lead to the severest half reduction of the gapping amplitude in the ϕ_s-channel. The second effect pertains to the frustration induced by the Fermi-velocity mismatch, which becomes pronounced upon increasing $t_\perp$ at $\phi = 0$. By contrast, when $\phi = \pi$, the two chains' bands are farthest separated from each other, so the gapping-amplitude reduction is minimized; at the same time, the two valleys remain symmetric under finite $t_\perp$, so the Fermi-velocity mismatch is absent. Furthermore, the commonly-expected frustration from the Fermi-momentum mismatch also gets avoided for $\phi = \pi$ due to the presence of umklapp processes. These basic comparisons partly explain why the topological Majorana modes are robust (fragile) against $t_\perp$ at $\phi = \pi$ ($\phi = 0$), which is consistent with the fact that $t_\perp$ breaks P_ℓ but preserves $\mathsf{L_s}$.

4.5 Numerical verification

In previous sections, we argued using bosonization that there exists a topological phase for strong interwire single-particle tunnelings, which is protected by the staggered leg-interchange

symmetry. To verify this, simulations based on density matrix renormalization group (DMRG) [100, 101] and exact diagonalization (ED) [102] have been performed to solve the lattice model (4.1) at $\phi = \pi$ and $t_\perp = 0.5t_\parallel$. The numerical outcomes provide strong evidence supporting our theoretical predictions. Fig. 4.3(a) demonstrates that in the low-filling region ($N/L = 1/3$), when pair hopping is strong ($W = -1.7t_\parallel$), the energy gap between the ground state and the 1st excited state gets closed exponentially as the ladder's size L increases. This is in contrast with a power-law gap closing resulting from the gapless charge sector. As anticipated, these two nearly degenerate eigenstates are distinguished by their eigenvalues of $\mathsf{L_s}$: The ground (1st excited) state has eigenvalue $+1$ (-1). The resulting ground-state manifold is further protected from other excitation states by a spectral gap which only decreases inversely with L (Fig. 4.3(b)). Moreover, the defining Majorana end modes can be visualized via the nonlocal correlations [80–82] in single-particle Green functions $G_{mn} \coloneqq \langle c^\dagger_{m,0} c_{n,0}\rangle = \langle c^\dagger_{m,1} c_{n,1}\rangle$ (see Fig. 4.3(c)). The presence of the edge states also gives rise to the even degeneracy in the entanglement spectrum (ES) [103, 104] on the central bond (Fig. 4.3(f)). These DMRG results have been confirmed by ED in small system's sizes. Nonetheless, when adding small $\mathsf{L_s}$-symmetry-breaking perturbations to (4.1), the energy gap of $E_1 - E_0$ grows rapidly, indicating the imperfection of topological degeneracy (see Section 4.6). Gathering information together, we believe that there exists a $\mathsf{L_s}$-symmetry protected (T-invariant in the present case) topological phase at $\phi = \pi$ and $t_\perp \neq 0$.

The existence of Majorana fermions is reinforced by detecting a topological quantum phase transition. Though at $\phi = \pi$ our model is robust to the single-particle interchain tunneling up to $t_\perp \approx t_\parallel$, Figs. 4.3(c)–(e) suggest that by $t_\perp = 3t_\parallel$, the system has undergone a transition to a nontopological regime. In particular, for this value we see that the nonlocal correlation in the single-particle Green function, an indicator of the presence of Majorana boundary modes, disappears. Further, the double degeneracy in the entanglement spectrum, another indicator of the topological boundary modes, disappears by $t_\perp = 2.5t_\parallel$. Finally, the spatial profile of the local fermion density $\rho_n \coloneqq \langle c^\dagger_{n,0} c_{n,0}\rangle = \langle c^\dagger_{n,1} c_{n,1}\rangle$ (shown in Fig. 4.3(g)) shows clear evidence of a fermion density-wave-type order for $t_\perp = 3t_\parallel$. In comparison, the bulk fermion density is uniform for $t_\perp \leq t_\parallel$, where the nonlocal correlation indicates the presence of Majorana boundary modes.

As concrete evidence of this transition, Fig. 4.4 shows the low-energy spectrum of the π-flux ladder as a function of $t_\perp/t_\parallel$ at fixed pair-hopping strength W calculated from ED for a

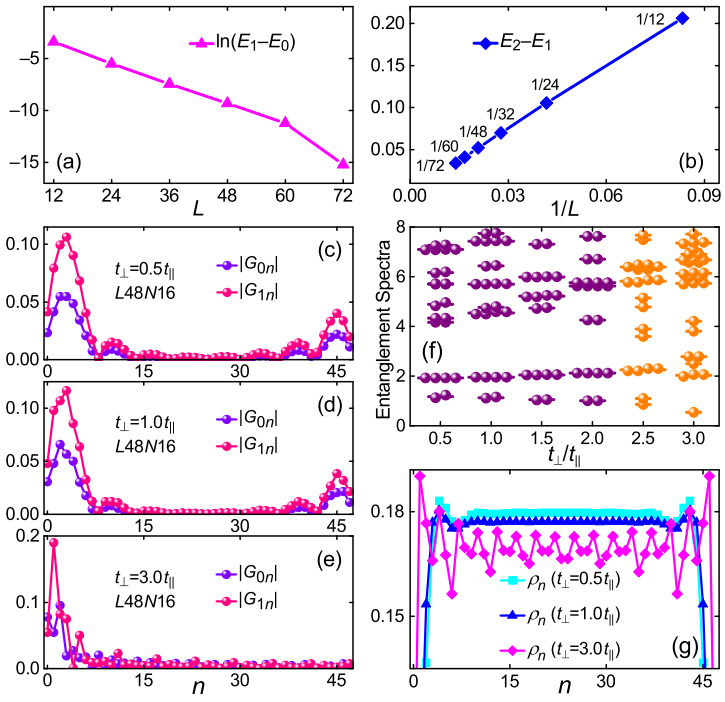

Figure 4.3: Scaling of energy gaps as functions of L from DMRG. (a) shows that the energy difference between the first two lowest-lying eigenstates of (4.1) decays exponentially with L. The protected ground-state manifold is separated from the rest of the spectrum by a gap that decreases inversely with L, as shown in (b). Here $W = -1.7t_{\|}$, $t_{\perp} = 0.5t_{\|}$, $\phi = \pi$, $N/L = 1/3$. Topological phase transition is illustrated in (c)–(g), where we fixed $W = -1.7t_{\|}$, $\phi = \pi$, $L = 48$, $N = 16$. (c)–(e) demonstrate the edge mode via the nonlocal correlations in single-particle Green functions. At $t_{\perp} = 3.0t_{\|}$, the edge mode disappears indicating the transition to a trivial state. This is in accordance with (f) and (g) which show the corresponding evolutions of entanglement spectra and local fermion densities as the transition is approached.

small system size. At approximately $t_{\perp} = 2.8t_{\|}$ a level crossing occurs between two states with opposite $\mathbb{Z}_2$ quantum numbers of the staggered leg-interchange symmetry L_s. For smaller $t_{\perp}$ the two lowest-energy states have opposite $\mathbb{Z}_2$ quantum numbers; whereas for larger $t_{\perp}$ both have the same $\mathbb{Z}_2$ eigenvalue $(+1)$. As explained in Section 4.4, this $\mathbb{Z}_2$ quantum number is associated with the fermion parity in the topological region, suggesting that this level crossing indicates a transition out of the topological regime. Such a level crossing is consistent with what we expect for a transition from a topological regime to a fermion-density-wave order: In the latter case we expect the lowest two states to be related by translation, and hence to have the

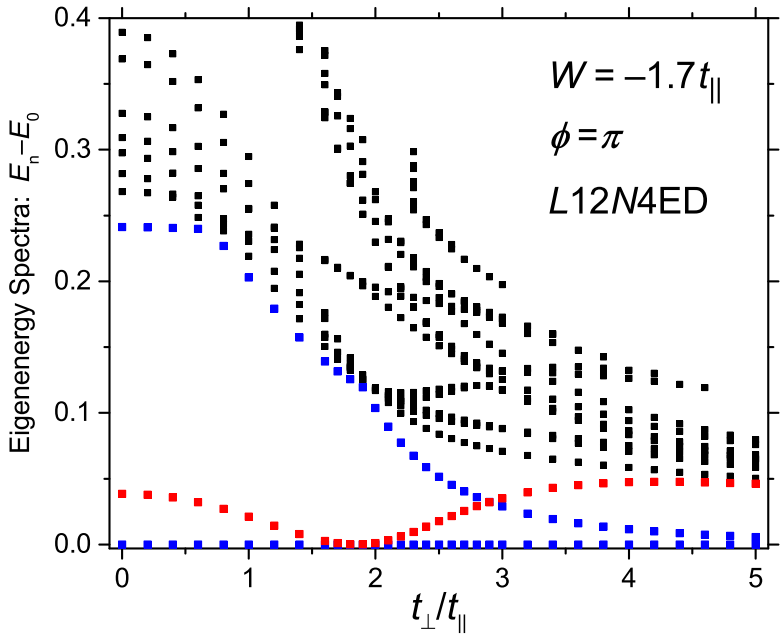

Figure 4.4: Exact diagonalization results show the evolution of the rescaled eigenenergies of H: $E_n - E_0$, as we increase $t_\perp$. Here we fixed $W = -1.7t_\parallel$, $\phi = \pi$, $L = 12$, $N = 4$, and set $t_\parallel = 1.0$ as the energy unit. We monitor the $\mathsf{L_s}$-quantum number for the lowest three eigenstates and use different colors to distinguish the $\mathbb{Z}_2$ eigenvalues of $\mathsf{L_s}$: Blue denotes $\langle \mathsf{L_s} \rangle = +1$, while red denotes $\langle \mathsf{L_s} \rangle = -1$. When $0 \leq t_\perp / t_\parallel \lesssim 2.5$, the lowest two eigenstates can be differentiated by their quantum numbers of $\mathsf{L_s}$. However, when $t_\perp / t_\parallel \gtrsim 3$, they possess the same quantum number $\langle \mathsf{L_s} \rangle = +1$ as the consequence of level crossing between the 1st and 2nd excited states.

same parity under the leg-exchange transformation $\mathsf{L_s}$.

4.5.1 Interleg Rashba spin-orbit interaction

Starting from here we have performed a series of numerical simulations to test the importance of different symmetries. In particular, we focus on the following points: (1) Check whether antiunitary symmetries are important. (We will see that they are not.) (2) Check the RG prediction that the topological phase requires $W < 0$. (3) Check that breaking $\mathsf{L_s}$ symmetry destroys the Majorana zero modes (see Section 4.6).

First, we are going to study a perturbation that breaks the antiunitary symmetry T but preserves $\mathsf{L_s}$. This interaction that fulfills the desired operations on the symmetries has the form of

a Rashba term. Therefore, due to the change of the underlying protecting symmetry, one possible advantage of the π-flux ladder model proposed in the above text is that it offers prospects for studying the interplay between Majorana zero modes and interchain single-particle interactions, in particular, the Rashba spin-orbit interaction. Since the Rashba spin-orbit term in the leg indices preserves leg-interchange symmetry but breaks time reversal T, the robust numerical signatures of the topological phase up to large values of the Rashba coupling provide evidence that it is indeed the unitary leg-interchange symmetry, rather than the antiunitary time-reversal symmetry, which is more responsible for the topological phase.

The interchain Rashba term in our two-leg ladder model is the following,

$$H_{\text{Rashba}} = -\lambda_R \sum_{n=0}^{L-2} \left(c^\dagger_{n,1} c_{n+1,0} - c^\dagger_{n,0} c_{n+1,1} + c^\dagger_{n+1,0} c_{n,1} - c^\dagger_{n+1,1} c_{n,0} \right), \tag{4.111}$$

where λ_R is a real parameter and we have treated the leg indexes as the pseudospin indexes: leg-$0 \mapsto \uparrow$ and leg-$1 \mapsto \downarrow$. It can be explicitly checked that H_{Rashba} is invariant under the *unitary* leg-interchange transformation $\mathsf{L_s}$:

$$\mathsf{L_s} H_{\text{Rashba}} \mathsf{L_s}^{-1} = -\lambda_R \sum_{n=0}^{L-2} \left(-c^\dagger_{n,0} c_{n+1,1} + c^\dagger_{n,1} c_{n+1,0} - c^\dagger_{n+1,1} c_{n,0} + c^\dagger_{n+1,0} c_{n,1} \right) = H_{\text{Rashba}}. \tag{4.112}$$

Here recall that $\mathsf{L_s} c^{(\dagger)}_{n,0} \mathsf{L_s}^{-1} = (-1)^{n+1} c^{(\dagger)}_{n,1}$ and $\mathsf{L_s} c^{(\dagger)}_{n,1} \mathsf{L_s}^{-1} = (-1)^{n+1} c^{(\dagger)}_{n,0}$ and $\mathsf{L_s} i \mathsf{L_s}^{-1} = i$. However, the Rashba SOC interaction explicitly breaks the *antiunitary* time-reversal symmetry T:

$$\mathsf{T} H_{\text{Rashba}} \mathsf{T}^{-1} = -\lambda_R \sum_{n=0}^{L-2} \left(c^\dagger_{n,0} c_{n+1,1} - c^\dagger_{n,1} c_{n+1,0} + c^\dagger_{n+1,1} c_{n,0} - c^\dagger_{n+1,0} c_{n,1} \right) = -H_{\text{Rashba}}. \tag{4.113}$$

Here we use the T-transformation defined previously by $\mathsf{T} c^{(\dagger)}_{n,0} \mathsf{T}^{-1} = c^{(\dagger)}_{n,1}$ and $\mathsf{T} c^{(\dagger)}_{n,1} \mathsf{T}^{-1} = c^{(\dagger)}_{n,0}$ and $\mathsf{T} i \mathsf{T}^{-1} = -i$. More interestingly, at $\phi = \pi$, this interchain Rashba SOC also preserves the crucial umklapp-scattering condition (see Fig. 4.5) such that the bosonization and renormalization group analysis in the above Section 4.3 of the chapter might be carried through in this case.

To verify this prediction, we numerically study the following Hamiltonian where both the

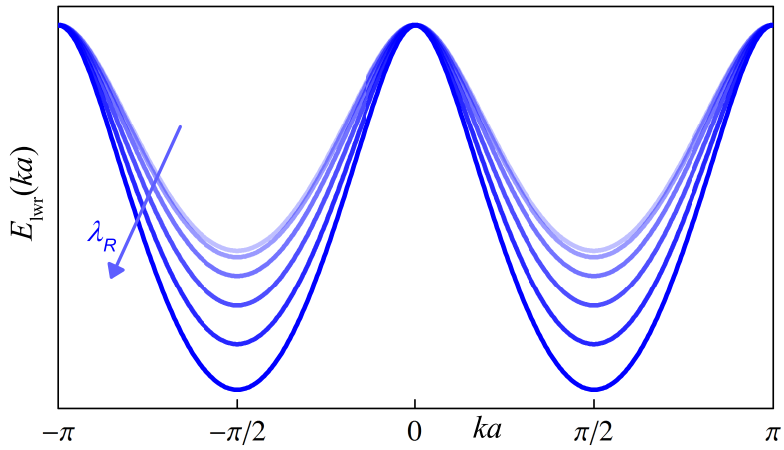

Figure 4.5: The evolution of the noninteracting band structure of $H_K + H_{\text{Rashba}}$ (see Eq. (4.114)) with the increase of Rashba SOC λ_R from $0.0t_\parallel$ to $1.0t_\parallel$. It is worth noting that the umklapp-scattering condition (Eq. (4.13)) remains valid under the change of λ_R. Here we have kept $t_\perp = t_\parallel,\ \phi = \pi$. As the upper band and lower band is symmetric, only the lower band is shown.

interleg single-particle tunneling $t_\perp$ and the interleg Rashba SOC λ_R are included,

$$\begin{aligned} H' =& H_K + H_{\text{Rashba}} + H_W \\ =& -\sum_{n=0}^{L-2}\left[\left(it_\parallel c^\dagger_{n,0}c_{n+1,0} - it_\parallel c^\dagger_{n,1}c_{n+1,1}\right) + \text{H.c.}\right] - \sum_{n=0}^{L-1}\left(t_\perp c^\dagger_{n,0}c_{n,1} + \text{H.c.}\right) \\ & - \lambda_R \sum_{n=0}^{L-2}\left(c^\dagger_{n,1}c_{n+1,0} - c^\dagger_{n,0}c_{n+1,1} + \text{H.c.}\right) + \sum_{n=0}^{L-2}\left(W c^\dagger_{n,0}c^\dagger_{n+1,0}c_{n,1}c_{n+1,1} + \text{H.c.}\right). \end{aligned} \tag{4.114}$$

Indeed, as is shown by Fig. 4.6, the topological signatures of the Majorana zero modes including the degeneracy in the entanglement spectra, the nonlocal correlations in the single-particle Green functions, and the uniform particle-density distribution in the bulk of the ladder have persisted up to $\lambda_R \approx 0.8t_\parallel$. Notice that in Fig. 4.6 we have fixed $t_\perp = t_\parallel,\ W = -1.7t_\parallel,\ L = 48,\ N = 16,\ \phi = \pi$. Therefore, it appears that the $\mathbb{Z}_2$ leg-interchange symmetry is central to stabilizing the Majorana boundary states.

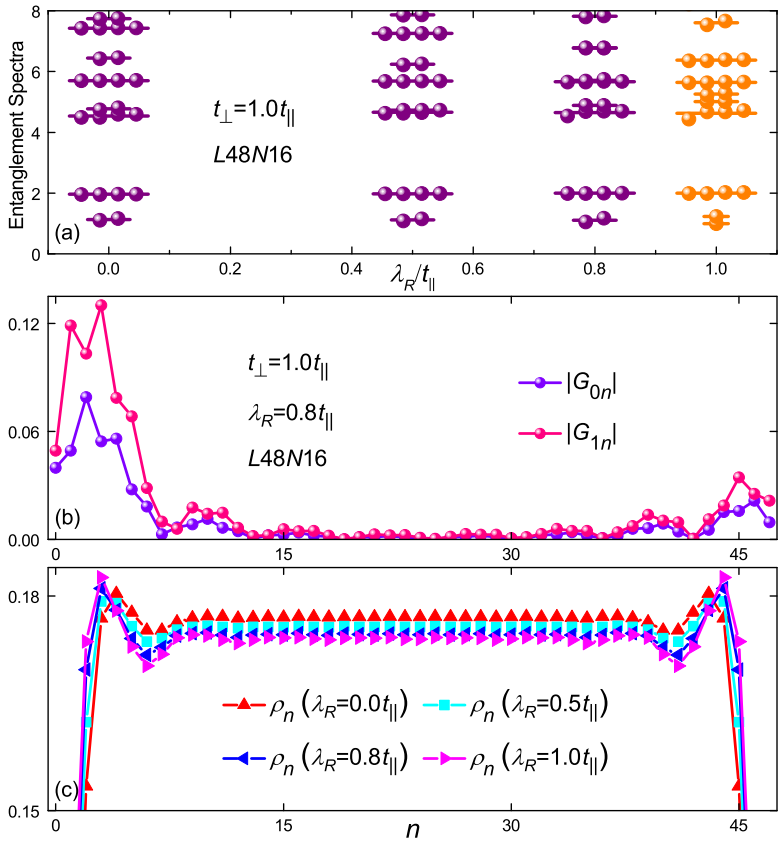

Figure 4.6: DMRG results for the Rashba SOC: (a) shows that the degeneracy of the entanglement spectra is robust up to $\lambda_R \approx 0.8t_\parallel$. (b) depicts the corresponding single-particle Green functions for $\lambda_R = 0.8t_\parallel$ where the nonlocal correlations are present. Up to $\lambda_R \approx 1.0t_\parallel$, the particle-density distributions in the bulk of the ladder remain uniform, as shown by (c). Here we have set $t_\perp = t_\parallel$, $W = -1.7t_\parallel$, $L = 48$, $N = 16$, $\phi = \pi$.

4.5.2 The pi-flux ladder for positive W

The RG analysis in Section 4.3 suggests that for finite $t_\perp$ when $W > 0$, $\phi = \pi$, the most relevant gapping channel of H_s for low fermion density $(3\pi/(4a) > k_{R,\mathrm{II}} > \pi/(2a))$ is the backscattering term g_{bs}. In this subsection we present the corresponding DMRG results to illustrate that the resulting phase exhibits no signatures of topological protection at finite $t_\perp$.

In particular, we evaluate the ES for $W = +1.7t_\parallel$ at several different values of $t_\perp$. The results in Fig. 4.7(a) demonstrate the significant splitting of the ES two-fold degeneracy at the lowest level even for the smallest nonzero values of $t_\perp \approx 0.1t_\parallel$. This is in sharp contrast to

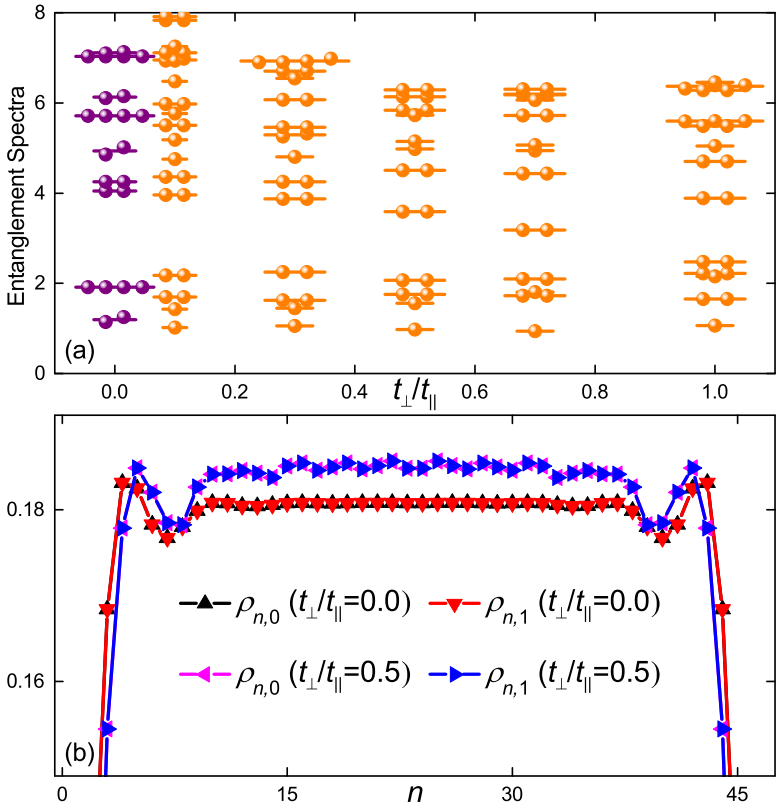

Figure 4.7: DMRG results: (a) shows the degeneracy splittings in the entanglement spectra as a function of $t_\perp$ for the ground state of the ladder system with the fixed parameters: $W = +1.7t_\parallel$, $\phi = \pi$, $L = 48$, $N = 16$. Two prototypical fermion-density profiles have been illustrated in panel (b), where for the trivial state there exist weak density modulations along the chain.

the situation of $W = -1.7t_\parallel$, where the even degeneracy in ES persists up to $t_\perp \approx 2.0t_\parallel$ (see Fig. 4.3). Further, for parameters where this degeneracy is lifted, the local fermion-density profile $\rho_{n,\ell}$ exhibits weak modulations along the chain, as can be seen from Fig. 4.7(b). Here we define $\rho_{n,0} = \langle c^\dagger_{n,0} c_{n,0} \rangle$, $\rho_{n,1} = \langle c^\dagger_{n,1} c_{n,1} \rangle$ for the upper and lower chains, respectively.

4.6 Leg-interchange-symmetry-breaking perturbations

Here, we demonstrate numerically that the $\mathbb{Z}_2$ leg-exchange symmetry and the flux $\phi = \pi$ are both central to protecting the topological features of our model. Specifically, we investigate

three different ways of breaking the leg-interchange symmetry, and show that small (but finite) values of all symmetry-breaking perturbations lift the degeneracies in the ES associated with the topological boundary modes. In addition, we perform an analysis of the effect of perturbing the flux away from $\phi = \pi$, which lifts the degeneracies in the entanglement spectrum and leads to a fermion-density-wave order.

4.6.1 Making the intrachain hoppings different

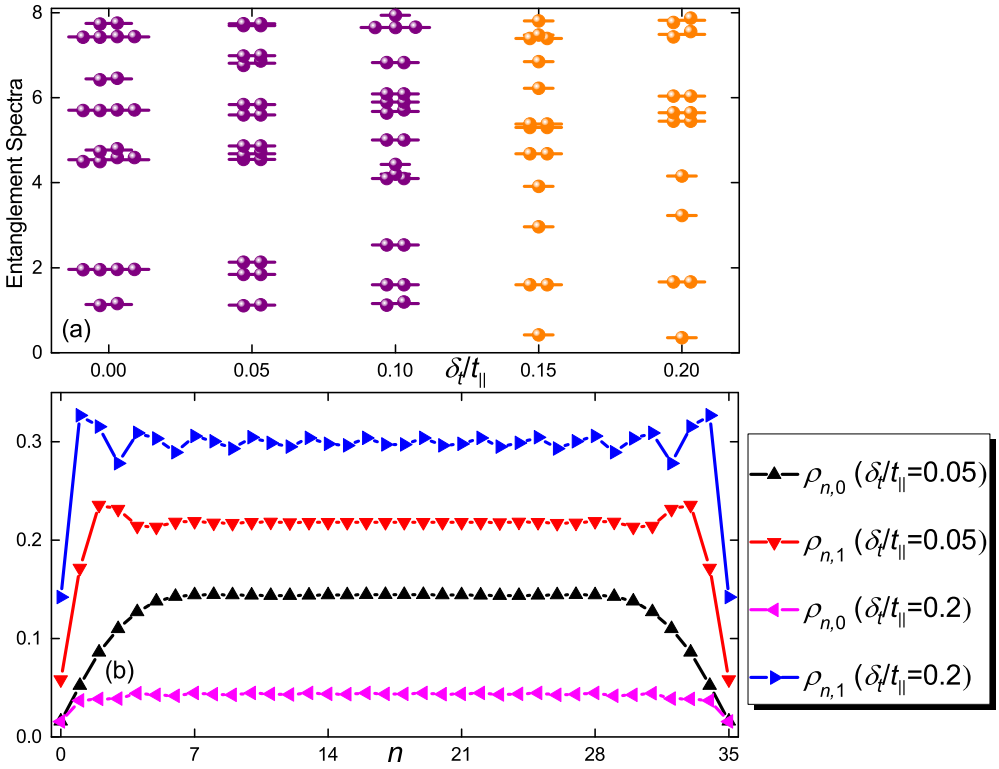

Figure 4.8: DMRG results: (a) shows the evolution of ES (for a system of $L = 36,\ N = 12$) as a function of $\mathsf{L_s}$-breaking perturbation $\delta_t/t_\parallel$ (see Eq. (4.115)). The even degeneracy of ES survives only up to small values of $\delta_t/t_\parallel \approx 0.125$. Panel (b) illustrates the local fermion-density profiles for the two different values of $\delta_t/t_\parallel$. Here $W = -1.7t_\parallel,\ t_\perp = t_\parallel,\ \phi = \pi$.

We first consider the result of explicitly breaking the leg-interchange symmetry by choosing $t_\parallel$ to be different on the two legs of the ladder. We thus modify the Hamiltonian in the following

way:

$$
\begin{aligned}
H' = &- \sum_{n=0}^{L-2} \Big[\Big(i \left(t_{\parallel} - \delta_t \right) c^{\dagger}_{n,0} c_{n+1,0} - i \left(t_{\parallel} + \delta_t \right) c^{\dagger}_{n,1} c_{n+1,1} \Big) + \text{H.c.} \Big] \\
&- \sum_{n=0}^{L-1} \Big(t_{\perp} c^{\dagger}_{n,0} c_{n,1} + \text{H.c.} \Big) \\
&+ \sum_{n=0}^{L-2} \Big(W c^{\dagger}_{n,0} c^{\dagger}_{n+1,0} c_{n,1} c_{n+1,1} + \text{H.c.} \Big) ,
\end{aligned} \tag{4.115}
$$

where we have set $\phi = \pi$, and the added δ_t-terms explicitly break the $\mathsf{L_s}$ symmetry.

The arguments given in Section 4.4 assert that breaking $\mathsf{L_s}$ should lift the degeneracy associated with the topological boundary modes, since there is no longer any reason for the fermion-parity even and fermion-parity odd states to be proximate in energy. This is apparent in the evolution of the ground-state entanglement spectra (shown in Fig. 4.8(a) for a system of $L = 36,\ N = 12$) as a function of $\delta_t / t_{\parallel}$. We observe that for fixed $W = -1.7 t_{\parallel},\ t_{\perp} = t_{\parallel}$, the two-fold degeneracy in the lowest level of the ES has completely disappeared by $\delta_t = 0.15 t_{\parallel}$. This suggests that the symmetry $\mathsf{L_s}$ is, as claimed, integral to protecting the topological boundary modes. Fig. 4.8(b) further supports this, by showing that for sufficiently large δ_t ($\delta_t = 0.2 t_{\parallel}$), the fermion density on the lower chain tends to develop weak spatial modulations, similar to those observed for positive W in the previous section. For smaller values ($\delta_t = 0.05 t_{\parallel}$), the density profiles appear to remain uniform in the bulk, though the relative populations of the two chains are generically different when the leg-interchange symmetry is broken.

It is somewhat surprising that for the smallest values of $\delta_t / t_{\parallel}$ the degeneracy in the ES and the uniform fermion density persist, suggesting that the topological boundary modes are only destroyed at finite values of the symmetry-breaking parameter. A similar effect was observed in Ref. [80], where the authors saw signatures of topological features in the $\phi = 0$ chain for small but finite interchain single-particle hopping—the relevant symmetry-breaking perturbation in that case. This may be because the spin sector is gapped and completely decoupled from the gapless charge sector; hence its behavior is robust to sufficiently small perturbations.

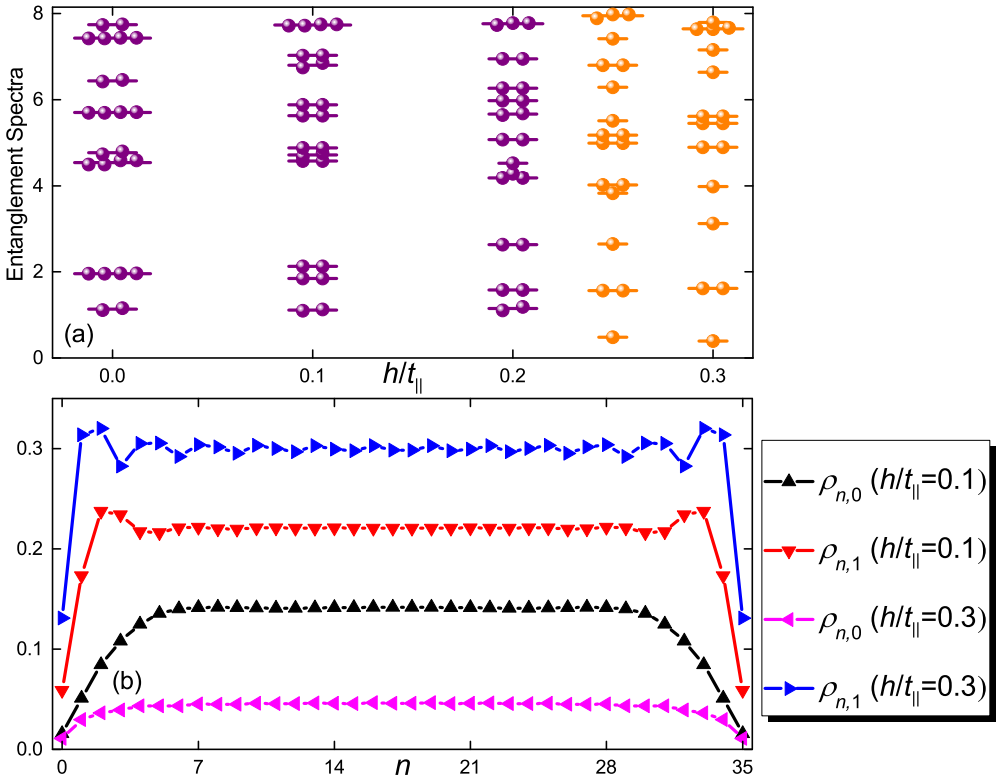

Figure 4.9: DMRG results: (a) shows the evolution of ES (for a system of $L = 36,\ N = 12$) as a function of $\mathsf{L_s}$-breaking perturbation $h/t_\parallel$ (see Eq. (4.116)). The even degeneracy of ES survives up to small values of $h/t_\parallel \approx 0.225$. Panel (b) shows the development of weak density modulations along the lower chain as $h/t_\parallel$ increases. Here $W = -1.7t_\parallel,\ t_\perp = t_\parallel,\ \phi = \pi$.

4.6.2 Making imbalanced local potentials

As a second test, we consider adding a chemical potential that is imbalanced between the two chains of the Fermi ladder. We thus take the Hamiltonian to be

$$\begin{aligned} H' = &-\sum_{n=0}^{L-2}\left[\left(it_\parallel c^\dagger_{n,0}c_{n+1,0} - it_\parallel c^\dagger_{n,1}c_{n+1,1}\right) + \text{H.c.}\right] - \sum_{n=0}^{L-1}\left(t_\perp c^\dagger_{n,0}c_{n,1} + \text{H.c.}\right) \\ &+ \sum_{n=0}^{L-2}\left(W c^\dagger_{n,0}c^\dagger_{n+1,0}c_{n,1}c_{n+1,1} + \text{H.c.}\right) + \sum_{n=0}^{L-1}\left(h c^\dagger_{n,0}c_{n,0} - h c^\dagger_{n,1}c_{n,1}\right), \end{aligned} \tag{4.116}$$

where the last h-terms also break the $\mathsf{L_s}$ symmetry explicitly.

Via DMRG, we find that the effect of h-terms (see Fig. 4.9) is similar to that of the δ_t-terms, both of which tend to destroy the topological Majorana boundary modes as indicated by the

splitting (or nondegeneracy) in the lowest level of ES. This perturbation also has a similar effect on the fermion-density profile, first changing the relative occupancies of the two chains, and at higher values leading to density modulations in the higher density chain. The two perturbations differ quantitatively, however: In this case, the two-fold ES degeneracy survives up to $h/t_{\|}$ between about 0.2 and 0.25. The other parameters are kept the same as that in Fig. 4.8: $W = -1.7t_{\|},\ t_{\perp} = t_{\|},\ \phi = \pi,\ L = 36,\ N = 12$.

4.6.3 Making the flux deviate from pi

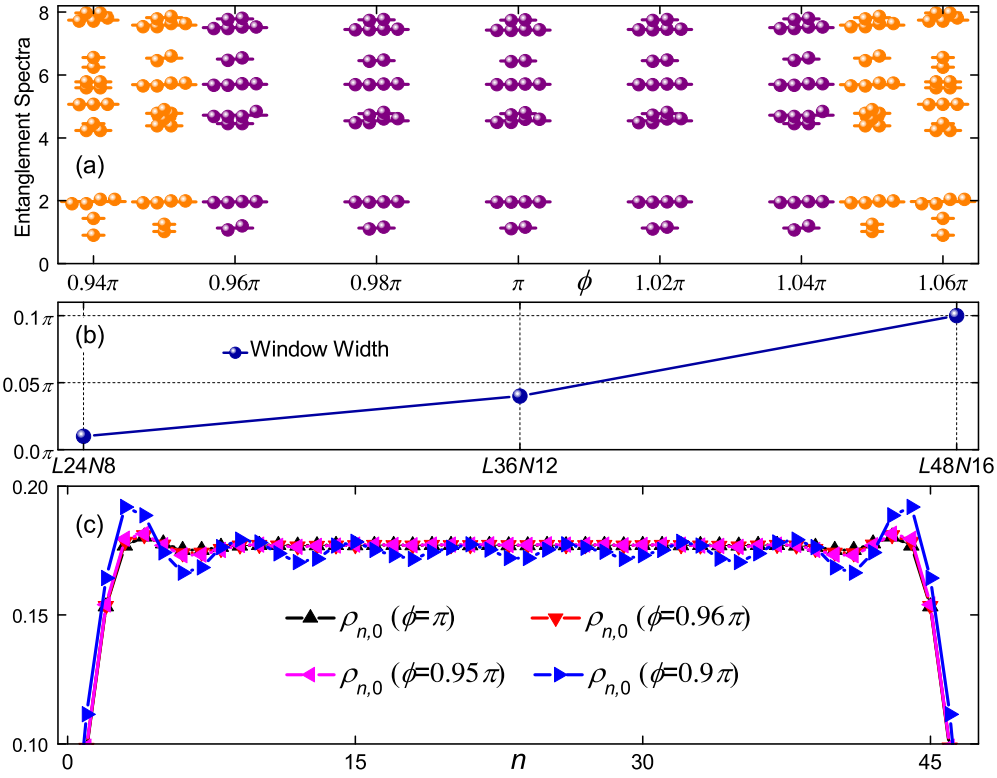

Figure 4.10: DMRG results: (a) shows the evolution of ES (for a system of $L = 48,\ N = 16$) as a function of L_s-breaking perturbation $\delta_\phi = \pi - \phi$ (see Eq. (4.117)). The even degeneracy of ES survives up to small values of $-0.05 \lesssim \delta_\phi/\pi \lesssim 0.05$, therefore the size of the window for detecting the topological boundary states is about 0.1π. Panel (b) shows the scaling behavior of the window width for the topological region. Panel (c) shows the development of a fermion-density-wave order under the increase of $|\delta_\phi|$. Here $W = -1.7t_{\|},\ t_{\perp} = t_{\|},\ N/L = 1/3$.

Finally, we check numerically the consequences of the deviations of ϕ from the specific

value of π. The corresponding Hamiltonian takes the following form,

$$H' = -\sum_{n=0}^{L-2}\left[\left(t_{\parallel}e^{\frac{i}{2}(\pi-\delta_\phi)}c^{\dagger}_{n,0}c_{n+1,0}+t_{\parallel}e^{-\frac{i}{2}(\pi-\delta_\phi)}c^{\dagger}_{n,1}c_{n+1,1}\right)+\text{H.c.}\right] - \sum_{n=0}^{L-1}\left(t_{\perp}c^{\dagger}_{n,0}c_{n,1}+\text{H.c.}\right)+\sum_{n=0}^{L-2}\left(Wc^{\dagger}_{n,0}c^{\dagger}_{n+1,0}c_{n,1}c_{n+1,1}+\text{H.c.}\right), \tag{4.117}$$

where the extra δ_ϕ-phases break the $\mathsf{L_s}$ symmetry explicitly.

Qualitatively, our results are similar to the two cases described above: A small perturbation δ_ϕ is sufficient to lift the degeneracy of the ES, signaling a loss of the topological boundary modes. However, as demonstrated in Fig. 4.10(a), for $t_\perp/t_\parallel = 1$ the topological ES degeneracy is more sensitive to the δ_ϕ-perturbations than to the δ_t- and h-terms. The lowest-level two-fold degeneracy in the ES becomes split at a small value of $|\delta_\phi/\pi| \lesssim 0.05$, indicating the instability of the Majorana boundary modes. We note, however, that this quantitative effect is necessarily sensitive to the system's filling and the magnitude of $t_\perp$, since for $t_\perp = 0$ the flux has less impact on the band structure. Thus for small interchain single-particle tunneling strengths and appropriate occupations, the ES degeneracy survives to larger values of δ_ϕ/π.

To demonstrate that there exists a finite-width window for observing the signatures of Majorana zero modes, in Fig. 4.10(b) we show the scaling behavior of the window width (defined by $2|\delta_{\phi,\text{critical}}|$) as a function of the system size. The overall trend indicates that the topological ES degeneracy persists to an appreciable value of the δ_ϕ-perturbation in large ladder lengths.

These numerical results are consistent with our theoretical expectations on the commensurate-incommensurate phase transition. Namely, when $\delta < \delta_\text{c} \sim \frac{1}{a}(y_{um})^{\frac{1}{2-2K_s^{-1}}}$, the incommensuration induced by the $\delta\cdot x$ term in our cosine interaction is sufficiently weak such that the term $\delta\cdot x$ can be dropped. Therefore, the signatures of Majorana zero modes should persist. However, when $\delta > \delta_\text{c}$, the $\cos(2\phi_s(x) - \delta\cdot x)$ term becomes rapidly oscillating such that it averages to zero and might be dropped completely. In this case, the Majorana zero modes disappear. In Fig. 4.10(c) we show by numerics that for $W = -1.7t_\parallel,\ t_\perp = t_\parallel,\ L = 48,\ N = 16$, this transition is toward a regime with a fermion density-wave-type order.

4.7 Beyond Kitaev paradigm

To some extent, the π-flux ladder model generalizes the SC proximitrized spin-orbit-coupled (SOC) nanowire model [5, 6] to a number-conserving setting. Specifically, the flux gives rise to

the leg-momentum locking, similar to the spin-momentum locking in SOC systems. The inter-chain single-particle tunneling $t_\perp$ plays the role of a Zeeman field that opens gaps at band crossings. Finally, the quadratic p-wave pairing terms are replaced by the four-fermion pair-hopping terms to ensure number conservation. Notice that the flux-equals-π configuration cannot be achieved for a spin-orbit interaction as that requires its strength to be infinity. (This might be due to the fact that there is no spinless analog of Kitaev chain in 1D number-conserving systems.) While in the π-flux model umklapp scattering is present at any filling [105]. This is a significant advantage for the π-flux model relative to an actual spin-orbit coupling, since in number-conserving systems these umklapp terms are essential to enabling the topological regime. Indeed, as our 1D system is not exactly at half-filling, the particle-hole and chiral operations [15] are not symmetries of the wavefunction, such that the topologically nontrivial state requires interactions (which effectively generate these as emergent symmetries at low energies).

For illustrating the interesting connections to the celebrated 1D Kitaev chain [1] and the popular 1D spin-orbit-coupled Majorana nanowire model with proximity-induced superconductivity [5, 6], we make a *structure diagram* in Fig. 4.11 to further clarify the status of our present π-flux ladder model as a many-body generalization of the Majorana nanowire model into the number-conserving settings that goes beyond the standard Kitaev paradigm.

In particular, we emphasize that it is the novel leg-interchange symmetry protecting the newly-discovered Majorana boundary states at $\phi = \pi$ that *distinguishes* our present paper from all the previous works [1, 5, 6, 80].

Ever since Kitaev [1], boundary Majorana zero modes are closely tied to the presence of a microscopic symmetry of fermion parity. This point is most transparent in the free fermion models: First, at the mean-field level, once we introduce the quadratic Cooper pairing terms such as $c_i^\dagger c_{i+1}^\dagger$ and $c_{i+1}c_i$ into the Hamiltonian, the resulting fermion-parity symmetry (namely the total number of particles is only conserved module 2) is particularly robust in the sense that this exact symmetry is not allowed to be broken under the quadratic mean-field approximation. Next, within the framework of Bogoliubov–de Gennes (BdG) theory, there is this built-in particle-hole symmetry, which is an antiunitary symmetry arising from an inherent redundancy built into the BdG formalism. Then according to the ten-fold way [15], it is clear how to construct (and classify) the topological invariants to signal the presence of Majorana zero modes.

However, this robustness (or unbreakableness) of fermion-parity symmetry in mean-field

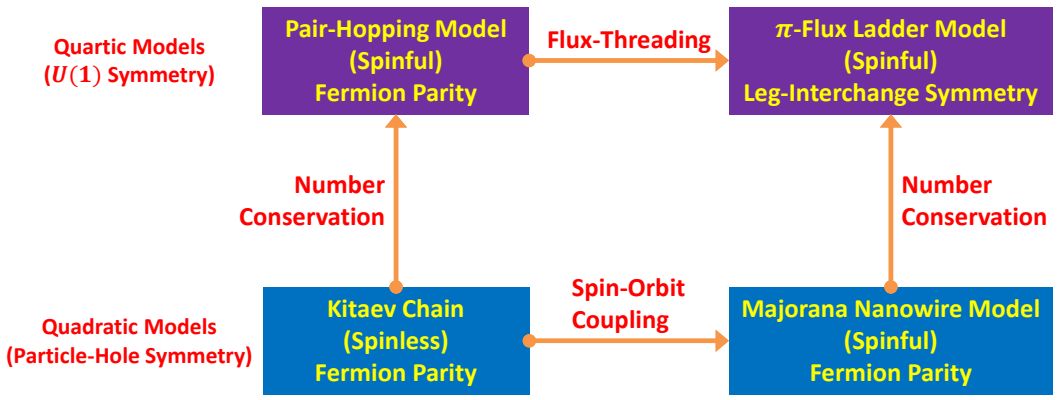

Figure 4.11: The *structure* diagram showing the generalization relationships between the 1D Kitaev chain [1], the spin-orbit-coupled Majorana nanowire model [5, 6], the pair-hopping-coupled Fermi wire model [80], and the present fermionic π-flux ladder model. See text for detailed explanation.

theory is based on the assumption of spontaneously breaking the $U(1)$ particle-number conservation, which somehow obscures the necessity of the existence of such a microscopic unitary symmetry at the first place to ensure the topological nature and thus the stability of Majorana zero modes in a general circumstance.

The importance of such a microscopic fermion-parity symmetry and in particular the existence of the associated two symmetry sectors becomes most striking when we impose the $U(1)$ particle-number conservation. As a direct consequence, we immediately know that there is *no* spinless analog of Kitaev chain in 1D number-conserving systems. Indeed, as highlighted in the work by Kraus et al. [80], the minimal generalization of Kitaev's model into the number-conserving setting needs at least two spinless wires, which is equivalent to a spinful wire. The resulting pair-hopping model now relies on a delicate (breakable) single-chain fermion-parity symmetry; however, for such a strongly coupled two-leg ladder, there seems no obvious reason why such a fermion-parity symmetry in a single chain should be present in experiments, let alone being robust.

In essence, from the viewpoint of *symmetry*, both the mean-field Majorana nanowire model [5, 6] and the interacting pair-hopping model [80] are intriguing manifestations of the same Kitaev's chain model [1] in different contexts. The underlying symmetry principle (fermion parity) might not yet be radically shifted.

In sharp contrast, the π-flux ladder model represents an entirely new class of topological

superconducting/superfluid systems where the Majorana zero modes are protected by a more realistic leg-interchange symmetry. Importantly, in the present work we also revealed a subterranean connection between the *microscopic* leg-interchange symmetry and an *emergent* valley fermion-parity symmetry (which is at best approximate) in stabilizing the nontrivial topological edge states. This newly-established conceptual framework is itself beyond Kitaev paradigm, thus enriching the research field of Majorana fermions. To our knowledge, the π-flux ladder Hamiltonian might be the first concrete lattice model that exhibits topological superconductivity/superfluidity *without* an exact fermion-parity symmetry. Fig. 4.11 illuminates the key observations of the above paragraphs in a pictorial way.

4.8 Summary

To summarize, with the π-flux threading, we predict a class of interaction-driven Majorana bound state in fermionic wires coupled by single-particle and pair tunnelings. *En route* we generalize the chain fermion parity to the valley degree of freedom and identify the vital role of umklapp scatterings in establishing the novel topological phase. The connection we unravel between the valley fermion parity and the exact leg-interchange symmetry shall be illuminating and useful, which helps clarify the role of the $U(1) \times \mathbb{Z}_2^{\mathsf{L_s}}$ symmetry in stabilizing the newly-discovered Majorana zero modes. Our theory has been substantiated by the extensive DMRG and ED calculations. The proposed π-flux fermionic ladder model thus enriches the paradigm of Majorana physics in 1D. Higher dimensional generalizations of the present work would be interesting but might also be challenging.

Chapter 5

Detecting Anyonic Boundary States by Noise Spectrum

5.1 Motivation

In realistic physical realizations of topological bound states (such as Majorana fermions), the topological region of the sample is always in contact with some kind of dissipative reservoir. For Majoranas, the reservoir can include normal or SC leads, as well as thermal quasiparticles in the bulk 3D superconductor. In the quantum Hall systems we have discussed, this reservoir can also consist of quasiparticles pinned to impurities in the 2D bulk of the quantum Hall system. Due to interactions with these reservoirs, the total parity (i.e. the eigenvalue of P) is not conserved by the real experimental systems. Physically, the bath gives a limit to how slowly you can do things without losing coherence. On the other hand, for short 1D systems topological bound states can be detected by the splitting of the ground state degeneracy due to finite-size effects. This small splitting gives an upper bound on time-scales for measurements that involve adiabatic processes within this low-energy manifold. This raises a general question: Under what circumstances can you expect to detect zero modes at all? And, how much can you tell about the nature of the zero modes?

In this chapter we will study possible dynamical signatures of topological bound states, and specifically of parafermion (as opposed to Majorana) zero modes. To model the effect of coupling one of the quantum Hall parafermion systems described previously to a bath, we first restrict our attention to energies that are small compared to the gap in the bulk of the 1D

system. At these low energy scales, the only relevant degrees of freedom are the parafermionic zero modes. Then we use techniques from quantum optics to study the dynamics of these parafermionic zero modes system coupled to the bath. We evaluate the reduced density matrix operator and the parity (number) correlation functions of the restricted system in order to find some noise spectrum signatures of the inherent entanglement between the two weakly coupled topological segments.

5.2 Dissipation via coupling to thermal reservoirs

To model a system coupled to a thermal reservoir, in principle we want to write down the density matrix for the entire (system+resevoir) system. Since we only care about the system, we can then trace out the bath. This gives an equation known as the master equation. In cases where the dynamics of the bath is simple (i.e. free fermions or bosons) we can usually solve the resulting dynamics at least for small systems.

To this end, let me briefly remind you about the density matrix formalism. (More detailed derivations for the Majorana and parafermion cases can be found in the next few sections.) Recall that the density matrix operator is defined by $\rho \equiv \sum_i p_i |\Phi_i\rangle\langle\Phi_i|$ where $0 \leq p_i \leq 1$ denotes the probability of being in the state $|\Phi_i\rangle$ with $\sum_i p_i = 1$. For any physical system ρ must fulfill three essential properties: (1) hermiticity: $\rho = \rho^\dagger$. (2) normalization: $\mathrm{Tr}\rho = 1$. (3) semi-positivity: $\rho \geq 0$. Specifically its eigenvalues must be non-negative. Finally, the dynamical evolution of a density matrix is determined by the von Neumann equation,

$$i\hbar \frac{d}{dt}\rho(t) = [H,\ \rho(t)]. \tag{5.1}$$

To incorporate the quantum dissipation effects, we adopt the so-called system plus reservoir approach which models the environmental interactions through coupling the undamped subsystem S to a reservoir R with the general Hamiltonian $H = H_S + H_R + H_{SR}$. If we denote the density matrix operator of the closed system $S \otimes R$ as $\chi(t)$, then the reduced density operator for the subsystem S can be expressed as $\rho(t) = \mathrm{Tr}_R\{\chi(t)\}$. The average of an operator $\hat{O}$ in the Hilbert space of the subsystem S can be calculated in the Schrödinger picture with the knowledge of only $\rho(t)$, $\langle\hat{O}\rangle = \mathrm{Tr}_{S\otimes R}\{\hat{O}\chi(t)\} = \mathrm{Tr}_S\{\hat{O}\mathrm{Tr}_R[\chi(t)]\} = \mathrm{Tr}_S\{\hat{O}\rho(t)\}$.

The Schrödinger equation for the time evolution of $\rho(t)$ in the integro-differential form is known as the master equation. Within the Born and Markov approximations, the Lindblad

master equation typically reads,

$$\frac{\partial\rho(t)}{\partial t} = \hat{\mathcal{L}}(t)\rho(t) = -\frac{i}{\hbar}[H(t),\ \rho(t)] + \Gamma\sum_i \left(L_i\rho(t)L_i^\dagger - \frac{1}{2}\left\{ L_i^\dagger L_i,\ \rho(t) \right\} \right). \tag{5.2}$$

Here, refer to earlier equation with just time evolution of ρ, the Liouville superoperator $\hat{\mathcal{L}}(t)$ contains both the normal time evolution driven by the system Hamiltonian H and the dissipation processes encoded by the set of Lindblad operators L_i, which raise or lower the values of the quantum number q of the ground states. To obtain Eq. (5.2), two approximations are used. First, the Born approximation states that the total density operator $\chi(t)$ can be factorized as the product of $\rho(t)$ and the initial reservoir density operator R_0 which is true if we neglect the correction terms higher than the second order in H_{SR}. The second major approximation, the Markov approximation, ignores the memory or past history effects in the future evolution of $\rho(t)$. Namely, the future behavior of a Markovian system depends only on its present state.

5.3 Application to systems with Majorana zero modes

As a direct application and also a warm-up exercise, here I will give a detailed microscopic derivation of the master equations employed in Ref. [106] for the setups of Majorana zero modes. The more complicated calculation for parafermions will be presented in the next section.

The Hamiltonian of the two coupled Majorana segments is

$$\begin{aligned} H_A = &(t_{12}+t_{34})\,|0,0\rangle\langle 0,0| + (-t_{12}-t_{34})\,|1,1\rangle\langle 1,1| \\ &+ (t_{12}-t_{34})\,|0,1\rangle\langle 0,1| + (-t_{12}+t_{34})\,|1,0\rangle\langle 1,0| \\ &+ t_{23}|0,0\rangle\langle 1,1| + t_{23}|1,1\rangle\langle 0,0| \\ &+ t_{23}|0,1\rangle\langle 1,0| + t_{23}|1,0\rangle\langle 0,1|, \end{aligned} \tag{5.3}$$

where we use the basis of the two fermion number n_L and n_R as in Ref. [106]: $|n_L, n_R\rangle = (|0,0\rangle, |1,1\rangle, |0,1\rangle, |1,0\rangle)^{\mathrm{T}}$. In this basis, the matrix elements of the Hamiltonian H_A are

$$\begin{pmatrix} t_{12}+t_{34} & t_{23} & 0 & 0 \\ t_{23} & -t_{12}-t_{34} & 0 & 0 \\ 0 & 0 & t_{12}-t_{34} & t_{23} \\ 0 & 0 & t_{23} & -t_{12}+t_{34} \end{pmatrix}. \tag{5.4}$$

Operators A_α act in the space of the states of the interested system A, and we assume that $A_1 = c_R,\ A_2 = c_R^\dagger$. Temporarily we just focus on the right-hand side of the whole system. Similar analyses can be generalized to the left-hand side.

We further assume that the interacting Hamiltonian between the wire and the fermionic bath reads

$$\delta H = \sum_\alpha A_\alpha \otimes X_\alpha = \sum_\alpha A_\alpha^\dagger \otimes X_\alpha^\dagger. \tag{5.5}$$

A_α are operators which act in the space of the state of the wire system, while operators X_α correspond to the space of the fermionic reservoir's states. Because operators A_α and X_α act in different spaces, they are independent and commute with each other: $[A_\alpha,\ X_\alpha]_- = 0$. It is only important that the whole interacting Hamiltonian δH is Hermitian.

The corresponding master equation reads

$$\frac{d}{dt}\rho_A(t) = -\frac{i}{\hbar}\left[H_A,\ \rho_A(t)\right]_- + \frac{1}{\hbar^2}\sum_\Omega \sum_{\alpha,\beta} \Gamma_{\alpha\beta}(\Omega)\left\{A_\beta(\Omega)\rho_A(t)A_\alpha^\dagger(\Omega) - \frac{1}{2}\left[A_\alpha^\dagger(\Omega)A_\beta(\Omega),\ \rho_A(t)\right]_+\right\}. \tag{5.6}$$

The reduced density operator $\rho_A(t)$ describes the state of the interested system A interacting with the reservoir B. The factors $\Gamma_{\alpha\beta}(\Omega)$ are the Fourier transforms of the corresponding correlation functions of the fermionic reservoir,

$$\Gamma_{\alpha\beta}(\Omega) = \int_{-\infty}^{\infty} d\tau e^{i\Omega\tau} \mathrm{Tr}_B\left\{\tilde{X}_\alpha^\dagger(\tau)X_\beta\rho_B\right\} = \int_{-\infty}^{\infty} d\tau e^{i\Omega\tau}\left\langle \tilde{X}_\alpha^\dagger(\tau)X_\beta\right\rangle, \tag{5.7}$$

where $\tilde{X}_\alpha^\dagger(\tau) = e^{iH_B^R\tau/\hbar}X_\alpha^\dagger e^{-iH_B^R\tau/\hbar}$; H_B^R is the Hamiltonian of the fermionic bath: $H_B^R = \sum_\epsilon \hbar\omega_\epsilon|\epsilon\rangle\langle\epsilon|$, which means that $\tilde{f}_{\alpha,\epsilon}^\dagger(\tau) = f_{\alpha,\epsilon}^\dagger e^{i\omega_\epsilon\tau};\ \tilde{f}_{\alpha,\epsilon}(\tau) = f_{\alpha,\epsilon}e^{-i\omega_\epsilon\tau}$.

In our case, we only consider the first line of Eq. (6) in Ref. [106]. Namely

$$(\delta H)_R = \sum_\epsilon\left[\alpha_R^{(1)}c_R^\dagger f_{R,\epsilon} + \bar{\alpha}_R^{(1)}f_{R,\epsilon}^\dagger c_R + \alpha_R^{(2)}c_R^\dagger f_{R,\epsilon}^\dagger + \bar{\alpha}_R^{(2)}f_{R,\epsilon}c_R\right], \tag{5.8}$$

where the subscript R is for the right-hand side (not to be confused with reservoir); also, this dissipation gives us $c^\dagger$ and c for A, and $f^\dagger$ and f for X. Here as emphasized $[c_R,\ f_{R,\epsilon}]_- = [c_R^\dagger,\ f_{R,\epsilon}]_- = [c_R,\ f_{R,\epsilon}^\dagger]_- = [c_R^\dagger,\ f_{R,\epsilon}^\dagger]_- = 0$, and we are making an assumption that the eigenstates of the bath are free fermion states, created by the operators $f^\dagger$.

5.3.1 The first dissipative term

With these preparations, what we are doing is starting with H_A and δH given above, and finding appropriate Lindblad operators and couplings to describe the action within the 4-state system described by (5.3) and (5.4). Let us first focus on the following term

$$\frac{1}{\hbar^2}\sum_{\Omega}\sum_{\alpha,\beta}\Gamma_{\alpha\beta}(\Omega)A_\beta(\Omega)\rho_A(t)A_\alpha^\dagger(\Omega). \tag{5.9}$$

Part 1 Let us choose $A_\alpha = A_1 = c_R;\ A_\beta = A_1 = c_R$. Then we have

$$X_\alpha = \sum_\epsilon \left[\bar{\alpha}_R^{(1)} f_{R,\epsilon}^\dagger + \bar{\alpha}_R^{(2)} f_{R,\epsilon}\right], \tag{5.10}$$

$$X_\beta = \sum_\epsilon \left[\bar{\alpha}_R^{(1)} f_{R,\epsilon}^\dagger + \bar{\alpha}_R^{(2)} f_{R,\epsilon}\right], \tag{5.11}$$

and

$$\tilde{X}_\alpha(\tau) = \sum_\epsilon \left[\bar{\alpha}_R^{(1)} f_{R,\epsilon}^\dagger e^{i\omega_\epsilon\tau} + \bar{\alpha}_R^{(2)} f_{R,\epsilon} e^{-i\omega_\epsilon\tau}\right], \tag{5.12}$$

$$\tilde{X}_\alpha^\dagger(\tau) = \sum_\epsilon \left[\alpha_R^{(1)} f_{R,\epsilon} e^{-i\omega_\epsilon\tau} + \alpha_R^{(2)} f_{R,\epsilon}^\dagger e^{i\omega_\epsilon\tau}\right]. \tag{5.13}$$

Combine these two, we would have

$$\tilde{X}_\alpha^\dagger(\tau)X_\beta = \sum_\epsilon \left[\alpha_R^{(1)} f_{R,\epsilon} e^{-i\omega_\epsilon\tau} + \alpha_R^{(2)} f_{R,\epsilon}^\dagger e^{i\omega_\epsilon\tau}\right] \times \sum_{\epsilon'} \left[\bar{\alpha}_R^{(1)} f_{R,\epsilon'}^\dagger + \bar{\alpha}_R^{(2)} f_{R,\epsilon'}\right], \tag{5.14}$$

and

$$\langle\tilde{X}_\alpha^\dagger(\tau)X_\beta\rangle = \sum_\epsilon \left[|\alpha_R^{(1)}|^2 n_F(-\hbar\omega_\epsilon) e^{-i\omega_\epsilon\tau} + |\alpha_R^{(2)}|^2 n_F(\hbar\omega_\epsilon) e^{i\omega_\epsilon\tau}\right]. \tag{5.15}$$

Considering the degeneracy of the fermionic bath, we can specify $\sum_\epsilon = \sum_{[\epsilon]} \rho_R$, where ρ_R is the density of states with eigenenergies $\hbar\omega_\epsilon$ in the right reservoir. Then we have

$$\langle\tilde{X}_\alpha^\dagger(\tau)X_\beta\rangle = \sum_{[\epsilon]} \left[|\alpha_R^{(1)}|^2 n_F(-\hbar\omega_\epsilon)\rho_R e^{-i\omega_\epsilon\tau} + |\alpha_R^{(2)}|^2 n_F(\hbar\omega_\epsilon)\rho_R e^{i\omega_\epsilon\tau}\right], \tag{5.16}$$

$$\langle\tilde{X}_1^\dagger(\tau)X_1\rangle = \sum_{[\epsilon]} \left(|\alpha_R^{(1)}|^2 + |\alpha_R^{(2)}|^2\right)\rho_R n_F(\hbar\omega_\epsilon) e^{i\omega_\epsilon\tau}. \tag{5.17}$$

Since $\Gamma_{11}(\Omega) = \int_{-\infty}^{\infty} d\tau e^{i\Omega\tau} \langle \tilde{X}_1^\dagger(\tau) X_1 \rangle$, we derive

$$\Gamma_{11}(\Omega) = \sum_{[\epsilon]} \left(|\alpha_R^{(1)}|^2 + |\alpha_R^{(2)}|^2 \right) \rho_R n_F(\hbar\omega_\epsilon) \delta(\Omega + \omega_\epsilon). \tag{5.18}$$

Similarly, $\Gamma_{22}(\Omega)$ has the same expression as $\Gamma_{11}(\Omega)$,

$$\Gamma_{22}(\Omega) = \sum_{[\epsilon]} \left(|\alpha_R^{(1)}|^2 + |\alpha_R^{(2)}|^2 \right) \rho_R n_F(\hbar\omega_\epsilon) \delta(\Omega + \omega_\epsilon). \tag{5.19}$$

Next, Let us specify the form of the operator $A_\alpha(\Omega)$. First we assume that the wire system can be described by the Hamiltonian

$$H_A = \sum_a \hbar\omega_a |a\rangle\langle a|, \tag{5.20}$$

where states $|a\rangle$ constitute the complete and orthonormal basis in the space of states of the wire system A. The eigenfrequencies ω_a may or may not be degenerate. We now define the operator $A_\alpha(\Omega)$ via the following relations:

$$A_\alpha(\Omega) = \sum_{a,b} \delta(\omega_{ba} - \Omega) |a\rangle\langle a| A_\alpha |b\rangle\langle b|, \tag{5.21}$$

$$A_\alpha^\dagger(\Omega) = \sum_{a,b} \delta(\omega_{ab} - \Omega) |a\rangle\langle a| A_\alpha^\dagger |b\rangle\langle b|. \tag{5.22}$$

This representation may be called the decomposition of operator A_α into the eigenprojectors of Hamiltonian H_A.

Now the term $\frac{1}{\hbar^2}\sum_\Omega \Gamma_{11}(\Omega)A_1(\Omega)\rho_A(t)A_1^\dagger(\Omega)$ can be calculated straightforwardly as follows:

$$\begin{aligned}
&\frac{1}{\hbar^2}\sum_{\Omega}\Gamma_{11}(\Omega)A_1(\Omega)\rho_A(t)A_1^\dagger(\Omega)\\
&\quad=\frac{1}{\hbar^2}\sum_{\Omega}\sum_{[\epsilon]}\left(|\alpha_R^{(1)}|^2+|\alpha_R^{(2)}|^2\right)\rho_R n_F(\hbar\omega_\epsilon)\delta(\Omega+\omega_\epsilon)\\
&\quad\times\sum_{a,b}\delta(\omega_{ba}-\Omega)|a\rangle\langle a|c_R|b\rangle\langle b|\rho_A(t)\times\sum_{a',b'}\delta(\omega_{a'b'}-\Omega)|a'\rangle\langle a'|c_R^\dagger|b'\rangle\langle b'|\\
&\quad=\frac{1}{\hbar^2}\sum_{[\epsilon]}\left(|\alpha_R^{(1)}|^2+|\alpha_R^{(2)}|^2\right)\rho_R n_F(\hbar\omega_\epsilon)\\
&\quad\times\sum_{a,b,a',b'}\delta(\omega_{ba}+\omega_\epsilon)\delta(\omega_{a'b'}+\omega_\epsilon)\times|a\rangle\langle a|c_R|b\rangle\langle b|\rho_A(t)|a'\rangle\langle a'|c_R^\dagger|b'\rangle\langle b'|\\
&\quad=\frac{\left(|\alpha_R^{(1)}|^2+|\alpha_R^{(2)}|^2\right)\rho_R}{\hbar^2}\sum_{a,b}\sum_{a',b'}n_F(-\hbar\omega_{ba})\delta(\omega_{a'b'}-\omega_{ba})\\
&\quad\times|a\rangle\langle a|c_R|b\rangle\langle b|\rho_A(t)|a'\rangle\langle a'|c_R^\dagger|b'\rangle\langle b'|. \qquad (5.23)
\end{aligned}$$

These matrix elements have a simple form if we neglect the off-diagonal terms "t_{23}" in the Hamiltonian (5.3). In this case, the non-vanishing matrix elements are:

$$\hbar\omega_{ba}=-2t_{34}\begin{cases}\langle 1,0|c_R|1,1\rangle=-1\\ \langle 0,0|c_R|0,1\rangle=+1\end{cases}, \qquad (5.24)$$

and

$$\hbar\omega_{ab}=-2t_{34}\begin{cases}\langle 1,1|c_R^\dagger|1,0\rangle=-1\\ \langle 0,1|c_R^\dagger|0,0\rangle=+1\end{cases}. \qquad (5.25)$$

Therefore we have noticed that for these nonzero terms, we have the same factor $n_F(-\hbar\omega_{ba})=n_F(2t_{34})$, and the Kronecker δ-function will be automatically satisfied. Finally we would derive

$$\begin{aligned}
&\frac{1}{\hbar^2}\sum_{\Omega}\Gamma_{11}(\Omega)c_R(\Omega)\rho_A(t)c_R^\dagger(\Omega)\\
&\quad=\frac{1}{\hbar^2}\left(|\alpha_R^{(1)}|^2+|\alpha_R^{(2)}|^2\right)\rho_R n_F(2t_{34})\\
&\quad\times\sum_{a,b}\sum_{a',b'}|a\rangle\langle a|c_R|b\rangle\langle b|\rho_A(t)|a'\rangle\langle a'|c_R^\dagger|b'\rangle\langle b'|. \qquad (5.26)
\end{aligned}$$

If we set $\Gamma_2 = \frac{1}{\hbar^2}\left(|\alpha_R^{(1)}|^2 + |\alpha_R^{(2)}|^2\right)\rho_R n_F(2t_{34})$ and $L_2 = c_R$ (this operator is a matrix in the $|a\rangle$ basis),

$$\frac{1}{\hbar^2}\sum_{\Omega}\Gamma_{11}(\Omega)c_R(\Omega)\rho_A(t)c_R^\dagger(\Omega) = \Gamma_2 L_2\rho_A(t)L_2^\dagger \tag{5.27}$$

in the matrix form. Analogously,

$$\begin{aligned}\frac{1}{\hbar^2}\sum_{\Omega}&\Gamma_{22}(\Omega)c_R^\dagger(\Omega)\rho_A(t)c_R(\Omega)\\ &= \frac{1}{\hbar^2}\left(|\alpha_R^{(1)}|^2 + |\alpha_R^{(2)}|^2\right)\rho_R n_F(-2t_{34})\\ &\times\sum_{a,b}\sum_{a',b'}|a\rangle\langle a|c_R^\dagger|b\rangle\langle b|\rho_A(t)|a'\rangle\langle a'|c_R|b'\rangle\langle b'|.\end{aligned} \tag{5.28}$$

If we set $\Gamma_1 = \frac{1}{\hbar^2}\left(|\alpha_R^{(1)}|^2 + |\alpha_R^{(2)}|^2\right)\rho_R n_F(-2t_{34})$ and $L_1 = c_R^\dagger$ (in matrix form),

$$\frac{1}{\hbar^2}\sum_{\Omega}\Gamma_{22}(\Omega)c_R^\dagger(\Omega)\rho_A(t)c_R(\Omega) = \Gamma_1 L_1\rho_A(t)L_1^\dagger \tag{5.29}$$

in matrices. Note that the off-diagonal terms vanish. The rest of the derivations for the first dissipative term can be found in Appendix A.1.

5.3.2 The second dissipative term

Next let us focus on the remaining term

$$-\frac{1}{2\hbar^2}\sum_{\Omega}\sum_{\alpha,\beta}\Gamma_{\alpha\beta}(\Omega)[A_\alpha^\dagger(\Omega)A_\beta(\Omega)\rho_A(t) + \rho_A(t)A_\alpha^\dagger(\Omega)A_\beta(\Omega)]. \tag{5.30}$$

Part 1 Let's choose $A_\alpha = A_1 = c_R;\ A_\beta = A_1 = c_R$, then from Subsection 5.3.1, we know that

$$\Gamma_{11}(\Omega) = \sum_{[\epsilon]}\left(|\alpha_R^{(1)}|^2 + |\alpha_R^{(2)}|^2\right)\rho_R n_F(\hbar\omega_\epsilon)\delta(\Omega+\omega_\epsilon), \tag{5.31}$$

thus

$$
\begin{aligned}
-\frac{1}{2\hbar^2}\sum_{\Omega}&\Gamma_{11}(\Omega)[A_1^\dagger(\Omega)A_1(\Omega)\rho_A(t)+\rho_A(t)A_1^\dagger(\Omega)A_1(\Omega)] \\
&=-\frac{\left(|\alpha_R^{(1)}|^2+|\alpha_R^{(2)}|^2\right)}{2\hbar^2}\rho_R\sum_{[\epsilon]}n_F(\hbar\omega_\epsilon) \\
&\times[A_1^\dagger(-\omega_\epsilon)A_1(-\omega_\epsilon)\rho_A(t)+\rho_A(t)A_1^\dagger(-\omega_\epsilon)A_1(-\omega_\epsilon)] \\
&=-\frac{\left(|\alpha_R^{(1)}|^2+|\alpha_R^{(2)}|^2\right)}{2\hbar^2}\rho_R\sum_{[\epsilon]}n_F(\hbar\omega_\epsilon) \\
&\times\sum_{a,b,a',b'}[\delta(\omega_{ab}+\omega_\epsilon)\delta(\omega_{b'a'}+\omega_\epsilon)\times(|a\rangle\langle a|c_R^\dagger|b\rangle\langle b|a'\rangle\langle a'|c_R|b'\rangle\langle b'|\rho_A(t) \\
&+\rho_A(t)|a\rangle\langle a|c_R^\dagger|b\rangle\langle b|a'\rangle\langle a'|c_R|b'\rangle\langle b'|)] \\
&=-\frac{\left(|\alpha_R^{(1)}|^2+|\alpha_R^{(2)}|^2\right)}{2\hbar^2}\rho_R\sum_{a,b,a',b'}n_F(-\hbar\omega_{ab})\delta(\omega_{b'a'}-\omega_{ab}) \\
&\times\left[|a\rangle\langle a|c_R^\dagger|b\rangle\langle b|a'\rangle\langle a'|c_R|b'\rangle\langle b'|\rho_A(t)+\rho_A(t)|a\rangle\langle a|c_R^\dagger|b\rangle\langle b|a'\rangle\langle a'|c_R|b'\rangle\langle b'|\right].
\end{aligned}
\tag{5.32}
$$

Remember that

$$
\hbar\omega_{ab}=-2t_{34}\begin{cases}\langle 1,1|c_R^\dagger|1,0\rangle=-1\\ \langle 0,1|c_R^\dagger|0,0\rangle=+1\end{cases},
$$

we would have

$$
\begin{aligned}
-\frac{1}{2\hbar^2}\sum_{\Omega}&\Gamma_{11}(\Omega)[c_R^\dagger(\Omega)c_R(\Omega)\rho_A(t)+\rho_A(t)c_R^\dagger(\Omega)c_R(\Omega)] \\
&=-\frac{\left(|\alpha_R^{(1)}|^2+|\alpha_R^{(2)}|^2\right)}{2\hbar^2}\rho_R n_F(2t_{34}) \\
&\times\sum_{a,b,b'}\left[|a\rangle\langle a|c_R^\dagger|b\rangle\langle b|c_R|b'\rangle\langle b'|\rho_A(t)+\rho_A(t)|a\rangle\langle a|c_R^\dagger|b\rangle\langle b|c_R|b'\rangle\langle b'|\right].
\end{aligned}
\tag{5.33}
$$

As before, we set $\Gamma_2=\frac{1}{\hbar^2}(|\alpha_R^{(1)}|^2+|\alpha_R^{(2)}|^2)\rho_R n_F(2t_{34})$, and finally we find

$$
\begin{aligned}
-\frac{1}{2\hbar^2}\sum_{\Omega}&\Gamma_{11}(\Omega)[c_R^\dagger(\Omega)c_R(\Omega)\rho_A(t)+\rho_A(t)c_R^\dagger(\Omega)c_R(\Omega)] \\
&=-\frac{1}{2}\Gamma_2(L_2^\dagger L_2\rho_A(t)+\rho_A(t)L_2^\dagger L_2)
\end{aligned}
\tag{5.34}
$$

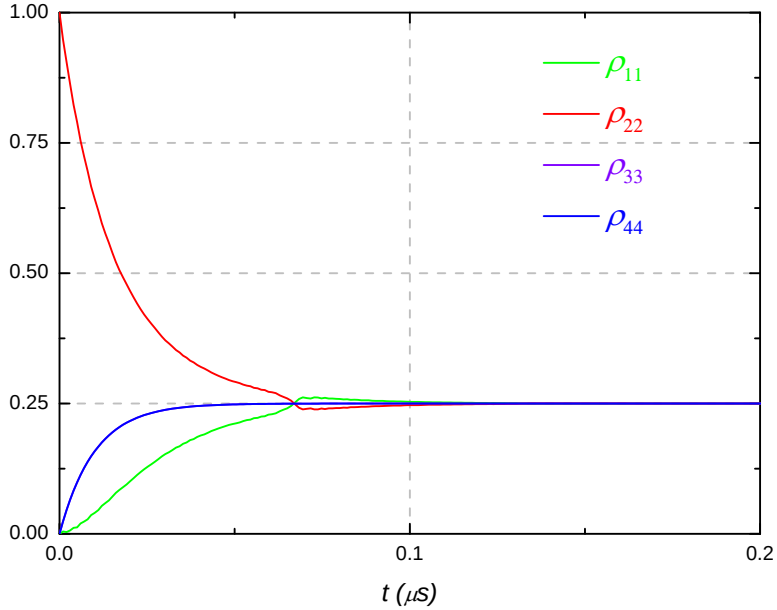

Figure 5.1: Diagonal elements of density matrix ρ. Here $\frac{t_{12}^0}{\hbar} = 5$, $\frac{t_{23}}{\hbar} = 0.5$, $\frac{t_{34}}{\hbar} = 2.5$, $\Gamma_i = \frac{0.05}{2}, \omega = 2\pi \times (0.005)$.

in matrix forms. Similarly, it can be derived that

$$-\frac{1}{2\hbar^2}\sum_{\Omega}\Gamma_{22}(\Omega)[c_R(\Omega)c_R^\dagger(\Omega)\rho_A(t) + \rho_A(t)c_R(\Omega)c_R^\dagger(\Omega)]$$
$$= -\frac{1}{2}\Gamma_1(L_1^\dagger L_1\rho_A(t) + \rho_A(t)L_1^\dagger L_1) \tag{5.35}$$

in matrix forms, and the off-diagonal terms vanish. The rest of the derivations for the second dissipative term have been relegated to Appendix A.2.

5.3.3 Summary of the above derivations

In summary, we have explicitly derived the master equation for Majorana zero modes [106]. Namely

$$\dot{\rho} = -\frac{i}{\hbar}[H,\ \rho]_- + \sum_{n=1,2}\Gamma_n\left[L_n\rho L_n^\dagger - \frac{1}{2}(L_n^\dagger L_n\rho + \rho L_n^\dagger L_n)\right]. \tag{5.36}$$

Although we just give the derivations for the right-hand side of the system, the generalization to the left-hand side should be straightforward and we only need to switch $R \to L$.

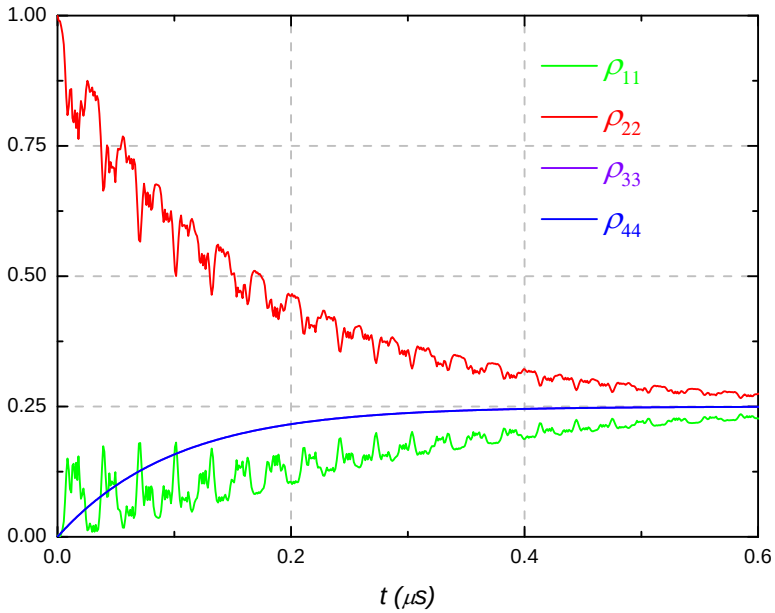

Figure 5.2: Diagonal elements of density matrix ρ. Here $\frac{t_{12}^0}{\hbar} = 1$, $\frac{t_{23}}{\hbar} = 0.1$, $\frac{t_{34}}{\hbar} = 0.5$, $\Gamma_i = \frac{0.005}{2}$, $\omega = 0.403$.

5.3.4 Numerical results for Majorana setups

We performed the numerical calculation by solving the 20 coupled first-order differential equations of the reduced density matrix elements ρ_{ij}. The typical results are reproduced in Figs. 5.1, 5.2, and 5.3. Basically, we are varying the coupling that determines the energy of having a "1" vs a "0" for the rightmost pair of Majoranas (in the limit that $t_{23} = 0$). But because the total fermion parity is conserved, even though the energy of 1 vs 0 on the left remains unchanged, we drive oscillations between the states $|11\rangle$ and $|00\rangle$ (or $|01\rangle$ and $|10\rangle$, depending on the initial condition. Thus the fermion parity of the right pair also oscillates. Measuring this nonlocal response is a direct probe of the conservation of fermion parity in these systems. For example, Fig. 5.3 shows the ideal case, where the driving frequency is small compared to t_{23} but is large compared to the inverse decay time. Please refer to the Appendix B in Ref. [106] for more details.

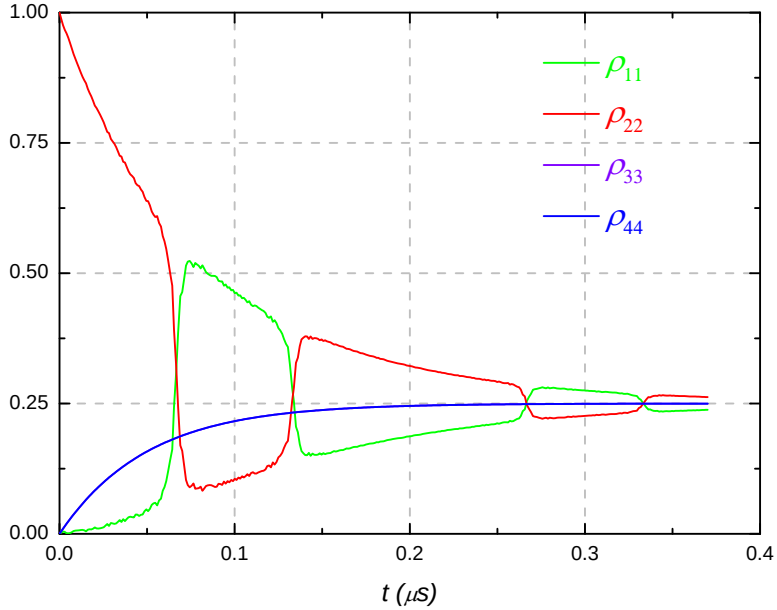

Figure 5.3: Diagonal elements of density matrix ρ. Here $\frac{t_{12}^0}{\hbar} = 15$, $\frac{t_{23}}{\hbar} = 1.5$, $\frac{t_{34}}{\hbar} = 7.5$, $\Gamma_i = \frac{0.01}{2}$, $\omega = 2\pi \times (0.005)$.

5.4 Dissipative model for parafermion zero modes and numerical simulations

5.4.1 Notational convention

With the above understanding on the Majorana setup, now we are ready to focus on the dynamics of the dissipative parafermionic system. First let's fix the notation of the basis states that we use to construct the Hamiltonian matrix and also list the table of the resulting states when the parafermion operators act on them. These basis vectors are defined by the following convention

$$|q_A, q_B\rangle = \left(\alpha_{L,A}^\dagger\right)^{q_A} \left(\alpha_{L,B}^\dagger\right)^{q_B} |0_A, 0_B\rangle, \quad q_{A,B} = 0,\ 1, \ldots,\ N, \tag{5.37}$$

where $\alpha_{L/R,A/B}$ is the parafermion operator at the left/right end of wire A/B, which satisfies the following nontrivial commutation relations,

$$\begin{aligned} &\alpha_j^N = 1, \ \ \alpha_j^\dagger = \alpha_j^{N-1}, \ \text{ and } \ \alpha_j \alpha_{j'} = \alpha_{j'} \alpha_j e^{i\frac{2\pi}{N}\mathrm{sgn}(j'-j)}, \\ &\alpha_j^\dagger \alpha_{j'} = \alpha_{j'} \alpha_j^\dagger e^{-i\frac{2\pi}{N}\mathrm{sgn}(j'-j)}, \ \ \alpha_{j'}^\dagger \alpha_j^\dagger = \alpha_j^\dagger \alpha_{j'}^\dagger e^{-i\frac{2\pi}{N}\mathrm{sgn}(j'-j)}. \end{aligned} \tag{5.38}$$

The labeling order of these four parafermion operators is shown in the diagram of the setup (see Fig. 5.4). From Eqs. (5.37) and (5.38), we can make the following table illustrating the action of parafermion operators on the basis states (from now on, we implicitly set $N = 3$, and the actual values of q_A and q_B should be modulo $N = 3$),

$$\begin{aligned}
&\alpha^\dagger_{L,A}|q_A, q_B\rangle = |q_A + 1, q_B\rangle; \quad \alpha_{L,A}|q_A, q_B\rangle = |q_A - 1, q_B\rangle;\\
&\alpha^\dagger_{R,A}|q_A, q_B\rangle = -e^{-i\frac{2\pi}{N}\left(q_A+\frac{1}{2}\right)}|q_A + 1, q_B\rangle;\\
&\alpha_{R,A}|q_A, q_B\rangle = -e^{+i\frac{2\pi}{N}\left(q_A-\frac{1}{2}\right)}|q_A - 1, q_B\rangle.
\end{aligned} \tag{5.39}$$

$$\begin{aligned}
&\alpha^\dagger_{L,B}|0, q_B\rangle = |0, q_B + 1\rangle; \quad \alpha^\dagger_{L,B}|1, q_B\rangle = e^{-i\frac{2\pi}{N}}|1, q_B + 1\rangle;\\
&\alpha^\dagger_{L,B}|2, q_B\rangle = e^{+i\frac{2\pi}{N}}|2, q_B + 1\rangle;\\
&\alpha_{L,B}|0, q_B\rangle = |0, q_B - 1\rangle; \quad \alpha_{L,B}|1, q_B\rangle = e^{+i\frac{2\pi}{N}}|1, q_B - 1\rangle;\\
&\alpha_{L,B}|2, q_B\rangle = e^{-i\frac{2\pi}{N}}|2, q_B - 1\rangle;\\
&\alpha^\dagger_{R,B}|0, q_B\rangle = -e^{-i\frac{2\pi}{N}\left(q_B+\frac{1}{2}\right)}|0, q_B + 1\rangle;\\
&\alpha^\dagger_{R,B}|1, q_B\rangle = e^{-i\frac{2\pi}{N}} \cdot \left(-e^{-i\frac{2\pi}{N}\left(q_B+\frac{1}{2}\right)}\right)|1, q_B + 1\rangle;\\
&\alpha^\dagger_{R,B}|2, q_B\rangle = e^{+i\frac{2\pi}{N}} \cdot \left(-e^{-i\frac{2\pi}{N}\left(q_B+\frac{1}{2}\right)}\right)|2, q_B + 1\rangle;\\
&\alpha_{R,B}|0, q_B\rangle = -e^{+i\frac{2\pi}{N}\left(q_B-\frac{1}{2}\right)}|0, q_B - 1\rangle;\\
&\alpha_{R,B}|1, q_B\rangle = e^{+i\frac{2\pi}{N}} \cdot \left(-e^{+i\frac{2\pi}{N}\left(q_B-\frac{1}{2}\right)}\right)|1, q_B - 1\rangle;\\
&\alpha_{R,B}|2, q_B\rangle = e^{-i\frac{2\pi}{N}} \cdot \left(-e^{+i\frac{2\pi}{N}\left(q_B-\frac{1}{2}\right)}\right)|2, q_B - 1\rangle.
\end{aligned} \tag{5.40}$$

5.4.2 Model Hamiltonian

Physically, we consider the experimental setup consisting of two weakly coupled topological wires each supporting two edge parafermions obeying the algebra of $N = 3$ (see Fig. 5.4). We can only allow tunneling processes that conserve q_{total}, since q is associated with the total charge of each wire (in units of $e/3$). In the two-wire system, fractional charge can tunnel between wires, but the total charge (modulo $2e$) must be conserved. Because the overlaps between these zero-energy states are finite, generically there exist appreciable tunneling amplitudes among the four parafermions. Furthermore, we will suppose that it is feasible to make one of the tunneling amplitudes time varying. In the absence of dissipation, this time-varying coupling can be used to probe generalized parity conservation, by noting that a time-varying coupling between the

left pair of parafermions induces time-dependence in the autocorrelation function of the right pair.

The model Hamiltonian can thus be written as

$$\begin{aligned} H_{\text{para}} &= t_A(t)\alpha^\dagger_{L,A}\alpha_{R,A} + t^*_A(t)\alpha^\dagger_{R,A}\alpha_{L,A} + t_B\alpha^\dagger_{L,B}\alpha_{R,B} + t^*_B\alpha^\dagger_{R,B}\alpha_{L,B} \\ &+ t_{s,L}\alpha^\dagger_{L,A}\alpha_{L,B} + t^*_{s,L}\alpha^\dagger_{L,B}\alpha_{L,A} + t_{s,R}\alpha^\dagger_{R,A}\alpha_{R,B} + t^*_{s,R}\alpha^\dagger_{R,B}\alpha_{R,A} \\ &+ t_p\alpha^\dagger_{L,A}\alpha^\dagger_{R,A}\alpha_{R,B}\alpha_{L,B} + t^*_p\alpha^\dagger_{L,B}\alpha^\dagger_{R,B}\alpha_{R,A}\alpha_{L,A} \\ &+ t'_p\alpha^\dagger_{L,A}\alpha^\dagger_{R,B}\alpha_{R,A}\alpha_{L,B} + t'^*_p\alpha^\dagger_{L,B}\alpha^\dagger_{R,A}\alpha_{R,B}\alpha_{L,A}, \end{aligned} \tag{5.41}$$

where $t_A(t) = t_A(0)\cos(\omega_A t + \delta_A)$. All the other parameters are assumed to be independent of time. First, by directly using Eqs. (5.39) and (5.40), we can derive that

$$\langle q_A, q_B|\alpha^\dagger_{L,A}\alpha_{R,A}|q_A, q_B\rangle = -e^{+i\frac{2\pi}{N}\left(q_A-\frac{1}{2}\right)};\;\; \langle q_A, q_B|\alpha^\dagger_{L,B}\alpha_{R,B}|q_A, q_B\rangle = -e^{+i\frac{2\pi}{N}\left(q_B-\frac{1}{2}\right)}. \tag{5.42}$$

Eq. (5.42) is valid for arbitrary parafermion systems; however, here we will specialize to the case $N = 3$. In this case the remaining matrix elements are:

$$\begin{aligned} &\langle 1,2|\alpha^\dagger_{L,A}\alpha_{L,B}|0,0\rangle = 1;\;\; \langle 1,0|\alpha^\dagger_{L,A}\alpha_{L,B}|0,1\rangle = 1;\;\; \langle 1,1|\alpha^\dagger_{L,A}\alpha_{L,B}|0,2\rangle = 1; \\ &\langle 2,2|\alpha^\dagger_{L,A}\alpha_{L,B}|1,0\rangle = e^{+i\frac{2\pi}{N}};\;\; \langle 2,0|\alpha^\dagger_{L,A}\alpha_{L,B}|1,1\rangle = e^{+i\frac{2\pi}{N}}; \\ &\langle 2,1|\alpha^\dagger_{L,A}\alpha_{L,B}|1,2\rangle = e^{+i\frac{2\pi}{N}}; \\ &\langle 0,2|\alpha^\dagger_{L,A}\alpha_{L,B}|2,0\rangle = e^{-i\frac{2\pi}{N}};\;\; \langle 0,0|\alpha^\dagger_{L,A}\alpha_{L,B}|2,1\rangle = e^{-i\frac{2\pi}{N}}; \\ &\langle 0,1|\alpha^\dagger_{L,A}\alpha_{L,B}|2,2\rangle = e^{-i\frac{2\pi}{N}}. \end{aligned} \tag{5.43}$$

$$\begin{aligned} &\langle 1,2|\alpha^\dagger_{R,A}\alpha_{R,B}|0,0\rangle = e^{-i\frac{2\pi}{N}};\;\; \langle 1,0|\alpha^\dagger_{R,A}\alpha_{R,B}|0,1\rangle = 1; \\ &\langle 1,1|\alpha^\dagger_{R,A}\alpha_{R,B}|0,2\rangle = e^{+i\frac{2\pi}{N}}; \\ &\langle 2,2|\alpha^\dagger_{R,A}\alpha_{R,B}|1,0\rangle = e^{-i\frac{2\pi}{N}};\;\; \langle 2,0|\alpha^\dagger_{R,A}\alpha_{R,B}|1,1\rangle = 1; \\ &\langle 2,1|\alpha^\dagger_{R,A}\alpha_{R,B}|1,2\rangle = e^{+i\frac{2\pi}{N}}; \\ &\langle 0,2|\alpha^\dagger_{R,A}\alpha_{R,B}|2,0\rangle = e^{-i\frac{2\pi}{N}};\;\; \langle 0,0|\alpha^\dagger_{R,A}\alpha_{R,B}|2,1\rangle = 1; \\ &\langle 0,1|\alpha^\dagger_{R,A}\alpha_{R,B}|2,2\rangle = e^{+i\frac{2\pi}{N}}. \end{aligned} \tag{5.44}$$

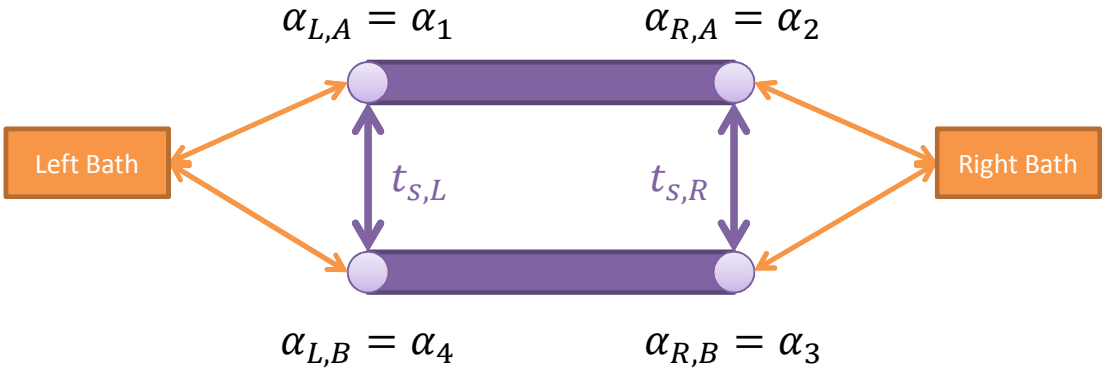

Figure 5.4: The schematic of the setup we theoretically modeled. The two purple rods represent the coupled wire system, where each rod carries two edge parafermionic zero modes denoted by the light purple circles. We label the four parafermionic operators in a clockwise way. There also exist single-particle and pair-hopping tunnelings at the edges of the wires. To mimic the dissipation effects, we further couple the wire system to the left and right electronic baths.

$$
\begin{aligned}
&\langle 2,1|\alpha^\dagger_{L,A}\alpha^\dagger_{R,A}\alpha_{R,B}\alpha_{L,B}|0,0\rangle = e^{+i\frac{2\pi}{N}};\ \langle 2,2|\alpha^\dagger_{L,A}\alpha^\dagger_{R,A}\alpha_{R,B}\alpha_{L,B}|0,1\rangle = e^{-i\frac{2\pi}{N}};\\
&\langle 2,0|\alpha^\dagger_{L,A}\alpha^\dagger_{R,A}\alpha_{R,B}\alpha_{L,B}|0,2\rangle = 1;\\
&\langle 0,1|\alpha^\dagger_{L,A}\alpha^\dagger_{R,A}\alpha_{R,B}\alpha_{L,B}|1,0\rangle = e^{-i\frac{2\pi}{N}};\ \langle 0,2|\alpha^\dagger_{L,A}\alpha^\dagger_{R,A}\alpha_{R,B}\alpha_{L,B}|1,1\rangle = 1;\\
&\langle 0,0|\alpha^\dagger_{L,A}\alpha^\dagger_{R,A}\alpha_{R,B}\alpha_{L,B}|1,2\rangle = e^{+i\frac{2\pi}{N}};\\
&\langle 1,1|\alpha^\dagger_{L,A}\alpha^\dagger_{R,A}\alpha_{R,B}\alpha_{L,B}|2,0\rangle = 1;\ \langle 1,2|\alpha^\dagger_{L,A}\alpha^\dagger_{R,A}\alpha_{R,B}\alpha_{L,B}|2,1\rangle = e^{+i\frac{2\pi}{N}};\\
&\langle 1,0|\alpha^\dagger_{L,A}\alpha^\dagger_{R,A}\alpha_{R,B}\alpha_{L,B}|2,2\rangle = e^{-i\frac{2\pi}{N}}.
\end{aligned}
\tag{5.45}
$$

$$
\begin{aligned}
&\langle 0,0|\alpha^\dagger_{L,A}\alpha^\dagger_{R,B}\alpha_{R,A}\alpha_{L,B}|0,0\rangle = e^{+i\frac{2\pi}{N}};\ \langle 0,1|\alpha^\dagger_{L,A}\alpha^\dagger_{R,B}\alpha_{R,A}\alpha_{L,B}|0,1\rangle = 1;\\
&\langle 0,2|\alpha^\dagger_{L,A}\alpha^\dagger_{R,B}\alpha_{R,A}\alpha_{L,B}|0,2\rangle = e^{-i\frac{2\pi}{N}};\\
&\langle 1,0|\alpha^\dagger_{L,A}\alpha^\dagger_{R,B}\alpha_{R,A}\alpha_{L,B}|1,0\rangle = e^{-i\frac{2\pi}{N}};\ \langle 1,1|\alpha^\dagger_{L,A}\alpha^\dagger_{R,B}\alpha_{R,A}\alpha_{L,B}|1,1\rangle = e^{+i\frac{2\pi}{N}};\\
&\langle 1,2|\alpha^\dagger_{L,A}\alpha^\dagger_{R,B}\alpha_{R,A}\alpha_{L,B}|1,2\rangle = 1;\\
&\langle 2,0|\alpha^\dagger_{L,A}\alpha^\dagger_{R,B}\alpha_{R,A}\alpha_{L,B}|2,0\rangle = 1;\ \langle 2,1|\alpha^\dagger_{L,A}\alpha^\dagger_{R,B}\alpha_{R,A}\alpha_{L,B}|2,1\rangle = e^{-i\frac{2\pi}{N}};\\
&\langle 2,2|\alpha^\dagger_{L,A}\alpha^\dagger_{R,B}\alpha_{R,A}\alpha_{L,B}|2,2\rangle = e^{+i\frac{2\pi}{N}}.
\end{aligned}
\tag{5.46}
$$

With the above matrix elements, we can construct the Hamiltonian matrix of H_{para} accordingly.

To incorporate the dissipations, we further add the couplings between the two-wire system

and the external fermion baths to H_{para}. The dissipative terms are as follows,

$$\begin{aligned}\delta H_{AB} = &\sum_{\varepsilon_L}\left(\tau_L\alpha^\dagger_{L,A}f_{L,\varepsilon_L} + \tau^*_L f^\dagger_{L,\varepsilon_L}\alpha_{L,A} + \tau_L\alpha^\dagger_{L,B}f_{L,\varepsilon_L} + \tau^*_L f^\dagger_{L,\varepsilon_L}\alpha_{L,B}\right)\\ &+\sum_{\varepsilon_R}\left(\tau_R\alpha^\dagger_{R,A}f_{R,\varepsilon_R} + \tau^*_R f^\dagger_{R,\varepsilon_R}\alpha_{R,A} + \tau_R\alpha^\dagger_{R,B}f_{R,\varepsilon_R} + \tau^*_R f^\dagger_{R,\varepsilon_R}\alpha_{R,B}\right) + H_{\text{bath}},\end{aligned} \tag{5.47}$$

where f and $f^\dagger$ are creation and annihilation operators for bath particles with charge $2e/3$ (such that the total charge is conserved) with the excitation energy indices ε. Here we will treat these as fermions for simplicity, though in practice they must arise from strong correlations to carry fractional charge, so this is necessarily an approximation. In comparison, unlike the Majorana case we do not include terms like $f^\dagger\alpha^\dagger$ in Eq. (5.47), which would conserve charge only mod $4e/3$, rather than mod $2e$. (Violating charge mod $2e$ is allowed in the presence of a bulk superconductor, whereas violating charge conservation mod $4e/3$ is not allowed.)

5.4.3 The master equation

As briefly introduced in Section 5.2, the Schrödinger equation for the time evolution of the density matrix $\rho(t)$ in the integro-differential form is known as the master equation (see Eq. (5.2)). Explicitly, the master equation for the present case has the following form,

$$\begin{aligned}\frac{d}{dt}\rho(t) = &-\frac{i}{\hbar}[H_{\text{para}},\rho(t)] + \frac{1}{\hbar^2}\sum_{\Omega}\sum_{\alpha,\beta}\Gamma_{\alpha\beta}(\Omega)A_\beta(\Omega)\rho(t)A^\dagger_\alpha(\Omega)\\ &-\frac{1}{2\hbar^2}\sum_{\Omega}\sum_{\alpha,\beta}\Gamma_{\alpha\beta}(\Omega)\{A^\dagger_\alpha(\Omega)A_\beta(\Omega),\rho(t)\}.\end{aligned} \tag{5.48}$$

The derivation of this equation is completely parallel to that in Section 5.3 on deriving the master equation for the Majorana wires. Following the same steps we used to derive the results there, we find the second term on the right-hand side of Eq. (5.48) assumes the form ($\hbar = 1, \tau_L = \tau_R = \tau$),

$$\begin{aligned}&\frac{1}{\hbar^2}\sum_{\Omega}\sum_{\alpha,\beta}\Gamma_{\alpha\beta}(\Omega)A_\beta(\Omega)\rho(t)A^\dagger_\alpha(\Omega)\\ &\quad=\Gamma\sum_{a,b;a',b'}n_F(-\hbar\omega_{ba})\delta(\omega_{a'b'}-\omega_{ba})\times|a\rangle\langle a|A_\beta|b\rangle\langle b|\rho(t)|a'\rangle\langle a'|A^\dagger_\alpha|b'\rangle\langle b'|.\end{aligned} \tag{5.49}$$

Similarly, the third term on the right-hand side of Eq. (5.48) can be reformulated as

$$
\begin{aligned}
&-\frac{1}{2\hbar^2}\sum_{\Omega}\sum_{\alpha,\beta}\Gamma_{\alpha\beta}(\Omega)\{A_\alpha^\dagger(\Omega)A_\beta(\Omega),\rho(t)\} \\
&\quad=-\frac{\Gamma}{2}\sum_{a,b,b'}n_F(-\hbar\omega_{ab})\delta(\omega_{b'b}-\omega_{ab}) \\
&\quad\times\{|a\rangle\langle a|A_\alpha^\dagger|b\rangle\langle b|A_\beta|b'\rangle\langle b'|\rho(t)+\rho(t)|a\rangle\langle a|A_\alpha^\dagger|b\rangle\langle b|A_\beta|b'\rangle\langle b'|\}. \qquad (5.50)
\end{aligned}
$$

Here $\Gamma=\frac{|\tau|^2\cdot 2\pi\rho}{\hbar^2}$ is the strength of the dissipative coupling to the baths, and the states $|a\rangle$ represent the original basis vectors $|q_A,q_B\rangle$ with the correspondence that

$$
\begin{aligned}
&|0,0\rangle\rightarrow|1\rangle,\ |0,1\rangle\rightarrow|2\rangle,\ |0,2\rangle\rightarrow|3\rangle, \\
&|1,0\rangle\rightarrow|4\rangle,\ |1,1\rangle\rightarrow|5\rangle,\ |1,2\rangle\rightarrow|6\rangle, \\
&|2,0\rangle\rightarrow|7\rangle,\ |2,1\rangle\rightarrow|8\rangle,\ |2,2\rangle\rightarrow|9\rangle. \qquad (5.51)
\end{aligned}
$$

Inspection of Eq. (5.47) tells that we would have the following 16 possible terms. They are

$$
\begin{aligned}
&1^\circ\ A_\alpha=\alpha_{L,A};\quad A_\beta=\alpha_{L,A}; && 9^\circ\ A_\alpha=\alpha_{L,A};\quad A_\beta=\alpha_{L,B}; \\
&2^\circ\ A_\alpha=\alpha_{L,A}^\dagger;\quad A_\beta=\alpha_{L,A}^\dagger; && 10^\circ\ A_\alpha=\alpha_{L,B};\quad A_\beta=\alpha_{L,A}; \\
&3^\circ\ A_\alpha=\alpha_{R,A};\quad A_\beta=\alpha_{R,A}; && 11^\circ\ A_\alpha=\alpha_{L,A}^\dagger;\quad A_\beta=\alpha_{L,B}^\dagger; \\
&4^\circ\ A_\alpha=\alpha_{R,A}^\dagger;\quad A_\beta=\alpha_{R,A}^\dagger; && 12^\circ\ A_\alpha=\alpha_{L,B}^\dagger;\quad A_\beta=\alpha_{L,A}^\dagger; \\
&5^\circ\ A_\alpha=\alpha_{L,B};\quad A_\beta=\alpha_{L,B}; && 13^\circ\ A_\alpha=\alpha_{R,A};\quad A_\beta=\alpha_{R,B}; \\
&6^\circ\ A_\alpha=\alpha_{L,B}^\dagger;\quad A_\beta=\alpha_{L,B}^\dagger; && 14^\circ\ A_\alpha=\alpha_{R,B};\quad A_\beta=\alpha_{R,A}; \\
&7^\circ\ A_\alpha=\alpha_{R,B};\quad A_\beta=\alpha_{R,B}; && 15^\circ\ A_\alpha=\alpha_{R,A}^\dagger;\quad A_\beta=\alpha_{R,B}^\dagger; \\
&8^\circ\ A_\alpha=\alpha_{R,B}^\dagger;\quad A_\beta=\alpha_{R,B}^\dagger; && 16^\circ\ A_\alpha=\alpha_{R,B}^\dagger;\quad A_\beta=\alpha_{R,A}^\dagger; \qquad (5.52)
\end{aligned}
$$

which are different from the case of coupled Majorana wires, since in Eq. (5.47) there do not exist the terms like $f^\dagger\alpha^\dagger$ or $f\alpha$. Under the above-defined ordered basis states $|a\rangle$ and by using Eqs. (5.39) and (5.40), we can construct the matrix representations for the four parafermion

operators $\alpha_{L/R,A/B}$ as follows,

$$\alpha_{L,A} = \begin{pmatrix} 0 & 0 & 0 & 1 & 0 & 0 & 0 & 0 & 0 \\ 0 & 0 & 0 & 0 & 1 & 0 & 0 & 0 & 0 \\ 0 & 0 & 0 & 0 & 0 & 1 & 0 & 0 & 0 \\ 0 & 0 & 0 & 0 & 0 & 0 & 1 & 0 & 0 \\ 0 & 0 & 0 & 0 & 0 & 0 & 0 & 1 & 0 \\ 0 & 0 & 0 & 0 & 0 & 0 & 0 & 0 & 1 \\ 1 & 0 & 0 & 0 & 0 & 0 & 0 & 0 & 0 \\ 0 & 1 & 0 & 0 & 0 & 0 & 0 & 0 & 0 \\ 0 & 0 & 1 & 0 & 0 & 0 & 0 & 0 & 0 \end{pmatrix}, \tag{5.53}$$

$$\alpha_{R,A} = \begin{pmatrix} 0 & 0 & 0 & -e^{\frac{i\pi}{3}} & 0 & 0 & 0 & 0 & 0 \\ 0 & 0 & 0 & 0 & -e^{\frac{i\pi}{3}} & 0 & 0 & 0 & 0 \\ 0 & 0 & 0 & 0 & 0 & -e^{\frac{i\pi}{3}} & 0 & 0 & 0 \\ 0 & 0 & 0 & 0 & 0 & 0 & 1 & 0 & 0 \\ 0 & 0 & 0 & 0 & 0 & 0 & 0 & 1 & 0 \\ 0 & 0 & 0 & 0 & 0 & 0 & 0 & 0 & 1 \\ -e^{-\frac{i\pi}{3}} & 0 & 0 & 0 & 0 & 0 & 0 & 0 & 0 \\ 0 & -e^{-\frac{i\pi}{3}} & 0 & 0 & 0 & 0 & 0 & 0 & 0 \\ 0 & 0 & -e^{-\frac{i\pi}{3}} & 0 & 0 & 0 & 0 & 0 & 0 \end{pmatrix}, \tag{5.54}$$

$$\alpha_{L,B} = \begin{pmatrix} 0 & 1 & 0 & 0 & 0 & 0 & 0 & 0 & 0 \\ 0 & 0 & 1 & 0 & 0 & 0 & 0 & 0 & 0 \\ 1 & 0 & 0 & 0 & 0 & 0 & 0 & 0 & 0 \\ 0 & 0 & 0 & 0 & e^{\frac{2i\pi}{3}} & 0 & 0 & 0 & 0 \\ 0 & 0 & 0 & 0 & 0 & e^{\frac{2i\pi}{3}} & 0 & 0 & 0 \\ 0 & 0 & 0 & e^{\frac{2i\pi}{3}} & 0 & 0 & 0 & 0 & 0 \\ 0 & 0 & 0 & 0 & 0 & 0 & 0 & e^{-\frac{2i\pi}{3}} & 0 \\ 0 & 0 & 0 & 0 & 0 & 0 & 0 & 0 & e^{-\frac{2i\pi}{3}} \\ 0 & 0 & 0 & 0 & 0 & 0 & e^{-\frac{2i\pi}{3}} & 0 & 0 \end{pmatrix}, \tag{5.55}$$

$$\alpha_{R,B} = \begin{pmatrix} 0 & -e^{\frac{i\pi}{3}} & 0 & 0 & 0 & 0 & 0 & 0 & 0 \\ 0 & 0 & 1 & 0 & 0 & 0 & 0 & 0 & 0 \\ -e^{-\frac{i\pi}{3}} & 0 & 0 & 0 & 0 & 0 & 0 & 0 & 0 \\ 0 & 0 & 0 & 0 & 1 & 0 & 0 & 0 & 0 \\ 0 & 0 & 0 & 0 & 0 & e^{\frac{2i\pi}{3}} & 0 & 0 & 0 \\ 0 & 0 & 0 & -e^{\frac{i\pi}{3}} & 0 & 0 & 0 & 0 & 0 \\ 0 & 0 & 0 & 0 & 0 & 0 & 0 & -e^{-\frac{i\pi}{3}} & 0 \\ 0 & 0 & 0 & 0 & 0 & 0 & 0 & 0 & e^{-\frac{2i\pi}{3}} \\ 0 & 0 & 0 & 0 & 0 & 0 & 1 & 0 & 0 \end{pmatrix}, \tag{5.56}$$

which are then inserted into Eqs. (5.49) and (5.50) to generate the explicit form of the coupled first-order differential equations of the density matrix.

Here we numerically solved the coupled differential equations for the 45 complex matrix elements of $\rho(t)$. Moreover, we also need to always check the energy conservation constraints imposed by the δ-functions in Eqs. (5.49) and (5.50).

5.4.4 Numerical results for parafermion setups

We are now ready to use our master equation formalism to investigate theoretically the feasibility of detecting the predicted parafermionic edge zero modes via the finite-frequency response measurements. Specifically, we take t_A to be time-varying, and study the autocorrelation function of the fermion parity in the right wire segment (composed of $\alpha_{R,A}$ and $\alpha_{R,B}$) via examining the dynamics of the resulting Hamiltonian H_{para} (see Eq. (5.41)).

The matrix elements for the Hamiltonian in the $|q_A, q_B\rangle$ basis states are given in Eqs. (5.43)–(5.46). Through numerically diagonalizing the resulting 9×9 matrix, we obtain the exact spectrum of H_{para} as a function of $t_A(t)$. The results are shown in Fig. 5.5, where the nine eigenvalues are grouped according to their total parafermionic numbers by three different colors: The green, blue, and red curves correspond to $q_A + q_B \pmod{N = 3} = 0,\ 1,$ and 2, respectively. In this chapter, we will mainly focus on the effects of the single-particle tunneling between the wires, thus t_p and t'_p are set to be zero in Eq. (5.41). Also we keep $t_A(0) = 2t_B = 15 + 7.5i$. In the left panel of Fig. 5.5, we include both sets of the eigenvalues with (dashed lines) and without (solid lines) the interwire coupling $t_{s,L}$, from which several characteristics of the band structure can be noticed. For the illustration purpose, the dashed lines in the left panel are replotted in

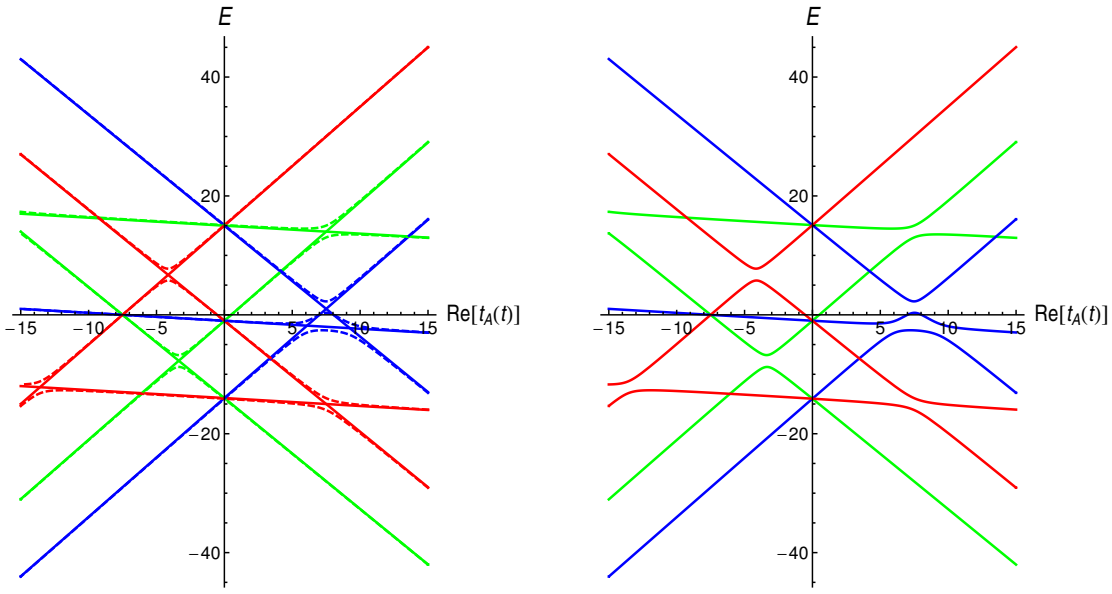

Figure 5.5: The dispersion or band structure of H_{para} (Eq. (5.41)) without the pair-hopping interactions in the basis of $|q_A, q_B\rangle$ is plotted as a function of $\text{Re}[t_A(t)]$, where we choose $t_A(0) = 15 + 7.5i,\ t_B = 7.5 + 3.75i,\ t_{s,R} = 0$. The solid lines in the left panel are the dispersion spectra of $t_{s,L} = 0$. While the dashed lines illustrate the resulting band structure and the avoided crossings when turning on the coupling $t_{s,L} = 2i$, which are represented in the right panel with the solid lines. In both panels, the nine lines are grouped by the total parafermionic number. The green, blue, and red curves correspond to $q_A + q_B \pmod{N = 3} = 0,\ 1,$ and 2, respectively.

the right panel of Fig. 5.5 by solid lines with the same color coding.

(i) Without dissipation, the exact conservation of the total parafermionic number prohibits the gap opening at the crossing of two lines with differing colors even in the presence of finite $t_{s,L}$. See the three unavoided crossings along vertical axes in Fig. 5.5 for instance.

(ii) $t_{s,L}$ opens a gap only at the avoided crossings of two lines with the same color. Around these avoided crossings, although the total parafermionic number is fixed, q_A and q_B are no longer conserved separately. This kind of parafermion-number mixing underpins the proposed parity experiments.

(iii) If we follow the ground state at some value of t_A adiabatically, these avoided crossings ensure that you will end up in an excited state. When $|t_A| > |t_B|$, this excited state has

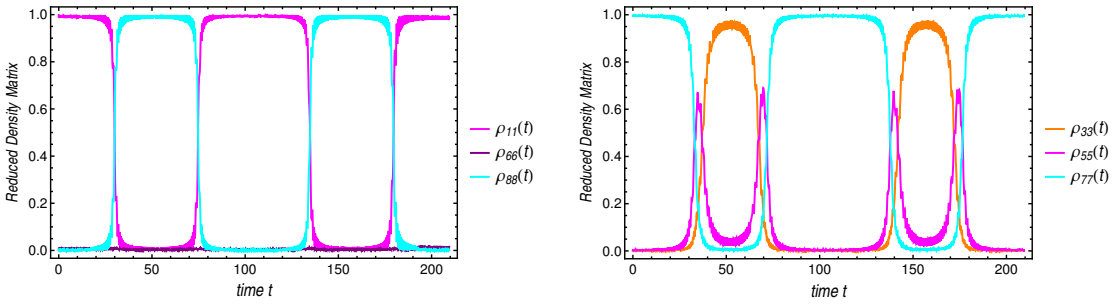

Figure 5.6: The adiabatic evolution of the diagonal elements of the reduced density matrix as a function of time without the dissipative couplings to the external baths. The driving frequency is low ($\omega_A = 0.06$). The phase $\delta_A = 0$ in the left panel, while for the right panel, $\delta_A = \pi$. All the other diagonal elements get vanished. All the parameters are the same as in Fig. 5.5.

approximately the "correct" ground-state eigenvalue for q_A, but has the "wrong" value of q_B.

(iv) There are two types of adiabatic trajectories. The lowest-energy state for $\mathrm{Re}[t_A] > 0$ has an unavoided crossing with one other level, so that if we evolve the system adiabatically from this ground state, it will switch between two states (with different values of (q_A, q_B)). The lowest-energy state for $\mathrm{Re}[t_A] < 0$ has an avoided crossing with two different states. Hence during its adiabatic evolution the system switches between three distinct states. (This is shown in Fig. 5.6.)

(v) By specifically choosing the phase δ_A in $t_A(t)$ or intentionally preparing the initial ground state of the system, we are able to drive the two coupled wires pass through the above-mentioned two different avoided crossings in sequence, and the resulting difference in the evolution of the reduced density matrix is observable (compare the left panel to the right panel in Fig. 5.6).

In a real system where t_A varies sinusoidally in time, the evolution will not be exactly adiabatic. The periodically driven time evolution of $t_A(t)$ will give rise to the non-adiabatic tunneling of the system across the avoided crossing. The probability that a non-adiabatic transition can take place is given by the Landau–Zener formula, which states that the probability of non-adiabatic tunneling will be exponentially suppressed if we increase the opened gap amplitude and/or decrease the driving frequency. To incorporate these effects, we numerically evaluate

the density matrix $\rho_{AB}(t)$ of the wire system. The time evolution of its diagonal matrix elements gives the probability of finding the system in each of the nine states at time t. Here we always construct the initial density matrix $\rho_{AB}(0)$ from the ground state of H_{para}, and by setting the phase δ_A, typically we could start either from the ground state at the bottom right corner ($\delta_A = 0$) or bottom left corner ($\delta_A = \pi$) of the band structure (see the right panel of Fig. 5.5). To set the stage, we first switch off the dissipative couplings to the baths for simplicity. Through numerically solving the reduced von Neumann equation, $i\hbar\frac{d}{dt}\rho_{AB}(t) = [H_{\text{para}}(t),\ \rho_{AB}(t)]$, we obtain the time evolution for each of the two choices of δ_A, which are presented in Fig. 5.6. Here the driving frequency is pretty low ($\omega_A = 0.06$), so that the evolution is nearly adiabatic. From the left panel, we see that if we start from the state $|0,0\rangle$, the nearly adiabatic evolution of $\rho_{AB}(t)$ will lead to the periodic exchange of the weights between states $|0,0\rangle$ and $|2,1\rangle$, which correspond to $\rho_{11}(t)$ and $\rho_{88}(t)$, respectively. This phenomenon is understandable by noticing that after passing through the avoided crossing of the two lowest green lines in Fig. 5.5, the dominant component of the system ground state is changed from $|0,0\rangle$ to $|2,1\rangle$. Thus, though we only periodically drive the tunneling amplitude of unpaired parafermions in wire A, the conservation of $q_A + q_B$ allows to measure the periodic change or response of q_B at the other wire B. Similar considerations also apply to the case of $\delta_A = \pi$, where we initially start from the state $|2,0\rangle$ and adiabatically pass through the state $|1,1\rangle$ and $|0,2\rangle$ subsequently, then switch back and forth. This leads to the results in the right panel of Fig. 5.6.

To incorporate the dissipations, we further add the couplings between the wire system and the external fermion baths to H_{para}. As discussed in Subsection 5.4.3, the effects of the dissipative coupling (5.47) are captured by the master equation (5.48) with Lindblad operators (5.52). Generally, depending on the time scales of the driving frequency, the parafermionic life time, and the magnitude of the energy gap, there might exist several distinct parameter regimes where the behaviors of $\rho_{ii}(t)$ are quite different. If the frequency is too high, there will be lots of Landau–Zener tunneling, which obscures the oscillations. However, if the frequency is too low relative to the parity lifetime (i.e. the time-scale for relaxation processes mediated by the coupling to the bath), then the system will relax to equilibrium too fast for the oscillations to be visible. Here we consider the case where the parity lifetime is long enough that the frequency can be low relative to the gaps in the spectrum, but fast compared to the relaxation rate. Typical numerical results with the same set of parameters as in Fig. 5.6 are plotted in Fig. 5.7, where we only concentrate on the high-temperature and weak coupling limit. Since charged fermions can

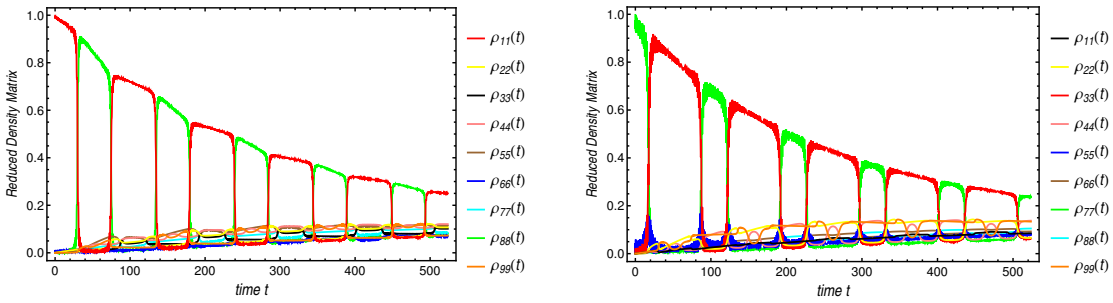

Figure 5.7: Time evolution of the reduced density matrix in the presence of dissipative couplings to the external baths. Here we only consider the high-temperature and weak coupling limit. The phase $\delta_A = 0$ in the left panel, while for the right panel, $\delta_A = \pi$. All the parameters are the same as in Fig. 5.6.

tunnel into the wire system, the exact conservation of the total parafermionic number is broken. Moreover, the stochastic jump or tunneling between different energy levels will also allow the wire system to reside in the excitation states with finite probability. In the long time limit, the system will eventually approach the equilibrium state with the equal probability ($\rho_{ii} = \frac{1}{9}$) to be in any of the nine basis states $|q_A, q_B\rangle$. Therefore, besides the driven oscillations, the amplitudes of ρ_{ii} will follow an exponential envelope with some time constant.

In order to see effect of parity conservation (i.e. the oscillations in q_B as t_A varies), it is sufficient to measure the autocorrelation function for the parafermionic number q_B in wire B, which is more practical experimentally. To do this we employ the quantum regression theorem to extract the necessary information from the time evolution of $\rho(t)$. By following a completely analogous derivation of the master equation, the required two-time average of the two system operators $\hat{O}_1(t+\tau)$ and $\hat{O}_2(t)$ $(\tau > 0)$ in the Heisenberg representation can be evaluated according to the quantum regression formula,

$$\langle \hat{O}_1(t+\tau)\hat{O}_2(t)\rangle = \mathrm{Tr}_S\left\{\hat{O}_1(0)e^{\int_t^{t+\tau}\hat{\mathcal{L}}(t')dt'}[\hat{O}_2(0)\rho(t)]\right\}. \tag{5.57}$$

Basically, we first project the initial density matrix onto the state of equal superposition of the three basis vectors with the same specified value of q_B, then after evolving the matrix $q_B\rho_{AB}(0)$ in time according to the master equation, we finally project the resulting matrix back to q_B at time t so as to measure the autocorrelation functions

$$C_{q_B}(t) = \left\langle \cos\left(\frac{2\pi}{3}(q_B(t)-\frac{1}{2})\right)\cdot\cos\left(\frac{2\pi}{3}(q_B(0)-\frac{1}{2})\right)\right\rangle. \tag{5.58}$$

The generic profiles of the autocorrelation functions are presented in Fig. 5.8, where we examine all the three possible values of $q_B(0)$. Starting from the specific initial mixture of three basis states, we can qualitatively understand the time evolutions of these autocorrelation functions by closely following the resulting trajectories in the band structure adiabatically (see the dashed lines in Fig. 5.5). Typically, for one approximate period, when passing through the avoided crossing, the dominant weights of the state will be switched, which leads to a change (either decrease or increase) in the autocorrelation function. One interesting part of this evolution is the possibility of switching back and forth to part of the initial state within half of the period, which gives rise to the appreciable peak at the middle of a complete sweep (see the left and right panels in Fig. 5.8). Since we are taking $1/3, 1/3, 1/3$ for the relative weights of the three states with the same q_B, we are effectively measuring q_B in a thermal state. Although the system starts at thermal equilibrium, by using a measurement to project onto definite q_B, we can still see the oscillations.

5.5 Summary and Outlook

In this chapter, we theoretically extend the proposed Majorana parity measurements to the more general parafermionic systems and for the special case of $N = 3$, we calculate the reduced density matrix and the autocorrelation functions of a particular dynamical setup that can be useful to characterize the properties associated with the parafermionic zero modes. Our major numerical results are consistent with previous studies on the coupled Majorana wires. The present work raises several questions that are important to fully understanding the dynamics

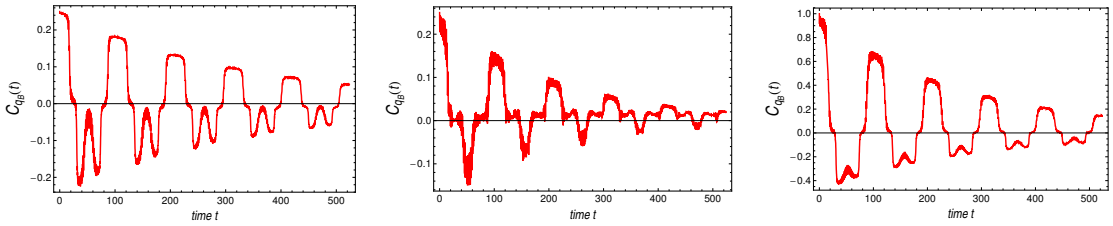

Figure 5.8: Time evolutions of the autocorrelation functions in the presence of dissipative couplings to the external baths. Here we only consider the high-temperature and weak coupling limit. The initial values of $q_B(0) = 0,\ 1,\ 2$ in the left, middle, and right panel, respectively. Namely, for $q_B = 0$, we set $\rho_{11} = \rho_{44} = \rho_{77} = 1/3$; for $q_B = 1$, we set $\rho_{22} = \rho_{55} = \rho_{88} = 1/3$; for $q_B = 2$, we set $\rho_{33} = \rho_{66} = \rho_{99} = 1/3$. All the parameters are the same as in Fig. 5.7.

of parafermion systems created from fractional quantum Hall systems. First, we assumed that the bath was fermionic; really the fractionally charged particles in the bath must come from the strongly interacting FQHE bulk, and are not fermions. Investigating what impact this has on dynamics is one interesting direction to pursue. Second, we have not attempted to derive realistic microscopic model of the coupling between the system and the bath. Since the strength of this coupling sets the scale for the parafermions' autocorrelation time, this calculation is also an important open direction. Finally, we have assumed values for the intrawire couplings $t_A,\ t_B$, but have not established realistic values, or whether these could be tuned as a function of time. In Chapter 6 we will discuss the origins of these couplings in detail, and derive their precise forms.

Another possible future direction is to look for other distinctive signatures of parafermion bound states. It is worth emphasizing here two unique features of the $N = 3$ model Hamiltonian of these four parafermions, which are absent from the $N = 2$ case (the coupled Majorana wires). The first point is obvious. Because now the parafermion operators are no longer self-conjugate ($\alpha_j^\dagger = \alpha_j^2$), the tunneling integrals between them can be complex variables in general, which might be useful to lift the degeneracy in the resulting spectra (the exact forms of these tunneling parameters should largely depend on the overlaps of the zero-energy wavefunctions). The second point concerns the attainable tunneling patterns between the two parafermion wires. It can be shown that the aforementioned algebra of the parafermionic operators admits the pair-hopping terms when two wires are put close enough in parallel.

$$\begin{aligned} H_{\text{pair-hopping}} = {} & t_p \alpha_{L,A}^\dagger \alpha_{R,A}^\dagger \alpha_{R,B} \alpha_{L,B} + t_p^* \alpha_{L,B}^\dagger \alpha_{R,B}^\dagger \alpha_{R,A} \alpha_{L,A} \\ & + t_p' \alpha_{L,A}^\dagger \alpha_{R,B}^\dagger \alpha_{R,A} \alpha_{L,B} + t_p'^* \alpha_{L,B}^\dagger \alpha_{R,A}^\dagger \alpha_{R,B} \alpha_{L,A}. \end{aligned}$$

Thus ideally we would have both single-particle tunnelings and pair-hopping terms as the two possible couplings between the parafermion wire segments, which might provide other signatures that are distinctive in these systems.

Chapter 6

Tunable Splitting of the Ground-State Degeneracy in Quasi-1D Parafermion Systems

6.1 Motivation and outline

Although systems with topologically protected ground-state degeneracies are currently of great interest due to their potential applications in quantum computing, in practice this degeneracy is never exact, and the magnitude of the ground-state degeneracy splitting imposes constraints on the timescales over which information is topologically protected. In this chapter we use an instanton approach to evaluate the splitting of topological ground-state degeneracy in quasi-1D systems with parafermion zero modes, in the specific case where parafermions are realized by inducing a superconducting gap in pairs of fractional quantum Hall (FQH) edges. We show that, like 1D topological superconducting wires, this splitting has an oscillatory dependence on the chemical potential, which arises from an intrinsic Berry phase that produces interference between distinct instanton tunneling events. These Berry phases can be mapped to chiral phases in a dual quantum clock model using a Fradkin–Kadanoff transformation. Comparing our low-energy spectrum to that of phenomenological parafermion models allows us to evaluate the real and imaginary parts of the hopping integral between adjacent parafermionic zero modes as functions of the chemical potential.

Parafermion bound states [8–12, 107–112], which have k ($k > 2$) topologically degenerate ground states, are particularly promising for quantum computing applications: In comparison to Majorana bound states ($k = 2$), parafermion bound states allow for a denser (albeit non-universal) set of computational gates, and are believed to be intrinsically more robust to environmental noise [9–11, 113]. Parafermions are significantly more challenging to produce than their Majorana counterparts: Most proposals entail generating them as defects in 2D Abelian FQH states, in ways that have yet to be carried out experimentally. (There have been some progress in bilayer graphene where at least QHE has been induced [114].) However, their non-Abelian statistics are also more complex than for Majoranas, which makes realizing them a particularly exciting prospect. It is noteworthy that parafermions cannot be realized in strictly 1D wire models according to the results by Refs. [97, 115].

For bound states confined to the endpoints of a system of finite length L, the topological ground-state degeneracy is split by an amount $\Delta E \sim e^{-L/\xi}$, where ξ is proportional to the correlation length in the bulk of the system, causing superpositions of ground states to decohere over time. Though theoretically it is possible to make this splitting as small as required by making L large, there are definite advantages when this splitting can be made small even for modest-length systems. For 1D topological superconducting wires [77, 116] or spin-Hall based superconductors [20, 117], this can be achieved by small adjustments in the appropriate chemical potential, since in addition to the exponential falloff in L the splitting has an oscillatory dependence on the Fermi momentum via $\Delta E \sim e^{-L/\xi} \cos(k_F L)$. The observed oscillations of the splitting of the zero-bias conductance peaks [31] can be viewed as evidence of Majorana bound states [77, 116, 118–120].

Despite the publicity it has had in Majorana systems [121–124], little attention has been given to the ground-state splitting in parafermion systems. Specifically, one might wonder whether these exhibit an analogue of the oscillatory $\cos(k_F L)$ term. In this chapter, we calculate the splitting of the topological ground-state degeneracy in parafermion platforms obtained by inducing superconductivity or ferromagnetism at certain types of edges in FQH states [9–12, 108, 109]. Following Ref. [77] in the Majorana case, we perform this calculation using a bosonized description of the strongly interacting 1D system, in which the splitting of the ground-state degeneracy is obtained by an instanton calculation in the resulting sine-Gordon model. Interestingly, as in the Majorana case we do find oscillations in the splitting as functions of chemical potential or applied magnetic field. These intriguing oscillations result from

a Berry phase term in the generic sine-Gordon action. We also use our calculation to deduce the magnitude and phase of the hopping coefficients that arise most naturally in parafermion chains, such as those studied by Refs. [8, 59, 108, 125–127].

6.2 Model of parafermion zero modes

Several groups [9–12, 108, 109] have suggested that parafermion zero modes can be generated in experimentally relevant architectures with counterpropagating chiral edges separating two FQH regions with opposite g-factors. The edge of interest consists of one right-moving and one left-moving mode with opposite spin polarizations from the adjacent 2D FQH fluids. Through proximity effects, two types of electron tunneling processes can open a gap at this edge: Inducing superconductivity (SC) generates a Cooper pairing $\Delta(\psi^\dagger_{L,\downarrow}\psi^\dagger_{R,\uparrow} + \text{H.c.})$, while spin backscattering $\mathcal{B}(\psi^\dagger_{L,\downarrow}\psi_{R,\uparrow} + \text{H.c.})$ can be induced by tunnel-coupling the edge to a ferromagnet (FM). Because the total charge in the middle SC region is conserved modulo $2e$, while the underlying elementary excitations carry the fractionalized $\frac{e}{n}$-charges owing to the strong correlation, there will be $2n$ degenerate ground states with differing (generalized) fermion charge parities. This emergent ground-state manifold is characterized by the interfacial parafermion zero modes that are localized at the domain walls separating the SC and FM regions, as is illustrated in Fig. 6.1. In principle, any interface between these different types of induced gaps will host parafermion bound states.

As we did in Chapter 4, we will find it convenient to express the fermion operators in our 1D system in terms of bosonic operators, via:

$$\psi^\dagger_{R/L} \sim \frac{1}{\sqrt{2\pi n\varsigma}} e^{-in\varphi_{R/L}},$$

where $\varphi_{R/L}$ are right (R) or left (L) moving bosonic fields, and $\nu = 1/n$ is the filling fraction of the corresponding FQH bulk regions. Here ς is related to the inverse energy cutoff (E_{cutoff}) of the bosonized theory via $\varsigma \sim v\hbar/E_{\text{cutoff}}$, where v is the velocity of the edge modes.

The two backscattering terms are most simply expressed in the basis $\phi = \frac{1}{2}(\varphi_{R,\uparrow} + \varphi_{L,\downarrow})$ and $\theta = \frac{1}{2}(\varphi_{R,\uparrow} - \varphi_{L,\downarrow})$. These nonchiral fields are related to the charge density ρ_C and spin density ρ_S via $\rho_C = \frac{1}{\pi}\partial_x\theta$ and $\rho_S = \frac{1}{\pi}\partial_x\phi$. In this bosonized basis, the two backscattering terms take the form $\Delta(\psi^\dagger_{L,\downarrow}\psi^\dagger_{R,\uparrow} + \text{H.c.}) \sim \Delta\sin(2n\phi)$ and $\mathcal{B}(\psi^\dagger_{L,\downarrow}\psi_{R,\uparrow} + \text{H.c.}) \sim \mathcal{B}\sin(2n\theta)$, and the 1D parafermion system is described by the following Euclidean sine-Gordon action

[9–12, 98, 108, 128, 129]:

$$S_E = \int d\tau dx \left\{ i\hbar \frac{n}{\pi} \partial_x \theta(x,\tau) \partial_\tau \phi(x,\tau) - \frac{\mu(x)}{\pi} \partial_x \theta(x,\tau) \right. \\ + \frac{\hbar n v}{2\pi} (\partial_x \theta(x,\tau))^2 + \frac{\mathcal{B}(x)}{\pi n \varsigma} [\sin(2n\theta(x,\tau)) + 1] \\ \left. + \frac{\hbar n v}{2\pi} (\partial_x \phi(x,\tau))^2 + \frac{\Delta(x)}{\pi n \varsigma} [\sin(2n\phi(x,\tau)) + 1] \right\}. \tag{6.1}$$

Here μ represents the chemical potential and $\mathcal{B},\ \Delta$ are energy gaps induced by spin- and charge-backscattering processes, respectively. The commutation relation $[\phi(x), \theta(x')] = i\frac{\pi}{n}\Theta(x - x')$ dictates that only one of the two possible gapping terms can have a nonvanishing expectation value at a given spatial position. However, if a region where $\Delta \sim \hbar v/\varsigma$ can be sandwiched between two regions where $\mathcal{B} \sim \hbar v/\varsigma$, parafermion bound states arise at the interfaces between them. In the bosonized picture, the resulting topological ground-state degeneracy is manifest in the $2n$ values of ϕ for which the sine term is minimized [9–12, 107, 108].

In the following, we consider the FM-SC-FM heterostructure shown in Fig. 6.1, on which we take $\mathcal{B} = 0$ ($\Delta,\ \mu = 0$) in the SC (FM) region $|x| < L/2$ ($|x| > L/2$). In the FM regions $|x| > L/2$, the field θ is therefore pinned to one of the potential minima, and ϕ is strongly fluctuating as required by the commutation relations. We will show that under these conditions the FM regions do not contribute to the ground-state energy splitting, and after integrating out

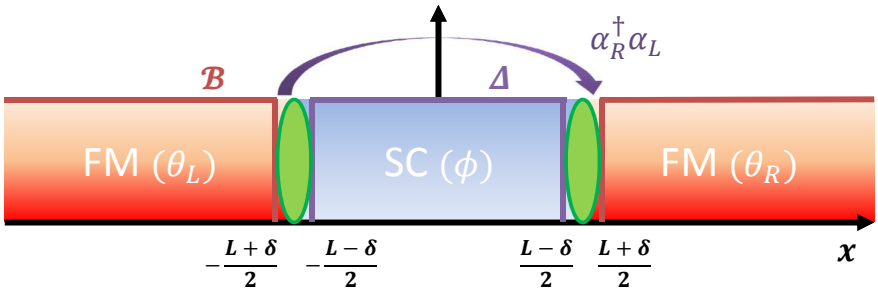

Figure 6.1: The spatial profiles of the proximity-induced gaps $\Delta(x)$ and $\mathcal{B}(x)$ for the FM-SC-FM setup. The two gapped regions are necessarily separated by a domain wall region of width δ that accommodates a parafermionic zero mode denoted by the green ellipse.

θ we obtain the following effective action for the SC region:

$$S_\phi = \int_{-\frac{T_\tau}{2}}^{\frac{T_\tau}{2}} d\tau \int_{-\frac{L}{2}}^{\frac{L}{2}} dx \left\{ \frac{\hbar n}{2\pi v}(\partial_\tau \phi(x,\tau))^2 + \frac{\hbar n v}{2\pi}(\partial_x \phi(x,\tau))^2 + \frac{\Delta}{\pi n \varsigma}[\sin(2n\phi(x,\tau)) + 1] + i\frac{\mu(x)}{\pi v}\partial_\tau \phi(x,\tau) \right\}. \quad (6.2)$$

This is the effective action that we will study to calculate the ground-state splitting. In the ground states of this reduced system the ϕ field is also approximately pinned at one of the $2n$ inequivalent local minima ϕ_{min} of the sine potential; we will take Δ to be sufficiently large that these low-energy states are well separated from the rest of the spectrum. The fluctuation-induced splitting between the $2n$ otherwise degenerate ground states is then determined by the amplitude for tunneling between adjacent local minima. As will be detailed below in Section 6.4, the parafermion hopping operator can be defined as $\alpha_L^\dagger \alpha_R$ ($\alpha_R^\dagger \alpha_L$), which is the translation operator along the ϕ-axis, whose eigenvalue is an exponential function of the momentum conjugate to the operator ϕ, which moves forward (backward) the system's ground state from one minimum of the interaction potential term $\sin(2n\phi)$ to the neighboring one. These processes, in which the expectation of ϕ tunnels between different classical minima, are known as instantons. In the presence of these tunneling processes, the original degenerate ground states become split, and the new good quantum number in the resulting ground-state manifold should be the eigenvalue of the translation operator $\alpha_L^\dagger \alpha_R$ ($\alpha_R^\dagger \alpha_L$) (or equivalently the eigenvalue of the momentum operator conjugate to ϕ).

The last term in Eq. (6.2) will be particularly important in our calculation: It plays the role of a topological Berry phase term $S_{\text{B-p}}$, contributing to the net action only for field configurations which start and end at different values of θ (i.e. only for instantons). It introduces oscillations in the splitting of the ground-state degeneracy as the chemical potential μ is varied. To the best of our knowledge, $S_{\text{B-p}}$ was not included in previous studies of instantons in the bosonized periodic sine-Gordon model, which considered the case $\mu = 0$ [77, 98, 130].

Before evaluating the ground-state splitting, we need to justify the effective action S_ϕ which is our starting point for studying instanton effects in the present chapter. Specifically, we will show that, for a short SC region sandwiched between two long FM regions, the effect of instantons is limited to the SC region. We will use this to justify that Eq. (6.2), together with appropriate boundary conditions, is sufficient to capture the ground-state splitting.

To address the details of this problem, we must be slightly more precise in what we mean

by FM and SC regions. We consider the FM-SC-FM heterostructure where the edge is gapped by FMs when $x \leq -\frac{1}{2}(L+\delta)$ and $x \geq \frac{1}{2}(L+\delta)$, while in the interval $-\frac{1}{2}(L-\delta) \leq x \leq \frac{1}{2}(L-\delta)$, the edge is gapped by SC. To simplify the calculation, we approximate these gaps as step functions (see Fig. 6.1). The commutation relations between θ and ϕ make it impossible to induce both kinds of gaps at the same spatial position; therefore there is necessarily a small domain wall (DW) region between FM and SC regions, whose width we take to be $\delta \ll L$.

Our derivation proceeds in three steps. First, we will argue that provided the FM gap is large the instanton configurations of interest have essentially no effect on physics in the FM region. This allows us to restrict our attention to the effective action in the SC and DW regions, with appropriate boundary conditions at each domain wall. Second, we integrate out θ in the SC and DW regions to obtain an effective action for the field ϕ. Finally, we argue that the specified boundary conditions mean that the contribution of the DW region to the tunneling amplitude is also essentially independent of the instanton configuration, allowing us to study the ground-state splitting using an effective action for the SC region alone.

The FM region. First, we will argue that the impact of the FM region on the ground-state splitting can be captured simply by choosing appropriate boundary conditions for the fields $\theta,\ \phi$ at $x = \pm\frac{1}{2}(L+\delta)$. Essentially, this is because the instanton profile vanishes for $|x| > \frac{1}{2}(L+\delta)$, and hence the path integral on these regions is indifferent to instanton effects.

To see why this must be so, we begin by considering the limit $\frac{2n\mathcal{B}}{\pi\varsigma} \to \infty$. In this limit θ is exactly frozen in each FM region to one of its $2n$ minimal values, and its spatial and temporal derivatives in this region vanish. Since $[\frac{n}{\pi}\partial_x\theta(x), \phi(x)] = i$, pinning $\partial_x\theta \equiv 0$ in this region forces ϕ to be evenly distributed on the interval $[0, 2\pi)$, irrespective of the behaviour of ϕ for $|x| < \frac{1}{2}(L+\delta)$. Hence in the limit that θ and its derivatives are perfectly pinned in the FM regions, their contribution to the tunneling amplitude is necessarily independent of the instanton configuration in the SC and DW regions. Hence in this limit, we can replace the FM region with the appropriate boundary condition for $\phi(\pm\frac{1}{2}(L+\delta))$, and a sum over all possible pinned values of θ at each of these boundaries. (This sum ensures that the system can access all possible values of q.)

In other words, for $\frac{2n\mathcal{B}}{\pi\varsigma} \to \infty$ the tunneling amplitude for the entire system can be expressed:

$$\mathcal{I} = \sum_{\theta_R,\theta_L} \int d\phi_1 d\phi_2 Z_{\text{FM}}[\theta_L, \phi_1]\mathcal{T}[\theta_L, \theta_R, \phi_1, \phi_2]Z_{\text{FM}}[\theta_R, \phi_2], \tag{6.3}$$

where the summation is over all values of $\theta_L,\ \theta_R \in \frac{\pi}{n}\{0, 1, \ldots, 2n-1\}$. Here we have defined $\phi\left(-\frac{1}{2}(L+\delta)\right) = \phi_1,\ \phi\left(\frac{1}{2}(L+\delta)\right) = \phi_2$. Note that we must integrate over all values of $\phi_1,\ \phi_2$, since $\partial_x\theta$ is pinned at this boundary.

From the form of the action in the FM regions (which depends only on derivatives of ϕ, with no potential term), it is evident that Z_{FM} will be independent of the particular values of $\phi_{1,2}$, and also of the choice of $\theta_{L,R}$ within the set of minima of the potential. Therefore any impact from instanton configurations must be contained in the tunneling amplitude $\mathcal{T}[\cdots]$, which describes the SC and DW regions.

Hence provided $\mathcal{B}$ is sufficiently large that fluctuations in θ in the FM region can be neglected, the FM region cannot contribute to the instanton transition amplitude. Including small fluctuations, to account for the fact that $\partial_x\theta$ is not exactly pinned in the FM region, we would find that the boundary values of ϕ need not be perfectly uniformly distributed, making some "leaking" of the instanton configuration into the FM region possible. However, provided the fluctuations in θ are small (i.e. the FM gap is large), the distribution of ϕ must be wide. The finite correlation length in this region also ensures that any correlation with the instanton solution occurs over a finite (and small) spatial extent. Therefore though the impact of the instanton configuration on the FM region in this case is not strictly 0, we will neglect it relative to the remaining terms, an approximation that is valid provided the FM gap remains large. Including such terms could result in corrections of order 1 of the magnitude of the instanton transition amplitude, but will not contribute to the Berry phase term in the action provided $\mu = 0$ in the FM regions.

Effective action in the SC and DW regions. Based on the previous discussion, to calculate the ground-state splitting we may focus on the region $|x| < \frac{1}{2}(L+\delta)$, where the potential term for θ vanishes. The boundary conditions on this region are that ϕ is free at both spatial boundaries, and that

$$\theta\left(-\frac{L+\delta}{2}\right) = \theta_L,\ \ \theta\left(\frac{L+\delta}{2}\right) = \theta_R, \tag{6.4}$$

where the transition amplitude contains a sum over the possible values $\frac{n}{\pi}\theta_{R,L} = 0, 1, \ldots, 2n-1$. Recall that the total charge in the SC segment is fixed by $q_\phi/n = \frac{1}{\pi}\left(\theta\left(\frac{L+\delta}{2}\right) - \theta\left(-\frac{L+\delta}{2}\right)\right) = 0, 1/n, \ldots, (2n-1)/n \pmod 2$; hence this sum ensures that all possible charges are included in the path integral.

Within this region, the potential term for θ vanishes, and we may complete the square in the

path integral to obtain:

$$S = \int d\tau \int_{|x|<\frac{L+\delta}{2}} dx \left\{ \frac{\hbar n v}{2\pi} \left[\partial_x \theta(x,\tau) - \frac{\mu(x)}{\hbar n v} + \frac{i}{v} \partial_\tau \phi(x,\tau) \right]^2 \right.$$
$$+ \frac{\hbar n}{2\pi v} \left(\partial_\tau \phi(x,\tau)\right)^2 + \frac{\hbar n v}{2\pi} \left(\partial_x \phi(x,\tau)\right)^2$$
$$\left. + \frac{\Delta(x)}{\pi n_\varsigma} \left[\sin(2n\phi(x,\tau)) + 1\right] + i \frac{\mu(x)}{\pi v} \partial_\tau \phi(x,\tau) - \frac{(\mu(x))^2}{2\pi \hbar n v} \right\}. \quad (6.5)$$

The second and third lines in Eq. (6.5) are the standard sine-Gordon action $S_{\text{s-G}}$, and the second term in the third line is the newly-derived Berry phase term $S_{\text{B-p}}$. Shifting θ and performing the Gaussian integral leads to the effective action given above:

$$S_\phi = \int d\tau \int_{|x|<\frac{L+\delta}{2}} dx \left\{ \frac{\hbar n}{2\pi v} \left(\partial_\tau \phi(x,\tau)\right)^2 + \frac{\hbar n v}{2\pi} \left(\partial_x \phi(x,\tau)\right)^2 \right.$$
$$\left. + \frac{\Delta(x)}{\pi n_\varsigma} \left[\sin(2n\phi(x,\tau)) + 1\right] + i \frac{\mu(x)}{\pi v} \partial_\tau \phi(x,\tau) \right\}, \quad (6.6)$$

where we have dropped the constant term.

The final step is to argue that, given the effective action (6.6) with the chosen boundary conditions, the contribution of the DW regions to the transition amplitude is approximately independent of the instanton configuration. This allows us to restrict our instanton calculation to the SC region, where ϕ is approximately uniform in space (provided $\Delta/(\pi n_\varsigma)$ is large).

Across the domain wall region, the field ϕ must go from being essentially pinned in the SC region, to totally free (i.e. an equal weight superposition over all possible values of ϕ_1 (ϕ_2) at the left (right) boundary of the FM region). In the DW region, the action depends only on the derivatives of ϕ, and hence for a given configuration depends only on the difference in ϕ between the region's two endpoints, as well as on the spatial and temporal fluctuations within the DW region. Because we must average over all boundary values at $|x| = \frac{1}{2}(L+\delta)$, the set of differences of ϕ across the spatial extent of the DW region is independent of the pinned value of ϕ in the SC region (and its time derivative). In other words, the spatial boundary conditions ensure that the distribution of $\partial_x \phi$ in the DW region is insensitive to the instanton configuration.

The distribution of $\partial_\tau \phi$ will be influenced by the instanton configuration, since near the SC region continuity of the fields ensures that the distribution of ϕ and its derivatives are sharply peaked about the instanton configuration. However, this adds a correction which is at most on the order of δ/L to the effective action of the instanton region, which can be neglected.

(We expect that corrections to the fluctuation determinant are similarly small.) Therefore, the partition function in the DW regions will also, to a good approximation, be independent of the instanton configuration in the SC region, in the limit that $\frac{2n\mathcal{B}}{\pi\varsigma} \to \infty$ (where our boundary condition at $|x| = \frac{1}{2}(L+\delta)$ is justified).

In summary, the contribution of the DW region to the instanton effective action is small in δ/L, and can be neglected. Though our approach is justified only in the limit that the fields are perfectly pinned in both SC and FM regions, we expect that small spatial variation in the instanton across the SC region, or "leakage" of the instanton into the FM region, will result in small corrections to the partition function in the FM and DW regions, and that our approach gives both the correct oscillatory phase and order of magnitude for the ground-state energy splitting.

For completeness, here we review a few technical aspects of the derivation of the effective action.

Boundary terms from integrating by parts. To obtain the action S_E given in Eq. (6.1), we have integrated a term of the form $\partial_\tau\theta\partial_x\phi$ by parts. Here we verify that the resulting boundary terms do not contribute to the effective action of the instanton. To show this, we use periodic boundary conditions in space and time on the fluctuating (i.e. non-classical) components of our fields.

The boundary terms in question are:

$$\int dx \left[(i\theta(x,\tau)\partial_x\phi(x,\tau)) \Big|_{-T_\tau/2}^{T_\tau/2} \right] - \int d\tau \left[(i\theta(x,\tau)\partial_\tau\phi(x,\tau)) \Big|_{L}^{R} \right]. \tag{6.7}$$

We begin with the first term. In the SC region, we may separate $\phi = \phi_{sol} + \eta$, where $\eta(x, T_\tau/2) = \eta(x, -T_\tau/2)$ and $\partial_x\phi_{sol} = 0$. In the FM region $\phi \equiv \eta$, and since there are no instantons in θ the configurations at $\pm T_\tau/2$ are identical. In the DW region the field does vary spatially, but this variation is not due to ϕ_{sol}, but rather due to the fluctuations (in other words, the distribution of $\partial_x\phi$ in the DW is time-independent, as emphasized above). Therefore the first term vanishes.

For the second term, (which we compute for the whole system, not only the region relevant

to the instanton action), we obtain:

$$\int d\tau \left[(i\theta(x,\tau)\partial_\tau \phi(x,\tau)) \Big|_{x=-\infty}^{x=\infty} \right] = (\theta_R - \theta_L) \int d\tau \, [i\partial_\tau \phi(\pm\infty,\tau)]$$
$$= (\theta_R - \theta_L)(\phi(\pm\infty, T_\tau/2) - \phi(\pm\infty, -T_\tau/2)) = 0, \tag{6.8}$$

where we have used periodic boundary conditions on fluctuations of both θ and ϕ at $x = \pm\infty$, and the fact that since each FM region is semi-infinite, there are no instantons in θ. The last equality follows from the fact that in the FM region ϕ consists only of fluctuations, which obey periodic boundary conditions in (imaginary) time.

Thus both of these boundary terms do indeed vanish.

Shifting θ. Here we present the details of the shift in θ, to confirm that the resulting integral is independent of the configuration of ϕ. For a one-instanton contribution, we have $\phi(x,\tau) = \phi_{sol}(x,\tau) + \eta(x,\tau)$, where the fluctuation field η obeys $\eta(x, \tau = \pm T_\tau/2) = 0$, and ϕ_{sol} is the classical instanton solution, which we argued above vanishes at $x = \pm\frac{1}{2}(L+\delta)$. We must now evaluate

$$\int \mathcal{D}\theta(x,\tau) \exp\left\{ -\frac{nv}{2\pi} \int d\tau \int_{|x|<\frac{L+\delta}{2}} dx [\partial_x \theta(x,\tau) \right.$$
$$\left. - \frac{\mu(x)}{\hbar n v} + \frac{i}{v}\partial_\tau \eta(x,\tau) + \frac{i}{v}\partial_\tau \phi_{sol}(x,\tau)]^2 \right\}. \tag{6.9}$$

Since the region in question is finite, one might worry that such a shift will result in different boundary conditions for θ and $\tilde{\theta}$, either in space or in time, leading to a different set of eigenvalues even for the same differential operator. However, the boundary conditions (BCs) are not affected by ϕ_{sol} or μ. First, both of these quantities vanish at the spatial boundary. Second, in the limit of interest $T_\tau \to \infty$, $\partial_\tau \phi_{sol}$ vanishes at the time-like boundaries, and μ is time independent. This leaves the fluctuation field η, which obeys free rather than fixed BCs at the spatial boundaries (but the same BCs in time). This change in spatial BCs between θ and $\tilde{\theta}$ does not, however, result in any additional dependence on η in the functional integral.

To perform the desired shift, we Fourier transform all fields by using

$$\theta(x,\tau) = \frac{1}{T_\tau L} \sum_{k,i\omega} \theta(k, i\omega) e^{ikx} e^{-i\omega\tau}$$

(and similarly for other fields), where ω are real, discrete frequencies, then shift the Fourier components $\theta(k, i\omega)$ to absorb the chemical potential and the soliton terms into the Gaussian

integral of θ. This gives:

$$\tilde{\theta}(k, i\omega) = \theta(k, i\omega) - \frac{i\mu(k)T_\tau \delta_{\omega,0}}{\hbar n v k} + \frac{i\omega}{kv}\left(\eta(k, i\omega) + \phi_{sol}(k, i\omega)\right), \tag{6.10}$$

where $\delta_{\omega,0}$ is the Kronecker δ-function. The resulting Gaussian integral over θ is independent of the specific form of both ϕ_{sol} and η, leading to the effective action (6.6).

6.3 Instanton calculation of level splitting

Now that we have verified that Eq. (6.2) is indeed the correct effective action, we are ready to evaluate how instantons lift the ground-state degeneracy. Most qualitative features of our result can be understood in terms of a quantum mechanical $(0+1)$D calculation, in which we ignore spatial fluctuations in the SC region. We present this calculation first, and then review how incorporating spatial fluctuations affects our result.

6.3.1 Introduction to instanton techniques

To set the stage for later $(1+1)$D field theoretical calculation of the level splitting, here we provide an introductory subsection for instanton techniques in quantum mechanics by deriving the analytical formula for the tunneling amplitude between two adjacent minima of the sine-Gordon potential in the presence of just one instanton. The effect of multiple instantons will be analyzed using the dilute-gas approximation in the next few subsections.

Let's begin with the Euclidean action for a quantum mechanical problem,

$$S_E[\phi] = \int_{-T_\tau/2}^{T_\tau/2} a\left[\frac{1}{2}\left(\frac{d\phi(\tau)}{d\tau}\right)^2 + V(\phi)\right] d\tau,$$

where we assume that the potential profile $U(\phi) = aV(\phi)$ has multiple degenerate global minima V_{min}, and for simplicity we have set $V_{\text{min}} = 0$. Note that we have factored out the dimensionful constant term a from both the kinetic and potential terms for the later convenience.

First, we calculate the effective action for one instanton, which gives the tunneling amplitude between two adjacent vacua (minima). From path integral, we have in Euclidean time,

$$\begin{aligned}\langle \phi_f, T_\tau/2 | \phi_i, -T_\tau/2\rangle &= \langle \phi_f | e^{-H_\phi T_\tau/\hbar} | \phi_i\rangle = \mathcal{N}\int \mathcal{D}\phi e^{-S_E[\phi]/\hbar} \\ &\approx \frac{\mathcal{N} e^{-S_E[\phi_{sol}(\tau)]/\hbar}}{\sqrt{\det\left[a\left(-\frac{d^2}{d\tau^2} + \frac{d^2V(\phi_{sol})}{d\phi_{sol}^2}\right)\right]}}.\end{aligned} \tag{6.11}$$

The stationary path $\phi_{sol}(\tau)$ is fixed by requiring that (1) $\frac{\delta S_E[\phi]}{\delta\phi(\tau)} = 0$, and (2) it interpolates between the two specified minima of $V(\phi)$ as τ evolves from $-\infty$ to ∞. The full (dynamical) field ϕ is parameterized by $\phi(\tau) = \phi_{sol}(\tau) + \eta(\tau)$, where the fluctuation field $\eta(\tau)$ obeys the boundary conditions $\eta(\pm T_\tau/2) = 0$.

For the sine-Gordon model described by Eq. (6.2), the minima of the potential term are at $\phi_{\text{min}} = -\frac{\pi}{4n} + \frac{j\pi}{n}$ where $j = 0, 1, \ldots, 2n-1$, with the j-th ground state denoted by $|j\rangle$. The classical soliton solution interpolating between vacua at $j\frac{\pi}{n} - \frac{\pi}{4n}$ and $(j \pm 1)\frac{\pi}{n} - \frac{\pi}{4n}$ has the form [131–133]:

$$\phi_{sol}(\tau) = -\frac{\pi}{4n} + j\frac{\pi}{n} \pm \frac{2}{n}\arctan[e^{\omega(\tau-\tau_0)}], \tag{6.12}$$

where $\omega = 2\sqrt{\Delta v/(\hbar\varsigma)} > 0$. To a good approximation, we may neglect spatial variations in the instanton solution due to boundary effects.

The classical instanton action $S_E[\phi_{sol}]$ can then be readily evaluated. The topological term contributes:

$$S_{\text{B-p}}[\phi_{sol}] = i\frac{\mu L}{\pi v}\left[\phi(\tau = T/2) - \phi(\tau = -T/2)\right], \tag{6.13}$$

which gives a complex phase proportional to the instanton number. To evaluate the remaining contribution, we use the virial identity:

$$\begin{aligned} S_{\text{s-G}}[\phi_{sol}] \equiv S_0 &= a\int_j^{j+1} d\phi_{sol}\sqrt{2V(\phi_{sol})} \\ &= a\sqrt{2}\left(\frac{\omega}{2n}\right)\int_{\frac{\pi}{n}j-\frac{\pi}{4n}}^{\frac{\pi}{n}j+\frac{3\pi}{4n}} d\phi_{sol}\sqrt{\sin(2n\phi_{sol})+1} = \frac{2a\omega}{n^2}. \end{aligned} \tag{6.14}$$

Symmetry dictates that this gives the anti-instanton value as well.

The second, more technically involved, part of the calculation is to evaluate the fluctuation determinant. This requires two steps: First, the Hermitian operator $a\left(-\frac{d^2}{d\tau^2} + \frac{d^2V(\phi_{sol})}{d\phi_{sol}^2}\right)$ has an exact zero mode, due to its time-translation invariance. We must account for this zero mode separately to avoid obtaining a determinant of 0. After having done this, we may evaluate the contribution of the remaining modes to the determinant. With proper normalization convention, we arrive at a ratio of determinants (the Fredholm determinant),

$$\frac{\mathcal{N}}{\sqrt{\det\left[a\left(-\frac{d^2}{d\tau^2} + \frac{d^2V(\phi_{sol})}{d\phi_{sol}^2}\right)\right]}} = \frac{\mathcal{N}'\left(S_0/\hbar\right)^{\frac{1}{2}}}{\sqrt{\det\left(-a\frac{d^2}{d\tau^2} + a\omega^2\right)}}\frac{\sqrt{\det\left(-a\frac{d^2}{d\tau^2} + a\omega^2\right)}}{\sqrt{\det'\left(-a\frac{d^2}{d\tau^2} + a\frac{d^2V}{d\phi_{sol}^2}\right)}},$$

where $\sqrt{S_0/\hbar}$ is the contribution of the zero mode, $\det'$ means that the zero eigenvalue has been excluded, and $\mathcal{N}'$ is a change in the overall normalization. If η is spatially uniform (i.e. $\eta(x,\tau) = \eta(\tau)$), the rest spectrum of the determinant operator may be obtained exactly (see Ref. [134]). Up to normalization, this gives the fluctuation determinant:

$$\frac{\det'\left(-a\frac{d^2}{d\tau^2} + a\frac{d^2V}{d\phi_{sol}^2}\right)}{\det\left(-a\frac{d^2}{d\tau^2} + a\omega^2\right)} = \left(4a\omega^2\right)^{-1}. \tag{6.15}$$

In this case, the amplitude for a single-instanton process becomes

$$\langle j+1|e^{-H_\phi T_\tau/\hbar}|j\rangle_{o.i.} = \left(\sqrt{\frac{a\omega}{\pi\hbar}}e^{-\frac{\omega T_\tau}{2}}\right)\cdot\left(\sqrt{\frac{2}{\pi}}\sqrt{\frac{S_0}{\hbar}}e^{-S_0/\hbar - i\gamma}\,\omega T_\tau\right), \tag{6.16}$$

where $S_0 = \frac{2a\omega}{n^2} = \frac{2\hbar\omega L}{\pi n v}$, $\gamma = \frac{\mu L}{\hbar n v}$, $\omega = 2\sqrt{\frac{\Delta v}{\hbar\varsigma}}$, with $a = \frac{\hbar n L}{\pi v}$, and we intentionally separate the transition amplitude into two pieces—the first one comes from the stationary solution in a harmonic oscillator potential and the second factor arises from the non-perturbative effect of one instanton (or anti-instanton).

6.3.2 Fluctuation determinant with spatial dependence

The main effect of the fluctuation determinant in the $(0+1)$-dimensional instanton calculation is to introduce a prefactor of $\sqrt{L}$, due to the zero mode. However, as we will show here, when spatial fluctuations are included the fluctuation determinant contains an additional factor of $1/\sqrt{L}$ for Neumann boundary conditions (BCs) (and $1/L$ for periodic BCs), meaning that the Fredholm determinant is actually L independent (or falls of as $1/\sqrt{L}$ with PBCs). To this end, we start again from the action (6.2). The classical action is the same as in $(0+1)$D, since the classical instanton solution is (to a good approximation) spatially uniform. To evaluate the tunneling amplitude, we again separate out the effect of the zero mode, which gives us

$$\begin{aligned}
&\frac{\mathcal{N}}{\sqrt{\det\left[-\frac{\hbar n}{\pi v}\partial_\tau^2 - \frac{\hbar n v}{\pi}\partial_x^2 - \frac{4n\Delta}{\pi\varsigma}\sin(2n\phi_{sol}(\tau))\right]}} \\
&= \frac{\mathcal{N}'\left(S_0/\hbar\right)^{\frac{1}{2}}}{\sqrt{\det\left[-\frac{\hbar n}{\pi v}\partial_\tau^2 - \frac{\hbar n v}{\pi}\partial_x^2 + \frac{4n\Delta}{\pi\varsigma}\right]}}\frac{\sqrt{\det\left[-\frac{\hbar n}{\pi v}\partial_\tau^2 - \frac{\hbar n v}{\pi}\partial_x^2 + \frac{4n\Delta}{\pi\varsigma}\right]}}{\sqrt{\det'\left[-\frac{\hbar n}{\pi v}\partial_\tau^2 - \frac{\hbar n v}{\pi}\partial_x^2 - \frac{4n\Delta}{\pi\varsigma}\sin(2n\phi_{sol}(\tau))\right]}}.
\end{aligned}$$

Our remaining task is to calculate the ratio

$$\frac{\sqrt{\det\left[-\frac{\hbar n}{\pi v}\partial_\tau^2-\frac{\hbar n v}{\pi}\partial_x^2+\frac{4n\Delta}{\pi\varsigma}\right]}}{\sqrt{\det{}'\left[-\frac{\hbar n}{\pi v}\partial_\tau^2-\frac{\hbar n v}{\pi}\partial_x^2-\frac{4n\Delta}{\pi\varsigma}\sin(2n\phi_{sol}(\tau))\right]}}, \tag{6.17}$$

where as above $\det'$ is the determinant with the zero mode removed.

In $(1+1)$D, unlike in $(0+1)$D, calculating the determinant requires the appropriate regularization scheme. Here we use the zeta-function regularization (or the heat kernel expansion) to treat the ratio of the divergent determinants.

For the ease of analytical manipulation, we first rewrite the original action,

$$S_\phi=\int_{-\frac{T_\tau}{2}}^{\frac{T_\tau}{2}}d\tau\int_0^L dx\left\{\frac{\hbar n}{2\pi v}(\partial_\tau\phi(x,\tau))^2+\frac{\hbar n v}{2\pi}(\partial_x\phi(x,\tau))^2+i\frac{\mu(x)}{\pi v}\partial_\tau\phi(x,\tau)\right.$$
$$\left.+\frac{\Delta}{\pi n\varsigma}[\sin(2n\phi(x,\tau))+1]\right\},$$

in the follow way,

$$S_\phi=S_{\tilde\phi}=\int_{-\frac{\sqrt{v}T_\tau}{2}}^{\frac{\sqrt{v}T_\tau}{2}}d\tau'\int_0^{L'}dx'\left\{\frac{1}{2}(\partial_{\tau'}\tilde\phi(x',\tau'))^2+\frac{1}{2}(\partial_{x'}\tilde\phi(x',\tau'))^2\right.$$
$$\left.+i\frac{\mu(x')}{\sqrt{\hbar n\pi v}}\partial_{\tau'}\tilde\phi(x',\tau')+\frac{\Delta}{\pi n\varsigma}[1-\cos\left(\sqrt{\frac{4\pi n}{\hbar}}\tilde\phi(x',\tau')\right)]\right\},$$

where we define

$$\tau=\frac{1}{\sqrt{v}}\tau',\quad x=\sqrt{v}x',\quad L=\sqrt{v}L',$$
$$\phi(x,\tau)=\sqrt{\frac{\pi}{\hbar n}}\tilde\phi(x',\tau')-\frac{\pi}{4n},\quad \eta(x,\tau)=\sqrt{\frac{\pi}{\hbar n}}\tilde\eta(x',\tau').$$

Under these new variables, the energy splitting we must calculate is,

$$E(q_\phi)=-2\hbar\sqrt{v}\cos\left(\frac{\pi}{n}q_\phi-\frac{\mu L}{\hbar n v}\right)\cdot\left(\sqrt{\frac{S_0}{2\pi\hbar}}\cdot e^{-S_0/\hbar}\right)$$
$$\times\left(\frac{\sqrt{\det\left[-\partial_{\tau'}^2-\partial_{x'}^2+\frac{4\Delta}{\hbar\varsigma}\right]}}{\sqrt{\det{}'\left[-\partial_{\tau'}^2-\partial_{x'}^2-\frac{4\Delta}{\hbar\varsigma}\sin(2n\phi_{sol}(\tau))\right]}}\right), \tag{6.18}$$

where the extra factor $\sqrt{v}$ comes from the fact that $\int_{-\sqrt{v}T_\tau/2}^{\sqrt{v}T_\tau/2}d\tau_0'=\sqrt{v}\int_{-T_\tau/2}^{T_\tau/2}d\tau_0=\sqrt{v}T_\tau$. It is worth noticing that when $\hbar=c=1$, the velocity v is dimensionless and [time] = [length].

Next, we introduce the generalized Riemann zeta function for a Hermitian operator $\hat{A}$ with the real positive eigenvalues E_n,

$$\zeta(z,\hat{A}) = \sum_n \frac{1}{E_n^z} = \frac{1}{\Gamma(z)} \int_0^\infty dt\, t^{z-1} \int dx \lim_{y\to x} G_{\hat{A}}(x,y;t) = \frac{1}{\Gamma(z)} \int_0^\infty dt\, t^{z-1} K_t(\hat{A}).$$

(The zeta function contains the finite part of the determinant, i.e. the part that we want to keep to obtain an answer.) Here we have specified to the $(1+1)$D system and the generalized heat kernel $K_t(\hat{A}) \coloneqq \mathrm{Tr}[e^{-t\hat{A}}] = \int dx \lim_{y\to x} G_{\hat{A}}(x,y;t)$ where $G_{\hat{A}} \coloneqq e^{-t\hat{A}}$. Then the desired determinant ratio can be expressed in terms of a special function which is analytically easier to be handled,

$$\log\left(\frac{\det' \hat{M}}{\det \hat{M}_0}\right) = -\int_0^\infty \frac{dt}{t}\{K_t(\hat{M}) - K_t(\hat{M}_0) - 1\}. \tag{6.19}$$

Here the Hermitian operators $\hat{M},\ \hat{M}_0$ and $\hat{Q},\ \hat{Q}_0$ are defined as follows,

$$\begin{aligned}\hat{M} &= -\partial_{x'}^2 - \partial_{\tau'}^2 - \frac{4\Delta}{\hbar\varsigma}\sin(2n\phi_{sol}(\tau)) = -\partial_{x'}^2 - \partial_{\tau'}^2 + m_0^2\left(1 - \frac{2}{\cosh^2(m_0(\tau'-\tau_0'))}\right) \\ &= -\partial_{x'}^2 + \hat{Q}, \end{aligned} \tag{6.20}$$

$$\hat{M}_0 = -\partial_{x'}^2 - \partial_{\tau'}^2 + \frac{4\Delta}{\hbar\varsigma} = -\partial_{x'}^2 - \partial_{\tau'}^2 + m_0^2 = -\partial_{x'}^2 + \hat{Q}_0, \tag{6.21}$$

where the mass term $m_0 = \sqrt{\frac{4\Delta}{\hbar\varsigma}}$. Note that the integral in Eq. (6.19) is ultraviolet divergent as can be seen by examining the asymptotic behavior of the heat kernels when $t \to 0$. However, the finite part of Eq. (6.19) can still be extracted after regularization by constructing the derivative of the associated zeta function

$$\log\left(\frac{\det' \hat{M}}{\det \hat{M}_0}\right) \longrightarrow -\frac{d}{dz}\zeta(z,\hat{M}) = -\frac{d}{dz}\left(\frac{1}{\Gamma(z)}\int_0^\infty dt\, t^{z-1}\{K_t(\hat{M}) - K_t(\hat{M}_0) - 1\}\right), \tag{6.22}$$

and eventually continuing it back to $z = 0$. It is important to notice that $-\frac{d\zeta(z,\hat{M})}{dz}\big|_{z=0}$ is finite as will be explicitly calculated below in the continuum limit.

We are now in the position to compute the regularized ratio of determinants in Eq. (6.19). To regularize the determinant, let us first isolate the divergent term. To do so, we expand the integrand as powers of t as the ultraviolet divergence happens at $t = 0^+$,

$$\begin{aligned} K_t(\hat{M}) - K_t(\hat{M}_0) &\xrightarrow{t=0^+} (L'/4)^{d-1}(4\pi t)^{-\frac{d-2}{2}}(4\pi t)^{-\frac{1}{2}}\mathrm{Erf}(m_0\sqrt{t}) \\ &= (L'/4)^{1-\epsilon}\frac{1}{\sqrt{4\pi t}}\cdot\frac{2}{\sqrt{\pi}}\left(m_0\sqrt{t} - \frac{m_0^3 t^{\frac{3}{2}}}{3}\right) \approx \frac{m_0 L'}{4\pi} + \cdots, \end{aligned}$$

where we only keep track of the pieces in the expansion that get divergent after integration, and it can be shown that the constant term $\frac{1}{2}$ in Eq. (6.29) gives the finite result after integration of t. Subtract and add back this divergent term in Eq. (6.19) yields the finite part and the logarithmically divergent part, respectively,

$$\begin{aligned}\log\left(\frac{\det'\hat{M}}{\det\hat{M}_0}\right) &= -\int_0^\infty \frac{dt}{t}\left\{K_t(\hat{M}) - K_t(\hat{M}_0) - 1 - \Theta(1-t)\cdot\frac{m_0L'}{4\pi}\right\} \\ &\quad -\int_0^\infty \frac{dt}{t}\left\{\Theta(1-t)\cdot\frac{m_0L'}{4\pi}\right\} \\ &= -\int_0^\infty \frac{dt}{t}\left\{K_t(\hat{M}) - K_t(\hat{M}_0) - 1 - \Theta(1-t)\cdot\frac{m_0L'}{4\pi}\right\} \\ &\quad +\frac{m_0L'}{4\pi}\log\epsilon_t;\ \ \epsilon_t = 0^+. \end{aligned} \tag{6.23}$$

The finite part of Eq. (6.23) can be recasted in terms of the ζ-function in Eq. (6.22) as follows,

$$\begin{aligned}-\frac{d}{dz}\zeta(z,\hat{M}) &= -\frac{d}{dz}\left(\frac{1}{\Gamma(z)}\int_0^\infty dt\, t^{z-1}\left\{K_t(\hat{M}) - K_t(\hat{M}_0) - 1 - \Theta(1-t)\cdot\frac{m_0L'}{4\pi}\right\}\right) \\ &\quad -\frac{d}{dz}\left(\frac{m_0L'}{4\pi}\frac{1}{\Gamma(z+1)}\right) \\ &= -\int_0^\infty \frac{dt}{t}\left\{K_t(\hat{M}) - K_t(\hat{M}_0) - 1 - \Theta(1-t)\cdot\frac{m_0L'}{4\pi}\right\} - \frac{m_0L'}{4\pi}\gamma_E, \end{aligned} \tag{6.24}$$

where γ_E is the Euler's constant and we have implicitly taken the limit $z = 0$. Comparing Eqs. (6.23) and (6.24) suggests that

$$-\frac{1}{2}\mathrm{Tr}'\log\left(\frac{\hat{M}}{\hat{M}_0}\right) = -\frac{1}{2}\log\left(\frac{\det'\hat{M}}{\det\hat{M}_0}\right) = \frac{1}{2}\frac{d}{dz}\zeta(z=0,\hat{M}) - \frac{m_0L'}{8\pi}\gamma_E - \frac{m_0L'}{8\pi}\log\epsilon_t. \tag{6.25}$$

It is useful to separate the zeta function into two main pieces,

$$\begin{aligned}\zeta(z,\hat{M}) &= \zeta_{\log}(z,\hat{M}) + \zeta_{\mathrm{mix}}(z,\hat{M}), \\ \zeta_{\log}(z,\hat{M}) &= \frac{1}{\Gamma(z)}\int_0^\infty dt\, t^{z-1}\left\{K_t(-\partial_{x'}^2) - 1\right\}, \\ \zeta_{\mathrm{mix}}(z,\hat{M}) &= \frac{1}{\Gamma(z)}\int_0^\infty dt\, t^{z-1}\left\{K_t(-\partial_{x'}^2)\cdot\left[K_t(\hat{Q}) - K_t(\hat{Q}_0) - 1\right]\right\}. \end{aligned}$$

We will show that $\zeta_{\log}$ gives rise to the extra $1/\sqrt{L}$ factor in the prefactor of the energy splitting, and ζ_{mix} induces the corrections that promote the classical instanton action S_0 to its quantum version.

Before starting the actual calculations of the operators' spectra, it is important to state and justify the proper spatial and temporal boundary conditions we impose on the eigenfunctions of the various operators. Let's start with the one-dimensional Laplacian operator $-\partial_{x'}^2$ on the interval $x' \in [0, L']$. Mathematically there exist two commonly-used boundary conditions: The Dirichlet one that requires the field values vanish at $x' = 0$ and $x' = L'$, and the von Neumann one that instead requires the spatial gradients of the field are zero at $x' = 0$ and $x' = L'$. In view of the expressions of the operators $\hat{M}$ and $\hat{M}_0$ in Eqs. (6.20) and (6.21), we can assume that the general $\tilde{\phi}$ fields and the fluctuation $\tilde{\eta}(x', \tau')$ fields have the following forms

$$\tilde{\phi}(x', \tau') = \tilde{\phi}_{sol}(\tau') + \tilde{\eta}(x', \tau') \quad \text{and} \quad \tilde{\eta}(x', \tau') = \tilde{f}(x')\tilde{g}(\tau').$$

Then with the Dirichlet boundary conditions, we would have

$$\tilde{f}(x')\big|_{x'=0,L'} = 0 \quad \text{and} \quad \tilde{f}_n(x') = \sqrt{\frac{2}{L'}} \sin\left(\frac{n\pi x'}{L'}\right), \quad n = 1, 2, 3, \ldots. \tag{6.26}$$

Obviously, $\tilde{f}_n(x')$ comprise a complete set of orthonormal basis functions for the general $\tilde{f}(x')$. While for the Neumann boundary conditions, we would have

$$\partial_{x'}\tilde{f}(x')\big|_{x'=0,L'} = 0 \quad \text{and} \quad \tilde{f}_n(x') = \begin{cases} \sqrt{\frac{1}{L'}} \cos\left(\frac{n\pi x'}{L'}\right), & n = 0 \\ \sqrt{\frac{2}{L'}} \cos\left(\frac{n\pi x'}{L'}\right), & n = 1, 2, 3, \ldots \end{cases}, \tag{6.27}$$

where the explicit inclusion of the zero-momentum state in Neumann boundary conditions is useful.

For the heterostructures that we are investigating, it is appropriate to choose the von Neumann boundary conditions because:

(1) In the free domain-wall region between SC and FM, due to the existence of parafermion zero mode, the Hamiltonian gets vanished. This is consistent with the boundary conditions that $\partial_{x'}\tilde{\phi}\big|_{x'=0,L'} = 0$. Similarly, for the FM segment, we could require $\partial_{x'}\tilde{\theta} = 0$ at the corresponding boundaries.

(2) If we directly impose the Dirichlet boundary conditions which is loosely equivalent to the hard-wall boundary conditions, then we apparently miss the simplest configuration of the spatially independent fluctuations since when $n = 0$, $\tilde{f}(x') = 0$ and $\tilde{\eta}(x', \tau') = 0$ in the whole interval. To fix this problem, we have to intentionally insert the $n = 0$ mode by

hand. However, by exploiting the Neumann boundary conditions, we neatly include all the modes for the spatial fluctuations in the finite interval, and the spatially independent configuration of the fluctuations is captured by $n = 0$ in this case.

Therefore, in the following we will concentrate on the von Neumann boundary conditions only. For the temporal boundary conditions, it can be shown that $\eta(x, \tau = \pm T_\tau/2) = 0$ as $T_\tau \to \infty$.

First, let's calculate the contribution of $\zeta_{\log}$ which can be computed in a closed form.

$$\begin{aligned}\zeta_{\log}(z, \hat{M}) &= \frac{1}{\Gamma(z)} \int_0^\infty dt\, t^{z-1} \{K_t(-\partial_{x'}^2) - 1\} \\ &= \sum_{n=1}^\infty \frac{1}{\Gamma(z)} \int_0^\infty dt\, t^{z-1} e^{-k_n^2 t} = \sum_{n=1}^\infty \left(\frac{1}{k_n^2}\right)^z .\end{aligned}$$

In the continuum limit with the von Neumann boundary conditions, the momentum $k_n = \frac{n\pi}{L'},\ n = 0, 1, 2, \ldots$, so

$$\zeta_{\log}(z, \hat{M}) = \left(\frac{L'^2}{\pi^2}\right)^z \sum_{n=1}^\infty \left(\frac{1}{n^2}\right)^z = \left(\frac{L'^2}{\pi^2}\right)^z \zeta(2z) \quad \text{and} \quad \exp\left(\frac{1}{2}\frac{d\zeta_{\log}}{dz}\Big|_{z=0}\right) = \frac{1}{\sqrt{2}}\frac{1}{\sqrt{L'}}.$$

It is noteworthy that the boundary conditions of the interval constrains that only the non-negative-momentum modes contribute to the spectrum of the Laplacian operator, which gives rise to the above special dependence on $1/\sqrt{L'}$.

Therefore, due to the spatial fluctuations in the finite-size interval with the Neumann boundary conditions, $\zeta_{\log}$ contributes an extra $1/\sqrt{L}$ factor in the prefactor of the ground-state degeneracy splitting. If we choose periodic boundary conditions (such as a periodic ring structure), then instead we get a factor of $1/L$ due to the inclusion of the modes with the negative momenta.

The calculation of ζ_{mix} can be simplified by noticing that in the continuum limit,

$$\sum_{n\in\mathbb{Z}} \exp\left[-\left(\frac{n\pi}{L'}\right)^2 t\right] = \frac{L'}{2\sqrt{4\pi t}} + \frac{L'}{2\sqrt{4\pi t}} \sum_{n\neq 0} \exp\left[-\frac{n^2 L'^2}{16t}\right], \tag{6.28}$$

where the Poisson summation formula is used. Therefore, under the von Neumann boundary

conditions,

$$
\begin{aligned}
K_t(-\partial_{x'}^2) &= \sum_{n=0}^{\infty} \exp\left[-\left(\frac{n\pi}{L'}\right)^2 t\right] \\
&= 1 + \sum_{n=1}^{\infty} \exp\left[-\left(\frac{n\pi}{L'}\right)^2 t\right] = \frac{1}{2} + \frac{1}{2}\sum_{n=-\infty}^{\infty} \exp\left[-\left(\frac{n\pi}{L'}\right)^2 t\right] \\
&= \frac{1}{2} + \frac{L'}{4\sqrt{4\pi t}} + \frac{L'}{4\sqrt{4\pi t}} \sum_{n\neq 0} \exp\left[-\frac{n^2 L'^2}{16t}\right] \xrightarrow{t=0^+} \frac{1}{2} + \frac{L'}{4\sqrt{4\pi t}}. \qquad (6.29)
\end{aligned}
$$

This shows that the divergence is in ζ_{mix}, as the second term here is obviously divergent as $t \to 0$. Since for finite n, the third term in Eq. (6.29) is exponentially damped as a function of L'^2, we can safely neglect their contributions which amount to exponentially small corrections in the bare instanton action. Accordingly, we divide

$$
\begin{aligned}
\zeta_{\text{mix}}(z,\hat{M}) &= \zeta_{\text{con}}(z,\hat{M}) + \zeta_{\text{lin}}(z,\hat{M}) + \zeta_{\text{exp}}(z,\hat{M}), \\
\zeta_{\text{con}}(z,\hat{M}) &= \frac{1}{\Gamma(z)} \int_0^\infty dt\, t^{z-1} \left\{ \frac{1}{2} \cdot \left[K_t(\hat{Q}) - K_t(\hat{Q}_0) - 1 \right] \right\}, \\
\zeta_{\text{lin}}(z,\hat{M}) &= \frac{1}{\Gamma(z)} \int_0^\infty dt\, t^{z-1} \left\{ \frac{L'}{4\sqrt{4\pi t}} \cdot \left[K_t(\hat{Q}) - K_t(\hat{Q}_0) - 1 \right] \right\}, \\
\zeta_{\text{exp}}(z,\hat{M}) &= \frac{1}{\Gamma(z)} \int_0^\infty dt\, t^{z-1} \left\{ \left(K_t(-\partial_{x'}^2) - \frac{1}{2} - \frac{L'}{4\sqrt{4\pi t}} \right) \cdot \left[K_t(\hat{Q}) - K_t(\hat{Q}_0) - 1 \right] \right\},
\end{aligned}
$$

and we will focus on the evaluation of ζ_{con} and ζ_{lin} and their derivatives. It will be shown that ζ_{con} is convergent and contributes to the prefactor that makes the dimensionality of the splitting correct, and ζ_{lin} gives the leading quantum corrections to the classical instanton action, while ζ_{exp} is the additional exponentially small modification to the action that we neglect.

By using the spectral functions of operators $\hat{Q}$ and $\hat{Q}_0$, we obtain that

$$
K_t(\hat{Q}) - K_t(\hat{Q}_0) = 1 - \frac{1}{\pi} \int_0^\infty dp \left(\frac{2m_0}{p^2 + m_0^2} \right) e^{-t(p^2+m_0^2)} = \text{Erf}(m_0\sqrt{t}). \qquad (6.30)
$$

Then, it is straightforward to compute ζ_{con} as follows,

$$\begin{aligned}\zeta_{\text{con}}(z,\hat{M}) &= \frac{1}{\Gamma(z)}\int_0^\infty dt\, t^{z-1}\left\{\frac{1}{2}\cdot\left[-\frac{1}{\pi}\int_0^\infty dp\left(\frac{2m_0}{p^2+m_0^2}\right)e^{-t(p^2+m_0^2)}\right]\right\}\\ &= -\frac{m_0}{\pi}\frac{1}{\Gamma(z)}\int_0^\infty dp\frac{1}{(p^2+m_0^2)}\int_0^\infty dt\cdot t^{z-1}\cdot e^{-t\left(p^2+m_0^2\right)}\\ &= -\frac{m_0}{2\pi}\int_{-\infty}^\infty dp\left(p^2+m_0^2\right)^{-(z+1)}\\ &= -\frac{1}{2\sqrt{\pi}}\cdot m_0^{-2z}\cdot\frac{\Gamma(z+1/2)}{\Gamma(z+1)}.\end{aligned}$$

Therefore, the extra contribution to the prefactor assumes

$$\frac{1}{2}\frac{d\zeta_{\text{con}}(z,\hat{M})}{dz}\Big|_{z=0} = \frac{1}{2}\log(2m_0), \tag{6.31}$$

$$\exp\left(\frac{1}{2}\frac{d\zeta_{\text{con}}(z,\hat{M})}{dz}\Big|_{z=0}\right) = \sqrt{2m_0} = \sqrt{2}\left(\frac{4\Delta}{\hbar\varsigma}\right)^{\frac{1}{4}} = \frac{\sqrt{2\omega}}{v^{\frac{1}{4}}}, \tag{6.32}$$

where we recall and use the definition of $\omega = 2\sqrt{\Delta v/(\hbar\varsigma)} = m_0\sqrt{v}$. In the absence of the other terms, this reproduces our previous result for the fluctuation determinant when the fluctuations are spatially uniform.

Similarly, ζ_{lin} can be calculated as follows,

$$\begin{aligned}\zeta_{\text{lin}}(z,\hat{M}) &= \frac{1}{\Gamma(z)}\int_0^\infty dt\, t^{z-1}\left\{\frac{L'}{4\sqrt{4\pi t}}\cdot\left[-\frac{1}{\pi}\int_0^\infty dp\left(\frac{2m_0}{p^2+m_0^2}\right)e^{-t(p^2+m_0^2)}\right]\right\}\\ &= \left(-\frac{m_0}{\pi}\right)\left(\frac{L'}{4\sqrt{4\pi}}\right)\frac{\Gamma(z-1/2)}{\Gamma(z)}\int_0^\infty\frac{2dp}{(p^2+m_0^2)^{z+\frac{1}{2}}}\\ &= -\left(\frac{L'}{8\pi}\right)\cdot m_0^{1-2z}\cdot\frac{\Gamma(z-1/2)}{\Gamma(z+1/2)}.\end{aligned}$$

This leads to a linear correction to the classical instanton action assumes

$$\frac{1}{2}\frac{d\zeta_{\text{lin}}(z,\hat{M})}{dz}\Big|_{z=0} = \frac{m_0L'}{4\pi}(1-\log m_0). \tag{6.33}$$

To compute the ratio of determinants in Eq. (6.25), we now have to do two things: (1) calculate $\frac{d}{dz}(\zeta(z=0,\hat{M}))$, and (2) regularize the divergence, which requires renormalizing the effective mass for η at one-loop order by expanding the sine-Gordon potential to the fourth power of the ϕ field. The obtained inverse Green function and the convergent vertex function take the following forms,

$$\Gamma_0^{(2)}(p) = p^2+m_0^2-\frac{g_0}{4\pi}\log\left(\frac{\Lambda}{m_0}\right),\quad \Gamma_0^{(4)}(p=0) = -g_0-\frac{3}{8\pi}g_0^2m_0^{-2}.$$

By adopting the zero-momentum renormalization, we can define the renormalized mass term and the coupling constant as follows,

$$m_{\rm R}^2 = m_0^2 - \frac{g_0}{4\pi}\log\left(\frac{\Lambda}{m_0}\right), \quad g_{\rm R} = g_0 + \frac{3}{8\pi}g_0^2 m_0^{-2}, \tag{6.34}$$

where Λ is the momentum cutoff and the bare coupling constant $g_0 = 16n\pi\Delta/(\hbar^2\varsigma)$.

Inverting Eq. (6.34), we can express the bare instanton action in terms of $m_{\rm R}$ and $g_{\rm R}$,

$$-\frac{S_0}{\hbar} = -\frac{2m_0}{n\pi}L' = -\frac{2m_{\rm R}}{n\pi}L' - \frac{g_{\rm R}L'}{4\pi^2 n m_{\rm R}}\log\left(\frac{\Lambda}{m_{\rm R}}\right). \tag{6.35}$$

We would be able to tune the cutoff to make the logarithmic divergence in Eq. (6.35) cancels the logarithmic divergence in Eq. (6.25).

The final finite result for the determinant thus assumes the following form,

$$\begin{aligned}&\frac{\mathcal{N}}{\sqrt{\det\left[-\frac{\hbar n}{\pi v}\partial_\tau^2 - \frac{\hbar n v}{\pi}\partial_x^2 - \frac{4n\Delta}{\pi\varsigma}\sin(2n\phi_{sol}(\tau))\right]}}\\ &\quad\approx -\hbar\sqrt{\omega}\sqrt{\frac{v}{L}}\sqrt{\frac{2}{\pi}}\sqrt{\frac{S_0}{\hbar}}\exp\left[-\frac{m_{\rm R}}{4\pi\sqrt{v}}\left(\log m_{\rm R} + \frac{\gamma_E}{2} - 1\right)L\right].\end{aligned} \tag{6.36}$$

After incorporating both the spatial and temporal fluctuations, the overall dependence of the prefactor on the system's size becomes independent of L, which results from the cancelation of the time-translational-invariant zero-mode effect and the interval spatial fluctuating effect under the Neumann boundary conditions. Moreover, the classical instanton action would also receive the nontrivial one-loop corrections. However, a more precise determination of the leading quantum corrections to S_0 may demand more advanced strategies and techniques. (For instance, it is not immediately clear how to compute the Feynman diagrams with the constraint of the von Neumann boundary conditions on the $\phi(x,\tau)$ fields. Will the virtual momenta in the loop diagrams be extended to the negative values?)

6.3.3 Consistent results from complementary methods

To recap, from the above subsections and following Refs. [130, 135–138], we have derived that the amplitudes for the one-instanton and one-anti-instanton processes are:

$$\begin{aligned}&\langle j|e^{-H_\phi T_\tau/\hbar}|j\mp 1\rangle_{o.i.}\\ &\quad = \left(\mathcal{N}e^{-\tilde{\omega}T_\tau/2}\right)\left(\sqrt{\frac{v}{L}}\sqrt{\frac{S_0}{2\pi\hbar}}e^{-S_0/\hbar\mp i\gamma}\right)\sqrt{\omega}T_\tau.\end{aligned} \tag{6.37}$$

Here $S_0 + (-)i\hbar\gamma$ is the effective action of an instanton (anti-instanton) tunneling event (with small quantum corrections omitted), where the imaginary contribution γ stems from $S_{\text{B-p}}$, and $\hbar\tilde{\omega}/2$ stands for the zero-point energy of the 1D harmonic oscillator. In terms of the parameters in Eq. (6.2), we have $S_0 = \frac{2\hbar\omega L}{n\pi v}$, $\gamma = \frac{\mu L}{\hbar n v}$. As anticipated, the amplitude for tunneling vanishes exponentially with the wire length L provided the bulk is gapped (i.e. $\Delta \neq 0$). More significantly, we now perceive the importance of the Berry phase term, which contributes a different net phase to the amplitude for instanton and anti-instanton processes.

The prefactor

$$\mathcal{K} = \sqrt{v\omega S_0/(2\pi\hbar L)} \tag{6.38}$$

is the calculated Fredholm determinant describing Gaussian fluctuations about the saddle-point solution (6.12) that we calculated in Subsection 6.3.2. This determinant is sensitive to spatial fluctuations in the SC region, and its scaling with L is sensitive to the choice of boundary conditions (BCs). As already shown in Subsection 6.3.2, for Neumann-type BCs appropriate to the setup shown in Fig. 6.1, this prefactor is independent of L, in agreement with existing work on Majorana bound states [116, 118, 139]. For the energy splitting in periodic BCs relative to antiperiodic ones, on the other hand, the prefactor contains an extra factor of $\frac{1}{\sqrt{L}}$ [130]. Fig. 6.2 compares this prediction to numerical values for the energy splitting in the Majorana nanowire for both BCs.

Armed with one-instanton solutions, the total instanton contribution is obtained using a dilute instanton gas approximation [136]. Basically we assume that instantons are well-separated in time, so that all one needs to do is to sum over arbitrary numbers of one-instanton and one-anti-instanton solutions. Importantly, the action for one anti-instanton is the same as that of one instanton, except for the Berry phase (which has a sign change). This gives:

$$\begin{aligned}\langle j_+|e^{-H_\phi T_\tau/\hbar}|j_-\rangle = \mathcal{N}\int_0^{2\pi}\frac{d\zeta}{2\pi}e^{i\zeta(j_- - j_+)} \\ \times\exp\left[-\frac{\tilde{\omega}}{2}T_\tau + 2\mathcal{K}T_\tau e^{-S_0/\hbar}\cos(\zeta-\gamma)\right],\end{aligned} \tag{6.39}$$

where $|j_+\rangle$ ($|j_-\rangle$) denotes the final (initial) vacuum position. The cosine term can be viewed as arising from interference between instanton and anti-instanton trajectories, for which $S_{\text{B-p}}$ has the opposite phase.

In the presence of instanton tunneling events, the eigenstates of H_ϕ are therefore Bloch-wave-like states of the form: $|\zeta\rangle \propto \left(\frac{1}{2\pi}\right)^{\frac{1}{2}}\sum_j e^{-i\zeta j}|j\rangle$. Imposing $\langle j_+ \pm 2n|e^{-H_\phi T_\tau/\hbar}|j_- \pm 2n\rangle =$

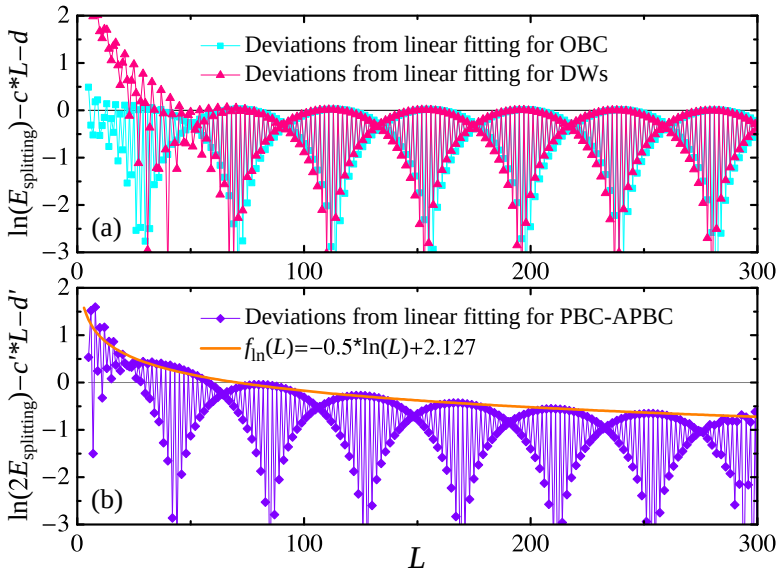

Figure 6.2: Numerical results for the *oscillatory* zero-energy splitting as a function of L in the 1D nanowire models hosting Majorana bound states [1,5,6], for (a) open and domain-wall BCs, and (b) periodic versus antiperiodic BCs (PBC-APBC). (Recall that for a Majorana SC ring, the ground state with PBC (APBC) is a parity-even (parity-odd) state.) The term linear in L has been subtracted off in both cases, leaving a result independent of L in (a), and depending logarithmically on L in (b).

$\langle j_+|e^{-H_\phi T_\tau/\hbar}|j_-\rangle$ to account for the fact that only $2n$ of these minima are physically distinct forces ζ to take on the $2n$ discrete values $\frac{\pi}{n}q_\phi$, with $q_\phi = 0, 1, \ldots, 2n-1$, which gives the $2n$ states:

$$|q_\phi\rangle \propto \left(\frac{1}{2n}\right)^{\frac{1}{2}} \sum_{j=0}^{2n-1} e^{-i\frac{\pi}{n}q_\phi j}|j\rangle. \tag{6.40}$$

From Eq. (6.39), the energies of these states are, up to an overall constant,

$$E(q_\phi) = -\frac{2\hbar\omega}{\pi}\sqrt{\frac{1}{n}}e^{-S_0/\hbar}\cos\left(\frac{\pi}{n}q_\phi - \frac{\mu L}{\hbar n v}\right), \tag{6.41}$$

where q_ϕ is the generalized charge parity conjugate to the discrete, compact variable ϕ_{min}.

It is also instructive to check Eq. (6.41) for the case of Majorana fermions $(n = 1)$, where the splitting can be calculated directly from a quadratic fermion Hamiltonian [116, 117, 121, 124]. The relevant calculation in the quantum Hall systems described here can be carried out as

for the nanowire case [116, 118]—see Appendix B and Ref. [139]. The result is

$$E_q = -C\frac{\Delta\mathcal{B}}{\Delta+\mathcal{B}}e^{-\frac{\Delta L}{\hbar v}}\cos\left(\pi q - \frac{\mu L}{\hbar v}\right),\ \ q=0,1, \tag{6.42}$$

where C is a constant of order unity. The coefficient of the decaying exponential differs from Eq. (6.41), since for $n=1$, $S_0/\hbar = \left(\frac{\Delta L}{\hbar v}\right)\frac{4}{\pi}\sqrt{\hbar v/(\Delta\varsigma)}$. However, in the instanton calculation of the exponential term we neglect all modes above the gap set by Δ; hence the cutoff energy $\hbar v/\varsigma$ should not be much larger than Δ. Further, the tunneling process requires the presence of virtual fluctuations up to an energy of approximately Δ, so the cutoff energy should also not be much smaller than Δ. The factor $\frac{4}{\pi}\sqrt{\hbar v/(\Delta\varsigma)}$, which parameterizes the difference in the exponential decay lengths from the two calculations, is therefore a constant of order 1. Parallel reasoning applies to the comparison of the prefactors. Remarkably, the argument of the cosine term agrees exactly with our instanton calculation, suggesting that this oscillatory dependence on μ is insensitive to the BCs and to the various approximations being made.

We note that the preceding analysis also applies to the case $\mathcal{B} > 0,\ \Delta = 0$ by taking $\phi \rightleftharpoons \theta$ and replacing the chemical potential term with a magnetic field term of the form $-\frac{h}{\pi}\partial_x\phi$. Therefore the oscillatory dependence of the ground-state energy splitting on chemical potential or magnetic field is a relatively ubiquitous feature of parafermion zero modes.

Finally, the energies we derived agree with the general result of Ref. [140]:

$$E(q_\phi) = \sum_{a=0}^{2n-1}\left(\Gamma_a[F_{q_\phi}^{\alpha a\alpha}]_{\alpha\alpha} + \text{H.c.}\right), \tag{6.43}$$

where α denotes the parafermion bound states, and F is a part of the topological data. Eq. (6.43) describes general splittings for anyons with local couplings. For completeness, we will derive this result here, and show how it corresponds to our solution. For the case at hand the possible choices of F are described in Ref. [141]; taking $[F_{q_\phi}^{\alpha a\alpha}]_{\alpha\alpha} = e^{i(\pi/n)[(a\cdot q_\phi) \bmod 2n]}$ and $\Gamma_a = -\hbar\mathcal{K}e^{-S_0/\hbar - i\gamma}\delta_{a,1}$ recovers the form (6.41) for the energies of these ground states.

For clarity, here we provide a simple topological quantum field theoretical (TQFT) derivation for the parafermion splitting. The anyon models that are suitable for our FQH setups contain one non-Abelian anyon σ, and $2n$ distinct Abelian anyons $a = 0, 1, 2, \ldots, 2n-1$. The

fusion rules among them are:

$$\begin{aligned} a \times b &= [a+b]_{2n}, \\ \sigma \times \sigma &= \sum_{a=0}^{2n-1} a, \\ \sigma \times a &= a \times \sigma = \sigma, \end{aligned} \tag{6.44}$$

where $[a+b]_{2n} = (a+b) \bmod 2n$. The claimed F-symbols are given by

$$[F_b^{\sigma a \sigma}]_{\sigma\sigma} = \chi(a,b). \tag{6.45}$$

The so-called bi-characters $\chi(a,b)$ are $U(1)$-valued symmetric functions. They fulfill some consistency conditions:

$$\begin{aligned} \chi(a,b) &= \chi(b,a), \\ \chi(a, b\times c) &= \chi(a,[b+c]_{2n}) = \chi(a,b)\chi(a,c), \\ \chi(a\times b, c) &= \chi([a+b]_{2n},c) = \chi(a,c)\chi(b,c), \end{aligned} \tag{6.46}$$

under the normalization conditions $\chi(0,a) = \chi(a,0) = 1$. The χ functions and the F-symbols are not unique. The proposed symmetric solutions appropriate for our models might be constructed as follows:

$$\chi(a,b) = \chi(b,a) = \exp\Big(i\frac{\pi}{n}[a\cdot b]_{2n}\Big). \tag{6.47}$$

Let us prove that this form of $\chi(a,b)$ indeed satisfies the consistency conditions Eq. (6.46):

$$\begin{aligned} \chi(a, b\times c) &= e^{i\frac{\pi}{n}[a\cdot([b+c]_{2n})]_{2n}} = e^{i\frac{\pi}{n}[a\cdot([b]_{2n}+[c]_{2n})]_{2n}} \\ &= e^{i\frac{\pi}{n}[[a]_{2n}\cdot([b]_{2n}+[c]_{2n})]_{2n}} \\ &= e^{i\frac{\pi}{n}([[a]_{2n}\cdot[b]_{2n}]_{2n}+[[a]_{2n}\cdot[c]_{2n}]_{2n})} \\ &= e^{i\frac{\pi}{n}[[a]_{2n}\cdot[b]_{2n}]_{2n}} \cdot e^{i\frac{\pi}{n}[[a]_{2n}\cdot[c]_{2n}]_{2n}} \\ &= e^{i\frac{\pi}{n}[a\cdot b]_{2n}} \cdot e^{i\frac{\pi}{n}[a\cdot c]_{2n}} \\ &= \chi(a,b)\chi(a,c). \end{aligned} \tag{6.48}$$

To evaluate the ground-state degeneracy splitting to the leading order for a pair of parafermionic anyons (σ,σ), we can directly apply Bonderson's results, namely for the fusion channel b, the

energy correction is

$$\begin{aligned} E_b^{(1)} &= \sum_a \left(\Gamma_a [F_b^{\sigma a \sigma}]_{\sigma\sigma} + \Gamma_a^* [F_b^{\sigma a \sigma}]_{\sigma\sigma}^*\right) \\ &= \sum_a \left(\Gamma_a \chi(a,b) + \Gamma_a^* \chi^*(a,b)\right) \\ &= \sum_a \left(\Gamma_a e^{i\frac{\pi}{n}[a\cdot b]_{2n}} + \Gamma_a^* e^{-i\frac{\pi}{n}[a\cdot b]_{2n}}\right). \end{aligned} \tag{6.49}$$

According to our instanton calculations,

$$E_b^{(1)} = -2\hbar\mathcal{K} e^{-S_0/\hbar} \cos\left(\frac{\pi}{n} b - \frac{\mu L}{\hbar n v}\right). \tag{6.50}$$

This result follows readily from Eq. (6.49) by choosing

$$\Gamma_{a=1} = -\hbar\mathcal{K} e^{-\frac{S_0}{\hbar} - i\frac{\mu L}{\hbar n v}} \quad \text{and} \quad \Gamma_{a\neq 1} = 0, \tag{6.51}$$

then

$$\begin{aligned} E_b^{(1)} &= \sum_a \left(\Gamma_a e^{i\frac{\pi}{n}[a\cdot b]_{2n}} + \Gamma_a^* e^{-i\frac{\pi}{n}[a\cdot b]_{2n}}\right) \\ &= \Gamma_{a=1} e^{i\frac{\pi}{n}[1\cdot b]_{2n}} + \Gamma_{a=1}^* e^{-i\frac{\pi}{n}[1\cdot b]_{2n}} \\ &= \Gamma_{a=1} e^{i\frac{\pi}{n} b} + \Gamma_{a=1}^* e^{-i\frac{\pi}{n} b} \\ &= -2\hbar\mathcal{K} e^{-S_0/\hbar} \cos\left(\frac{\pi}{n} b - \frac{\mu L}{\hbar n v}\right). \end{aligned} \tag{6.52}$$

The choice of Eq. (6.51) can be justified by noticing that the multiple charge tunneling amplitudes should be much smaller when compared with the dominant tunneling process of the unit charge, therefore it seems reasonable to only keep the exponentially small tunneling amplitude $\Gamma_{a=1}$. Also, by construction the tunneling amplitude for the trivial charge $a = 0$ is zero, namely $\Gamma_{a=0} = 0$ identically.

6.4 Hopping in parafermion chains

One interesting application of our calculation is that it allows us to infer the phase of intrawire parafermion hopping terms. This is of particular interest as chains of coupled parafermions can be used to generate even more exotic topological phases [59, 108].

In the setup we consider, the parafermion bound states can be described by operators $\alpha_L^{(\dagger)}$, $\alpha_R^{(\dagger)}$ which annihilate (create) parafermion zero modes at the left and right endpoints of the SC region, respectively, and satisfy the relations

$$\alpha_{L/R}^{2n} = 1, \;\; \alpha_{L/R}^{\dagger} = \alpha_{L/R}^{2n-1}, \;\; \text{and} \;\; \alpha_L \alpha_R = \alpha_R \alpha_L e^{i\frac{\pi}{n}}, \tag{6.53}$$

which are sufficient to ensure that these bound states have "parafermionic" non-Abelian statistics [9–12, 107].

In terms of the bosonized fields θ and ϕ, we have $\alpha_L^\dagger \alpha_R = e^{i\frac{\pi}{n}(q-1/2)}$, where $q = \frac{n}{\pi}(\theta(\frac{L}{2}) - \theta(-\frac{L}{2}))$ is the total charge in the SC segment modulo 2 [9–12]. From the commutation relation between ϕ and θ, it follows that

$$(\alpha_R^\dagger \alpha_L)\phi(\alpha_L^\dagger \alpha_R) = \phi + \frac{\pi}{n}, \quad (\alpha_L^\dagger \alpha_R)\phi(\alpha_R^\dagger \alpha_L) = \phi - \frac{\pi}{n},$$

which carrying out precisely the tunneling processes whose matrix elements we have just evaluated.

The low-energy Hamiltonian describing the parafermion tunneling between the two endpoints is therefore

$$H_A = t\alpha_L^\dagger \alpha_R + t^* \alpha_R^\dagger \alpha_L.$$

Its eigenstates are labeled by an integer $q = 0, 1, 2, \ldots, 2n-1$, and satisfy [9–12]

$$\alpha_L^\dagger \alpha_R |q\rangle = -e^{i\frac{\pi}{n}(q-\frac{1}{2})}|q\rangle, \quad \alpha_R^\dagger \alpha_L |q\rangle = -e^{-i\frac{\pi}{n}(q-\frac{1}{2})}|q\rangle. \tag{6.54}$$

Note that Eqs. (6.40) and (6.54) together also fix the phase associated with the action of the parafermion hopping term on the eigenstates of ϕ: $\alpha_L^\dagger \alpha_R |j\rangle = -e^{-i\frac{\pi}{2n}}|j+1\rangle$, $\alpha_R^\dagger \alpha_L |j\rangle = -e^{+i\frac{\pi}{2n}}|j-1\rangle$. The corresponding energies—which are precisely the energies that we have just obtained with our instanton calculation—are:

$$E(q) = -2\sqrt{t_\Re^2 + t_\Im^2}\cos\left[\frac{\pi}{n}\left(q - \frac{1}{2}\right) + \vartheta\right], \tag{6.55}$$

where we have defined $\tan\vartheta = t_\Im/t_\Re$, and $t_\Im$ ($t_\Re$) is the imaginary (real) part of t.

Comparing Eqs. (6.41) and (6.55) allows us to constrain $t_\Re$ and $t_\Im$. For Majorana fermions (i.e. $n = 1$), there is an additional constraint: Since $\alpha_{R/L}^\dagger = \alpha_{R/L}$, the two terms in Eq. (6.54) are not independent. This forces $t_\Re = 0$ (i.e. $\vartheta = \pm\pi/2$) and $t_\Im = \pm\hbar\mathcal{K}e^{-S_0/\hbar}\cos[\mu L/(\hbar n v)]$.

For $n > 1$ there is no such a constraint; however, in these cases matching the eigenvalues of both H and the operator $\alpha_L^\dagger \alpha_R = e^{i\left(\theta(\frac{L}{2})-\theta(-\frac{L}{2})-\pi/(2n)\right)}$ fixes ϑ, such that

$$t_{\Re} = \pm\hbar\mathcal{K} e^{-S_0/\hbar}\cos[\pi/(2n) - \mu L/(\hbar n v)], \tag{6.56}$$

$$t_{\Im} = \pm\hbar\mathcal{K} e^{-S_0/\hbar}\sin[\pi/(2n) - \mu L/(\hbar n v)]. \tag{6.57}$$

Using the analogous approach for an SC-FM-SC system (with $\mu \Rightarrow h$, $\Delta \Rightarrow \mathcal{B}$) gives the analogous conclusion. It is worth stressing that even at vanishing μ (or h), for $n > 1$ the hopping parameter t is complex with $\vartheta = \pi/(2n)$.

In the literature, there is a mapping (called Fradkin–Kadanoff transformation) between the parafermion chain and the chiral quantum clock model. We are now going to ask what the phase of t that we have calculated translates to in that mapping. More specifically, the μ-dependent contribution to ϑ in Eqs. (6.56) and (6.57) corresponds to a *chiral* phase [142–145] in the quantum clock model. To be concrete, let's briefly review the details of the Fradkin–Kadanoff mapping [8, 127, 146] between the parafermion chain and the chiral quantum clock model. We do this to explicitly demonstrate the relationship between the phase of the parafermion hopping terms and the resulting chiral phase in the clock model advertised above. Since the chiral phases do not arise in the Ising chain, here we consider the general parafermionic chain with $n > 1$.

We begin with a system of $2N$ parafermion zero modes $\{\alpha_{2k-1}, \alpha_{2k}\}, k = 1, 2, \ldots, N$ obtained by sequentially gapping the edges via Δ and $\mathcal{B}$. Depending on the sequential arrangement of the ferromagnets and the superconductors, there exist two types of inter-parafermion tunnelings. Specifically, we consider first the model of a parafermion chain whose leftmost structure assumes the arrangement of FM-SC-FM, where the leftmost FM region is semi-infinite. The corresponding Hamiltonian reads

$$H_{\text{FSF}} = \sum_{k=1}^{N}\left(t_{\text{SC}}\alpha_{2k-1}^\dagger\alpha_{2k} + t_{\text{SC}}^*\alpha_{2k}^\dagger\alpha_{2k-1}\right) + \sum_{k=1}^{N-1}\left(t_{\text{FM}}\alpha_{2k}^\dagger\alpha_{2k+1} + t_{\text{FM}}^*\alpha_{2k+1}^\dagger\alpha_{2k}\right), \tag{6.58}$$

where according to the results of our instanton calculation,

$$t_{\text{SC}} = \pm\hbar\mathcal{K}_\Delta e^{-S_\Delta/\hbar} e^{i\frac{\pi}{2n}} e^{-i\frac{\mu L}{\hbar n v}}, \quad t_{\text{FM}} = \pm\hbar\mathcal{K}_\mathcal{B} e^{-S_\mathcal{B}/\hbar} e^{i\frac{\pi}{2n}} e^{-i\frac{hL}{\hbar n v}}. \tag{6.59}$$

Here

$$S_\Delta = \frac{4\hbar L}{\pi n v}\sqrt{\Delta v/(\hbar\varsigma)}, \quad S_\mathcal{B} = \frac{4\hbar L}{\pi n v}\sqrt{\mathcal{B} v/(\hbar\varsigma)},$$
$$\mathcal{K}_\Delta = 2\sqrt{\Delta v/(\hbar\varsigma)}\cdot\sqrt{2S_\Delta/(\pi\hbar)}, \quad \mathcal{K}_\mathcal{B} = 2\sqrt{\mathcal{B} v/(\hbar\varsigma)}\cdot\sqrt{2S_\mathcal{B}/(\pi\hbar)}.$$

The low-energy parafermion Hamiltonian can be expressed in terms of the clock variables $\sigma_k,\ \tau_k$, which act on a $2n$-state-per-site spin Hilbert space and satisfy

$$\sigma_k^{2n} = \tau_k^{2n} = 1, \quad \sigma_k^\dagger = \sigma_k^{2n-1}, \quad \tau_k^\dagger = \tau_k^{2n-1}, \quad \sigma_k\tau_k = \tau_k\sigma_k e^{i\frac{\pi}{n}}. \tag{6.60}$$

The Fradkin–Kadanoff mapping implies the following relationships between the clock variables and the parafermion operators:

$$\tau_k = -e^{i\frac{\pi}{2n}}\alpha_{2k-1}^\dagger\alpha_{2k}, \quad \sigma_k^\dagger\sigma_{k+1} = -e^{i\frac{\pi}{2n}}\alpha_{2k}^\dagger\alpha_{2k+1}. \tag{6.61}$$

Inserting these expressions into Eq. (6.58), we obtain the Hamiltonian for the chiral quantum clock model:

$$\begin{aligned} H_{\text{clock}} &= -|t_{\text{SC}}|\sum_{k=1}^{N}\left(\pm e^{-i\frac{\mu L}{\hbar n v}}\tau_k \pm e^{i\frac{\mu L}{\hbar n v}}\tau_k^\dagger\right) - |t_{\text{FM}}|\sum_{k=1}^{N-1}\left(\pm e^{-i\frac{hL}{\hbar n v}}\sigma_k^\dagger\sigma_{k+1} \pm e^{i\frac{hL}{\hbar n v}}\sigma_{k+1}^\dagger\sigma_k\right) \\ &= -g\sum_{k=1}^{N}\left(e^{i\kappa}\tau_k^\dagger + e^{-i\kappa}\tau_k\right) - J\sum_{k=1}^{N-1}\left(e^{i\chi}\sigma_{k+1}^\dagger\sigma_k + e^{-i\chi}\sigma_k^\dagger\sigma_{k+1}\right), \end{aligned} \tag{6.62}$$

where the real non-negative clock couplings

$$g = |t_{\text{SC}}| = \hbar\mathcal{K}_\Delta e^{-S_\Delta/\hbar}, \quad J = |t_{\text{FM}}| = \hbar\mathcal{K}_\mathcal{B} e^{-S_\mathcal{B}/\hbar}.$$

For the "+" sign in Eq. (6.59), we find that the chiral phases $\kappa = \frac{\mu L}{\hbar n v},\ \chi = \frac{hL}{\hbar n v}$ ($\neq 0 \bmod \frac{\pi}{2n}$), while for the "−" sign in Eq. (6.59), the chiral phases become $\kappa = \frac{\mu L}{\hbar n v} + \pi,\ \chi = \frac{hL}{\hbar n v} + \pi$ ($\neq 0 \bmod \frac{\pi}{2n}$).

Analogously, for a parafermion chain whose leftmost segment takes the SC-FM-SC structure, we find the parallel results with the substitutions $\Delta \rightleftharpoons \mathcal{B},\ \mu \rightleftharpoons h$. Namely, in this case the real non-negative clock couplings $g = |t_{\text{FM}}| = \hbar\mathcal{K}_\mathcal{B} e^{-S_\mathcal{B}/\hbar},\ J = |t_{\text{SC}}| = \hbar\mathcal{K}_\Delta e^{-S_\Delta/\hbar}$. For the "+" sign in Eq. (6.59), we find that the chiral phases $\kappa = \frac{hL}{\hbar n v},\ \chi = \frac{\mu L}{\hbar n v}$ ($\neq 0 \bmod \frac{\pi}{2n}$), while for the "−" sign in Eq. (6.59), the chiral phases assume $\kappa = \frac{hL}{\hbar n v} + \pi,\ \chi = \frac{\mu L}{\hbar n v} + \pi$ ($\neq 0 \bmod \frac{\pi}{2n}$).

Therefore, our result shows that by tuning the chemical potential and the magnetic field at the FQH edges, the synthetic chiral phases κ and χ ($\neq 0 \bmod \frac{\pi}{2n}$) can be continuously varied in the sense that a system of $2N$ tunnel-coupled parafermion zero modes is dual via the Fradkin–Kadanoff mapping to an N-site chiral quantum clock chain, where with appropriate conventions hopping across a SC (FM) region maps to the transverse field (ferromagnetic clock) coupling.

Under duality, the phases of the parafermion hopping terms t map to a chiral phase of $\pm e^{i\frac{hL}{\hbar nv}}$ for the ferromagnetic clock coupling, as well as a chiral phase of $\pm e^{i\frac{\mu L}{\hbar nv}}$ for the transverse field term. Notice that the oscillatory dependence of the ground-state degeneracy splitting on the chiral phases and the system's size has been observed numerically for these chiral clock systems [127] recently.

6.5 Summary

In summary, our non-perturbative calculation shows that it is possible, in principle, to tune the magnitude of the ground-state splitting in parafermion systems (as well as the phase of the parafermion hopping parameter, for $n > 1$) by means of a chemical potential or an external magnetic field due to interference between distinct instanton trajectories resulting from a topological term in the effective action. Because the period of the resulting oscillations is given by $\mu L/(\hbar nv)$ (or $hL/(\hbar nv)$), this splitting can be fine-tuned with relatively small changes in μ (or h). As for Majorana fermions, we anticipate that this fact will be both of practical use to achieve quantum-coherent systems, and a potential signature of the existence of parafermions in these systems. Finally, our results might also be applicable to the spin-unpolarized $\nu = 2/3$ FQH heterostructures proposed by Refs. [108, 109].

References

[1] A. Y. Kitaev, Phys.-Usp. **44**, 131 (2001).

[2] L. Fu and C. L. Kane, Phys. Rev. Lett. **100**, 096407 (2008).

[3] J. Alicea, Phys. Rev. B **81**, 125318 (2009).

[4] J. D. Sau, R. M. Lutchyn, S. Tewari, and S. Das Sarma, Phys. Rev. Lett. **104**, 040502 (2010).

[5] R. M. Lutchyn, J. D. Sau, and S. Das Sarma, Phys. Rev. Lett. **105**, 077001 (2010).

[6] Y. Oreg, G. Refael, and F. von Oppen, Phys. Rev. Lett. **105**, 177002 (2010).

[7] J. Alicea, Y. Oreg, G. Refael, F. von Oppen, and M. P. A. Fisher, Nat. Phys. **7**, 412 (2011).

[8] P. Fendley, J. Stat. Mech. **2012**, 11020 (2012).

[9] D. J. Clarke, J. Alicea, and K. Shtengel, Nat. Commun. **4**, 1348 (2013).

[10] N. H. Lindner, E. Berg, G. Refael, and A. Stern, Phys. Rev. X **2**, 041002 (2012).

[11] M. Cheng, Phys. Rev. B **86**, 195126 (2012).

[12] A. Vaezi, Phys. Rev. B **87**, 035132 (2013).

[13] N. Read and D. Green, Phys. Rev. B **61**, 10267 (2000).

[14] C. Nayak, S. H. Simon, A. Stern, M. Freedman, and S. Das Sarma, Rev. Mod. Phys. **80**, 1083 (2008).

[15] A. P. Schnyder, S. Ryu, A. Furusaki, and A. W. W. Ludwig, Phys. Rev. B **78**, 195125 (2008).

[16] M. Franz, Nat. Nanotechnol. **8**, 149 (2013).

[17] E. Majorana, Nuovo Cimento **14**, 171 (1937).

[18] V. Mourik, K. Zuo, S. M. Frolov, S. R. Plissard, E. P. A. M. Bakkers, and L. P. Kouwenhoven, Science **336**, 1003 (2012).

[19] S. M. Albrecht, A. P. Higginbotham, M. Madsen, F. Kuemmeth, T. S. Jespersen, J. Nygård, P. Krogstrup, and C. M. Marcus, Nature **531**, 206 (2016).

[20] L. Fu and C. L. Kane, Phys. Rev. B **79**, 161408 (2009).

[21] V. S. Pribiag, A. J. A. Beukman, F. Qu, M. C. Cassidy, C. Charpentier, W. Wegscheider, and L. P. Kouwenhoven, Nat. Nanotechnol. **10**, 593 (2015).

[22] S. Hart, H. Ren, T. Wagner, P. Leubner, M. Mühlbauer, C. Brüne, H. Buhmann, L. W. Molenkamp, and A. Yacoby, Nat. Phys. **10**, 638 (2014).

[23] D. C. Tsui, H. L. Stormer, and A. C. Gossard, Phys. Rev. Lett. **48**, 1559 (1982).

[24] R. B. Laughlin, Phys. Rev. Lett. **50**, 1395 (1983).

[25] P. Fulde and R. A. Ferrell, Phys. Rev. **135**, A550 (1964).

[26] A. I. Larkin and Y. N. Ovchinnikov, Zh. Eksp. Teor. Fiz. **47**, 1136 (1964) [Sov. Phys. JETP **20**, 762 (1965)].

[27] C. Chen, Phys. Rev. Lett. **111**, 235302 (2013).

[28] C. Chen, W. Yan, C. S. Ting, Y. Chen, and F. J. Burnell, arXiv:1701.01794 (2017).

[29] C. Chen and F. J. Burnell, Phys. Rev. Lett. **116**, 106405 (2016).

[30] J. C. Budich and E. Ardonne, Phys. Rev. B **88**, 075419 (2013).

[31] H. O. H. Churchill, V. Fatemi, K. Grove-Rasmussen, M. T. Deng, P. Caroff, H. Q. Xu, and C. M. Marcus, Phys. Rev. B **87**, 241401 (2013).

[32] C. Zhang, S. Tewari, R. M. Lutchyn, and S. Das Sarma, Phys. Rev. Lett. **101**, 160401 (2008).

[33] M. Sato, Y. Takahashi, and S. Fujimoto, Phys. Rev. Lett. **103**, 020401 (2009).

[34] M. Sato, Y. Takahashi, and S. Fujimoto, Phys. Rev. B **82**, 134521 (2010).

[35] L. Jiang, T. Kitagawa, J. Alicea, A. R. Akhmerov, D. Pekker, G. Refael, J. I. Cirac, E. Demler, M. D. Lukin, and P. Zoller, Phys. Rev. Lett. **106**, 220402 (2011).

[36] R. Wei and E. J. Mueller, Phys. Rev. A **86**, 063604 (2012).

[37] X.-J. Liu and H. Hu, Phys. Rev. A **85**, 033622 (2012).

[38] F. Wu, G.-C. Guo, W. Zhang, and W. Yi, Phys. Rev. Lett. **110**, 110401 (2013).

[39] Y.-J. Lin, K. Jiménez-García, and I. B. Spielman, Nature (London) **471**, 83 (2011).

[40] V. Galitski and I. B. Spielman, Nature (London) **494**, 49 (2013).

[41] P. Wang, Z.-Q. Yu, Z. Fu, J. Miao, L. Huang, S. Chai, H. Zhai, and J. Zhang, Phys. Rev. Lett. **109**, 095301 (2012).

[42] L. W. Cheuk, A. T. Sommer, Z. Hadzibabic, T. Yefsah, W. S. Bakr, and M. W. Zwierlein, Phys. Rev. Lett. **109**, 095302 (2012).

[43] C. Chin, R. Grimm, P. Julienne, and E. Tiesinga, Rev. Mod. Phys. **82**, 1225 (2010).

[44] I. Bloch, J. Dalibard, and W. Zwerger, Rev. Mod. Phys. **80**, 885 (2008).

[45] I. Bloch, J. Dalibard, and S. Nascimbène, Nature Physics **8**, 267 (2012).

[46] A. C. Potter and P. A. Lee, Phys. Rev. Lett. **105**, 227003 (2010).

[47] A. C. Potter and P. A. Lee, Phys. Rev. B **83**, 094525 (2011).

[48] X.-J. Liu, H. Hu, and P. D. Drummond, Phys. Rev. A **76**, 043605 (2007).

[49] L. Radzihovsky, Phys. Rev. A **84**, 023611 (2011).

[50] Y.-a. Liao, A. S. C. Rittner, T. Paprotta, W. Li, G. B. Partridge, R. G. Hulet, S. K. Baur, and E. J. Mueller, Nature (London) **467**, 567 (2010).

[51] Y. A. Bychkov and E. I. Rashba, J. Phys. C **17**, 6039 (1984).

[52] G. Dresselhaus, Phys. Rev. **100**, 580 (1955).

[53] J. E. Birkholz and V. Meden, Phys. Rev. B **79**, 085420 (2009).

[54] J. You, C. H. Oh, and V. Vedral, Phys. Rev. B **87**, 054501 (2013).

[55] J. Alicea, Rep. Prog. Phys. **75**, 076501 (2012).

[56] P. Ghosh, J. D. Sau, S. Tewari, and S. Das Sarma, Phys. Rev. B **82**, 184525 (2010).

[57] H. Zhai, Rep. Prog. Phys. **78**, 026001 (2015).

[58] J. J. Kinnunen, J. E. Baarsma, J.-P. Martikainen, and P. Törmä, arXiv:1706.07076 (2017).

[59] E. M. Stoudenmire, J. Alicea, O. A. Starykh, and M. P. A. Fisher, Phys. Rev. B **84**, 014503 (2011).

[60] M. M. Vazifeh and M. Franz, Phys. Rev. Lett. **111**, 206802 (2013).

[61] J. Klinovaja, P. Stano, A. Yazdani, and D. Loss, Phys. Rev. Lett. **111**, 186805 (2013).

[62] B. Braunecker and P. Simon, Phys. Rev. Lett. **111**, 147202 (2013).

[63] R. S. K. Mong, D. J. Clarke, J. Alicea, N. H. Lindner, P. Fendley, C. Nayak, Y. Oreg, A. Stern, E. Berg, K. Shtengel, and M. P. A. Fisher, Phys. Rev. X **4**, 011036 (2014).

[64] Y.-H. Chan, C.-K. Chiu, and K. Sun, Phys. Rev. B **92**, 104514 (2015).

[65] C. Zhang, S. Tewari, R. M. Lutchyn, and S. Das Sarma, Phys. Rev. Lett. **101**, 160401 (2008).

[66] M. Sato, Y. Takahashi, and S. Fujimoto, Phys. Rev. Lett. **103**, 020401 (2009).

[67] C. Qu, Z. Zheng, M. Gong, Y. Xu, L. Mao, X. Zou, G. Guo, and C. Zhang, Nat. Commun. **4**, 2710 (2013).

[68] W. Zhang and W. Yi, Nat. Commun. **4**, 2711 (2013).

[69] X.-J. Liu and H. Hu, Phys. Rev. A **88**, 023622 (2013).

[70] J. Dalibard, F. Gerbier, G. Juzeliūnas, and P. Öhberg, Rev. Mod. Phys. **83**, 1523 (2011).

[71] N. Goldman, G. Juzeliūnas, P. Öhberg, and I. B. Spielman, Rep. Prog. Phys. **77**, 126401 (2014).

[72] N. Goldman, J. C. Budich, and P. Zoller, Nat. Phys. **12**, 639 (2016).

[73] A. P. Higginbotham, S. M. Albrecht, G. Kiršanskas, W. Chang, F. Kuemmeth, P. Krogstrup, T. S. Jespersen, J. Nygård, K. Flensberg, and C. M. Marcus, Nat. Phys. **11**, 1017 (2015).

[74] S. Nadj-Perge, I. K. Drozdov, J. Li, H. Chen, S. Jeon, J. Seo, A. H. MacDonald, B. A. Bernevig, and A. Yazdani, Science **346**, 602 (2014).

[75] A. Das, Y. Ronen, Y. Most, Y. Oreg, M. Heiblum, and H. Shtrikman, Nat. Phys. **8**, 887 (2012).

[76] M. T. Deng, C. L. Yu, G. Y. Huang, M. Larsson, P. Caroff, and H. Q. Xu, Nano Lett. **12**, 6414 (2012).

[77] L. Fidkowski, R. M. Lutchyn, C. Nayak, and M. P. A. Fisher, Phys. Rev. B **84**, 195436 (2011).

[78] M. Cheng and H.-H. Tu, Phys. Rev. B **84**, 094503 (2011).

[79] J. D. Sau, B. I. Halperin, K. Flensberg, and S. Das Sarma, Phys. Rev. B **84**, 144509 (2011).

[80] C. V. Kraus, M. Dalmonte, M. A. Baranov, A. M. Läuchli, and P. Zoller, Phys. Rev. Lett. **111**, 173004 (2013).

[81] N. Lang and H. P. Büchler, Phys. Rev. B **92**, 041118 (2015).

[82] F. Iemini, L. Mazza, D. Rossini, R. Fazio, and S. Diehl, Phys. Rev. Lett. **115**, 156402 (2015).

[83] G. Sun and T. Vekua, Phys. Rev. B **93**, 205137 (2016).

[84] M. Aidelsburger, M. Atala, S. Nascimbène, S. Trotzky, Y.-A. Chen, and I. Bloch, Phys. Rev. Lett. **107**, 255301 (2011).

[85] M. Aidelsburger, M. Atala, M. Lohse, J. T. Barreiro, B. Paredes, and I. Bloch, Phys. Rev. Lett. **111**, 185301 (2013).

[86] H. Miyake, G. A. Siviloglou, C. J. Kennedy, W. C. Burton, and W. Ketterle, Phys. Rev. Lett. **111**, 185302 (2013).

[87] M. Atala, M. Aidelsburger, J. T. Barreiro, D. Abanin, T. Kitagawa, E. Demler, and I. Bloch, Nat. Phys. **9**, 795 (2013).

[88] M. Atala, M. Aidelsburger, M. Lohse, J. T. Barreiro, B. Paredes, and I. Bloch, Nat. Phys. **10**, 588 (2014).

[89] G. Jotzu, M. Messer, R. Desbuquois, M. Lebrat, T. Uehlinger, D. Greif, and T. Esslinger, Nature (London) **515**, 237 (2014).

[90] L. F. Livi, G. Cappellini, M. Diem, L. Franchi, C. Clivati, M. Frittelli, F. Levi, D. Calonico, J. Catani, M. Inguscio, and L. Fallani, Phys. Rev. Lett. **117**, 220401 (2016).

[91] F. A. An, E. J. Meier, and B. Gadway, Sci. Adv. **3**, e1602685 (2017).

[92] S. Kolkowitz, S. L. Bromley, T. Bothwell, M. L. Wall, G. E. Marti, A. P. Koller, X. Zhang, A. M. Rey, and J. Ye, Nature **542**, 66 (2017).

[93] M. Mancini, G. Pagano, G. Cappellini, L. Livi, M. Rider, J. Catani, C. Sias, P. Zoller, M. Inguscio, M. Dalmonte, and L. Fallani, Science **349**, 1510 (2015).

[94] C. J. Kennedy, W. C. Burton, W. C. Chung, and W. Ketterle, Nat. Phys. **11**, 859 (2015).

[95] M. Aidelsburger, M. Lohse, C. Schweizer, M. Atala, J. T. Barreiro, S. Nascimbène, N. R. Cooper, I. Bloch, and N. Goldman, Nat. Phys. **11**, 162 (2015).

[96] J. Struck, C. Ölschläger, M. Weinberg, P. Hauke, J. Simonet, A. Eckardt, M. Lewenstein, K. Sengstock, and P. Windpassinger, Phys. Rev. Lett. **108**, 225304 (2012).

[97] L. Fidkowski and A. Kitaev, Phys. Rev. B **81**, 134509 (2010).

[98] T. Giamarchi, *Quantum Physics in One Dimension*, (Oxford University Press, New York, 2004).

[99] L. Fidkowski and A. Kitaev, Phys. Rev. B **83**, 075103 (2011).

[100] S. R. White, Phys. Rev. Lett. **69**, 2863 (1992).

[101] M. Dolfi, B. Bauer, S. Keller, A. Kosenkov, T. Ewart, A. Kantian, T. Giamarchi, and M. Troyer, Comput. Phys. Commun. **185**, 3430 (2014).

[102] A. W. Sandvik, AIP Conf. Proc. **1297**, 135 (2010).

[103] H. Li and F. D. M. Haldane, Phys. Rev. Lett. **101**, 010504 (2008).

[104] F. Pollmann, A. M. Turner, E. Berg, and M. Oshikawa, Phys. Rev. B **81**, 064439 (2010).

[105] A. Jaefari and E. Fradkin, Phys. Rev. B **85**, 035104 (2012).

[106] F. J. Burnell, A. Shnirman, and Y. Oreg, Phys. Rev. B **88**, 224507 (2013).

[107] M. Barkeshli and X.-L. Qi, Phys. Rev. X **2**, 031013 (2012).

[108] R. S. K. Mong, D. J. Clarke, J. Alicea, N. H. Lindner, P. Fendley, C. Nayak, Y. Oreg, A. Stern, E. Berg, K. Shtengel, and M. P. A. Fisher, Phys. Rev. X **4**, 011036 (2014).

[109] D. J. Clarke, J. Alicea, and K. Shtengel, Nat. Phys. **10**, 877 (2014).

[110] J. Klinovaja and D. Loss, Phys. Rev. Lett. **112**, 246403 (2014).

[111] A. S. Jermyn, R. S. K. Mong, J. Alicea, and P. Fendley, Phys. Rev. B **90**, 165106 (2014).

[112] M. Barkeshli, C.-M. Jian, and X.-L. Qi, Phys. Rev. B **88**, 235103 (2013).

[113] J. Alicea and P. Fendley, Annu. Rev. Condens. Matter Phys. **7**, 119 (2016).

[114] J. D. Sanchez-Yamagishi, J. Y. Luo, A. F. Young, B. M. Hunt, K. Watanabe, T. Taniguchi, R. C. Ashoori, and P. Jarillo-Herrero, Nat. Nanotechnol. **12**, 118 (2016).

[115] A. M. Turner, F. Pollmann, and E. Berg, Phys. Rev. B **83**, 075102 (2011).

[116] S. Das Sarma, J. D. Sau, and T. D. Stanescu, Phys. Rev. B **86**, 220506 (2012).

[117] S. R. Elliott and M. Franz, Rev. Mod. Phys. **87**, 137 (2015).

[118] A. A. Zyuzin, D. Rainis, J. Klinovaja, and D. Loss, Phys. Rev. Lett. **111**, 056802 (2013).

[119] D. Rainis, L. Trifunovic, J. Klinovaja, and D. Loss, Phys. Rev. B **87**, 024515 (2013).

[120] F. Maier, J. Klinovaja, and D. Loss, Phys. Rev. B **90**, 195421 (2014).

[121] M. Cheng, R. M. Lutchyn, V. Galitski, and S. Das Sarma, Phys. Rev. B **82**, 094504 (2010).

[122] M. Baraban, G. Zikos, N. Bonesteel, and S. H. Simon, Phys. Rev. Lett. **103**, 076801 (2009).

[123] V. Lahtinen, G. Kells, A. Carollo, T. Stitt, J. Vala, and J. K. Pachos, Ann. Phys. (N.Y.) **323**, 2286 (2008).

[124] M. Cheng, R. M. Lutchyn, V. Galitski, and S. Das Sarma, Phys. Rev. Lett. **103**, 107001 (2009).

[125] R. S. K. Mong, D. J. Clarke, J. Alicea, N. H. Lindner, and P. Fendley, J. Phys. A: Math. Theor. **47**, 452001 (2014).

[126] W. Li, S. Yang, H.-H. Tu, and M. Cheng, Phys. Rev. B **91**, 115133 (2015).

[127] Y. Zhuang, H. J. Changlani, N. M. Tubman, and T. L. Hughes, Phys. Rev. B **92**, 035154 (2015).

[128] X.-G. Wen, *Quantum Field Theory of Many-Body Systems*, (Oxford University Press, New York, 2004).

[129] X.-G. Wen, Advances in Physics **44**, 405 (1995).

[130] Z. Bajnok, L. Palla, G. Takács, and F. Wágner, Nucl. Phys. B **587**, 585 (2000).

[131] Y. I. Frenkel and T. K. Kontorova, Zh. Éksp. Teor. Fiz. **8**, 1340 (1938) [Phys. Z. Sowjetunion **13**, 1 (1938)].

[132] T. H. R. Skyrme, Proc. Roy. Soc. Lond. A **247**, 260 (1958).

[133] T. H. R. Skyrme, Proc. Roy. Soc. Lond. A **262**, 237 (1961).

[134] L. Landau and E. Lifshitz, *Quantum Mechanics*, (Pergamon Press, New York, 1977), 3rd ed., Vol. 3.

[135] A. M. Polyakov, Nucl. Phys. B **120**, 429 (1977).

[136] S. Coleman, *Aspects of symmetry*, (Cambridge University Press, New York, 1985).

[137] A. I. Vaĭnshteĭn, V. I. Zakharov, V. A. Novikov, and M. A. Shifman, Usp. Fiz. Nauk **136**, 553 (1982) [Sov. Phys. Usp. **25**, 195 (1982)].

[138] G. Münster, Nucl. Phys. B **324**, 630 (1989).

[139] V. Shivamoggi, G. Refael, and J. E. Moore, Phys. Rev. B **82**, 041405 (2010).

[140] P. Bonderson, Phys. Rev. Lett. **103**, 110403 (2009).

[141] M. Barkeshli, P. Bonderson, M. Cheng, and Z. Wang, arXiv:1410.4540v2 (2014).

[142] P. Fendley, J. Phys. A: Math. Theor. **47**, 075001 (2014).

[143] R. J. Baxter, J. Phys. A: Math. Theor. **47**, 315001 (2014).

[144] H. Au-Yang and J. H. H. Perk, J. Phys. A: Math. Theor. **47**, 315002 (2014).

[145] It is worth noticing that the chiral phases are not allowed in the Ising chain.

[146] E. Fradkin and L. P. Kadanoff, Nucl. Phys. B **170**, 1 (1980).

Appendix A

Additional derivations of the dissipative terms

A.1 The first dissipative term

Part 2 Let us further choose $A_\alpha = A_2 = c_R^\dagger;\ A_\beta = A_2 = c_R^\dagger$. Then we would have

$$X_\alpha = \sum_\epsilon \left[\alpha_R^{(1)} f_{R,\epsilon} + \alpha_R^{(2)} f_{R,\epsilon}^\dagger\right], \tag{A.1}$$

$$X_\beta = \sum_\epsilon \left[\alpha_R^{(1)} f_{R,\epsilon} + \alpha_R^{(2)} f_{R,\epsilon}^\dagger\right], \tag{A.2}$$

and

$$\tilde{X}_\alpha(\tau) = \sum_\epsilon \left[\alpha_R^{(1)} f_{R,\epsilon} e^{-i\omega_\epsilon \tau} + \alpha_R^{(2)} f_{R,\epsilon}^\dagger e^{i\omega_\epsilon \tau}\right], \tag{A.3}$$

$$\tilde{X}_\alpha^\dagger(\tau) = \sum_\epsilon \left[\bar{\alpha}_R^{(1)} f_{R,\epsilon}^\dagger e^{i\omega_\epsilon \tau} + \bar{\alpha}_R^{(2)} f_{R,\epsilon} e^{-i\omega_\epsilon \tau}\right]. \tag{A.4}$$

Analogously, when combining them, we would get

$$\tilde{X}_\alpha^\dagger(\tau) X_\beta = \sum_\epsilon \left[\bar{\alpha}_R^{(1)} f_{R,\epsilon}^\dagger e^{i\omega_\epsilon \tau} + \bar{\alpha}_R^{(2)} f_{R,\epsilon} e^{-i\omega_\epsilon \tau}\right] \times \sum_{\epsilon'} \left[\alpha_R^{(1)} f_{R,\epsilon'} + \alpha_R^{(2)} f_{R,\epsilon'}^\dagger\right], \tag{A.5}$$

and the expectation value reads

$$\langle \tilde{X}_\alpha^\dagger(\tau) X_\beta \rangle = \sum_\epsilon \left[|\alpha_R^{(1)}|^2 n_F(\hbar\omega_\epsilon) e^{i\omega_\epsilon \tau} + |\alpha_R^{(2)}|^2 n_F(-\hbar\omega_\epsilon) e^{-i\omega_\epsilon \tau}\right]. \tag{A.6}$$

Or

$$\langle \tilde{X}_2^\dagger(\tau) X_2 \rangle = \sum_{[\epsilon]} \left(|\alpha_R^{(1)}|^2 + |\alpha_R^{(2)}|^2 \right) \rho_R n_F(\hbar\omega_\epsilon) e^{i\omega_\epsilon \tau}. \tag{A.7}$$

Therefore we can derive the expression for $\Gamma_{22}(\Omega)$, which is defined by $\int_{-\infty}^{\infty} d\tau e^{i\Omega\tau} \langle \tilde{X}_2^\dagger(\tau) X_2 \rangle$, as follows:

$$\Gamma_{22}(\Omega) = \sum_{[\epsilon]} \left(|\alpha_R^{(1)}|^2 + |\alpha_R^{(2)}|^2 \right) \rho_R n_F(\hbar\omega_\epsilon) \delta(\Omega + \omega_\epsilon). \tag{A.8}$$

Similarly the term $\frac{1}{\hbar^2} \sum_\Omega \Gamma_{22}(\Omega) c_R^\dagger(\Omega) \rho_A(t) c_R(\Omega)$ can be calculated straightforwardly as follows:

$$\begin{aligned}
&\frac{1}{\hbar^2} \sum_\Omega \Gamma_{22}(\Omega) c_R^\dagger(\Omega) \rho_A(t) c_R(\Omega) \\
&\quad = \frac{1}{\hbar^2} \sum_\Omega \sum_{[\epsilon]} \left(|\alpha_R^{(1)}|^2 + |\alpha_R^{(2)}|^2 \right) \rho_R n_F(\hbar\omega_\epsilon) \delta(\Omega + \omega_\epsilon) \times c_R^\dagger(\Omega) \rho_A(t) c_R(\Omega) \\
&\quad = \frac{1}{\hbar^2} \sum_{[\epsilon]} \left(|\alpha_R^{(1)}|^2 + |\alpha_R^{(2)}|^2 \right) \rho_R n_F(\hbar\omega_\epsilon) \times c_R^\dagger(-\omega_\epsilon) \rho_A(t) c_R(-\omega_\epsilon) \\
&\quad = \frac{1}{\hbar^2} \sum_{[\epsilon]} \left(|\alpha_R^{(1)}|^2 + |\alpha_R^{(2)}|^2 \right) \rho_R n_F(\hbar\omega_\epsilon) \times \sum_{a,b,a',b'} \delta(\omega_{ba} + \omega_\epsilon) \delta(\omega_{a'b'} + \omega_\epsilon) \\
&\quad \times |a\rangle\langle a| c_R^\dagger |b\rangle\langle b| \rho_A(t) |a'\rangle\langle a'| c_R |b'\rangle\langle b'| \\
&\quad = \frac{\left(|\alpha_R^{(1)}|^2 + |\alpha_R^{(2)}|^2 \right) \rho_R}{\hbar^2} \sum_{a,b} \sum_{a',b'} n_F(-\hbar\omega_{ba}) \delta(\omega_{a'b'} - \omega_{ba}) \\
&\quad \times |a\rangle\langle a| c_R^\dagger |b\rangle\langle b| \rho_A(t) |a'\rangle\langle a'| c_R |b'\rangle\langle b'|.
\end{aligned} \tag{A.9}$$

It can be easily checked that

$$\hbar\omega_{ab} = 2t_{34} \begin{cases} \langle 1,0|c_R|1,1\rangle = -1 \\ \langle 0,0|c_R|0,1\rangle = +1 \end{cases}, \tag{A.10}$$

and

$$\hbar\omega_{ba} = 2t_{34} \begin{cases} \langle 1,1|c_R^\dagger|1,0\rangle = -1 \\ \langle 0,1|c_R^\dagger|0,0\rangle = +1 \end{cases}, \tag{A.11}$$

then

$$\begin{aligned}\frac{1}{\hbar^2}\sum_{\Omega}&\Gamma_{22}(\Omega)c_R^\dagger(\Omega)\rho_A(t)c_R(\Omega)\\ &=\frac{1}{\hbar^2}\left(|\alpha_R^{(1)}|^2+|\alpha_R^{(2)}|^2\right)\rho_R n_F(-2t_{34})\\ &\times\sum_{a,b}\sum_{a',b'}|a\rangle\langle a|c_R^\dagger|b\rangle\langle b|\rho_A(t)|a'\rangle\langle a'|c_R|b'\rangle\langle b'|.\end{aligned}\tag{A.12}$$

If we set $\Gamma_1=\frac{1}{\hbar^2}\left(|\alpha_R^{(1)}|^2+|\alpha_R^{(2)}|^2\right)\rho_R n_F(-2t_{34})$ and $L_1=c_R^\dagger$ (in matrix form),

$$\frac{1}{\hbar^2}\sum_{\Omega}\Gamma_{22}(\Omega)c_R^\dagger(\Omega)\rho_A(t)c_R(\Omega)=\Gamma_1 L_1\rho_A(t)L_1^\dagger\tag{A.13}$$

in matrices.

Part 3 Let us next prove that if we choose $A_\alpha=A_1=c_R;\ A_\beta=A_2=c_R^\dagger$, the dissipation term will vanish because the two δ-functions cannot be simultaneously satisfied in this case.

Similarly, we would have

$$X_\alpha=X_1=\sum_{\epsilon}\left[\bar{\alpha}_R^{(1)}f_{R,\epsilon}^\dagger+\bar{\alpha}_R^{(2)}f_{R,\epsilon}\right],\tag{A.14}$$

$$X_\beta=X_2=\sum_{\epsilon}\left[\alpha_R^{(1)}f_{R,\epsilon}+\alpha_R^{(2)}f_{R,\epsilon}^\dagger\right],\tag{A.15}$$

and

$$\tilde{X}_\alpha(\tau)=\sum_{\epsilon}\left[\bar{\alpha}_R^{(1)}f_{R,\epsilon}^\dagger e^{i\omega_\epsilon\tau}+\bar{\alpha}_R^{(2)}f_{R,\epsilon}e^{-i\omega_\epsilon\tau}\right],\tag{A.16}$$

$$\tilde{X}_\alpha^\dagger(\tau)=\sum_{\epsilon}\left[\alpha_R^{(1)}f_{R,\epsilon}e^{-i\omega_\epsilon\tau}+\alpha_R^{(2)}f_{R,\epsilon}^\dagger e^{i\omega_\epsilon\tau}\right].\tag{A.17}$$

Analogously, when combining them, we would get

$$\begin{aligned}\tilde{X}_\alpha^\dagger(\tau)X_\beta&=\tilde{X}_1^\dagger(\tau)X_2\\ &=\sum_{\epsilon}\left[\alpha_R^{(1)}f_{R,\epsilon}e^{-i\omega_\epsilon\tau}+\alpha_R^{(2)}f_{R,\epsilon}^\dagger e^{i\omega_\epsilon\tau}\right]\\ &\times\sum_{\epsilon'}\left[\alpha_R^{(1)}f_{R,\epsilon'}+\alpha_R^{(2)}f_{R,\epsilon'}^\dagger\right],\end{aligned}\tag{A.18}$$

and the expectation value reads

$$\langle \tilde{X}_1^\dagger(\tau) X_2 \rangle = \sum_\epsilon 2\alpha_R^{(1)}\alpha_R^{(2)} n_F(\hbar\omega_\epsilon) e^{i\omega_\epsilon \tau}. \tag{A.19}$$

Thus

$$\Gamma_{12}(\Omega) = \sum_{[\epsilon]} [2\alpha_R^{(1)}\alpha_R^{(2)} n_F(\hbar\omega_\epsilon)\delta(\Omega+\omega_\epsilon)]. \tag{A.20}$$

However, when plugging in the *differing* expressions for the *same* operators $c_R^\dagger$ before and after the density operator $\rho_A(t)$, we find that the resulting two δ-functions cannot be matched,

$$\begin{aligned}
&\frac{1}{\hbar^2}\sum_\Omega \Gamma_{12}(\Omega) c_R^\dagger(\Omega)\rho_A(t)c_R^\dagger(\Omega) \\
&\quad = \frac{1}{\hbar^2}\sum_\Omega \sum_{[\epsilon]} [2\alpha_R^{(1)}\alpha_R^{(2)}\rho_R n_F(\hbar\omega_\epsilon)\delta(\Omega+\omega_\epsilon)] \\
&\quad \times \sum_{a,b,a',b'} \delta(\omega_{ba}-\Omega)\delta(\omega_{a'b'}-\Omega) \\
&\quad \times |a\rangle\langle a|c_R^\dagger|b\rangle\langle b|\rho_A(t)|a'\rangle\langle a'|c_R^\dagger|b'\rangle\langle b'| \\
&\quad = \frac{2\alpha_R^{(1)}\alpha_R^{(2)}\rho_R}{\hbar^2}\sum_{a,b}\sum_{a',b'} n_F(-\hbar\omega_{ba})\delta(\omega_{a'b'}-\omega_{ba}) \\
&\quad \times |a\rangle\langle a|c_R^\dagger|b\rangle\langle b|\rho_A(t)|a'\rangle\langle a'|c_R^\dagger|b'\rangle\langle b'| \\
&\quad = 0,
\end{aligned} \tag{A.21}$$

since

$$\begin{aligned} \hbar\omega_{ab} &= -2t_{34} \\ \hbar\omega_{ba} &= +2t_{34} \end{aligned} \quad \begin{cases} \langle 1,1|c_R^\dagger|1,0\rangle = -1 \\ \langle 0,1|c_R^\dagger|0,0\rangle = +1 \end{cases}, \tag{A.22}$$

and $\delta(\omega_{a'b'}-\omega_{ba})$ is identically vanishing.

Part 4 We can also prove that if we choose $A_\alpha = A_2 = c_R^\dagger;\ A_\beta = A_1 = c_R$, the corresponding dissipation term vanishes in a parallel way.

A.2 The second dissipative term

Part 2 Let's choose $A_\alpha = A_2 = c_R^\dagger;\ A_\beta = A_2 = c_R^\dagger$, then

$$\Gamma_{22}(\Omega) = \sum_{[\epsilon]} \left(|\alpha_R^{(1)}|^2 + |\alpha_R^{(2)}|^2 \right) \rho_R n_F(\hbar\omega_\epsilon)\delta(\Omega+\omega_\epsilon), \tag{A.23}$$

thus

$$
\begin{aligned}
&-\frac{1}{2\hbar^2}\sum_{\Omega}\Gamma_{22}(\Omega)[A_2^\dagger(\Omega)A_2(\Omega)\rho_A(t)+\rho_A(t)A_2^\dagger(\Omega)A_2(\Omega)] \\
&\qquad=-\frac{\left(|\alpha_R^{(1)}|^2+|\alpha_R^{(2)}|^2\right)}{2\hbar^2}\rho_R\sum_{[\epsilon]}n_F(\hbar\omega_\epsilon) \\
&\qquad\times[A_2^\dagger(-\omega_\epsilon)A_2(-\omega_\epsilon)\rho_A(t)+\rho_A(t)A_2^\dagger(-\omega_\epsilon)A_2(-\omega_\epsilon)] \\
&\qquad=-\frac{\left(|\alpha_R^{(1)}|^2+|\alpha_R^{(2)}|^2\right)}{2\hbar^2}\rho_R\sum_{[\epsilon]}n_F(\hbar\omega_\epsilon) \\
&\qquad\times\sum_{a,b,a',b'}[\delta(\omega_{ab}+\omega_\epsilon)\delta(\omega_{b'a'}+\omega_\epsilon) \\
&\qquad\times(|a\rangle\langle a|c_R|b\rangle\langle b|a'\rangle\langle a'|c_R^\dagger|b'\rangle\langle b'|\rho_A(t)+\rho_A(t)|a\rangle\langle a|c_R|b\rangle\langle b|a'\rangle\langle a'|c_R^\dagger|b'\rangle\langle b'|)\Big] \\
&\qquad=-\frac{\left(|\alpha_R^{(1)}|^2+|\alpha_R^{(2)}|^2\right)}{2\hbar^2}\rho_R\sum_{a,b,a',b'}n_F(-\hbar\omega_{ab})\delta(\omega_{b'a'}-\omega_{ab}) \\
&\qquad\times\left[|a\rangle\langle a|c_R|b\rangle\langle b|a'\rangle\langle a'|c_R^\dagger|b'\rangle\langle b'|\rho_A(t)+\rho_A(t)|a\rangle\langle a|c_R|b\rangle\langle b|a'\rangle\langle a'|c_R^\dagger|b'\rangle\langle b'|\right].
\end{aligned}
\tag{A.24}
$$

As usual, we know that

$$
\hbar\omega_{ab}=2t_{34}\begin{cases}\langle 1,0|c_R|1,1\rangle=-1\\ \langle 0,0|c_R|0,1\rangle=+1\end{cases},
$$

hence

$$
\begin{aligned}
&-\frac{1}{2\hbar^2}\sum_{\Omega}\Gamma_{22}(\Omega)[c_R(\Omega)c_R^\dagger(\Omega)\rho_A(t)+\rho_A(t)c_R(\Omega)c_R^\dagger(\Omega)] \\
&\qquad=-\frac{\left(|\alpha_R^{(1)}|^2+|\alpha_R^{(2)}|^2\right)}{2\hbar^2}\rho_R n_F(-2t_{34}) \\
&\qquad\times\sum_{a,b,b'}\left[|a\rangle\langle a|c_R|b\rangle\langle b|c_R^\dagger|b'\rangle\langle b'|\rho_A(t)+\rho_A(t)|a\rangle\langle a|c_R|b\rangle\langle b|c_R^\dagger|b'\rangle\langle b'|\right].
\end{aligned}
\tag{A.25}
$$

Remember $\Gamma_1=\frac{1}{\hbar^2}(|\alpha_R^{(1)}|^2+|\alpha_R^{(2)}|^2)\rho_R n_F(-2t_{34})$, and it can be derived that

$$
\begin{aligned}
&-\frac{1}{2\hbar^2}\sum_{\Omega}\Gamma_{22}(\Omega)[c_R(\Omega)c_R^\dagger(\Omega)\rho_A(t)+\rho_A(t)c_R(\Omega)c_R^\dagger(\Omega)] \\
&\qquad=-\frac{1}{2}\Gamma_1(L_1^\dagger L_1\rho_A(t)+\rho_A(t)L_1^\dagger L_1)
\end{aligned}
\tag{A.26}
$$

in matrix forms.

Part 3 and 4 It can be easily shown that terms containing $c_R(\Omega)c_R(\Omega)$ or $c_R^\dagger(\Omega)c_R^\dagger(\Omega)$ vanish. For instance,

$$\begin{aligned} c_R(\Omega)c_R(\Omega) &= \sum_{a,b}\sum_{a',b'} \delta(\omega_{ab}-\Omega)\delta(\omega_{b'a'}-\Omega) \times [|a\rangle\langle a|c_R|b\rangle\langle b|a'\rangle\langle a'|c_R|b'\rangle\langle b'|] \\ &= \sum_{a,b,b'} \delta(\omega_{ab}-\Omega)\delta(\omega_{b'a'}-\Omega)|a\rangle\langle a|c_R|b\rangle\langle b|c_R|b'\rangle\langle b'|. \end{aligned}$$

However, $\sum_b \langle a|c_R|b\rangle\langle b|c_R|b'\rangle = 0$. The same conclusion holds for the term with $c_R^\dagger(\Omega)c_R^\dagger(\Omega)$.

Appendix B

Splitting of ground-state energy in spin-Hall edge: A wavefunction approach

B.1 Wavefunctions of the Majorana bound states in quantum spin Hall heterostructures

For completeness and also as an important check, let us discuss the Majorana zero modes at the edge of a 2D quantum spin Hall system which is in close proximity to an s-wave superconductor and two ferromagnetic insulators. We assume that the right movers carry spin up and the left movers carry spin down. The Bogoliubov–de Gennes (BdG) Hamiltonian for the edge states is as follows,

$$\mathcal{H}(x) = -iv_F\tau_z\sigma_z\partial_x - \mu(x)\tau_z - \Delta(x)\tau_x + \mathcal{B}(x)\sigma_x. \tag{B.1}$$

The Pauli matrices $\vec{\tau}$ and $\vec{\sigma}$ act on the particle-hole and spin spaces, respectively. To focus our discussion, we consider the FM-SC-FM setup shown in Fig. 6.1. Neglecting the width of the domain wall region, this gives the following spatial profiles for the locally gated chemical

potential and the strengths of the proximity-induced potential terms:

$$\mu(x) = \mu\Theta(x + \frac{L}{2})\Theta(-x + \frac{L}{2}), \tag{B.2}$$

$$\Delta(x) = \Delta\Theta(x + \frac{L}{2})\Theta(-x + \frac{L}{2}), \tag{B.3}$$

$$\mathcal{B}(x) = \mathcal{B}(1 - \Theta(x + \frac{L}{2})\Theta(-x + \frac{L}{2})). \tag{B.4}$$

Here the potential strengths $\Delta \sim \mathcal{B} \gg |\mu| \neq 0$ and $\Theta(x)$ is the Heaviside step function. We also assume that the chemical potential term can be generated by locally gating the edge.

With the linear dispersion relation in Eq. (B.1), analytical solutions for the Majorana bound states can easily be obtained in the limit that the two bound states are infinitely far apart. Specifically, if we divide $\mathcal{H}(x)$ into the left and right parts for $x \in (-\infty, \infty)$,

$$\mathcal{H}(x) = \mathcal{H}_L(x) + \mathcal{U}_R(x) = \mathcal{H}_R(x) + \mathcal{U}_L(x), \tag{B.5}$$

where

$$\mathcal{H}_L(x) = \begin{pmatrix} -iv_F\partial_x - \mu_L(x) & \mathcal{B}_L(x) & -\Delta_L(x) & 0 \\ \mathcal{B}_L(x) & iv_F\partial_x - \mu_L(x) & 0 & -\Delta_L(x) \\ -\Delta_L(x) & 0 & iv_F\partial_x + \mu_L(x) & \mathcal{B}_L(x) \\ 0 & -\Delta_L(x) & \mathcal{B}_L(x) & -iv_F\partial_x + \mu_L(x) \end{pmatrix}, \tag{B.6}$$

$$\mathcal{U}_R(x) = \begin{pmatrix} -\tilde{\mu}_R(x) & \mathcal{B}_R(x) & -\tilde{\Delta}_R(x) & 0 \\ \mathcal{B}_R(x) & -\tilde{\mu}_R(x) & 0 & -\tilde{\Delta}_R(x) \\ -\tilde{\Delta}_R(x) & 0 & \tilde{\mu}_R(x) & \mathcal{B}_R(x) \\ 0 & -\tilde{\Delta}_R(x) & \mathcal{B}_R(x) & \tilde{\mu}_R(x) \end{pmatrix}, \tag{B.7}$$

with

$$\mu_L(x) = \mu\Theta(x + \frac{L}{2}),\ \Delta_L(x) = \Delta\Theta(x + \frac{L}{2}),\ \mathcal{B}_L(x) = \mathcal{B}\Theta(-x - \frac{L}{2}), \tag{B.8}$$

$$\tilde{\mu}_R(x) = -\mu\Theta(x - \frac{L}{2}),\ \tilde{\Delta}_R(x) = -\Delta\Theta(x - \frac{L}{2}),\ \mathcal{B}_R(x) = \mathcal{B}\Theta(x - \frac{L}{2}). \tag{B.9}$$

Similar forms can be constructed for $\mathcal{H}_R(x)$ and $\mathcal{U}_L(x)$ by noticing that

$$\mathcal{H}_L(x) = K\mathcal{H}_R(-x)K,\ \mathcal{U}_R(x) = \mathcal{U}_L(-x),\ \mu_L(x) = \mu_R(-x),$$
$$\tilde{\mu}_L(x) = \tilde{\mu}_R(-x),\ \Delta_L(x) = \Delta_R(-x),\ \tilde{\Delta}_L(x) = \tilde{\Delta}_R(-x),\ \mathcal{B}_L(x) = \mathcal{B}_R(-x).$$

Typically, $\mathcal{H}_{L,R}(x)$ and $\mathcal{U}_{R,L}(x)$ are spatially well-separated from each other, which allows to firstly approximately focus on the Majorana zero mode from only the part of $\mathcal{H}_{L,R}(x)$, then adding the treatment of $\mathcal{U}_{R,L}(x)$ as the perturbation.

Left Majorana zero mode. We are now in a position to find the analytical wavefunction for the normalizable Majorana bound state in the left domain wall $x = -\frac{L}{2}$ by solving the following reduced 1D Dirac equation with the proper boundary conditions,

$$\begin{pmatrix} -iv_F\partial_x - \mu_L(x) & \mathcal{B}_L(x) & -\Delta_L(x) & 0 \\ \mathcal{B}_L(x) & iv_F\partial_x - \mu_L(x) & 0 & -\Delta_L(x) \\ -\Delta_L(x) & 0 & iv_F\partial_x + \mu_L(x) & \mathcal{B}_L(x) \\ 0 & -\Delta_L(x) & \mathcal{B}_L(x) & -iv_F\partial_x + \mu_L(x) \end{pmatrix} \begin{pmatrix} u(x) \\ w(x) \\ w^*(x) \\ -u^*(x) \end{pmatrix} = 0. \quad \text{(B.10)}$$

The self-conjugate Majorana form of the spinor here is fixed by particle-hole symmetry, defined in real space by the operator $\Xi \equiv \tau_y \otimes \sigma_y K$, where $\tau_y \otimes \sigma_y$ is the charge conjugation matrix and K denotes complex conjugation. Ξ anticommutes with $\mathcal{H}(x)$, and hence constrains the form of the zero-energy solutions.

In the region $x \geq -\frac{L}{2}$, solving Eq. (B.10) yields the 2-component zero-mode eigenvector,

$$\chi_0(x) = \begin{pmatrix} u(x) \\ w^*(x) \end{pmatrix} = \chi_{-\frac{L}{2}} \begin{pmatrix} 1 \\ i \end{pmatrix} \exp\left(i\frac{\mu}{v_F}(x + \frac{L}{2}) - \frac{\Delta}{v_F}(x + \frac{L}{2}) \right), \quad \text{(B.11)}$$

where $\Delta > 0$, and $\chi_{-\frac{L}{2}}$ is a constant to be fixed by the continuity of the wavefunction.

Similarly, we can solve for the wavefunction of the left Majorana zero mode in the region $x \leq -\frac{L}{2}$, where the 2-component zero-mode eigenvector assumes

$$\zeta_0(x) = \begin{pmatrix} u(x) \\ w(x) \end{pmatrix} = \zeta_{-\frac{L}{2}} \begin{pmatrix} -i \\ 1 \end{pmatrix} \exp\left(\frac{\mathcal{B}}{v_F}(x + \frac{L}{2}) \right), \quad \text{(B.12)}$$

with $\mathcal{B} > 0$, and $\zeta_{-\frac{L}{2}}$ is a constant to be fixed by the continuity of the wavefunction.

The complex constants $\chi_{-\frac{L}{2}}$ and $\zeta_{-\frac{L}{2}}$ can be constrained by equating Eqs. (B.11) and (B.12) at $x = -\frac{L}{2}$ due to the continuity of the wavefunction: $\zeta_{-\frac{L}{2}} = -\chi_{\Im},\ \chi_{-\frac{L}{2}} = i\chi_{\Im}$, where $\chi_{\Im}$ is a real constant to be fixed by the normalization condition.

The 4-component wavefunction of the left Majorana zero mode Ψ_L thus becomes (up to

normalization),

$$\Psi_L(x) = \chi_{\Im}\left\{\begin{pmatrix} i\exp\left(i\frac{\mu}{v_F}(x+\frac{L}{2})\right) \\ -\exp\left(-i\frac{\mu}{v_F}(x+\frac{L}{2})\right) \\ -\exp\left(i\frac{\mu}{v_F}(x+\frac{L}{2})\right) \\ i\exp\left(-i\frac{\mu}{v_F}(x+\frac{L}{2})\right) \end{pmatrix} e^{-\frac{\Delta}{v_F}(x+\frac{L}{2})}\Theta(x+\frac{L}{2}) + \begin{pmatrix} i \\ -1 \\ -1 \\ i \end{pmatrix} e^{\frac{\mathcal{B}}{v_F}(x+\frac{L}{2})}\Theta(-x-\frac{L}{2})\right\}. \tag{B.13}$$

Right Majorana zero mode. Since $\mathcal{H}_L(x) = K\mathcal{H}_R(-x)K$, we can directly derive the wavefunction for the right Majorana zero mode $\Psi_R(x) = K\Psi_L(-x) = \Psi_L^*(-x)$, namely,

$$\Psi_R(x) = \chi_{\Im}\left\{\begin{pmatrix} -i\exp\left(i\frac{\mu}{v_F}(x-\frac{L}{2})\right) \\ -\exp\left(-i\frac{\mu}{v_F}(x-\frac{L}{2})\right) \\ -\exp\left(i\frac{\mu}{v_F}(x-\frac{L}{2})\right) \\ -i\exp\left(-i\frac{\mu}{v_F}(x-\frac{L}{2})\right) \end{pmatrix} e^{\frac{\Delta}{v_F}(x-\frac{L}{2})}\Theta(-x+\frac{L}{2}) + \begin{pmatrix} -i \\ -1 \\ -1 \\ -i \end{pmatrix} e^{-\frac{\mathcal{B}}{v_F}(x-\frac{L}{2})}\Theta(x-\frac{L}{2})\right\}. \tag{B.14}$$

B.2 Zero-bias splitting due to Majorana wavefunction overlaps in the FM-SC-FM setup

If we assume $|\Phi_g^+(x)\rangle$ is the eigenstate of the full BdG Hamiltonian $\mathcal{H}(x)$ with eigenenergy $\mathcal{E}_+$, namely $\mathcal{H}(x)|\Phi_g^+(x)\rangle = \mathcal{E}_+|\Phi_g^+(x)\rangle$, then according to the particle-hole symmetry, we will have $\mathcal{H}(x)\left(\Xi|\Phi_g^+(x)\rangle\right) = -\mathcal{E}_+\left(\Xi|\Phi_g^+(x)\rangle\right)$, therefore we denote $|\Phi_g^-(x)\rangle = \Xi|\Phi_g^+(x)\rangle$, which satisfies $\mathcal{H}(x)|\Phi_g^-(x)\rangle = \mathcal{E}_-|\Phi_g^-(x)\rangle = -\mathcal{E}_+|\Phi_g^-(x)\rangle$. One can check that $\Xi|\Psi_R(x)\rangle =$

$|\Psi_R(x)\rangle,\ \Xi|\Psi_L(x)\rangle = |\Psi_L(x)\rangle$, thus we can safely assume

$$|\Phi_g^{\pm}(x)\rangle = \frac{1}{\sqrt{2}}\left(|\Psi_R(x)\rangle \pm i|\Psi_L(x)\rangle\right) = \pm\frac{i}{\sqrt{2}}\left(|\Psi_L(x)\rangle \mp i|\Psi_R(x)\rangle\right), \tag{B.15}$$

$$\begin{aligned}|\Phi_g^{\pm}(-x)\rangle &= \frac{1}{\sqrt{2}}\left(|\Psi_R(-x)\rangle \pm i|\Psi_L(-x)\rangle\right) = \frac{1}{\sqrt{2}}\left(K|\Psi_L(x)\rangle \pm iK|\Psi_R(x)\rangle\right)\\ &= \pm iK|\Phi_g^{\pm}(x)\rangle.\end{aligned} \tag{B.16}$$

The eigenenergies of these two approximate eigenstates are given by

$$\mathcal{E}_{\pm} = \frac{\langle\Phi_g^{\pm}(x)|\mathcal{H}(x)|\Phi_g^{\pm}(x)\rangle}{\langle\Phi_g^{\pm}(x)|\Phi_g^{\pm}(x)\rangle} \approx \frac{1}{\sqrt{2}}\left(\langle\Phi_g^{\pm}(x)|\mathcal{U}_L(x)|\Psi_R(x)\rangle \pm i\langle\Phi_g^{\pm}(x)|\mathcal{U}_R(x)|\Psi_L(x)\rangle\right). \tag{B.17}$$

By using Eq. (B.16), we can arrive at the following expression for the eigenenergies,

$$\begin{aligned}\mathcal{E}_{\pm} &\approx \sqrt{2}\,\mathrm{Re}\left[\int_0^{+\infty}\left(\Phi_g^{\pm}(x)\right)^{\dagger}\mathcal{U}_L(x)\Psi_R(x)dx \pm i\int_0^{+\infty}\left(\Phi_g^{\pm}(x)\right)^{\dagger}\mathcal{U}_R(x)\Psi_L(x)dx\right]\\ &\approx \mp\,\mathrm{Im}\left[\int_0^{+\infty}\Psi_R^{\dagger}(x)\mathcal{U}_R(x)\Psi_L(x)dx\right],\end{aligned} \tag{B.18}$$

which can be further simplified:

$$\begin{aligned}\int_0^{+\infty}\Psi_R^{\dagger}(x)\mathcal{U}_R(x)\Psi_L(x)dx &= \int_0^{+\infty}\Psi_R^{\dagger}(x)\left(\mathcal{H}(x)-\mathcal{H}_L(x)\right)\Psi_L(x)dx\\ &= iv_F\Psi_R^{\dagger}(x=0)(\tau_z\otimes\sigma_z)\Psi_L(x=0),\end{aligned} \tag{B.19}$$

where we have integrated the kinetic term by parts. Therefore, we derive

$$\mathcal{E}_{\pm} \approx \mp\, v_F\mathrm{Re}[\Psi_R^{\dagger}(x=0)(\tau_z\otimes\sigma_z)\Psi_L(x=0)].$$

Thus far, our analysis is completely general, having used only the symmetries of the problem at hand. To obtain the final expression, we plug in the explicit forms for $\Psi_{L/R}$ in Eqs. (B.13) and (B.14), which gives:

$$\begin{aligned}E_{\pm} = \frac{1}{2}\mathcal{E}_{\pm} &\approx \pm\, 2v_F\chi_{\Im}^2\, e^{-\frac{\Delta L}{v_F}}\cos\left(\frac{\mu L}{v_F}\right)\\ &= \pm\,\frac{\Delta\mathcal{B}}{\Delta+\mathcal{B}}\, e^{-\frac{\Delta L}{v_F}}\cos\left(\frac{\mu L}{v_F}\right) \xrightarrow{\mathcal{B}\sim\Delta} \pm\,\frac{\Delta}{2}\, e^{-\frac{\Delta L}{v_F}}\cos\left(\frac{\mu L}{v_F}\right).\end{aligned} \tag{B.20}$$

A parallel evaluation of the energy splitting can be worked out for the SC-FM-SC setup with the inclusion of a finite magnetic field term.

It is instructive to compare this result with that obtained by instanton approach in Chapter 6. Importantly, we find that the oscillatory cosine term has exactly the same form in both calculations, and vanishes if the chemical potential is tuned to zero. However, they differ in both the exponential decay rate and the overall prefactor.

Physically there exist two probable mechanisms (or scenarios) that will lead to the splitting of the ground-state degeneracy for Majoranas (and parafermions alike): (1) The first mechanism is the direct overlaps between the two degenerate ground-state wavefunctions. This scenario is restricted to the ground-state manifold. (2) The second mechanism is a bit subtle. Because the ground-state manifold is not isolated or closed, quantum mechanically it will interact with the existing spectrum of the excitation states. It is this virtual interaction between the ground states and those higher-energy states that produces the additional splitting. This second mechanism is somehow overlooked in the literature. Since the bulk system is gapped, both the above-mentioned mechanisms will be exponentially suppressed. Therefore, to properly compute the topological degeneracy splitting, we may need to take into account the combined effects of these two scenarios in a systematic and controlled manner.

The adopted instanton approach may be a feasible way to include the virtual fluctuation effects into the energy-splitting calculation. The existence and the structure of the zero-mode soliton solution provide a semiclassical picture of the connection and overlap between the two ground states in the imaginary-time formalism. This classical soliton solution interpolates between the degenerate vacua by passing through a series of selected intermediate higher-energy states, thus manifesting the fluctuation effects at the saddle-point level. Moreover, when determining the prefactor, we further explicitly incorporate the Gaussian fluctuations about the saddle-point solution, which captures the leading impacts from a beam of paths near the extremal path. Clearly the variational wavefunction-overlap calculation involves only the first mechanism, while the second scenario is missing, which might lead to the discrepancy when compared with the instanton results.

Let us summarize the two key results of this section: (1) the zero-energy splitting in the spin-Hall edge has an oscillatory dependence on μ, which exactly matches that found in the instanton calculation; and (2) though the prefactors of the two calculations do not agree, one would expect the instanton calculation to give more accurate results than the variational approach presented here.